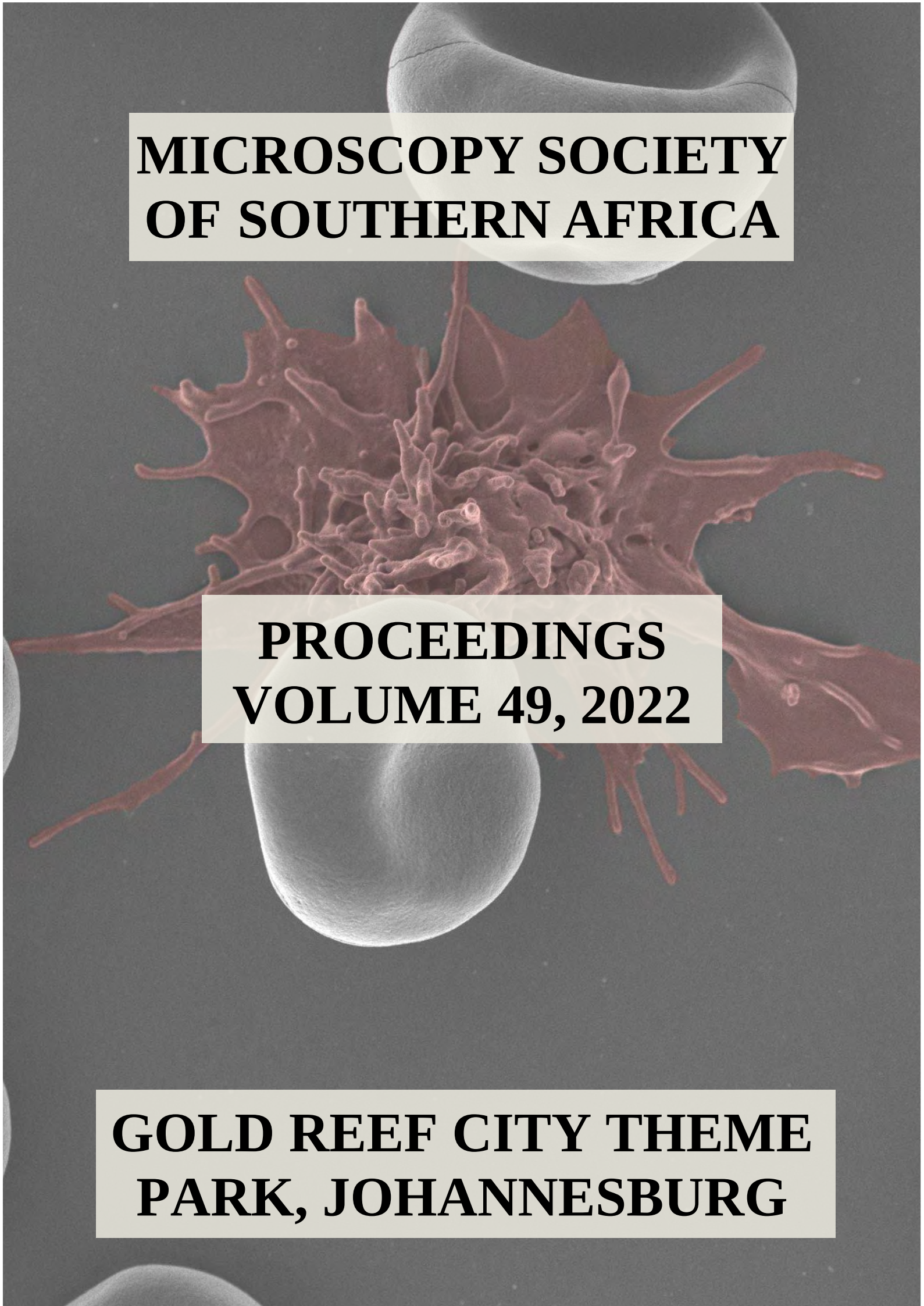

MICROSCOPY SOCIETY OF SOUTHERN AFRICA

PROCEEDINGS VOLUME 49, 2022

GOLD REEF CITY THEME PARK, JOHANNESBURG

THE MICROSCOPY SOCIETY OF SOUTHERN AFRICA

www.microscopy.co.za

The aim of the Society is to promote and develop microscopy and associated techniques at all levels in the South African region.

The Society was founded as the Electron Microscopy Society of Southern Africa (EMSSA) in 1962 and became a formal member of IFSM (the International Federation of Societies for Microscopy) in 1966. The Society changed its name to the Microscopy Society of Southern Africa (MSSA) in 1996 to accommodate all forms of microscopy

The primary objectives of the Society are:

- To further microscopy in the broadest sense all branches of science,
- To facilitate communication and co-operation between microscopists and with other scientists,
- To act as a liaison between members of the Society and IFSM,
- To provide an interface between research, education, government and the public.

This is achieved mainly through:

- an annual meeting of the Society,
- publication of a Newsletter,
- maintenance of an Instrument and Skills database,
- the establishment of regional groups to promote closer co-operative ties.
- an email list server: massa@kendy.up.ac.za

Honorary Members:

Prof B I Balinsky, Prof P Berjak, Prof J Coetzee, Dr N R Comins, Mr R H M Cross, Prof JAA Engelbrecht, Dr J T, Fourie, Mr D Geppert, Mr A N Hall, Mr L Harmsen Prof ME Lee, Dr J Murphy, Prof F Nabarro, Prof JH Neethling, Prof B T Sewell, Prof J T Soley, Dr E M Veenstra, Prof T A Villiers, Dr J Wesley-Smith, Prof H Wilsdorf, Prof M J Witcomb, Dr S Wolfe-Coote.

Cover Micrograph: Scanning Electron Micrograph of an activated platelet between red blood cells

Image taken by Chantelle Venter from Stellenbosch University

MICROSCOPY SOCIETY OF SOUTHERN AFRICA

MIKROSKOPIEVERENIGING VAN SUIDELIKE AFRIKA

UMBUTHO WABAKOPOLI BAMAZANTSI E-AFRIKA

PROCEEDINGS
VERRIGTINGE
INKQUBO-NGXOXO

VOLUME, UMQULU 49, 2022

GOLD REEF CITY THEME PARK, JOHANNESBURG

The 57th Annual Conference was held at Gold Reef City Theme Park, Johannesburg 5 to 8 December 2022.

This volume contains the Proceedings of the Microscopy Society of Southern Africa and is published annually to coincide with the conferences of the Society. The Society does not hold itself responsible for errors in the manuscripts and does not necessarily subscribe to the opinions and conclusions of the authors.

Die 57ste Jaarlikse Konferensie het by Gold Reef City Park, Johannesburg, plaasgevind vanaf 5 – 8 Desember 2022.

Hierdie volume bevat die Verrigtinge van die Mikroskopievereniging van Suidelike Afrika en word uitgegee om met die konferensies van die Vereniging saam te val. Die Vereniging aanvaar nie verantwoordelikeheid vir foute in die manuskripte nie en stem ook nie noodwendig met die menings en gevolgtrekkings van die outeurs saam nie.

Ingqungquthela yeminyaka yama 57 eyayibanjwelwe kwiziko lengqunqguthela lase Gold Reef City Theme Park, Johannesburg, kwisixeko sase Bela-Bela ukususka kumhla we 5 ukuyokuma kowe 8 kweyoMnga ngonyaka wama 2022.

Lomqulu uqulethe inkqubo-ngxoxo zendibano yequmrhu leziKopoli zase maZantsi e-Afrika epapashwa ngonyaka ukuze ingqamane nale ngqungquthela yeliqumrhu. Eliqumrhu liyazikhulula kwiimpazamo ezingakho kwiingqokelela zeentetho ezikulo mqulu kwaye ungarhumi nezimvo nezigqibo zababhali.

Published by the Microscopy Society of Southern Africa, c/o Council for Scientific and Industrial Research,1-Meiring Naude Road, Brummeria , Pretoria, 0001, South Africa

ISSN 0250-0418 : ISBN 978-0-6398435-0-6

MICROSCOPY SOCIETY OF SOUTHERN AFRICA
FIFTY SEVENTH ANNUAL CONFERENCE: 2022

Table of Contents

Invited Lectures

Life Sciences

Materials Sciences

LOW-VOLTAGE SCANNING ELECTRON MICROSCOPY: THE SECRETS OF ION-IRRADIATION INDUCED DAMAGE REVEALED

I. Jóźwik[1,2], J. Jagielski[1,3], E. Dumiszewska[2], P. Caban[2], M. Kamiński[2,4] and U. Kentsch[5]

[1]NOMATEN CoE, NOMATEN MAB+, National Centre for Nuclear Research, Poland, [2]Lukasiewicz Research Network – Institute of Microelectronics and Photonics, Poland, [3]Department of Materials Physics, National Centre for Nuclear Research, Poland, [4]Institute of Microelectronics and Optoelectronics, Warsaw University of Technology, Poland, [5]Institute of Ion Beam Physics and Materials Research, Helmholtz-Zentrum Dresden-Rossendorf e.V. (HZDR), Germany

The technique of implant isolation by ion irradiation with various energetic ions has found application in the microelectronic industry in the creation of insulating regions in electronic semiconductor devices. To verify the extent of the modified area, usually wet selective etching is used. However, it cannot be applied to materials, for which selective etchants do not exist (i.e., GaN). Low-voltage scanning electron microscopy (low-kV SEM) paves the way for new applications in semiconductor technology to detect contrast originating from highly insulating channels produced by ion damage in semiconductors.

The purpose of this study was to directly visualize the resistive areas created by ion irradiation in various semiconductors by means of low kV SEM. The imaging of the cross-sections of the irradiated specimens were performed under ultra-high vacuum conditions with the samples loaded quickly after they were cleaved.

The AlGaAs, GaAs, InAlP and GaN epitaxial layers grown by metalorganic chemical vapor deposition (MOCVD) technique were covered with a mask of gold strips and irradiated with He^+ ions of energy 600 keV with fluences ranging from 8×10^{12} to 5×10^{14} cm^{-2}. SEM images of the freshly cleaved cross sections of irradiated specimens were obtained using a low energy operation mode (E < 0.5 keV) with both a high-resolution SU8230 SEM (Hitachi) and Auriga SEM (Carl Zeiss), both equipped with the highly efficient in-lens SE detection systems.

The Damage-Induced Voltage Alteration (DIVA)[1-5] contrast mechanism is related to altered SE (secondary electron) emission/detection from the semiconductor surface where the local electrical potential has been modified during primary electron bombardment resulting in an increase of ion-damaged-induced resistivity. In the studied cases, the resistivity distribution in the ion-irradiated region is not homogenous, but the damage evolves along the ion irradiation direction, starting from the sample surface towards the bulk, along the initial ion beam direction. As observed, image contrast resulting from ion irradiation and subsequent damage formation within the irradiated layers evolves with the increase in ion fluence and depends on imaging conditions, sample composition and doping level. SEM imaging contrast related to resistivity changes is obtained using primary electrons with energies ranging from 10 keV to 10 eV. The problem of specimen charging in ultra-low energy range and its effect on the contrast in SEM images is addressed for the first time.

SEM imaging with DIVA contrast using low and ultra-low energies can serve as a tool to reveal qualitative information related to the internal resistivity distribution of ion-irradiated semiconductors in two dimensions. This imaging technique is unique and extremely valuable, since it can be applied to observe highly resistant areas even in materials where no alternative method of implant isolation visualization is available (i.e., wet chemical etching). This is extremely important in opto- and micro-electronics technologies involving gallium nitride and other compound semiconductors. The unrivalled advantage of the technique of low-kV SEM lies in its immediate image generation without the need for complex sample preparation.

References:
1. Jóźwik, I. *et al.* (2017) ECS J. Solid State Sci. Techn. 6, 415.
2. Jozwik, I. *et al.* (2019) Microsc. Microanal. 25(Suppl 2), 486.
3. Jóźwik, I. *et al.* (2019) Ultramicroscopy 204, 6.
4. Jóźwik, I. *et al.* (2021) Ultramicroscopy 228, 113333.
5. Jóźwik, I. *et al.* (2022) Mater. Sci. in Semiconductor Processing 138, 106293.

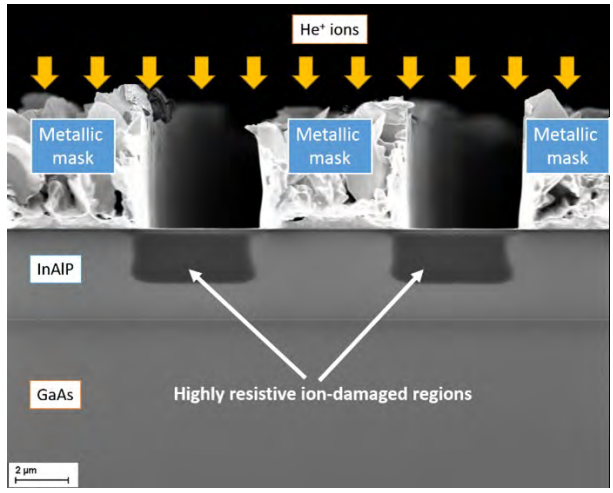

Figure 1. SEM image of InAlP layer cross-section with visible ion-damaged regions.

Corresponding author: iwona.jozwik@ncbj.gov.pl

REVEALING SECRETS HIDING IN *PLAIN SIGHT: ADVANCES IN MULTI-SCALE MULTI-MODAL IMAGING*

M.H. Ellisman[1]

[1]NCMIR, CRBS, University of California San Diego

A grand challenge of modern biology is to understand how molecular, cellular and tissue physiology plays out across a daunting range of spatial and temporal scales. Current imaging methods leave significant gaps in our knowledge, limiting our ability to connect information across scales.

How multiple methods are now being combined to fill and help bridge critical gaps will be shared; including where recent advances to multi-tilt electron tomography (mtEMT)[1] and development of new probes for correlated light (LM)[2,3] (Fig. 1), x-ray microCT (XRM)[4], correlated multi-ion mass spectroscopy imaging (MIMS)[5] and EM (MIMS-EM)[5] and state-of-the-art 3D EM technologies[6] (Fig. 2) add to our knowledge about structure and function in complex biological systems.

Examples of questions being addressed in ongoing research projects will be described to illustrate how development and application of new contrasting methods, imaging tools and data analysis strategies are allowing the observation of otherwise complex or hidden relationships between cellular, subcellular and molecular constituents of cells.

For example, how advances in methods apply to ongoing studies on the intact normal brain and to analyze brain cells and synapses during learning (or when cells and issues respond to stressors inducing degenerative brain disorders like Alzheimer's or Parkinson's) will be shown.

Recent accomplishments to be described include determination of the higher order structure and functional organization of chromatin of intact cell nuclei[7]; the analysis of actin-associated structures within specific brain postsynaptic structures "dendritic spines"[8]; as well as analysis of the extracellular matrix (ECM) around multiple types of synapses of mammalian brains[9].

The ECM work explores Roger Tsien's theory[10] postulating that the brain stores life-long memories by locally managing the activity of extracellular proteases to edit ECM and thereby influences the locations and relative strengths of synapses over time scales as long as life-spans.

References:
1. Phan S. *et al.* (2016) Adv Struct Chem Imaging. DOI: 10.1186/s40679-016-0021-2 .
2. Ellisman M.H. *et al.* (2015) J Chem Biol. 1864-6158.
3. Boassa D. *et al.* (2019) Cell Chem Biol. DOI: 10.1016/j.chembiol.2019.07.007.
4. Bushong E.A. *et al.* (2020) Using X-Ray Microscopy to Increase Targeting Accuracy in Serial Block-Face Scanning Electron Microscopy. New York, Volume Microscopy, Neuromethods, 155.
5. Shefali K.*et al.* (2021) Dev Cell. 2952-2965.e9.
6. Deerinck T.J.*et al* (2017) J Microsc. DOI: 10.1111/jmi.12667.
7. Ou H.D.*et al.* (2017) Science. DOI: 10.1126/science.aag0025.
8.Eberhardt F. *et al.* (2022). eNeuro. DOI: 10.1523/eneuro.0342-22.2022.
9. Kim K.Y. *et al.* (2019). Cell Rep. DOI: 10.1016/j.celrep.2019.09.006.
10. Tsien R.Y. (2013) PNAS. 110(30).

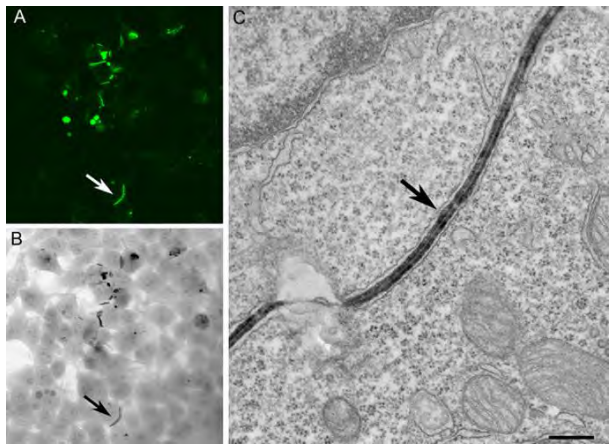

Figure 1. CLEM imaging of connexin43-GFP-APEX. Labeling of the same gap junction (*arrows*) is visualized by **a** confocal, **b** transmitted light, and **c** electron microscopy. *Bar* = 200 nm.

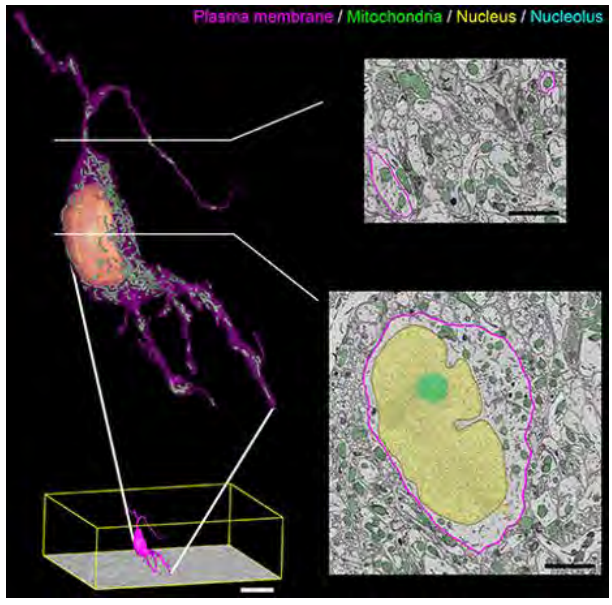

Figure 2. Output surface renderings of segmented organelles within a SCN neuron. *Bar* = 20 µm.

Corresponding author: mellisman@ucsd.edu

HERE IS LOOKING AT YOU, YEAST

C.H. Pohl[1]

[1]Dept. of Microbiology and Biochemistry, University of the Free State, Bloemfontein

Yeasts are often considered “simple unicellular fungi” and used as models of more complex systems. Although this is true, the statement masks the diversity of form and function within the yeasts. Many of them have life cycles containing both sexual and asexual stages. In a group of yeasts, called the Ascomycetes, sexual cells (ascospores) are formed within sac-like structures (plural: asci; singular: ascus). These structures can have a variety of shapes or ornamentations. We have studied these structures as well as lipids (3-hydroxy fatty acids) associated with them, in order to gain a better understanding of the diversity and biological function(s) of these structures.

Various microscopy techniques were used in these studies, ranging from immunofluorescence and confocal laser scanning microscopy to transmission and scanning electron microscopy. In addition, nano scanning Auger microscopy (NanoSAM) was employed to gain further ultrastructural information regarding cellular constituents of fermenting yeasts as well as the effect of antifungals on sexual reproduction of yeasts.

It was found that the morphology of both the asci as well as the ascospores allow for movement and release of the ascospores from confined spaces (i.e. asci) via various mechanisms, such as gear-like movement, cutting or piercing of the ascus or compression of the ascospore[1]. These physical mechanisms are often aided by the lubricating qualities of 3-hydroxy fatty acids. In addition, 3-hydroxy fatty acids were found to be produced in the mitochondria[2] and also play a role in aggregation of ascospores, once released[3], as well as cell-to-cell adherence or flocculation of yeast cells[4]. Interesting observations made using NanoSAM was that fermenting yeast cells are filled with gas bubbles[5] that may deform other organelles[6] and that the antifungal drug, fluconazole, negatively influences ascospore formation and thus sexual reproduction[7].

In conclusion it can be said that despite the relatively simple nature of yeasts, they display a variety of structural adaptations in order for them to achieve their goal of reproduction and growth and that there are numerous ways for us to investigate them. These structural and biochemical characterizations have laid the foundation for numerous other projects on lipid metabolism, virulence and inter species interactions of especially pathogenic yeasts and may even find application in biomimetic engineering.

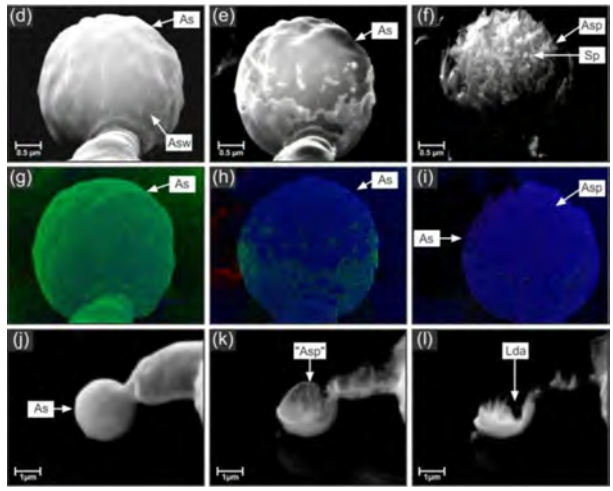

Figure 1. Nano Scanning Auger micrographs of the effect of fluconazole on the ascus (As) and ascospore (Asp) of the yeast, *Nadsonia fulvescence.*

Corresponding author: PohlCH@ufs.ac.za

References:
1. Kock, J.L.F. *et al.* (2004) SA J. Sci. 100, 237.
2. Sebolai, O.M. *et al.* (2008) Can. J. Microbiol. 54, 91.
3. Smith, D.P. *et al.* (2000) Ant. Leeuwenhoek 77, 389
4. Strauss, C.J. *et al.* (2007) Inst. Brew. 113, 42.
5. Swart, C.W. *et al.* (2012) FEMS Yeast Res. 12, 867.
6. Swart, C.W. *et al.* (2013) Inst. Brew. 119, 15.
7. Swart, C.W. *et al.* (2010) Sci. Res. Essay. 5, 3411.

NOVEL INSIGHTS INTO THE GENUS *Leiotrocha* (MOBILIDA: URCEOLARIIDAE)

G.P. de Jager[1,2], L. Basson[1], S. Colin[3] and C. Feldhaus[2]

[1]University of the Free State, [2]Max Planck Institute for Biology, Tübingen, [3]Max Plank Institute for Biology, Tübingen

The symbiotic ciliate Family Urceolariidae Dujardin, 1841, consists of three genera and 19 species, exclusive to invertebrate hosts. The genus *Leiotrocha* Fabré-Domergue, 1888, although cosmopolitan on marine intertidal invertebrate hosts, very little research during the last few decades have been devoted to them. This led to the need for an urgent revision of the genus.

This study introduces a standardized protocol for identifying new urceolariid species. One species from the southern coast of South Africa, *Leiotrocha* sp. A (South African south coast) collected from the spiny chiton, *Acanthochitona garnoti* was used as a "model" species for describing novel morphological and somatic characteristics. Using this protocol eight new South African species can be added to the genus *Leiotrocha* and two to the genus *Polycycla*.

Chiton, bristle worm and sea cucumber hosts were collected along the southern coast of South Africa and patellid hosts at the Livorno harbour in Italy. Leiotrochans were isolated and fixed (3% Glutaraldehyde for SEM, 10% buffered formalin for confocal-, Bouins to 70% ethanol for light microscopy, absolute ethanol for genomics) and stained accordingly. Silver-nitrate impregnated (adhesive disc) and Harris Haematoxylin stained (nuclear apparatus) smears were used for morphometric analysis[1,2] using a Zeiss Axiophot with an AxioCam ICc 5 digital camera.

Multi-photon experiments[3] from unstained individuals were accomplished with an inverted Zeiss LSM 780 multiphoton laser scanning confocal microscope, while Dappi, MitoView and anti a-tubulin-stained individuals were analysed using a Zeiss LSM 900 inverted laser scanning confocal microscope. Electron micrographs and analysis were obtained using a Joel WINSEM JSE 6400 scanning electron microscope at 5kV.

Electron microscopy revealed that all members of the genus *Leiotrocha* has an adoral spiral of 360° (Figs 1A & E) and unique vestigial scopular cilia (Fig. 1B). The plate structure (Figs 1 C, D & E) is less complex compared to their sister family, Trichodinidae and instead of interlocking parts, the plates curves around each other. The macronucleus is large and lobular, while the single micronucleus is small in most *Leiotrocha* species (Figs 1F & 2B). Hyper-symbiontism is present in this group, with many endosymbionts, both bacterial and photosynthetic zooxanthellae (Figs 1H & 2A). The cilia and adhesive disc are lined with extensive tubulin networks (Figs 2C & D). The multi-photon experiment corroborated the presence of chlorophyll *a* bearing endo- symbionts, but also that the adhesive disc, but not the plate, is constructed of a non-symmetrical organic crystalline structure.

During the last century various mobilines from the family Urceolariidae have been mistakenly classified into the genus *Urceolaria* due to insufficient methodology and no standard taxonomic protocol. This study confirmed that *Leiotrocha* consists of 18 species compared to the monophyletic *Urceolaria*, which can morphologically be separated by the complex macro nucleus structure and the presence of vestigial scopular cilia.

References:
1. Lom, J. (1958) J. Protozool. 5, 251.
2. van As, J.G., Basson, L. (1989). Syst. Parasitol. 14, 157.
3. Boyd, R.W. (1992). Non-linear Optics. San Diego, Academic Publishing.

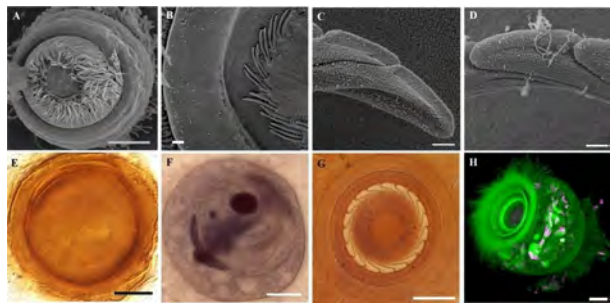

Figure 1. Micrographs of Leiotrocha sp. A from A. garnoti: (A & E) adoral view of ciliary feeding spiral; (B) scopular cilia; (C) adoral and (D) aboral view of plate structure; (F) nuclear apparatus; (G) aboral adhesive disc; (H) 3D reconstruction (Scale: A, E, F, G, H = 10*Leiotrocha* sp. A from *A. garnoti*: (A & E) adoral view of ciliary feeding spiral; (B) scopular cilia; (C) adoral and (D) aboral view of plate structure; (F) nuclear apparatus; (G) aboral adhesive disc; (H) 3D reconstruction (Scale: A, E, F, G, H = 10mm; B, C, D = 1mm).

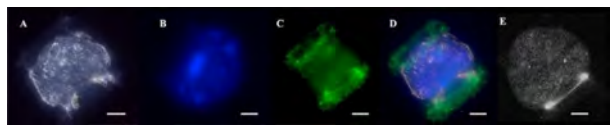

Figure 2. Confocal micrographs of Leiotrocha sp. A, where A – darkfield; B – Dappi stained nuclear material; C- *Leiotrocha* sp. A, where A – darkfield; B – Dappi stained nuclear material; C- a-tubulin stained with Alexa Flour 488 anti a-tubulin; D – compound image of A to D; E – second harmonic projection at 490 nm (Scale: 10mm).

Corresponding author: bassonl@ufs.ac.za

CHARACTERISTIC CAVITIES NO LONGER VALID

J. Hastings[1], L. Basson[1] and G.P. de Jager[1]

[1]Department of Zoology and Entomology, University of the Free State, Bloemfontein

Some of the most commonly encountered ciliates in the aquatic environment belong to the family Trichodinidae[1]. This family is represented by 11 genera of which the majority, seven, have been reported from fish[1]. Representatives of this family are easily identified by the presence of a complex ring of denticles in their aboral adhesive disc. Since the original description by Ehrenberg in 1838, upwards of 250 species have been described. In South Africa, however, only a single historic record exists of a trichodinid species occurring on the gills of the Super Klipfish, *Clinus superciliosus* (Linnaeus, 1758). This species was described as *Trichodina clini* by Fantham in 1930, now considered to be a *nomen nudem* species due to the lack of proper descriptions. In the present study, however, not one but two species were encountered on the gills of the same fish host.

Teleost hosts were collected from the intertidal pools at Jeffreys Bay, South Africa. Wet smears made from skin and gills were examined for ciliates. If trichodinids were present, slides were prepared accordingly for staining and impregnation techniques. Silver nitrate was used to impregnate the complex denticle ring and hæmatoxylin staining to examine the nuclear apparatus (Figs 1A and B). To aid with morphological descriptions material was also collected in 10% buffered neutral formalin and prepared using standard protocols prior to being examined under a JEOL JSM 7800F Field Emission scanning electron microscope at 5kV.

After thorough examination two species were encountered on the gills of *C. superciliosus*. The first species was initially identified as *Trichodina jadranica* Raabe, 1958. Due to the low prevalence of this trichodinid and numerous differences observed, more research is required before this identification can be confirmed. The second species encountered with a higher prevalence has a distinct cup-shaped body with an adoral spiral that consists of long smooth cilia that run along the periphery of the adoral surface (Fig. 2A). This spiral completes more than one full circle before plunging into the infundibulum (Fig. 2A). The prominent C-shaped macronucleus has a closely associated spherical micronucleus near one of the terminal ends (Fig. 1B). The aboral side of the organisms is composed of a ciliary girdle used for locomotion and a complex adhesive disc used for attachment (Fig. 2B). The most complex structure in the adhesive disc, the denticle ring, consists of numerous (range 23-32) interlinking denticles (Fig. 1A). The most striking feature of these denticles is the presence of a distinct cavity in the most distal section referred to as the blade (Figs 2C and D).

Only one other species is documented in the literature with a similar structure in the blade, i.e., *Trichodina rectuncinata* Raabe, 1958. This species is a well-documented and cosmopolitan species. The diagnostic characteristics of this species include pyriform blade cavities, triangular blades and short delicate rays[2,3]. To date all trichodinids encountered with a pyriform blade cavity have been described as *T. rectuncinata*.

Although a similar cavity has been encountered in the present species, there are numerous other morphological traits that differentiate the present species from *T. rectuncinata*. It is suspected that these differences along with its occurrence on an endemic fish host might suggest a new species. The pyriform cavity can therefore no longer be considered unique to *T. rectuncinata*.

References:
1. Basson, L. and van As, J.G. (2006) Fish Diseases and Disorders, Vol. 1, Protozoan and Metazoan Infections. Wallingford, CAB International.
2. Islas-Ortega, A.G. *et al.* (2018) Acta Protozool. 57(2), 145.
3. Islas-Ortega, A.G. *et al.* (2020) J. Parasitol. 106(5), 689.

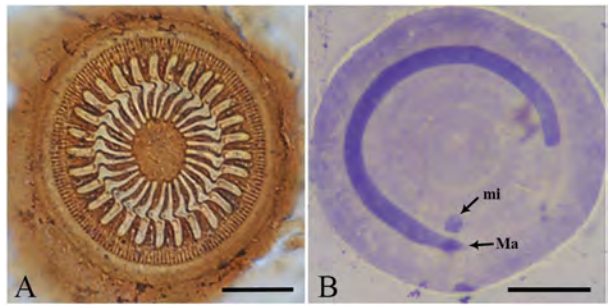

Figure 1. Light micrographs of *Trichodina* sp. A: The complex adhesive disc present in a silver nitrate impregnated individual. B: Hæmatoxylin stained individual indicating the prominent C-shaped macronucleus (Ma) and spherical micronucleus (mi) (scale = 10µm).

Figure 2. Scanning electron micrographs of *Trichodina* sp. A: Body shape, contractile vacuole opening (Cv), adoral spiral (AS) and infundibulum (Inf). B: Adhesive disc with the complex ciliary girdle (CG). C: Aboral view of the denticle ring indicating the (D) prominent blade cavity (scale = 10 µm).

Corresponding author: BassonL@ufs.ac.za

MICROSTRUCTURE OF TOOTH ENAMELOID IN TWO SHARK SPECIES

M.E Waldron[1], J. Wilmers[2] and S. Bargmann[3]

[1]Electron Microscope Unit, University of Cape Town, Cape Town, [2]Department of Solid Mechanics, University of Wuppertal, Wuppertal, Germany, [3]Wuppertal Centre for Smart Materials, University of Wuppertal, Wuppertal, Germany

Hard tissues such as shark enameloid are biological composites of nanoscale mineral crystals, arranged in intricate hierarchical patterns and interspersed with minor amounts of remnant protein. The microstructural design in these tissues results in a macroscopic material that is stiff, strong and tough despite consisting almost completely of brittle mineral[1].

The microstructure of shark enameloid can be complex with variations between species attributable to differences in feeding behaviour and thus, mechanical loads[2]. This study characterizes and compares the enameloid microstructure of two modern lamniform sharks, *Isurus oxyrinchus* (shortfin mako shark) and *Carcharias taurus* (spotted ragged-tooth shark).

Samples of *I. oxyrinchus* and *C. taurus* teeth were placed in moulds and covered in Spurr's epoxy resin which was cured in the oven for 12 hours. The teeth were ground in the longitudinal and transverse planes and the exposed areas were polished with 0.2 μm aluminium powder. The samples were sonicated at 50 Hz in distilled water for 2 minutes, etched with 10% hydrochloric acid for 2 minutes and rinsed in distilled water for 5 minutes. They were carbon coated in an evaporation coater and viewed with a Tescan MIRA SEM at 5 kV.

The microstructural arrangements in the enameloid found in the longitudinal and transverse sections of both species were remarkably similar. The outer layer of dense, randomly orientated crystals was followed by a layer of parallel bundles of crystals and an inner layer of tangled crystal bundles near the core of dentine (Fig. 1). All the bundles were composed of highly aligned crystals of about 60 nm cross-section, in close contact within the bundle, even when the bundle was curved.

In *I. oxyrinchus* the area of parallel bundles and tangled bundles were of similar thickness, but in *C. taurus*, the tangled bundle layer made up approximately two thirds of the enameloid. The layer of parallel bundles in both species, consisted of parallel bundles regularly interspersed with radial bundles at 90O (Fig. 2). This microstructure is thought to increase fracture resistance by providing ‘easy’ crack propagation paths along the discontinuities in crystal orientation. This results in energy dissipation through crack deflection and can guide fractures away from sensitive parts of the tooth[3].

The hierarchical structure of the enameloid was evident in both species. Level 0 is a single nanocrystal, level I is the orientation of the crystals together, level II is the formation of crystal bundles. In level III, bundles were arranged in different orientations and in level IV, the formation of different layers completed the enameloid layer. This microstructure can also be found in the dental enamel of some herbivores, where it is thought to be an adaptation to horizontal mastication movements[4].

Information about the unique microstructure of the enameloid can be applied to the design of synthetic materials such as self-sharpening knives or impact resistant glass.

References:
1. Enax, J. *et al.* (2012) J. Struct. Biol. 178, 290.
2. Frazzetta, T. (1988) Zoomorphology 108, 93.
3. Wilmers, J. and Bargmann, S. (2020) Acta Biomater. 107, 1.
4. Pfretzschner, H.(1992) Enamel microstructure and hypsodonty in large mammals. In Structure, Function and Evolution of Teeth; Smith, P., Tchernov, E., Eds.; Freund Publishing House Ltd.: Tel Aviv, Israel.

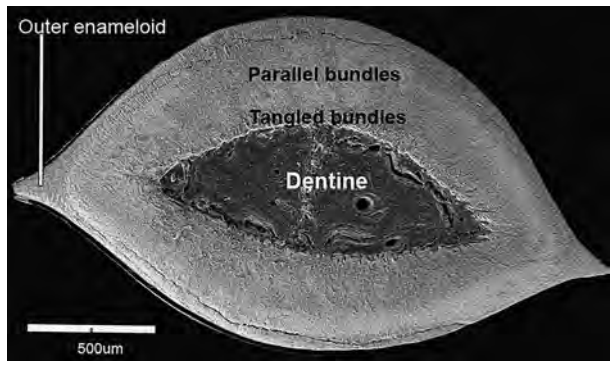

Figure 1. Cross section of *C. taurus* tooth showing three enameloid layers.

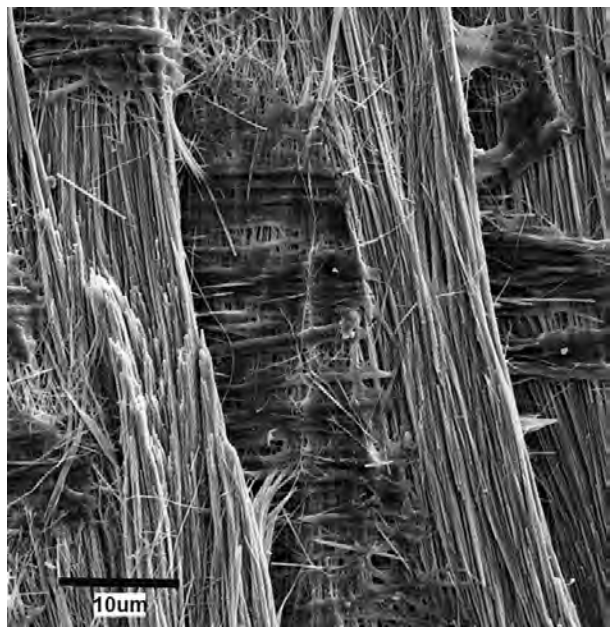

Figure 2. Parallel bundles lying at 90° to each other.

Corresponding author: miranda.waldron@uct.ac.za

PARASITIC FISH PROTISTS - FROM BAD TO GLAM TO DOWNRIGHT PECULIAR

L Basson[1]

[1]University of the Free State

Ectoparasitic protists are found on fish from both freshwater and marine environments, mostly under culture conditions, although some also occur in natural host populations. Most of these belong to the Ciliophora[1], except one that belongs to the phylum Euglenozoa. Some of protists cause serious pathology on fish with high mortalities often reported[1,2]. Others are seldom, if ever, problematic, illustrating some astounding morphological traits, while a third category contains unusual adaptaions to their symbiotic life style.

Fish were collected from freshwater and marine habitats and screened for ectosymbionts. Wet smears were either stained with Mayer's hæmatoxylin to elucidate the nuclear material, or stained with silver nitrate to show specific morphological characteristics. Light micrographs were taken with a Zeiss Axiophot Compound Microscope and a AxioCam ICc 5 camera. Glutaraldehyde fixed samples were prepared for scanning electron microscopy. Standard procedures were followed, where all specimens were dehydrated and critical point dried, mounted on aluminium stubs, sputter coated with gold and examined at 5 kV in a JEOL WINSEM JSM 6400 Scanning Electron Microscope.

The flagellate *Ichthyobodo necator* (Henneguy, 1883) and two ciliates, *Chilodonella piscicola* (Zacharias, 1894) and *Ichthyophthirius multifiliis* Fouquet, 1876 are notorious pathogens, responsible for fish mortalities in various parts of the world[1,2]. *Ichthyobodo necator* has a worldwide distribution, reported from both freshwater and marine hosts. This small flagellate, attaches to the host's dorsal fins or the tips of secondary gill lamellae by a pointed anterior end. In the case of both the cosmopolitan ciliates, *C. piscicola* (Fig. 1A) and *I. multifiliis* (Fig. 1B), these are restricted to freshwater hosts. Both have been implicated in massive mortalities of fish under culture conditions, with the latter considered to be one of the most pathogenic fish ciliates.

Representatives of the picturesque peritrichs are some of the most commonly encountered ectosymbionts on both freshwater and marine fish[1]. However, these ciliates do not feed on their hosts and are never directly responsible for fish mortalities. Some notable morphological traits of these ciliates are truly remarkable. Studies have revealed that the mobilines specifically contain structures in their aboral adhesive discs (Fig. 1C), that not only look like vertebrae in a spinal column, but actually function in exactly the same manner as well.

The last group of protists are just downright odd, in both appearance and lifestyle, even for protists. These are the suctorians (Fig. 1D), also belonging to the phylum Ciliophora. Peculiarities include the fact that adult organisms never contain any cilia, they are always sessile, but yet they are the predators of the microscopical world, and very efficient predators. Tentacles are their weapons of choice, used to capture mostly ciliate prey and extracting their content in a bizarre manner, but not always killing their prey outright.

These parasitic protists grab the attention of scientists sometimes, mainly due to the potential problems these cause under culture conditions. However, we have definitely not begun the journey in discovering the extraordinary and bizarre forms of microscopic life we share our planet with.

References:

1. Basson, L. and van As, J.G. (2006) Fish Diseases and Disorders, Vol 1, Protozoan and Metazoan Infections. Wallingford, CAB International.
2. Woo, P.T.K. (2006) Fish Diseases and Disorders, Vol 1, Protozoan and Metazoan Infections. Wallingford, CAB International.

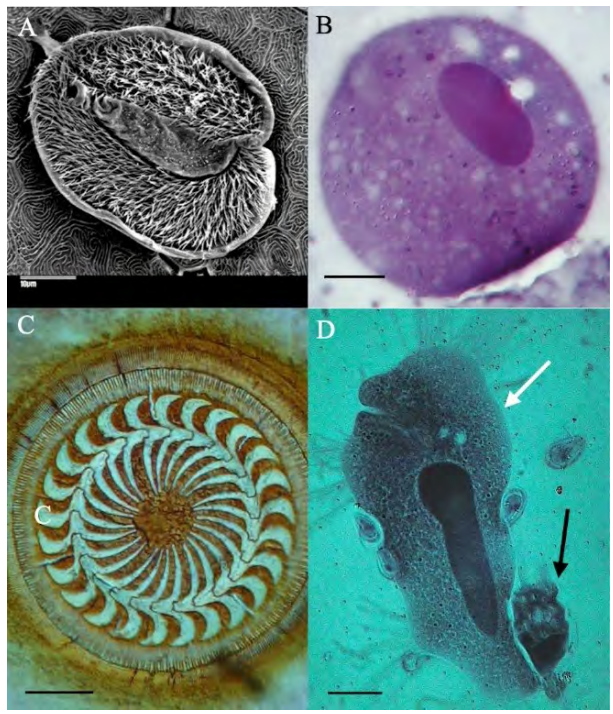

Figure 1. Scanning electron (A) and light micrographs (B-D) of A. *Chilodonella piscicola* (Zacharias, 1894) from *Perca fluviatilis* (Tasmania), B. *Ichthyophthirius multifiliis* Fouquet, 1876 from *Oreochromis andersonii* (Botswana), C. *Trichodina magna* van As and Basson, 1989 from *O. andersonii* (Botswana) and D. *Erastophrya* sp. (white arrow), attached to *Apiosoma* sp. (black arrow) from *Pseudocrenilabrus philander* (Botswana). B & D: Hæmatoxylin stained individuals, C: Silver nitrate impregnations. (Scale = 10 µm (A), 20 µm B-D).

Corresponding author: BassonL@ufs.ac.za

ANTISECRETORY FACTOR (AF16) AS A POTENTIAL THERAPEUTIC AGENT IN A MODEL OF TRAUMATIC BRAIN INJURY

N. Heathcote[1], J. Kriel [2] and B. Loos[1]

[1]Department of Physiological Sciences, University of Stellenbosch, [2]Central Analytical Facilities, University of Stellenbosch

Traumatic brain injury (TBI) is commonly referred to as the silent epidemic and is caused by an external mechanical force to the head which altersnormal brain function and results in clinical manifestations such as headaches, nausea, vomiting and seizures[1]. These clinical manifestations are caused by delayed activation of downstream pathological cascades. The secondary injury, specifically excitotoxicity, excessive calcium ion influx, mitochondrial dysfunction, increased oxidative stress and resulting cell death through altered cell death pathways such as that of autophagy, all contribute to the heterogeneity of TBI[2]. Due to the injury complexity, no effective treatment intervention exists to date.

Antisecretory factor was discovered in 1984 and is a ubiquitously expressed endogenous protein[3]. Synthesis of the anti-secretory motif of this endogenously expressed protein, resulted in a 16 amino acid peptide, named anti-secretory peptide (AF16)[3]. Recently, AF16 has received increasing attention as a possible therapeutic agent for the treatment of brain injuries due to its potential to inhibit fluid secretion and inflammation[4] and its possible role in decreasing intracranial pressure (ICP) and interstitial fluid build-up[5]. However, the molecular mechanisms through which AF16 is able to exert its protective effects, especially in the context of neuronal injury, are largely unknown.

Within this study we aimed to investigate the uptake and localisation of AF16 intracellularly as well as to investigate the protective effect of AF16 in a model of neuronal scratch injury. Mouse Neuroblastoma wild type ($N2A^{wt}$) cells were treated with 10 µM AF16 for 24 hours, whereafter intracellular uptake analysis was performed using a ZEISS LSM780 microscope. Correlative light and electron microscopy (CLEM) was performed to further elucidate the intracellular localisation of AF16 within the ultrastructural context. Cells were then injured using a scratch assay and treated with 10 µM AF16. Post-injury, cells were observed for 36 hours with representative images acquired using a ZEISS Merlin FE SEM every 6 hours,allowing for the analysis of neuronal surface area, surface adhesion and process morphology of cells within the migration zone.

Analysis revealed a significant uptake and distinct cytoplasmic signal of AF16 intracellularly, with AF16 localising significantly to lysosomes. When further elucidated within the ultrastructural context using CLEM, AF16 further localised to double membraned structures characteristic of the autophagosome compartment. When analysing the effect of AF16 on wound closure, AF16 showed an increase in the rate of neuronal wound closure, with further analysis using SEM revealing an observed increase in the length of processes as well as a decrease in filopodia-like structures over time.

We can therefore conclude that AF16 is possibly taken up through a pathway similar to that of endocytosis and that AF16 substantially localises to lysosomes. This, together with the CLEM-based observation that AF16 localises to the autophagy compartment suggests that AF16 may confer neuronal protection post-injury through regulating the autophagy pathway to some extent. This, together with the enhanced neuronal migration upon AF16 exposure, through an increase in process length as well a decrease in filopodia-like structures suggests that AF16 indeed shows promise effects as a potential therapeutic agent.

References:
1. Dewan, M.C. *et al.* (2019) J. of Neurosurgery. 130(4), 1080.
2. Thapa, K. *et al.* (2021) J. of Molecular Neuroscience. 71(9), 1725.
3. Lönnroth, I. and Lange, S. (1984) *FEBS Letters* 177(1), 104.
4. Lönnroth, I. and Lange, S. (1986) BBA - General Subjects 883(1), 138.
5. Al-Olama, M. *et al.* (2015) Acta Neurochirurgica. 157(1), 129.

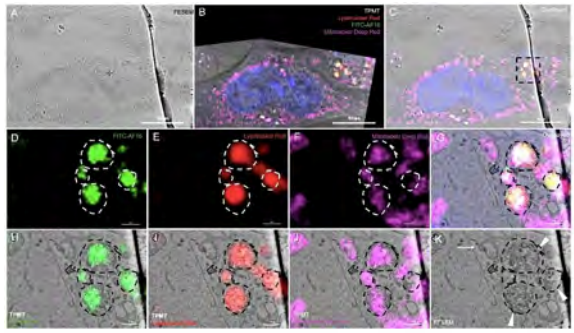

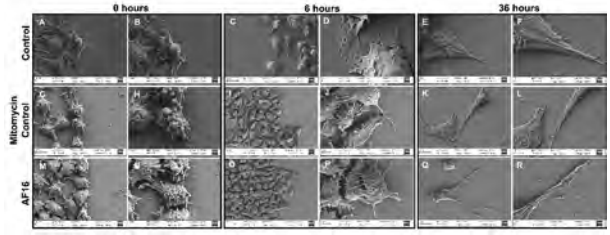

Figure 2. Representative scanning electron micrographs revealing neuronal surface area, surface adhesion and process morphology of cells within the migration zone at 0, 6 and 36 hours post injury.

Corresponding author: nicola.heathcote@outlook.com

IN VITRO EFFECTS OF MAZ-51 IN COMBINATION WITH EGCG IN MELANOMA CELLS

C.C. Nadasen[1], J.C. Serem[1], Y.N. Hlophe [2] and K. Ncube[3]

[1]Department of Anatomy, [2]Department of Physiology, [3]Department of Pharmacology, University of Pretoria, Pretoria, South Africa

Cancer is the growth and division of cells without regulatory systems. In 2020, the international agency for cancer reported 10 million deaths worldwide, with a quarter of those representing South African cases[1]. Melanoma is a cancer of the skin melanocytes which has an aggressive malignancy and a low survival rate[2]. Current therapeutics for melanoma are limited in either efficacy or safety[3]. Epigallocatechin gallate (EGCG), a flavonoid found in green tea, is an ester of epigallocatechin and gallic acid. It interacts with certain cellular targets to inhibit tumour cell proliferation through apoptotic induction and cell cycle arrest[4]. 3-(4-Dimethylamino-naphthelen-1-ylmethylene)-1, 3-hydroindolo-2-one) (MAZ-51) is a selective tyrosine kinase inhibitor that acts as an antagonist in ligand-induced vascular endothelial growth factor receptor 3 (VEGFR-3) autophosphorylation. MAZ-51 blocks tumour cell proliferation by inhibiting the receptor tyrosine kinase domains activated by VEGF ligands C/D[5]. The aim of this project is to determine the possible anticancer effects of EGCG and MAZ-51 on melanoma cells.

The *in vitro* effects of MAZ-51 and EGCG on tumour cell survival was determined using B16F10 melanoma and non-cancerous RAW 264.7 murine macrophage cell lines. Using the crystal violet assay, EGCG (50 – 200 µM) and MAZ-51 (11 – 16 µM) was used to determine percentage cytotoxicity at 25 and 50% inhibitory concentrations (IC_{25} and IC_{50}) (Fig.1). Additionally, polarization-optical differential interference contrast (PlasDIC) microscopy and bright field light microscopy (using haematoxylin and eosin staining) was used to determine morphological changes in intact monolayer cells at the IC combinations. Refer to Fig. 2 for PlasDIC image of untreated B16F10 cells.

The most significant IC_{50} values for B16F10 cells were obtained at 48 hours, 107 µM for EGCG ($p<0.0001$, IC_{50} compared control, no cell death in RAW 264.7 cells) and 34 µM for MAZ-51 ($p<0.0001$, IC_{50} compared control, less cell death in RAW 264.7 cells). Morphological changes concurred with the cytotoxicity data, showing decreased cell density, cell rounding and blebbing indicative of apoptosis in B16F10 cells. Combinations of MAZ-51 and EGCG at IC_{50} and IC_{25} concentrations showed an additive effect.

In conclusion, both MAZ-51 and EGCG showed a significant reduction in B16F10 cells, less so in RAW 264.7 cells. The results of this study agree with the literature thus far, indicating that individually each compound has demonstrated a significant reduction in tumour cell growth. Going forward, the morphological observations of apoptosis will be confirmed using flow cytometry (caspase-3 and cell cycle analysis).

References:
1. Domingues, B. *et al.* (2018) ImmunoTargets and Therapy. 7(7), 35.
2. Sung, H. *et al.* (2021) A Cancer Journal for Clinicians 0(1), 1-41.
3. Singh, S. *et al.* (2017) Life Sciences. 174(7), 50.
4. Aggarwal, V. *et al.* (2020) Seminars in Cancer Biology 7(12), 26.
5. Kirkin, V. *et al.* (2004) International Journal of Cancer 112(6), 986.
6. Zhang, X.*et al.* (2020) Fitoterapia 145, 104634.

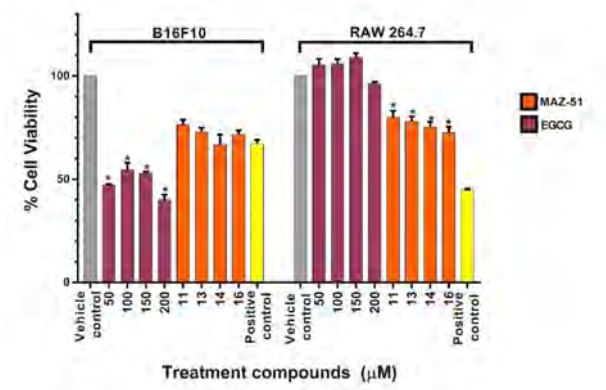

Figure 1. A graph showing the 48-hour crystal violet analysis for B16F10 and RAW 264.7 cells after exposure to MAZ-51 and EGCG. Data is presented as mean ± SEM. ***** represents significant differences ($p<0.05$) between the vehicle control and treatment groups. Drawn using GraphPad Prism v6.01 (California, USA).

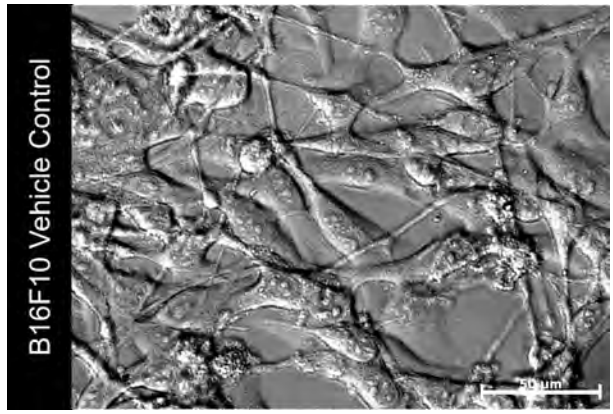

Figure 2. PlasDIC image of untreated B16F10 cells after 48 hours. This image shows the typical morphology of the B16F10 cell which indicates a spindle-shaped morphology[6].

Corresponding author: u18008438@tuks.co.za

MICROSTRUCTURE OF COMMONLY USED AUTOGRAFTS FOR ACL RECONSTRUCTION: QUADRICEPS, PATELLAR AND SEMITENDINOSUS TENDONS

S. Latiff[1] and O. I. Olateju[1]

[1]School of Anatomical Sciences, Faculty of Health Sciences, University of the Witwatersrand, Johannesburg, South Africa

Anterior cruciate ligament (ACL) is a commonly damaged ligament of the knee. An injured or torn ACL requires surgical repair[1]. The goal of achieving and maintaining long-term knee health and stability after an injury is realizable through an ACL reconstruction using autografts, which are harvested from the same individual to reconstruct the damaged or torn ligament[2]. Several tendons, for example the quadriceps (QT), the patellar (PT) or the semitendinosus (ST) tendon can be used as an autograft. The composition of the tendons is similar to the ACL but there are no data that directly compare the compositions of the QT, PT and ST. Therefore, the present study used light microscopy to investigate the microstructures of QT, PT and ST commonly used for ACL reconstruction by quantifying and comparing the tenocyte distribution and collagen content in these tendons obtained from cadavers of South Africans of European Ancestry (Ethics Waiver Number: W-CJ-140604-1).

Samples of the QT, PT and ST of the right leg were collected from 9 female and 7 male formalin-fixed cadavers. A tissue sample of the QT or PT (1 cm x 0.5 cm) was removed from the central half of the tendon while a tissue sample of about 1 cm long was cut half-way along the ST. The tissues were further fixed in 10% buffered formalin and thereafter was processed for histology. Sections were cut at 9 μm thickness using a sliding microtome. The slides with the sections were kept at room temperature before staining with (a) hematoxylin and eosin (H&E) to reveal the general microstructure and to quantify the distribution of tenocytes, or with (b) Masson's Trichrome (MT): to reveal collagen fibers and to quantify the collagen content. The tenocyte distribution and the collagen content were assessed using ImageJ software[4].

At a microscopic level, the three tendons have similar micro-architectural arrangements (Fig. 1). Fascicles made up of aggregates of collagen molecules were organized side–by–side and end–to–end along the tendon as seen in the H&E or the MT stains. Several fascicles aggregate to form the tendon fibers. The tenocytes appeared blue–stained in the H&E (Figs 1a–c) and were mostly spindle or flat in shape, sparsely distributed along the fascicles in the form of longitudinal arrays. Numerous collagen deposits appeared green–stained in the MT (Figs 1d–f). Similarly, collagen was conspicuously present and widely distributed in all the tendons assessed. Tendons were generally composed of closely packed collagen fibers with tenocytes interspersed within the collagen bundles. The tenocytes and collagen contribute to the strength of tendons which are essential for the success of an ACL reconstruction. From these observations, the microstructural arrangements in all the tendons (QT, PT and ST) were similar.

The tenocyte distribution or the collagen content was compared across the tendons. The results showed similarities in the collagen contents across the tendons. On the other hand, the tenocyte distribution was significantly higher in the QT ($p=0.003$) or the ST ($p=0.019$) than in the PT in the female, but no difference was found in the male ($p=0.872$). This shows that a large harvestable area may not be directly associated with a more abundant collagen content or tenocyte distribution. In addition, the differences in tenocyte distribution between both sexes is an important observation that underpins the possible influence of underlying biological factors (e.g. hormones) on the composition of each tendon and which may impact on the healing process and the return of knee functions. It has been shown that biological factors influence growth factors and the impact of growth factors on the tenocytes and collagen cannot be overlooked[3]. The reason for the female-specific tenocyte distribution patterns in the present study remains unknown and which requires further investigation. This study provides additional cues on the differences in the tenocyte distribution and collagen contents of commonly used autografts and highlights the possible role of biological factors on the tendon composition. Overall, this study will contribute to knowledge and assist orthopedic surgeons in making an informed decision on the choice of graft.

References:
1. Sayampanathan, A.A. *et al*. (2017) J. Orthop. Surg. 25(1), 1.
2. Lalwani, R. *et al*. (2020) Anat. Cell Biol. 53(4), 398.
3. Spelsberg, T.C. *et al*. (1999) Mol. Endocrinol. 13, 819.
4. Schneider, C. A., Rasband, W. S., and Eliceiri, K. W. (2012) Nature Methods, 9(7), 671, doi:10.1038/nmeth.2089.

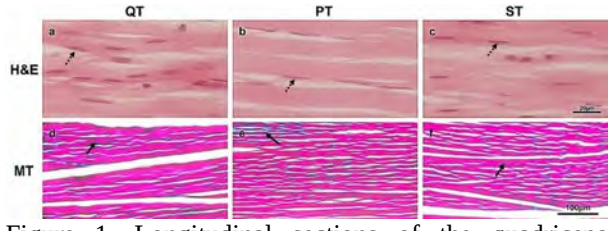

Figure 1. Longitudinal sections of the quadriceps tendon (a, d), the patellar tendon (b, e) and the semitendinosus tendon (c, f). In the H&E staining, the blue–stained tenocytes (broken arrows) appeared spindle or flat in shape. In the MT staining, collagen appeared green–stained (solid arrows).

Corresponding author: oladiran.olateju@wits.ac.za

AN *IN VITRO* INVESTIGATION OF KYNURENINE COMPOUNDS ON MELANOMA GROWTH AND INTRACELLULAR MORPHOLOGY

C. Basson[1], J. Serem[2], P. Bipath[1] and Y. Hlophe[1]

[1]Department of Physiology, [2]Department of Anatomy, University of Pretoria, Pretoria

Although melanoma is a rare type of cancer, accounting for less than 5% of all skin cancers[1], it is amongst the most deadly as it accounts for 75% of skin cancer mortality worldwide[2]. The increase in the melanoma-related mortality rate demonstrates the urgency for new treatment strategies[3]. Compounds implicated in the kynurenine pathway, namely L-kynurenine (L-kyn), quinolinic acid (Quin) and kynurenic acid (KA) [4] previously displayed antiproliferative and cytotoxic effects *in vitro* against cancer cells[5]. Therefore, the aim of this study was to expound on the effect of the aforementioned metabolites on the *in vitro* cytotoxic effects on melanoma cells.

Melanoma cells (B16 F10) and a non-cancerous control murine macrophage cell line (RAW 264.7) were treated with L-kyn (1.74 mM), Quin (8.23 mM) and KA (21.52 mM) for 48 hours. Standard operating procedure (including conventional chemical fixation) for transmission electron microscopy (TEM) was used to assess intracellular morphological changes. Flow cytometry was then used to quantify apoptosis via dual staining with Annexin V and propidium iodide (PI), as well as caspase-3 (human/mouse cleaved caspase-3 (asp 175) 405nm) expression levels.

B16 F10 melanoma cells exposed to KA resulted in non-specific cytotoxicity towards cancer and KA was thus excluded from subsequent experiments. Morphologically, L-kyn and Quin at IC_{50} induced moderate swelling of the rough endoplasmic reticulum (figure 2) and Golgi as well as produced myelin figures in the cytoplasm of B16 F10 cells. Flow cytometry revealed an increase in apoptosis (Annexin V) after treatment with L-kyn and Quin in both cell lines cells. In addition, L-kyn but not Quin, significantly increased caspase-3 expression in both cell lines, confirming apoptotic effects in L-kyn exposed cells.

L-kyn and Quin are potential exogenous compounds which reduced cellular proliferation, induced intracellular changes and promoted cell death (Annexin V (apoptosis) and PI (necrosis)) in melanoma cells. Furthermore, L-kyn was shown to be the most potent compound and may offer future treatment strategies in combination with other viable treatments against melanoma. Future research is required to substantiate the finding of this study.

This study was supported by the Research Development Program (RDP) of Dr Hlophe and Dr Serem as well as the Faculty of Health Sciences School of Medicine Research Committee of the University of Pretoria.

References:

1. Rebecca V.W., Somasundaram R. and Herlyn M. (2020) Nat. Commun. 11(1), 2858.
2. Davis L.E. *et al.* (2019) Cancer Biol. Ther. 20(11),1366.
3. Guan M. *et al.* (2021) Front. Bioeng. Biotechnol. 9(182), 661214.
4. Macchiarulo A. *et al.* (2008) Amino acids. 3, 219.
5. Walczak K. *et al.* (2020) Int J Mol Sci. 21(21), 7946.

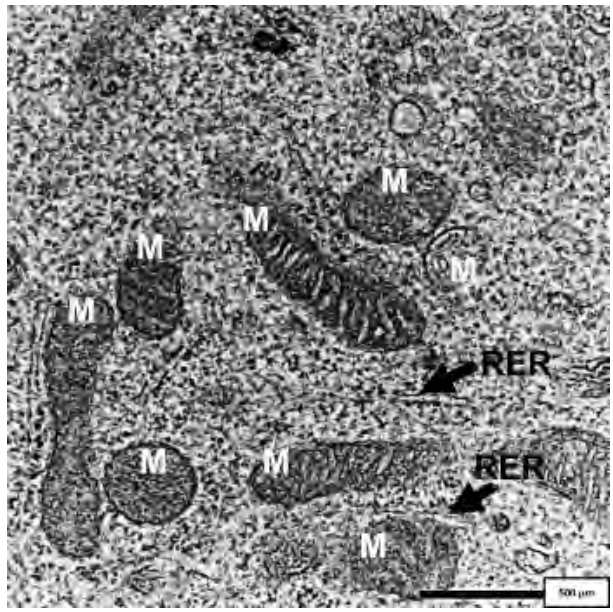

Figure 1. Transmission electron micrograph of control B16 F10 cell at 48 hours after exposure to PBS. M, Mitochondria; RER, rough endoplasmic reticulum.

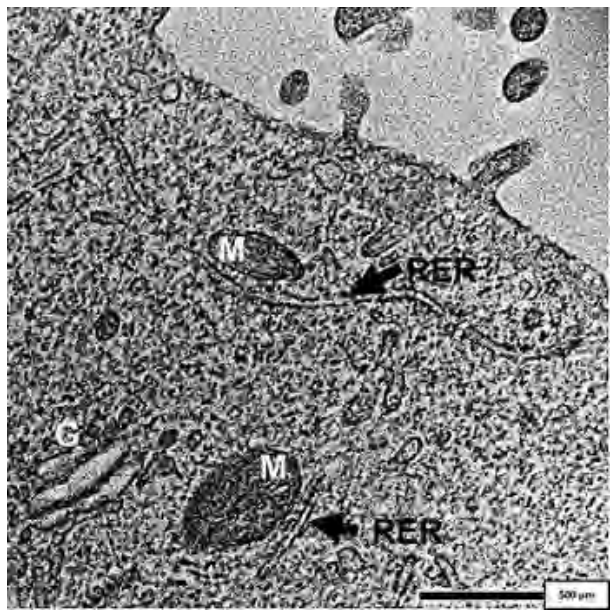

Figure 2. Transmission electron micrograph of B16 F10 cell at 48 hours after exposure to L-kyn at 1.74 mM. G, Golgi complex; M, Mitochondria; RER, rough endoplasmic reticulum.

Corresponding author: charlise.basson@gmail.com

MORE THAN JUST A PRETTY PICTURE: EXPLORING THE TRUE IMPORTANCE OF MICROSCOPY

A.C. Swanepoel[1]

[1]The Centre of Excellence for Nutrition, North-West University, South Africa

Female coagulatory health has been my research focus since 2011. This includes investigating the characteristics of different blood clotting components during normal physiological processes in women namely the menstrual cycle and pregnancy, which are governed by endogenous, natural hormones. I have also investigated the effect that synthetic hormones, used in oral contraceptive pills (OCPs), have on coagulation. OCPs are commonly prescribed, not only for their contraceptive properties but also as treatment for other conditions such as polycystic ovarian syndrome (PCOS) and protection against endometrial and ovarian cancer.[1] The synthetic hormones found in OCPs are known to increase the risk of blood clots.[2]

Blood clotting is an intricate process where platelets and fibrin, along with red blood cells, play an important role in maintaining haemostasis.[3]

For microscopy analysis whole blood (WB) and platelet poor plasma (PPP) obtained from healthy female participants (classified as either 1) non-pregnant and not using any hormonal treatment (controls); or 2) pregnant; or 3) using different oral contraceptives) were analysed using scanning electron microscopy (SEM) in conjunction with other methods.

For SEM analysis blood smears (WB or PPP) were prepared on round glass cover slip, which were placed onto a 24-well plate and immersed in 0.075 M phosphate buffer solution (PBS) for 15 minutes. Primary fixation with 4% formaldehyde for 30 minutes was followed by three rinsing steps with PBS for 3 minutes each. Secondary fixation with osmium tetroxide (15 minutes) was followed by a rinsing step as before. The samples were dehydrated using a series of ethanol rinses (30, 50, 70, 90, and 100% ethanol for 3 minutes each) with the 100% ethanol step done in triplicate. The samples were immersed in 1,1,1,3,3,3-Hexa-methyldisilazane (HMDS) for 30 minutes after which only a single drop of HMDS was placed directly onto the samples and left to air dry over-night. An aluminum platform was used to mount the samples on using carbon tape and then coated with carbon, after which the samples were examined at 1 kV accelerating voltage in a Zeiss Crossbeam 540 Field Emission Gun High-resolution CryoSEM (Zeiss), located at the Microscopy and Microanalysis Unit at the University of Pretoria.

I have found that SEM has proven to be essential for individualized patient-centered precision medicine and accentuating interactions between certain coagulation factors that cannot be determined with other haemostatic testing. Microscopy is not only a useful tool for qualitative research (although a picture is worth a thousand words) but can be implemented to provide quantitative outputs that strengthens your research findings, as I have found when examining fibrin networks prepared from PPP of pregnant women as well as women using OCPs. A multidisciplinary approach, where microscopy is combined with other techniques in your own field of expertise (for my research other coagulation analysis like thromboelastography and turbidimetry) or with those of another discipline/department/specialty (such as metabolomics), will provide support for your microscopy findings and eliminate the need for speculation. My collaborations with researchers from other faculties and universities have been essential for understanding the mechanisms that drive the changes observed with SEM. I aim to substantiate and elaborate on the true importance of microscopy from the lessons that I have learned, and the micrographs I have taken, during my research over the past decade.

References:
1. Sha, D. and Patil, M. (2018) J. Hum. Reprod. Sci. 11(2), 96.
2. Dragoman, M.V. *et al.* (2018) Int. J. Gynaecol. Obstet. 141(3), 287.
3. Herd, C. and Page, C. (1994) Eur. Respir. J. 7, 1145.

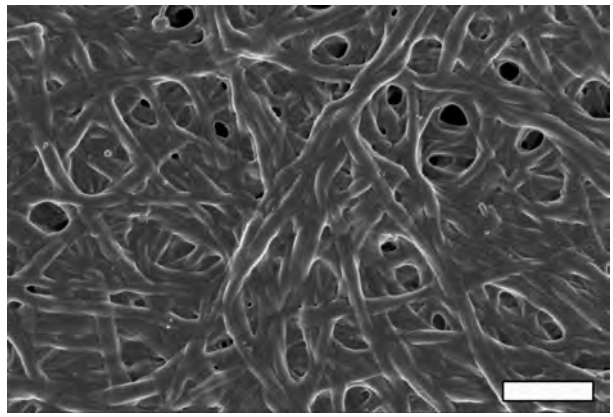

Figure 1. Alterations to fibrin network when using OCPs.

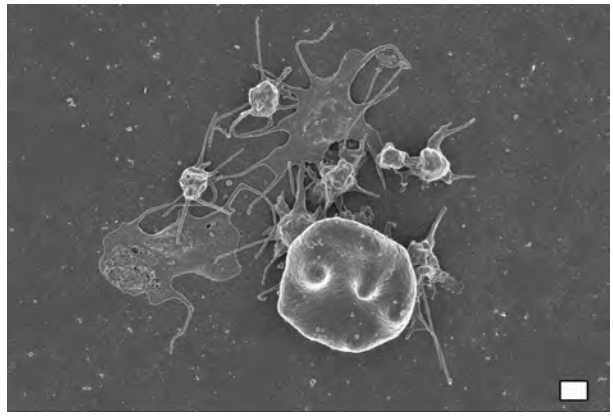

Figure 2. Changes to red blood cells and platelets associated with OCP use.

Corresponding author: albe.swanepoel@nwu.ac.za

THE EFFECT OF CALCITRIOL ON CLOT FORMATION AND STRUCTURE IN PROSTATE CANCER

J. Bester[1], M. Schultz[1] and M. Hoek[2]

[1]Department of Physiology, [2]Department of Urology, University of Pretoria, Pretoria

It is known that prostate cancer (PCa) patients have an increased risk for thrombo-embolic events, specifically triggered by tissue factor activation[1]. Vitamin D (Vit D) has anticoagulant properties which down-regulate tissue factor expression[2, 3]. In a study a high-dose of Vit D supplementation was associated with a reduction in *in vitro* thrombin generation and decreased clot density, signifying that Vit D supplementation can improve the prothrombotic profile[4]. In this study, the effect of Calcitriol on clot formation, structure, and viscoelastic properties was evaluated in PCa patients. Calcitriol or 1,25-dihydroxycholecalciferol is the active form of Vit D, which is normally made by the kidney.

The study consisted of a total of 81 participants divided into metastatic, non-metastatic and control groups. Blood samples were exposed *ex vivo* with a single dose of 0.5 ug/kg of Calcitriol for 10 minutes before analyses. Thromboelastography® (TEG®) was used to assess clot kinetics during clot formation. Citrated whole blood (WB) was used and 340 µL of the blood was added to 20 µL of 0.2 M CaCl2 in a disposable TEG® cup. The samples were then inserted and analyzed in the computer-controlled Thromboelastograph® 5000 Hemostasis Analyzer System (Haemonetics Inc., Braintree, MA, USA) at 37°C. Clot morphology was studied using scanning electron microscopy (SEM). Smears were made with WB samples and 10 µL of blood was placed on a glass coverslip with the addition of thrombin at 6.66 IU/mL (donated by the South African National Blood Service). After this the samples were washed, fixed, dehydrated and carbon coated before viewing the samples with a high-resolution crossbeam 540 Zeiss SEM at the Unit for Microscopy and Microanalysis at the University of Pretoria. Micrographs were taken at 1kV with the InLens detector.

There were no noteworthy differences between the non-metastatic group before and after treatment compared to the control group with regard to the SEM and TEG® analyses (Figs 1 A, B, D and E). In both groups, the red blood cells (RBCs) had a normal biconcave shape and an organized network of fibrin fibers. The morphological analysis of the metastatic group before treatment revealed that the metastatic group had obvious changes with regard to platelet activity and fibrin morphology (Fig 1 C). The RBCs mostly had a normal biconcave shape however the fibrin network of the metastatic group was thick, fused and disorganized fibers when compared to the control group. The TEG® showed an increased viscoelastic profile for the metastatic group indicative of a hypercoagulable state. After treatment there were slight improvements visible with the SEM (Fig. 1 F) however this was not seen in the TEG®. Therefore, the metastatic group was not significantly affected by a single dose as a hypercoagulable state was still evident.

Vitamin D supplementation may improve clot morphology of PCa patients, however, limited changes were observed in the viscoelasticity of clot formation. A higher dose or more frequent doses of Vit D might lead to less-lethal clot formation, as seen in the non-metastatic group. The metastatic group showed greater resistance to improvement therefore further evaluation with *in vivo* supplementation with multiple doses is needed.

Acknowledgments: The authors would like to thank all the volunteers from the Urology clinic that participated in this study.

References:
1. Chaturvedi, S. *et al*. (2014) PLoS One 9(8), e94048.
2. Ehsanian, R. *et al*. (2019) PM&R. 11(2), 125.
3. Targher, G., Pichiri. I., Lippi, G. (2012) Semin. Thromb. Hemost. 38(01), 114.
4. Blondon, M. *et al*. (2019) Endocr. Connect. 8(11), 1447.

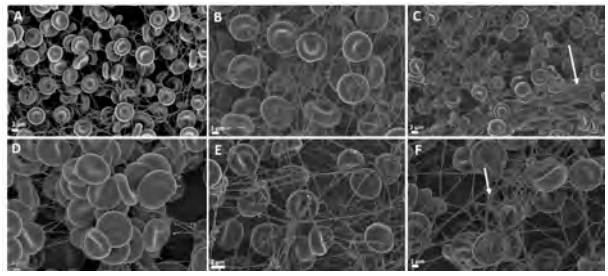

Figure 1. **A)** SEM image of a control individual showing normal cell morphology and fibrin network BTx, this was also seen in the group ATx in Figure D. **B)** Non-metastatic PCa group BTx with normal RBCs and fibrin fibers. **C)** Metastatic PCa group BTx showing normal RBC morphology with an abnormal fibrin network (arrow). The fibers are fused and not evenly distributed. **E)** Non-metastatic PCa group ATx with normal RBCs and fibrin fibers. **F)** Metastatic PCa group after treatment showing normal RBC morphology with some abnormal fibrin fibers (arrow). BTx: before treatment, ATx: after treatment

Corresponding author: janette.bester@up.ac.za

INVESTIGATING THE EFFECTS OF COVID-19 VACCINES ON THE COAGULATION SYSTEM

C. Venter[1] and E. Pretorius[1]

[1]Department of Physiological Sciences, Stellenbosch University, Stellenbosch, South Africa

In March 2020 the World Health Organization (WHO) declared the new coronavirus disease 2019 (COVID-19) outbreak, a global pandemic[1,2]. Since then, vaccines were developed to help to fight the COVID-19 virus and began with the mRNA Pfizer BioNTech (BNT162b2) COVID-19 vaccine followed by the viral vector vaccines Oxford/AstraZeneca (ChAdOx1-S) and Johnson & Johnson (J&J) (Ad26.COV 2.S)[3].

The two main vaccines made available in South Africa included the single dose J&J and double dose Pfizer vaccines[3]. Because the development and testing of the new vaccines was done in record breaking time it caused many controversies regarding the safety and effectiveness of the vaccines. As with all other vaccines, some side-effects are expected, and despite these side-effects the vaccines have shown to reduce the symptoms and severity of COVID-19 infections and reduce the chance for hospitalization[3]. In recent articles published by Pretorius, *et.al.*, effects on the coagulation system has been noticed after exposure to COVID-19 and also later in Long COVID patients[4]. Changes include platelet hyper activation and microclot formation in the blood[4,5]. Thus, the aim of the study was to investigate the possible effects that Pfizer and J&J vaccines might have on the coagulation system.

Human blood was collected from 11 consenting donors before and week one and two after their vaccine administration (Ethics Number: C22/09/004_COVID-19 and Project ID: 26437). Whole blood (WB) was used for scanning electron microscopy (SEM) and thromboelastography® (TEG®) analysis, where after centrifugation, the platelet poor plasma (PPP) and haematocrit was used for the fluorescence microscopy analysis. Whole blood samples were processed according to the standard SEM processing procedure followed by mounting, carbon coating, and examined with the Zeiss Merlin FEG-SEM. Viscoelastic analysis was completed by adding 340µℓ WB in a cup of the TEG® (TEG® 5000 Hemostasis Analyzer) together with 20µℓ of 0.2M calcium chloride to activate the coagulation process[6]. The process was allowed to run until maximal amplitude was reached.

For the fluorescence platelet analysis, CD62P-PE (IM1759U, Beckman Coulter) and PAC-1 FITC (340507, BD Biosciences) was added to the haematocrit for 30 minutes. To visualize the platelets, the excitation wavelength for PAC-1 was set at 450-488nm and the emission at 499-529nm and for the CD62P marker it was set at 540-570nm and the emission 577-607nm. The PPP samples was exposed to Thioflavin T (Sigma-Aldrich) for 30 minutes and visualize using the same settings as the PAC-1 marker. The samples were viewed using the Zeiss Axio Observer 7 fluorescent microscope. Results were analyzed using the platelet and plasma microclot criteria system[7].

From the fluorescence platelet and microclot analysis a trend was seen that after the first vaccine administration an increase in platelet activation (Figs 1A and B) and microclots were seen after the first week, but these pathologies decreased after the second week. The SEM results showed a similar trend. This is in line with wat is seen in other publications that state that after vaccine administration there is an increase in platelet activations[8]. The TEG® results indicated a hypercoagulable trend two weeks after vaccine administration.

Vaccines are crucial in reducing fatalities in diseases like COVID-19 and vaccination roll-out and global accessibility is vital in pandemic. The current findings show that both vaccines cause an increase in platelet activation, microclot formation within the first week of administration, but subsides after two weeks, with hypercoagulation still seen in the second week after the vaccine injection. Thus, our results support previous work suggesting that patients with comorbidities should be monitored by their physicians when they receive their vaccines[9,10]. These findings may in future help to refine the guidelines for safer administration of the COVID-19 vaccines.

References:
1. Lone, S.A. and Ahmad, A. (2020) Emerg. microbes & infect. 9(1), 1300.
2. Mussi, F., Mussi, N., and Dioaiuti, F. (2020) Clin. Neuropsychiatry 17(2), 63.
3. W.H.O. 2022. (Online). https://www.who.int/.
4. Pretorius, E. *et al.* (2021) Cardiovasc. Diabetol. 20(1), 1.
5. Venter, C. *et al.* (2020). Int. J. Mol. Sci. 21, 8234.
6. Van Rooy, M.-J. *et al.* (2015) Cardiovasc. Diabetol. 14(86), 1.
7. Laubscher, G.J. *et al.* (2021). J. Clin. Med. 10(22), 5381.
8. Greinacher, A. *et al.* (2021) Blood. 138(22), 2256.
9. Liu, J. *et al.* (2021). Cell Discov. 7(1), 1.
10. Ostrowski, S.R. *et al.* (2021). Front. Immunol. 12, 779453.

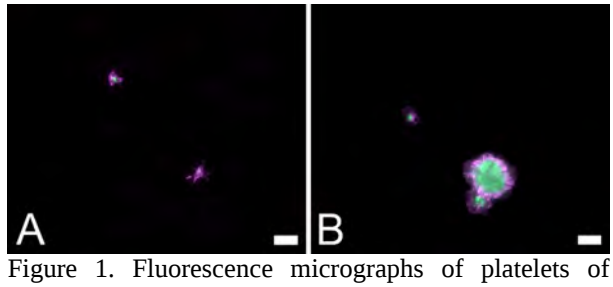

Figure 1. Fluorescence micrographs of platelets of control (A) and 1 week after 1st vaccine injection (B) [CD62P-PE (pink) and PAC-1 FITC (green)] (Scale bars: 10µm).

Corresponding author: chantellev@sun.ac.za

FIBRINALOID MICROCLOTS AND HYPERACTIVATED PLATELETS IN MYALGIC ENCEPHALOMYELTITIS/CHRONIC FATIGUE SYNDROME

J.M. Nunes[1] and E. Pretorius[1]

[1]Department of Physiological Sciences, Stellenbosch University, Stellenbosch

Myalgic encephalomyelitis/chronic fatigue syndrome (ME/CFS) is a complex, debilitating, multisystem disease characterized by unresolved fatigue and an intolerance to physical and cognitive exertion. There is neither a diagnostic biomarker, nor a treatment available, and a clear aetiological explanation is yet to be established. ME/CFS shares many similarities with the post-viral syndrome caused by the SARS-CoV-2 virus, called Long COVID. Symptoms overlap and both are triggered by infection[1]. Previously, we identified small amyloid clots, called fibrinaloid microclots, and hyperactivated platelets associated with a hypercoagulable state in the blood of Long COVID patients[2]. Hence, we set out to assess whether the clotting pathology present within Long COVID is reflected in ME/CFS.

Blood was obtained from 25 ME/CFS individuals, along with 15 gender- and age-matched controls. All participants were previously uninfected with SARS-CoV-2, and had not received a SARS-CoV-2 vaccine within the three weeks prior to blood collection. In order to measure fibrinaloid microclots, platelet-poor plasma (PPP) samples were incubated with the fluorescent probe, thioflavin T (ThT), which binds to hydrophobic areas on fibrinogen indicative of amyloid protein changes[3], at a final concentration of 0.005 mM. Samples were viewed with a Zeiss Axio Observer 7 fluorescent microscope with a Plan-Apochromat 63×/1.4 Oil DIC M27 objective (Carl Zeiss Microscopy, Munich, Germany), using an excitation and emission wavelength of 450-488nm and of 499-529nm, respectively.The % area amyloid was determined using ImageJ 1.53e. Platelets were visualised using hematocrit samples incubated with PAC-1 (FITC-conjugated) and CD62P (PE-conjugated) antibodies. 20 µL of hematocrit was exposed to 4 µL of each fluorescent antibody for 30 minutes. The excitation and emission wavelength for PAC-1 was set at 450-488nm and 499-529nm, respectively; that for CD62P was set at 540-570nm and 577-607nm. Viscoelastic properties of both whole-blood (WB) and PPP was assessed using the Thrombelastograph® (TEG®) 5000 Hemostasis Analyzer, whereby 340 µL of sample was exposed to 20 µL of 0.01M calcium chloride to initiate coagulation. WB samples from the ME/CFS group were assessed against a standard clinical range, whereas PPP samples were compared between control and ME/CFS groups.

Significant levels (p=0.0001) of fibrinaloid microclots were observed in the ME/CFS group as determined by an unpaired Mann-Whitney test, with a mean % area amyloid of 1.37 ± 3.05, compared to 0.10 ± 0.54 for the controls. Platelets from the ME/CFS population exhibited a greater extent of activation than the control group, as indicated by spreading (arrow) and clumping (Fig. 1). ME/CFS platelets also expressed extensive granulation. Roughly half of the ME/CFS WB samples fell out of standard range, directed to the hypercoagulable terminal, for 5 out of 7 of the TEG® parameters assessed. Significant differences were observed in α-angle (p=0.002) and MRTG (p=0.0009) measurements in PPP samples as determined by unpaired Mann-Whitney tests.

The presence of fibrinaloid microclots and hyperactivated platelets brings attention to their potential role in ME/CFS pathology. Fibrinaloids can damage the endothelium, block microcapillaries and reduce tissue perfusion[4], perhaps accounting for, in part, the symptoms associated with ME/CFS and Long COVID. The hyperactivity of platelets, in addition to increasing clotting propensity, may also drive ME/CFS pathology by secreting inflammagens that affect endothelial cells and immune function.

Here we present data supporting the notion that ME/CFS is accompanied by vascular pathology involving the coagulation system, and that this pathology is mirrored in the similarly presenting Long COVID. It also points at novel treatment strategies using drugs and/or nutraceuticals that target platelet hyperactivity, anomalous clotting and potential endothelial inflammation.

References:
1. Wong, T. and Weitzer, D. (2021) Medicina, 57(5), 418.
2. Pretorius, E. *et al*. (2021) Cardiovascular Diabetology, 20(1).
3. Gade Malmos, K., *et* al. (2017) Amyloid, 24(1), 1.
4. Kell, D., Laubscher, G. and Pretorius, E. (2022) Biochemical Journal, 479(4), 537

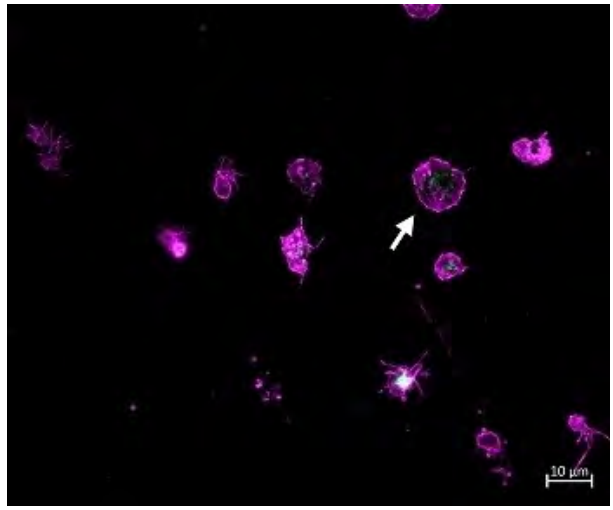

Figure 1. Hyperactivated platelets from an ME/CFS individual exposed to both PAC-1 and CD62P antibodies. Arrow indicates spreading. Scale bars: 10 µm.

Corresponding author: resiap@sun.ac.za

EVALUATION OF APOPTOTIC IMPACT OF ATORVASTATIN ON PERIPHERAL BLOOD MONONUCLEAR CELLS INFECTED WITH *M. tuberculosis*

S. Sabeel[1], B. Motaung[1] and R. Guler[1]

[1]ICGEB Cape Town and IDM, Department of Pathology, Division of Immunology, UCT, Cape Town

Tuberculosis remains one of the major causes of morbidity and mortality globally. According to WHO report in 2021, a quarter of the world's population has been infected with *Mycobacterium tuberculosis* (Mtb)[1]. Atorvastatin (ATO) belongs to a class of drugs called HMG-CoA reductase inhibitors also known as statins[2]. Besides, its ability to reduce cholesterol biosynthesis in patients with hypercholesterolemia as well as the prevention of cardiovascular diseases; it has anti-inflammatory properties[2]. Currently, several studies reported that statins-treated cells are more protected against Mtb infection[3]. Apoptosis is one of the effector mechanisms that limit the intracellular growth of Mtb. Therefore, the aims of this study were identification of the mycobacterial killing capacity of ATO-treated peripheral blood mononuclear cells (PBMCs) and investigated the apoptotic effects of ATO following Mtb infection.

Blood samples from healthy donors were collected; then PBMCs were isolated using Ficoll-Paque density media. Isolated PBMCs were pre-treated with Dimethyl sulfoxide (DMSO) as control and with different concentrations of ATO 50 µM, 100 µM, and 200 µM overnight at 37˚C. Next, treated PBMCs were infected with Mtb strains (H37Rv, HN878, and CDC1551) for 1 Day post-infection (DPI) and 3DPI. Triton-X was used to lyse PBMCs which were subsequently plated in 7H11 media and incubated at 37˚C for 14 days. Using an overhead microscope, the colony-forming units (CFU) were calculated. TUNEL assay was used to detect apoptotic cells that undergo extensive DNA degradation during the late stages of apoptosis. It was performed on PBMCs pre-treated on various ATO concentrations overnight; thereafter PBMCs were infected with GFP-H37Rv strain; Multiplicity of Infection (MOI:5). Fragmented DNA of apoptotic cells were stained at 1DPI and then the mean fluorescence intensity was assessed using a laser scanning confocal microscope.

ATO decreased bacterial load in PBMCs infected with Mtb strains at 1DPI and 3DPI in Figure 1. ATO induced DNA breaks formed during apoptosis in a dose-dependent manner are shown in Figure 2.

In this study, the effects of ATO on the growth of Mtb strains in PBMCs were evaluated. The results showed ATO significantly reduced the bacterial burden of Mtb in a dose-dependent manner. These finding are similar to Parihar *et al.* study that confirmed the inhibitory effects of simvastatin on the growth of Mtb in infected macrophages[4].

References:
1. World Health Organization. GLOBAL TUBERCULOSIS REPORT 2018. https://apps.who.int/iris/bitstream/handle/10665/274453/9789241565646-eng.pdf.
2. Guler, R. and Brombacher, F. (2015). Nat. Chem. Biol., 11(10), 748.
3. Guerra-De-Blas, P. *et al*. (2018). J. Immunol. Res. 2018, 1.
4. Parihar, S. P. *et al*. (2014). J. Infect. Dis. 209(5), 754.

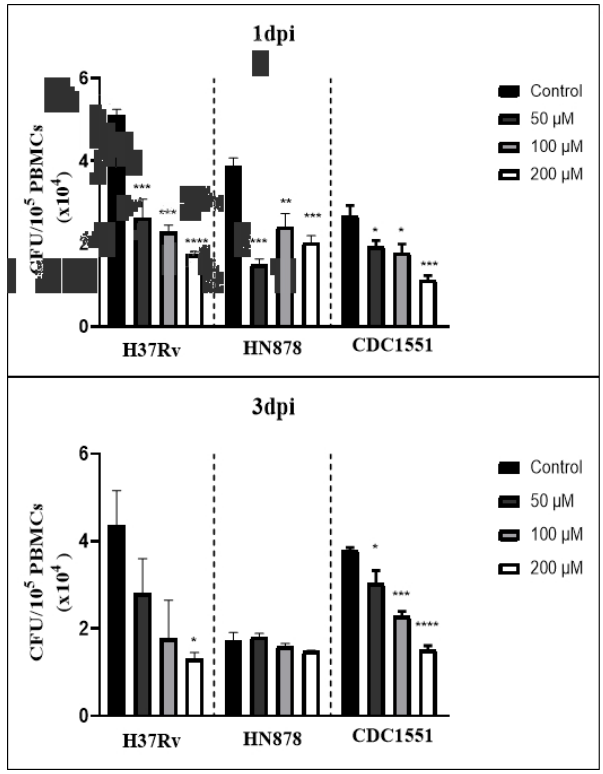

Figure 1. Effects of ATO on the growth of Mtb in PBMCs (A) CFU at 1DPI and (B) CFU at 3DPI. Data represent Mean±SD (* p <0.05, ** p <0.01, *** p <0.001, **** p <0.0001).

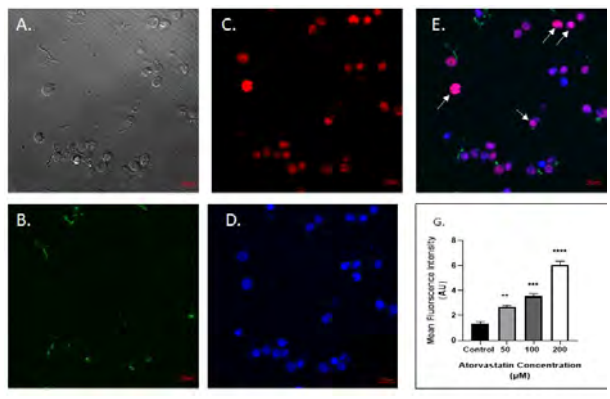

Figure 2. Confocal images of PBMCs treated with ATO (A) Bright field image (B) Green:Mtb bacteria labeled with green fluorescence protein (C) Red: PBMCs with fragmented DNA indicating apoptosis labeled with AF467 (D) Blue: nuclear stain (E) Overlay. (G) Mean Fluorescent Intensity Scale bar = 10µm.

Corresponding author: Reto.Guler@myuct.ac.za

NECTAR SPUR DEVELOPMENT IN *Nemesia* (SCROPHULARIACEAE)

H. Grobler[1,2], M. Jackson[1] and L. Joubert[1]

[1]Department of Plant Sciences (Botany), University of the Free State, Bloemfontein, [2]Centre for Microscopy, University of the Free State, Bloemfontein

The nectar spur is a hollow, tubular outgrowth of a floral organ which often contains a reward, such as nectar, for attracting pollinators. Nectar spurs evolved independently in multiple angiosperm lineages, promoting increased diversification[1]. Differences in spur development, such as variation in cell number (cell division)[2] or cell size (cell elongation)[3], result in the variety of nectar spur morphologies among species. Despite the ecological importance of nectar spurs, their developmental basis in *Nemesia*, a genus endemic to southern Africa, is still unknown. *Nemesia* consists of approximately 77 species, which show great diversity in floral colour, shape, size, and spur morphology.

We used a comparative approach to investigate variation in spur length among three *Nemesia* species. The selected study species included *N. barbata* (Fig. 1A), *N. strumosa* (Fig. 1B) and *N. macrocarpa* (Fig. 1C), with spur lengths measuring 2 mm, 4 mm and 6 mm (from the spur base to the tip of the spur), respectively. Using scanning electron microscopy (SEM) of the outer nectar spur epidermal surface throughout spur development, the relative roles of cell number and cell size were determined.

For each species, five floral replicates at five key stages of development were collected. The samples were fixed in 3% glutaraldehyde in sodium phosphate buffer, dehydrated in a graded ethanol series and critical-point dried. Samples were mounted on SEM specimen stubs and sputter coated with gold. Multiple SEM images were captured along the spur length using a JEOL JSM-7800F Extreme-resolution Analytical Field Emission SEM. Image analyses were performed using Fiji (ImageJ) and statistical analyses were performed using R version 4.0.3.

We observed that different developmental mechanisms contributed towards spur length variation in *Nemesia*. When comparing *N. barbata* and *N. strumosa*, more cells (Fig. 2A) resulted in the longer spur of *N. strumosa*, since cell size (Fig. 2B, Figs 3A and B) did not differ significantly. When comparing *N. strumosa* and *N. macrocarpa*, cell number over spur length were similar (Fig. 2A), and only cell elongation (Fig. 2B, Fig. 3B and C) contributed towards spur length variation. When comparing *N. barbata* and *N. macrocarpa*, both cell number (Fig. 2A) and cell elongation (Fig. 2B, Figs 3 A and C) resulted in the longer spur of *N. macrocarpa*.

In conclusion, by using SEM, we were able to identify the developmental basis (cell division and/or cell size) involved in spur length variation among three *Nemesia* species. Further comparative studies on nectar spur development will reveal to what extent other species utilize similar or different developmental mechanisms to obtain their various spur morphologies.

References:
1. Hodges, S.A. and Arnold, M.L. (1995) Proc. R. Soc. B: Biol. Sci. 262, 343.
2. Cullen, E., Fernández-Mazuecos, M. and Glover, B.J. (2018) Ann. Bot. 122, 801.
3. Puzey, R.J. *et al*. (2012) Proc. R. Soc. B 279, 1640.

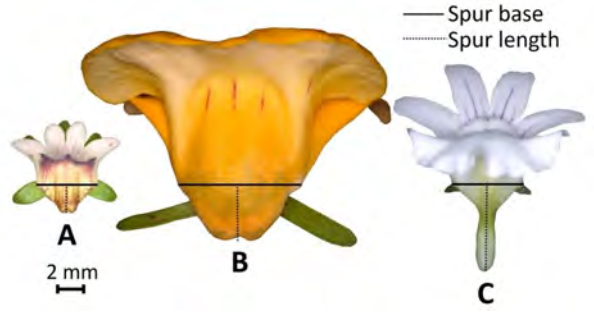

Figure 1. (A) *Nemesia barbata*, (B) *N. strumosa* and (C) *N. macrocarpa*. Scale bar = 2 mm.

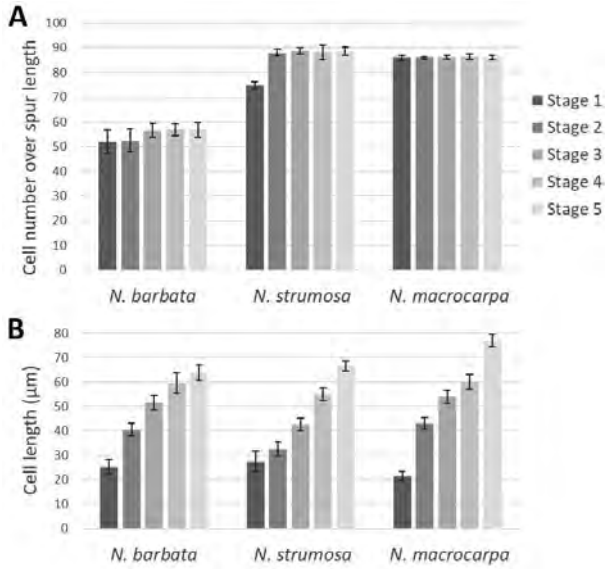

Figure 2. (A) Cell number over spur length for the three species. Cell number is represented by the mean of 5 biological replicates, with ± s.e. (B) Cell size (in µm) at the middle area of the spur for the three species. Cell size is represented by the mean of 30 cells, with ± s.e.

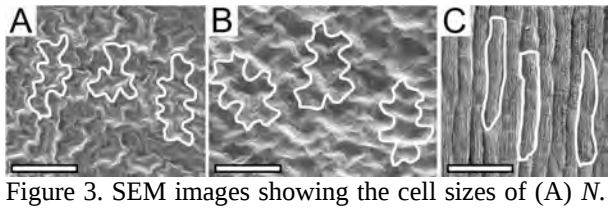

Figure 3. SEM images showing the cell sizes of (A) *N. barbata*, (B) *N. strumosa* and (C) *N. macrocarpa*. Scale bar = 50 µm.

Corresponding author: groblerh@ufs.ac.za

TRANSLOCATION, FATE AND BIOACCUMULATION STUDY OF MICRO- AND NANOPLASTICS IN MICE MODEL ORGANISMS

A. Gada[1,2], S. Muniyasamy[2], P. Hlangothi[1], P. Melariri[3] and C. Hoyo[4]

[1]Department of Chemistry, Nelson Mandela University (NMU), [2]Nanostructured and Advanced Materials, Chemicals Cluster,Council for Scientific and Industrial Reasearch (CSIR), [3]Department of Environmental Health, Nelson Mandela University (NMU), [4]Department of Biological Sciences, Norh Carolina States University (NCSU), Raleigh, USA.

Recent studies have shown humans to be susceptible to great exposure measures of environmental micro- and nano-plastics[1], with an estimated rise in environmental concentrations of nano-plastics[2]. Only recently, has the impact of these plastic fragments drew concern towards human health due to the potential daily exposure by varying exposure routes, with possibility of eliciting toxicological activities[3]. Furthermore, the aspects of these microscopic plastic particles in relation to effects, fate and behavior in the human body remains a great mystery. Given the anatomical, physical and biological similarities to humans, this study investigated the fate or translocation of micro- and nano-sized polystyrene (PS) plastic particles using mice model organisms through a histopathological experimental approach relying on spectroscopic and microscopic techniques.

Uncoated polystyrene particles of sizes 100nm, 200nm, 300nm, 5µm and 10 µm were procured from a commercial vendor (Magsphere) in 5ml aliquots. Mice model organisms of C57BL6 strain (black 6) were used. The first experimental run tested all 5 sizes (including control), and the second run tested two treatment groups of i) cocktails, and ii) impregnated dams (including control). Mice were exposed to test particles once every week by oral gavage, for 4 weeks at 4 mg/kg doses, 1 mg/ml concentration and a maximum volume of 100 microliters. Mice were euthanized by CO_2 inhalation, and death was confirmed by cervical dislocation. Fetuses of pregnant dams were removed during necropsy and decapitated with sharp scissors. Tissues were then extracted, affixed into histological slides and analyzed.

At a light microscopy level, particulate matter was observed but could not be distinguished or identified as plastics due to the instrumental analyzing limitations. These could have been air bubbles, dust particles or non-plastic debris (not shown). Using Raman spectroscopy, peaks were observed in treated samples, characteristic of polystyrene (Fig. 1A) under the 700 cm-1 to 900cm-1 region (C-S, C-O-C, O-O; Fig. 1B). To verify their presence, the same set of samples were observed in a fluorescent microscope. The observations revealed a presence of fluorescing particles sized within our particle ranges (Fig.1C).

Resuts obtained support the potential to study the fate and translocation of plastic particles using spectroscopy and microscopy but setbacks still exist regarding identification. Advanced material analytical and identification techniques such as Raman Imaging Scanning electron (RISE) microscopy is needed.

References:

1. Science Advice for Policy by European Academies (2019). A Scientific Perspective on Microplastics in Nature and Society | SAPEA. Evidence Review Report. 176.
2. Avio, C. G. *et al.* (2017). Marine Env. Res.128, 2.
3. Alimba C.G. and Faggio C. (2019). Microplastics in the marine environment: Current trends in environmental pollution and mechanisms of toxicological profile. In: Environmental Toxicology and Pharmacology, 68, 61.

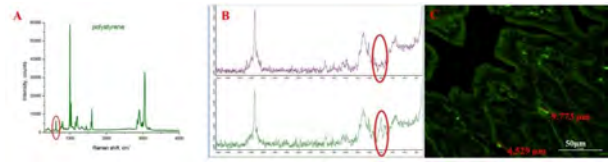

Figure 1. Figure 1. A) Raman spectrum of pristine Polystyrene B) Raman spectra of gut tissue with estimated polystyrene (Observed new peak), C) Fluorescing particles observed under a fluorescent microscope sized approximately 5µm and 10 µm.

Corresponding author: abongilegada9@gmail.com

APPLICATION OF ANIMAL MODELS IN HEAVY METAL TOXICITY RESEARCH

H.M. Oberholzer[1]

[1]Department of Anatomy, Faculty of Health Sciences, University of Pretoria, Pretoria

Heavy metals have a density of at least five times greater than that of water and are found naturally in the earth's crust[1]. The composition of heavy metals in the crust varies between different environmental areas. The presence of heavy metals in large quantities in the human body are associated with severe health complications that can ultimately be fatal. The main source of heavy metal toxicity in the environment is linked to anthropogenic activities, such as mining, and smelting. Heavy metal exposure occurs via contaminated air, water, soil, and food. In South Africa the mining sector is estimated to be the fifth largest in the world which can be attributed to some of the largest reserves of manganese and platinum group metals, gold, diamond, chromium ore and vanadium. People living in mining areas are the most vulnerable as they are exposed to various heavy metals on a daily basis by using this water for bathing, growing crops, cooking and to drink. Some heavy metals are essential elements and are beneficial at low concentrations. However, at higher concentrations, these may have adverse effects on various organ systems. Heavy metals can enter the human body orally through ingestion, absorbed through the skin, or inhaled via polluted air. The degree of toxicity is dependent on the route and duration of exposure. In general exposure is not limited to a single metal but rather a mixture of different metals at different concentrations. Animal models have been successfully implemented over the years in the heavy metal toxicity research field. By using Spraque-Dawley rat models exposed to different heavy metals alone and as part of mixtures, blood parameters as well as tissue and cellular structure can be determined, by using various microscopy techniques to identify specific target cells, tissues and organs, even when standard laboratory blood analyses are normal. This can then provide information on the role of heavy metals in the development of anatomical and physiological pathologies associated with heavy metal exposure. Heavy metals have been shown to adversely affect the liver, kidneys, heart, lungs, blood vessels and coagulation system of Spraque-Dawley rats[2-6]. The latter is shown in Figure 1[2]. Platelet morphology studied in the metal exposed groups, shows increased activation; illustrated by pseudopodia formation and platelet spreading. Platelet–platelet interactions and spontaneous fibrin fiber formation are also indicative of increased activation and consequently increased thrombotic potential of the exposed groups. Some heavy metals have the ability to increase reactive oxygen species thereby inducing oxidative damage.

References:
1.Tchounwou, P.B. *et al.* (2014) Pub Med Central. 101,133.
2. Arbi, S. *et al.* (2017) Ultrastruct. Pathol. 40(4), 275.
3. Dhanraj, P. *et al.* (2020) Ultrastruct. Pathol. 44(2), 182.
4. Janse van Rensburg, M. *et al.* (2020) Environ. Toxicol. Pharm. 75, 103314.
5. Naidoo, S.V.K. *et al.* (2019) Environ. Toxicol. Pharm. 69, 86.
6. Venter, C. *et al.* (2017) Microsc. Res. Tech. 80(8), 878.

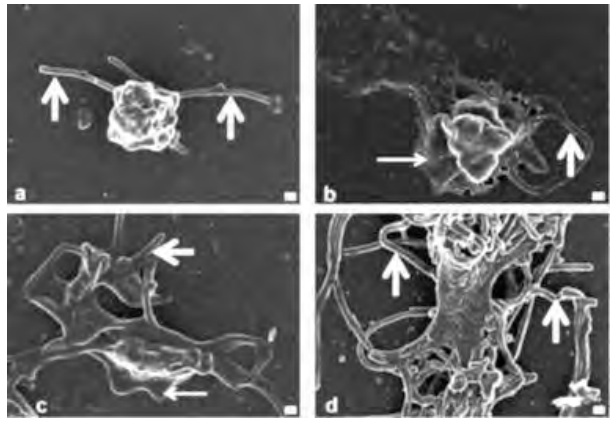

Figure 1. SEM micrographs of platelets prepared from platelet rich plasma. A representative of the (a) control group with the arrows indicating pseudopodia, (b) Cd-exposed group with pseudopodia and platelet spreading indicated by the thick and thin arrows, respectively, (c) platelets from the Hg-exposed group where pseudopodia (thick arrow) and platelet spreading (thin arrow) are also present, and (d) combination group where the presence of many pseudopodia can be seen (thick arrows) (Scale bars: 200 nm).

Corresponding author: nanette.oberholzer@up.ac.za

HISTOMORPHOLOGICAL EFFECTS OF MELATONIN AND cART ON THE PANCREAS AND KIDNEY IN RATS

D. Venter[1,2], H. Strijdom[3], I. Webster[3] and S.H. Kotzé[1]

[1]Div. of Anatomy and Histology, University of Stellenbosch, Tygerberg, [2]Dept. of Anatomy and Physiology, University of Pretoria, Pretoria, [3]Div. of Medical Physiology, University of Stellenbosch, Tygerberg

Combination antiretroviral therapy (cART) in HIV positive patients has shown to cause histologically observable side effects in the pancreas and kidneys[1,2]. These conditions are often associated with inflammatory changes and cellular injury. Melatonin, however, has been successful in the prevention and reduction of inflammatory markers, oxidative stress and cellular damage, and has been observed as a treatment option in various conditions[3,4].

The aim of this study was to evaluate the observable morphometric changes caused by cART as well as the potential therapeutic effects of melatonin on the pancreas, liver and kidney of the control, cART (ART+), melatonin (M+) and cART and melatonin (ART+/M+) groups in HIV-negative rats. Melatonin was administered at 0.01 mg/g/day and the cART was administered as a cocktail of 25.8, 51.6 and 17.4 mg/kg/day Tenofovir, Efavirenz and Emtricitabine, respectively. Tissue samples (N=40) of the pancreas and kidney of male Wistar rats were collected, processed and stained with hematoxylin and eosin (H&E). The H&E slides were evaluated for histopathology by a pathologist. Additional slides of the pancreata and kidneys were labelled with anti-insulin and anti-glucagon and periodic acid Schiff (PAS), respectively. The kidney PAS slides were used to measure the area, perimeter, diameter and radius of the renal corpuscles, glomeruli and proximal convoluted tubules (PCTs). Additionally, blood samples were collected to measure haemoglobin and serum lipids.

The haemoglobin value in the ART+ group was significantly higher than in the control group. The M+ group showed a decrease in serum lipids compared to the control group. No significant changes in the histopathology of the pancreas or kidney were seen. The mean islets per mm^2 in the pancreas was significantly higher in the M+ group than in the control and ART+/M+ groups. In addition, the α-cell area was increased in the M+ group compared to the ART+ group. In the kidneys, all parameters (area, perimeter, diameter, radius) of the renal corpuscle were significantly lower in the ART+ and M+ groups compared to the control group. In the glomeruli, the area, diameter and radius were significantly smaller in the ART+ group compared to the other three groups. All parameters of the PCTs were significantly decreased in the ART+ group compared to the control group.

Previous studies[5] have shown that cART has restored anaemic haemoglobin levels in HIV positive patients. Melatonin in the absence of cART has shown to decrease serum lipids, possibly due to its inhibitory effect on peroxidation of cellular lipids via free radicals[6]. Melatonin, in the absence of cART, stimulated the abundance of pancreatic islets, as well as the α-cell area, and thus indirectly the availability of α-cells. The renal corpuscle, glomeruli and PCTs were affected by cART, whereas only the renal corpuscle were affected by melatonin.

In conclusion, this study showed that cART, administered alone, could cause renal damage (tubular dysfunction and a decreased estimated glomerular filtration rate[7]), however, in combination with melatonin no effects were seen on the kidney. It is important to note that melatonin, in the absence of cART, may affect the kidneys in a lesser capacity[8].

References:
1. Adjene, J.O., Ajakaye, I.O., Nosakhare, P.O. (2011) Genomic Med. Biomarkers Heal. Sci. 3(2), 76.
2. Max, B. and Sherer, R. (2000) Clin. Infect. Dis. 30(2), S96.
3. Acuña-Castroviejo, D. *et al*. (2014) Cell. Mol. Life Sci. 71, 2997.
4. Radogna, F., Diederich, M., Ghibelli, L. (2010) Biochem. Pharmacol. 80(12), 1844.
5. Johannessen, A., *et al*. (2011) BMC infectious diseases. 11(1), 190.
6. Sener, G. *et al.* (2002) J. Pineal Res. 32(2), 120–126.
7. Squillace, N. *et al*. (2017) PLoS One 12(6), 1.
8.Truter, D. *et al*. (2018) Acta Histochem. 120(4),347.

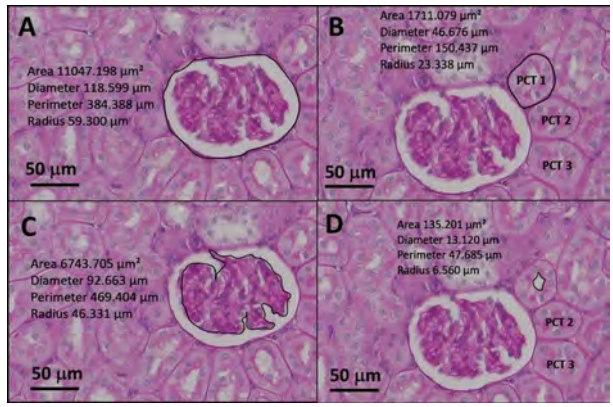

Figure 1. Examples of measurements of the kidney in a control rat, including the renal corpuscle, glomerulus, PCTs and lumen of the PCTs. The area, diameter, perimeter and radius were measured for, A) the renal corpuscle, B) proximal convoluted tubule including the lumen, C) glomerulus and, D) lumen of the PCT

Corresponding author: danelle.venter@up.ac.za

HISTOLOGY OF THE SOUTHERN GROUND-HORNBILL (*Bucorvus leadbeateri*) GASTRO-INTESTINAL TRACT

A.D. Naudé[1,2], K.N. Koeppel[2,3] and M.R. Crole[1,2]

[1]Department of Anatomy and Physiology, [2]Centre for Veterinary Wildlife Research, [3]Department of Production Animal Studies, Faculty of Veterinary Science, University of Pretoria, Onderstepoort 0110, South Africa

The Southern Ground-Hornbill (SGH) (*Bucorvus leadbeateri*) is the largest cooperatively breeding bird species and the only entirely carnivorous hornbill. Therefor the gastro-intestinal tract (GIT) of the SGH may display specific adaptations which could be of significance in the husbandry of this endangered species. Factors that contribute to unnatural mortality in SGHs in South Africa are poisoning, electrocution on transformer boxes, shooting and trafficking[1]. Lead contamination of hunting offal from the use of lead-based ammunition as well as non-discriminate object ingestion in the wild and in captivity is a persistent threat[2]. Carnivorous bird species have important GIT differences in respect of anatomy, physiology, nutrition and disease aetiologies that greatly affect the success of medical and surgical intervention during GIT diseases[3].

Nine adult SGHs, which succumbed to natural or unknown causes, attack from other birds, euthanasia for humane reasons such as untreatable conditions and management considerations (usually reproductive failure) were used in this study. On post mortem, the GIT was removed and immersion-fixed in 10% neutral-buffered formalin. GIT sections were routinely prepared for light microscopy and stained with Haematoxylin & Eosin (H&E), Periodic-Acid Schiff (PAS), Masson's Trichrome and Alcian Blue.

The *Lamina epithelialis* of the proventriculus, ventriculus and intestine presents folds lined by simple columnar epithelium (Fig. 1). Additionally, koilin, secreted in horizontal layers, is present in the ventriculus. The *Lamina propria* contains substantial simple, branched tubular glands in the proventriculus and intestine (Fig. 1a), and long simple tubular glands in the ventriculus. The massive compound tubular proventricular glands contain secretory cuboidal cells. Infiltrations of internodular lymphoid tissue are present in the *Lamina propria* of the proventriculus and intestine. A single inner longitudinal layer of *Lamina muscularis mucosae* is present in the proventriculus, rectum and an additional outer circular layer in the rest of the intestine (Fig. 1b). The *L. muscularis* was not observed in the ventriculus. *Plicae circulares* are absent in the intestine. *Villi intestinales* become shorter and broader, the *Tunica muscularis intestinae* less well-developed and goblet cells more numerous when moving from the duodenum (Fig. 1a) aborally.

The proventricular glands and the thin-walled gizzard (ventriculus) support enzymatic digestion and not the grinding of ingesta. The layered secretion of the koilin may assist this layer to be both tough and flexible to allow distention to accommodate large prey. The heavy reliance on enzymatic digestion is important in the husbandry of the SGH as stress may lead to a breakdown in the gizzard lining leading to ulcers[4]. Additionally the well-developed muscular layers (Fig. 1) indicate the importance of maintaining intestinal motility. Stress slows gastric emptying and ion exchange, causes colonic mucin depletion and increased intestinal permeability leading to the passage of antigens to the *Lamina propria* and bacterial translocation[4]. Stress poses a major risk factor for wild bird species in captivity and in a hospital setting[5]. Widespread empirical evidence across various vertebrate taxa shows that handling wildlife generally induces a severe stress response resulting in increased stress hormones[5]. It is inevitable that when wild birds such as the SGH are treated in hospitals, they will experience stress. GIT stasis is life threatening in the SGH, and as veterinary intervention for this bird is on the rise, this study provides insight into features impacting treatment. Further studies aim to elucidate how the GIT contributes to the SGH's high susceptibility to lead poisoning.

References:
1. Botha, A. *et al.* (2011) Southern Ground Hornbill (*Bucorvus leadbeateri*) Species Recovery Plan for South Africa. Johannesburg, Johannesburg Zoo/Endangered Wildlife Trust.
2. Koeppel, K.K. and Kemp, L.V. (2015) J. Avian Med. Surg. 29, 340.
3. Klaphake, E. and Clancy, J. (2005) Vet. Clin. North. Am. Exot. Anim. Pract. 8, 307.
4. Bhatia, V. and Tandon, R.K. (2005) J. Gasteroenterol. Hepatol. 20, 332.
5. Huber, N. *et al*. (2019) Front. Vet. Sci. 6, 105.

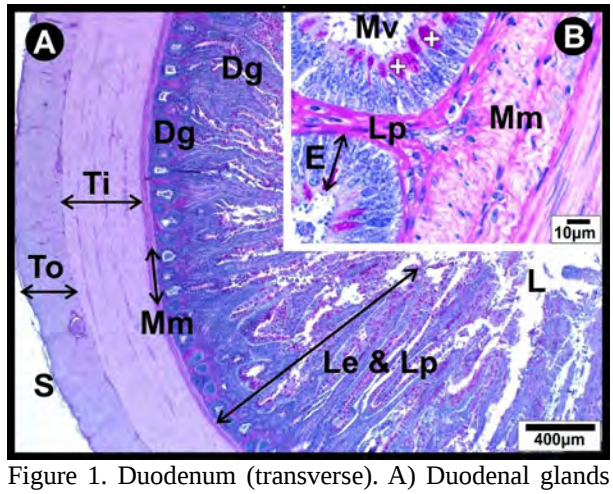

Figure 1. Duodenum (transverse). A) Duodenal glands (Dg), lumen (L), *Lamina epithelialis* & *Lamina propria* (Le & Lp), *Lamina muscularis mucosae* (Mm), *Tunica muscularis* inner circular (Ti) and outer longitudinal (To) layer and serosa (S). B) Simple columnar epithelium (E), microvilli (Mv), goblet cells (PAS +).

Corresponding author: martina.crole@up.ac.za

MICROSCOPIC ARCHITECTURE OF JAPANESE QUAIL LUNGS CHALLENGED BY THERMAL EXPOSURE

A. Abdulkadir[1,2] and D. Reddy[3]

[1]School of Anatomical sciences, University of the Witwatersrand, [2]Department of Anatomy, Federal University Birnin Kebbi, [3]Microscopy and Microanalysis unit, University of the Witswatersrand

The Japanese quail is a compact grassland bird first domesticated in China during the fourteenth century[1]. It is farmed in several countries for profit and personal consumption[2]. Heat stress has threatened poultry welfare and productivity, leading to economic loss. Several studies investigated the impact of heat stress on poultry production and ways of mitigating the problem using Japanese quail as the model[3]. Hormonal and electrolytes derangements were reported in addition to impaired immunity in the heat-exposed quail[3]. There are reports on the changes in the morphology of the intestine, liver, and reproductive organs[4]. These organs are generally related to the production performance of the quail. However, the lungs, did not receive attention. Hence, this study aimed to investigate the microscopic changes in the lung of the Japanese quail, which underlie the coping mechanisms during heat exposure. Generally, the respiratory system of the Japanese quails is involved with evaporative cooling during heat exposure to maintain normal body temperature[5].

Japanese quail were obtained through the Wits Research Animal Facility. The experiment procedures were approved by the Animal Research Ethics Committee of the University of the Witwatersrand (2020/10/01/D) following a pilot study which assessed the feasibility of the experiment. The birds were randomly divided into Control (C) and Heat stressed (HS), with four birds in each group. C was maintained at 24°C while HS was at 40°C for 24 hours. At the end of the experiment, the birds were euthanized, and the lungs were removed and fixed for microscopic analysis. Lung tissues were processed for light microscopy (H&E stain and Gomori's trichrome stain) and scanning electron microscopy (SEM).

The Gomori's trichrome-stained sections (Fig. 1) showed an increased amount of collagen in the parenchyma to preserve the integrity of the atria in the HS group and diffuse congestion around the parabronchi. In addition, red blood cells were seen in the airway lumen, which could suggest a rupture of the blood vessel. Evidence in the SEM images (Fig. 2) indicates that surfactant deposition increased in the HS group. The diffuse congestion around the parabronchi might indicate increased blood flow to the gas exchange sites.

Results from this study suggest that heat stress can cause morphological changes in the lungs of Japanese quail, which could lead to permanent damage and mortality.

References:
1. Mills A.D. *et al.* (1997) Neurosci Biobehav Rev. 21(3), 261.
2. Lukanov H. (2019) Worlds Poult Sci J. 75(4), 547.
3. Mehaisen G.M.K. *et al.* (2019) PLoS One 14(4), e0214839.
4. de Moraes L.R.*et al.* (2021) PLoS One 16(1), e0245615.
5. Smith E.K. *et al.* (2015) J. Exp. Biol. 218(Pt 22), 3636.

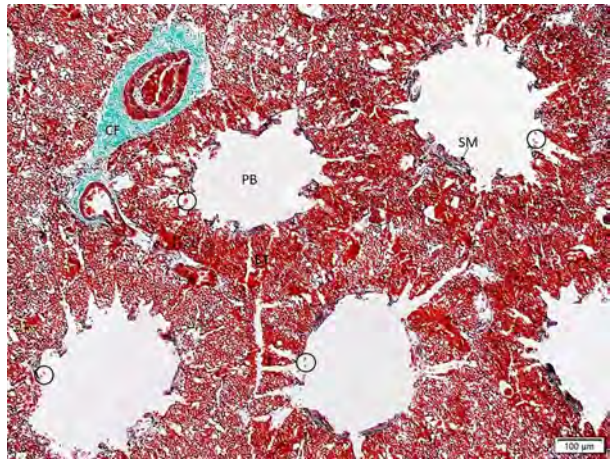

Figure 1. A representative micrograph of the HS quail lung. Note the diffuse congestion of ET (squares) and the presence of erythrocytes in the airway (circled), increased collagen fiber (CF) deposition around the artery (Gomori's trichrome stain, x10). PB – parabronchi, SM – smooth muscle, ET – exchange tissue, IA – interparabronchial artery.

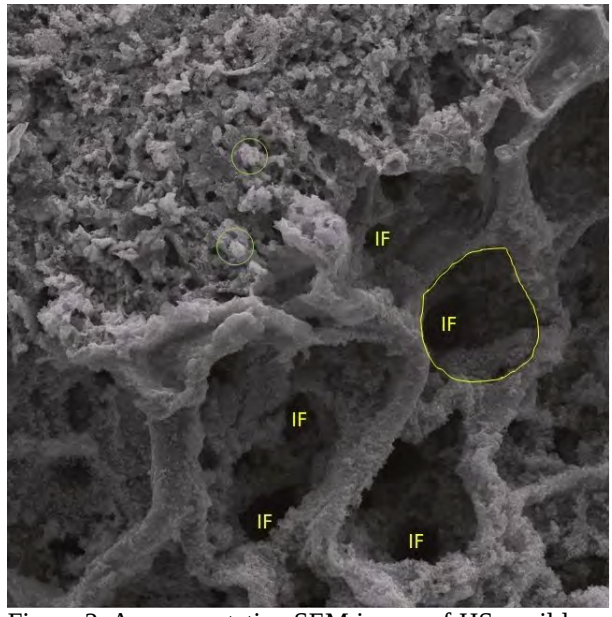

Figure 2. A representative SEM image of HS quail lung showing the increased surfactant over the exchange tissue surface (green circle). The opening into the atria (yellow circle) leads into the infundibulae (IF).

Corresponding author: a.abdulkaadir@fubk.edu.ng

A MORPHOLOGICAL STUDY OF THE PULMONARY COMPONENTS IN THE LUNGS OF THE RED-EARED SLIDER

S. Mulder[1], D. Reddy[1,2] and A. Abdulkadir[1]

[1]The School of Anatomical Sciences, Faculty of Health Sciences, University of the Witwatersrand, Johannesburg, South Africa, [2]Microscopy and Microanalysis Unit, University of the Witwatersrand, Johannesburg South Africa

Innate success of invasive species poses major threats to indigenous flora and fauna worldwide[1]. Evolutionary adaptations, whether at a macroscopic or microscopic level, contribute considerably to this level of invasive success[1,2]. The Red-eared slider, Trachemys scripta elegans, ranks as one of the IUCN's "Top 100" Worst Invasive Species[2]. The ecological detriment of this terrapin, although well documented, lacks a detailed anatomical rationale behind this success[3]. Their heterogenous multicameral lungs have been identified as an important contributor, highlighted by their ability to survive in hypoxic conditions for extensive periods of time[3,4]. However, very few studies have been conducted on the Red-eared Slider lungs, and the full understanding of the dynamic nature of the lung parenchyma tissue specialisations and localisations would illustrate the possible extent of its functionality in relation to the animal and its habits and habitats[5,6]. This could provide further insight to underpin a scientifically sound, species-specific management practice[1]. This study examined the terrapin lung morphology regarding the occurrence and regionalisation of various muscle types and connective tissues which comprise the integral parenchyma of the lung.

The morphology was captured, documented, and analysed using gross morphology images, light microscopy using Mayer's H&E and New Pentachrome, and fluorescence microscopy. The latter utilised a novel triple labelling technique, where Alexa Fluor 488 conjugated to Anti-alpha Smooth Muscle Actin, Alexa fluor 594 conjugated to Anti-collagen II, and DAPI was used to label the nuclei. The microstructural assessment of the lungs yielded internal parenchymal heterogeneity from the cranial to the caudal region. The cranial region was found to be highly subdivided, the middle region transitional in parenchymal composition, and the caudal region minimally subdivided. Smooth muscle was abundant in the caudal region, decreasing in the middle region, and minimal in the cranial region, with no discernible structural support from cartilage. Specialised smooth muscle, *Muscularis striatum pulmonale*, was seen in the dorsal cranial region only, which highlights the extensive heterogenous nature of the lung. The high parenchymal heterogeneity supports the hypothesis that the Red-eared slider has innate adaptations that allow for hypoxic tolerance using a unidirectional airflow ventilation mechanism aided by specific parenchyma within each lung region[4,5]. The hypothesis, along with the concept of intra-species phenotypic plasticity and the overall dynamic nature of the lung morphology, could provide further explanation towards the adaptability and invasive success of the Red-eared slider[4,6].

References:

1. van Wilgen, B., Zengeya, T. and Richardson, D. (2021) Biological Invasions in South Africa. London, Springer Cham.
2. Pendelbury, P. (2021) http://www.iucngisd.org/gisd/species.php?sc=71
3. Polo-Cavia, N., López, P. and Martín, J. (2010) Bio. Invasions, 12(7), 2141.
4. Farmer, C. and Carrier, D. (2000) J. Exp. Biol., 203, 1679.
5. Perry, S.F. (1978) Respir. Physiol. 35(3), 245.
6. Reddy, D. (2013) Ph.D. Thesis. https://wiredspace.wits.ac.za/items/e24a4695-eab1-4a81-9ca1-4f9bd4f7f05a

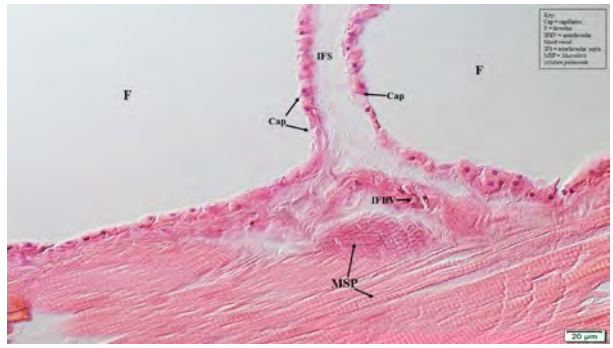

Figure 1. Section stained with Mayer's H&E showing the thin blood-gas barrier of the faveoli in the dorsal cranial region and the double capillary network, with specialised smooth muscle (MSP).

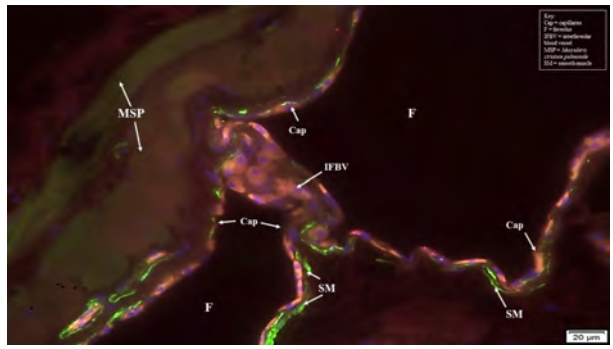

Figure 2. A fluorescent micrograph depicting the thin blood-gas barrier and double capillary network, with MSP in longitudinal and cross-sectional orientation in the dorsal cranial region.

Corresponding author: svenjabottner@gmail.com

MICROSTRUCTURE OF THE SPLEEN OF THE SOUTHERN WHITE RHINOCEROS (*Ceratotherium simum simum*)

A. Metzinger[1,2], M.R. Crole[2,3], S.J. Clift[2,4], L.C.R. Meyer[2,5], P. Buss[5,6], J. Meuffels[7], U. Teubenbacher[1,8] and F. Pohlin[1,2]

[1]Research Institute of Wildlife Ecology, Department of Interdisciplinary Life Sciences, University of Veterinary Medicine Vienna, 1160 Vienna, Austria, [2]Centre for Veterinary Wildlife Research, [3]Department of Anatomy and Physiology, [4]Department of Paraclinical Sciences, [5]Department of Production Animal Studies, Faculty of Veterinary Science, University of Pretoria, Onderstepoort 0110, South Africa, [6]Veterinary Wildlife Services, South African National Parks, Kruger National Park, Skukuza, South Africa, [7]Rhino Force SA NPC, P.O. Box 31570, Tokai 7966, South Africa, [8]Clinic for Diagnostic Imaging, Vetsuisse Faculty, University of Zurich, Switzerland

Intensive management, for conservation of the southern white rhinoceros (SWR) (*Ceratotherium simum simum*), has become a strategy to mitigate poaching[1]. This strategy includes capture and chemical immobilisation, which are associated with a severe physiological stress response in the SWR[2]. Increases in hematocrit, red blood cell count and hemoglobin concentration in immobilised, compared to standing but sedated SWRs, have been documented[3]. These changes may be related to the spleen, which is an organ for hematopoiesis (fetus), immune response, blood filtration and blood storage[4]. The aim of this study is to describe the microstructure of the spleen of the SWR to better understand hematological changes in chemically immobilised SWRs.

Spleens from 21 SWRs, deceased or euthanized after poaching or untreatable injuries (Kruger National Park), were sampled during routine post-mortem examinations and fixed in 10% neutral-buffered formaldehyde. Cut sections were routinely processed for light microscopy and stained with Haematoxylin & Eosin (H&E). Ten spleens were further stained with Periodic-Acid Schiff, Masson´s trichrome, Gomori´s reticulin (GRI), Perls and Verhoeff´s reagent. Immunohistochemical (IHC) labeling was implemented to distinguish α-smooth muscle actin (Actin), nervous tissue (S100), histiocytes (Iba-1), vascular endothelial cells (F VIII) and T (CD3) and B (CD20) lymphocytes.

The typical splenic components, namely the capsule, trabeculae, and splenic pulp, are present in the SWR (Fig. 1). The serosa is supported by a subserosa, which directly contacts the outer connective tissue layer of the capsule. Blood vessels are prominent in the latter. A thickened portion of the capsule, carrying the splenic blood vessels, lymphatics and non-medullated nerves, represents the hilus. The inner smooth muscle cell layer of the capsule, supported by abundant elastic fibres, continues as primary and then secondary splenic trabeculae (composed of smooth muscle cells, collagen, elastic and reticular fibres) into the parenchyma. The red pulp is a 3-dimensional, complex arrangement of splenic cords and venous sinuses. The predominant cells are the reticular cells with reticular fibres and myofibroblasts. Histiocytes and hemosiderin are extensive in the splenic cords and form concentrations around arterioles (ellipsoids). The white pulp represents the lymphatic tissue of the spleen and contains the typical arrangement of B (germinal zone) (Fig. 1 – inset) and T (periarterial lymphatic sheath) lymphocytes as seen with IHC labelling.

The features noted in the present study confirm the immunological and hematological function of the spleen in the SWR. Although the basic structure and function of the mammalian spleen remains similar, there is a great deal of variation in the splenic microstructure of various species[4]. The abundance of trabeculae supported by elastic fibres and smooth muscle cells, the elastic fibres, muscular capsule and myofibroblasts in the splenic cords, all innervated by non-medullated nerves, support the importance of the contractile function of the SWR spleen. Also of significance is the vascularity of the capsule, suggesting that blood storage could be significant here. Many drugs used during intensive management of the SWR will affect the spleen[3] and sympathetic stimulation (e.g., exercise and excitement), will result in splenic contraction and blood cells moving into the circulation[5]. The SWR spleen appears specifically adapted to store and mobilise blood. This should be accounted for during intensive management and in the interpretation of hematological analyses.

References:
1. Breed, D. *et al.* (2019) Conserv. Physiol. 7, 1.
2. Miller, M. and Buss, P. (2015) Fowler´s Zoo and Wild animal Medicine. St. Louis, Elsevier.
3. Pohlin, F. *et al* (2020) Front. Vet. Sci. 7, 1.
4. Cesta, M.F. (2006) Toxicol. Pathol. 34, 455.
5. Poole, D.C. and Erickson, H.H. (2015) Dukes´ Physiology of Domestic Animals. Iowa, Wiley.

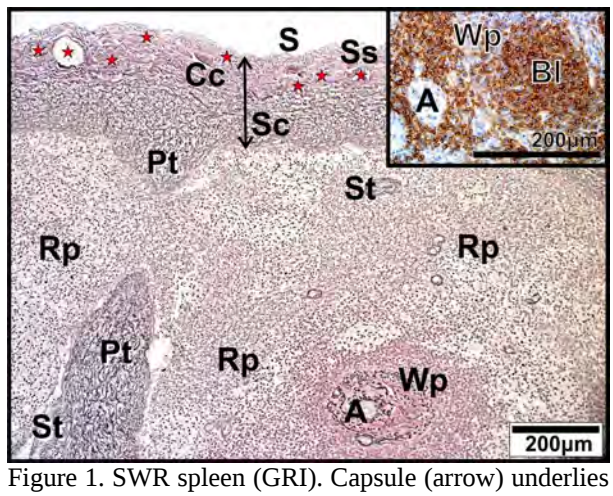

Figure 1. SWR spleen (GRI). Capsule (arrow) underlies the serosa (S) and subserosa (Ss). Connective tissue (Cc), blood vessels (red stars), primary (Pt) and secondary (St) trabeculae, smooth muscle (Sc), red pulp (Rp) and artery (A) of the white pulp (Wp). Inset: CD20 labeling shows B lymphocytes (Bl).

Corresponding author: martina.crole@up.ac.za

AMELIORATION OF OLFACTORY DEFICITS BY *Nigella Sativa* OIL IN DEVELOPMENTALLY MODELLED SCHIZOTYPY IN BALB/c MICE

A.A. Bello[1] and R.O. Folarin[2]

[1]Neurophytotherapy Research Lab, Department of Anatomy, Faculty of Basic Medical Sciences, Olabisi OnabanjoUniversity,Ogun State., [2]Neurophytotherapy Research Lab, Department of Anatomy, Faculty of Basic Medical Sciences, Olabisi OnabanjoUniversity, Ogun State.

Schizophrenia is a serious mental disorder that is characterized by the inability of an individual to interpret reality. It may result in hallucinations, delusion and disorder in thinking and behavior. It affects approximately 1% of the population[1]. Olfactory deficit is an endophenotype of schizophrenia as characterised by disruption in synaptic transmission in the olfactory apparatus[2]. *Nigella sativa* oil (NSO) is a highly therapeutic and scientifically tested herbal medicine. Numerous studies have demonstrated its main active constituent, thymoquinone, to be medicinally very effective against various illnesses[3]. Social isolation is a preclinical neurodevelopmental model of schizophrenia. that attempts to model the effects that human social isolation can have on normal brain development[4]. With our hypothesis of ameliorative tendencies, this study investigated the effects of *Nigella sativa* oil (NSO) on the olfactory parameters of social isolation rearing (SIR) models of developmental schizophrenia through neurobehavioural, neurochemical and histological assays on the olfactory bulb of BALB/c mice.

Sixty (60) BALB/c mice (3 weeks) were equally divided immediately post-weaning into 6 groups namely, CTRL (reared socially on normal chow only), SIR (socially isolated on normal chow only), NS (administered 1ml/kg NSO daily), SIR-NSC (socially isolated but concurrently administered 1ml/kg NSO daily), SIR-NS (socially isolated on normal chow before administration with 1ml/kg NSO for same duration as isolated), NS-SIR (Adult female mice were pre-administered 1ml/kg NSO for 10 days prior to mating. After parturition, their pups were then commenced on isolation immediately after weaning). Social isolation rearing was executed through individualised holding of each mouse in a separate cage (with adequate spacing and ventilation) devoid of all tactile and visual cues from all other mice. Isolation and NSO administration periods each lasted 8 weeks.

Olfactory sensitivity and discrimination was defective in SIR mice, but higher in all mice that were pre-, post or concurrently treated with NSO. Glutamate and GABA levels were higher in the olfactory bulb of mice that received NSO compared with untreated SIR mice. Brain:body weight ratio was also higher in all NSO-treated mice than the untreated ones. NSO treated groups had lower neural density compared to the SIR group.

While olfactory deficits were re-affirmed in socially isolated mice as models of schizophrenia, NSO was shown to ameliorate and protect against the neurobehavioural, histological and neurochemical olfacto-schizophrenic endophenotypes in BALB/c mice. There is need for translational research to ascertain if the result of this study can be transformed into new treatments to improve the health of the population.

References:
1. Jablensky, A. (2010) Dialogues in Clin. Neurosci. 12(3), 271.
2. Figueres-Oñate, M., Gutiérrez, Y. and López-Mascaraque, L. (2014) Front. in Neuroanat. 8(55).
3. Ahmad, A. *et al.* (2013) Asian Pacific J. of Trop. Biomed. 3(5), 337.
4. Watson, D. et al. (2012) Int. J. Neuropsychopharm. 15(4), 471. *et al.* (2012) Int. J. Neuropsychopharm. 15(4), 471.

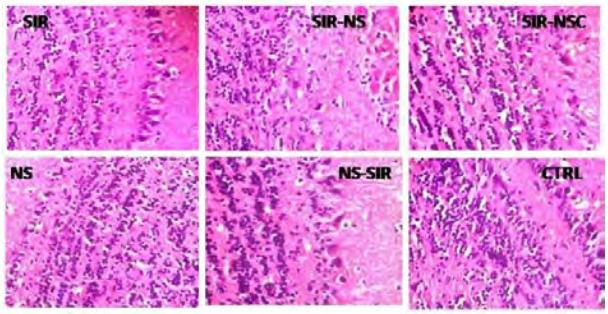

Figure 1. Sections through the olfactory bulb of mice for the six groups. (H and E stain)

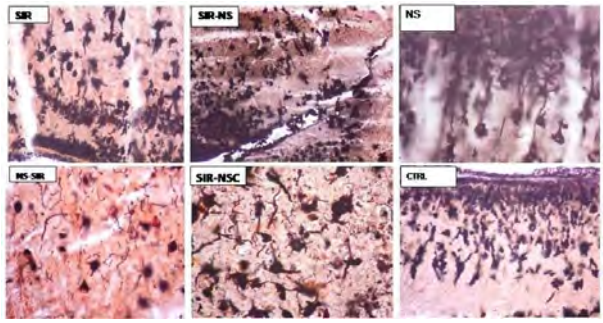

Figure 2. Section through the olfactory bulb of mice for the six groups. (Golgi stain)

Corresponding author:
royhaanfolarin.oouagoiwoye.edu.ng

25-HYDROXYVITAMIN D_3 INDUCES BIOCHEMICAL AND MORPHOLOGICAL APOPTOSIS IN THE HELA CELL LINE

E.V.M. Zhou[1], S. Bhoora[1], T.S. Pillay[1,2] and R. Punchoo[1,2]

[1]Department of Chemical Pathology, Faculty of Health Sciences, University of Pretoria, [2]National Health Laboratory Services, Tshwane Academic Division, Pretoria

Vitamin D and its metabolites have exhibited numerous anti-cancer actions, such as apoptotic cell death, in various pre-clinical cancer studies. Apoptosis is most commonly known as programmed cell death (PCD) type I and is essential during development, after injury and in disease prevention. Biochemical features include cell membrane asymmetry, caspase activation, changes in mitochondrial membrane potential ($\Delta\Psi m$), and DNA damage. Morphological features of apoptosis include reduction of cellular volume, chromatin condensation (pyknosis), nuclear fragmentation (karyorrhexis), nuclear breakdown (karyolysis), cytoplasmic blebbing and apoptotic bodies.[1,2]

Cervical cancer is one of the leading causes of cancer related deaths among South African women, affecting approximately 1 in 40 women. Few studies have explored the anti-cancer effects of vitamin D metabolites in cervical cancer.[3] In this study, cervical adenocarcinoma cell line, HeLa was treated with 25-hydroxyvitamin D_3 ($25(OH)D_3$), and biochemical and morphological features of apoptosis were assessed.

HeLa cells were seeded at a concentration of 30 000 cells/ml an incubated for 16 hours. Cells were then treated with $25(OH)D_3$ at a physiological concentration (260 nM) and a supraphysiological concentration (5000 nM). Medium and solvent (0.5 % ethanol v/v controls were also used. After a 72 hours incubation, cells were trypsinised and resuspended in fresh culture media. The cells were then stained with either annexin V, tetramethyl rhodamine ethyl ester (TMRE) or DEVD peptide-linked DNA dye. All samples were then stained with 7-aminoactinomycin D (7-AAD). Samples were then acquired using the Luminex® Guava® Muse® Cell Analyzer. Biological and technical repeats were triplicated (expressed as mean ± SEM) and analysed by one-way ANOVA with post-hoc Bonferroni testing at significance $p< 0.05$.

To assess morphological features of apoptosis, HeLa cells were seeded on glass coverslips at a concentration of 50 000 cells/ml and treated as previously described. After 72 hours incubation with treatment, cells were fixed and stained with Mayer's Hemalum and eosin. Cells were viewed with brightfield microscopy.

Annexin V staining and DEVD peptide-linked dye showed that $25(OH)D_3$ treatment at 5000 nM significantly increased the percentage of apoptotic cells when compared to the solvent control ($p=0.0323$ and $p=0.0219$, respectively). In addition, 5000 nM treatment significantly induced mitochondrial membrane depolarisation when compared to the solvent control ($p= 0.0061$).

Brightfield microscopy showed that treatment with $25(OH)D_3$ at both the physiological and supraphysiological concentrations induced apoptosis. Vitamin D treated cells exhibited apoptotic bodies, cytoplasmic blebbing, hyper-condensed chromatin, shrunken nuclei and a reduction in cell volume (Fig. 1).

In the intrinsic pathway of apoptosis, the exposure of cells to external stimuli initiates a cascade of molecular events.[1,2] Our results showed that annexin V staining was increased with $25(OH)D_3$ treatment, indicating an increased externalisation of phosphatidylserine on the plasma membrane. Similar results were seen in osteosarcoma cell lines (SAOS-2 and 143B)[4] treated with $25(OH)D_3$ at 1000 nM. Depolarisation of the mitochondrial membrane releases proteins that activate caspases.[1] Our results show that $25(OH)D_3$ treatment resulted in the depolarisation of the mitochondria and induction of caspase-3 and -7 activity[2], implying that $25(OH)D_3$ induces the intrinsic pathway of apoptosis. Active caspase-3 and -7 are involved in the fragmentation of DNA during apoptosis. Brightfield microscopy revealed cells with hyper-condensed chromatin, indicating potential DNA damage. The presence of apoptotic bodies in $25(OH)D_3$ further confirms the induction of apoptosis. In conclusion, $25(OH)D_3$ induces apoptosis at a supraphysiological concentration, potentially via the intrinsic pathway. Further investigation of the cell cycle and DNA content need to be conducted to corroborate findings.

References:
1. Elmore, S. (2007) Toxicol Pathol. 35(4), 495.
2. Galluzzi, L. *et al*. (2018) Cell Death Differ. 25, 486.
3. Herbst, M.C. (2022) Fact Sheet on Cervical Cancer. Johannesburg, Cancer Association of South Africa.
4. Thompson, L. *et al*. (2012) J.Orthopaed. Res. 30, 831.

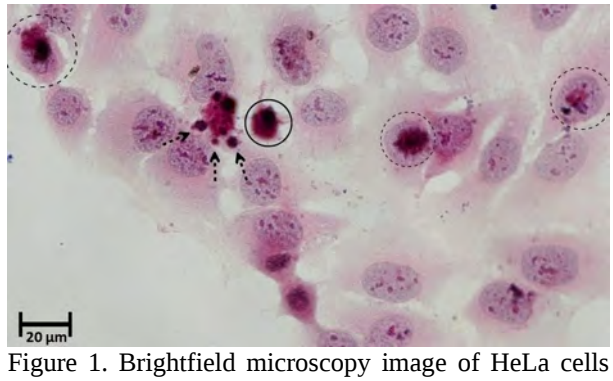

Figure 1. Brightfield microscopy image of HeLa cells treated with 5000 nM $25(OH)D_3$. Cells with apoptotic bodies (arrow), shrunken cells (circle) and hyper-condensed chromatin (dashed circle) were visible.

Corresponding author: rivak.punchoo@up.ac.za

MODULATORY EFFECTS OF *Nigella sativa* OIL ON HIPPOCAMPUS OF DIZOCILPINE-INDUCED SCHIZOPHRENIA IN BALB/c MICE

R. O. Folarin[1,2], O. Owoeye[2] and A O Malomo[2]

[1]Dept. of Anatomy, Olabisi Onabanjo University, Sagamu, Nigeria, [2]Dept. of Anatomy, Univ. of Ibadan, Ibadan, Nigeria

Schizophrenia is a neuropsychiatric disorder characterised by positive, negative and cognitive behavioral symptoms. Despite years of research, the need for suitable therapy remains elusive. *Nigella sativa* oil (NSO) is a medicinal plant notable for its dietary, neuroprotective and anti-inflammatory properties. However, there is paucity of information on its neuroprotective potentials in schizophrenia. This study was designed to investigate the modulatory effects of NSO on the hippocampus of dizocilpine-induced schizophrenia in mice.

Sixty 14-weeks old male BALB/c mice (23-25g) were divided into five groups (n=12); control (normal saline, 1 mL/kg), NSO (1 mL/kg), dizocilpine-control (0.5 mg/kg) all for 7 days, while NSO (1 mL/kg for 7 days) + dizocilpine (0.5 mg/kg, for another 7 days) for preventive measure, and dizocilpine (0.5 mg/kg for 7 days) + NSO (1 mL/kg for another 7 days) for reversal. Dizocilpine and NSO were administered intraperitoneally and orally, respectively. Open field box was used for stereotypic popping; while anxiety and recognition memory were measured using the elevated plus maze and novel object recognition tests, respectively. Animals were euthanised after behavioral studies, and harvested brains were weighed. Hippocampal glutamate was determined spectrophotometrically. Neuronal arrangement, sizes and densities were determined in perfused brain tissues using haematoxylin and eosin stain. Dendritic arborisations were assessed using Golgi stain. Metabotropic glutamate receptor-II (mGluR-2) and Glia Fibrilliary Acidic Protein (GFAP) were evaluated immunohistochemically. Data were analysed using descriptive statistics and ANOVA at α= 0.05.

Stereotypic popping was observed in dizocilpine-control but not in the preventive and reversal NSO-treated animals. The NSO increased open arm entry index in the preventive (45.45±7.5%) and reversal (43.01±4.1%) groups when compared to dizocilpine-control (42.22±5.3%). Similarly, NSO also increased open arm exploration index in the preventive (25.97±9.7%) and reversal (30.22±9.9%) groups when compared to dizocilpine-control (24.41±3.3%). Furthermore, NSO significantly increased novel object recognition index in the preventive (31.17±5.7%) and reversal measures (33.75±12.7%) relative to dizocilpine-control (15.63±2.6%). The relative brain weight was higher in the preventive (2.26±0.10%) and reversal (2.91±0.01%) measures compared to dizocilpine-control (1.64±0.10%). The NSO increased glutamate levels in the reversal (0.19±0.00 µM/µg tissue) but not in the preventive (0.18±0.00 µM/µg tissue) groups relative to dizocilpine-control (0.18±0.00 µM/µg tissue). Hippocampal neuronal density was significantly increased by dizocilpine (21.25±1.1neurons/100µm^2) but modulated by NSO in the preventive (17.25±0.5 neurons/100µm^2) and reversal groups (12.00±0.71 neurons/100µm^2). Significant neuronal de-arborisation that occurred in the dizocilpine-control (989.90±253.9 µm^2/2.5mm^2 area) was inhibited by NSO in the preventive (1678±370.90 µm^2/2.5mm^2 area) and reversal (1639±314.8 µm^2/2.5mm^2 area) treatments. Compared to dizocilpine-control (4219±127.3 ODU), NSO increased mGluR-2 expression in the preventive (4945±17 ODU) and reversal (4116±24.9 ODU) groups (Fig. 1). The GFAP expression in NSO-treated animals relative to dizocilpine-control (5510±38.4 ODU) was significantly reduced in the preventive (4945±17 ODU) and reversal (4116±24.9 ODU) measures.

In conclusion, *Nigella sativa* oil mitigated schizophrenic symptoms induced by dizocilpine in mice via modulation of hippocampal glutamate, metabotropic glutamate receptor–II upregulation, astrogliosis inhibition and neuroprotective mechanisms.

References:

1. National Institute of Mental Health. (2016) Schizophrenia. https://www.nimh.nih.gov/health/topics/schizophrenia/index.shtml

2. Naz, H. (2011) Pakistan J. Biochem. Mol. Biol.. 44(1), 44.

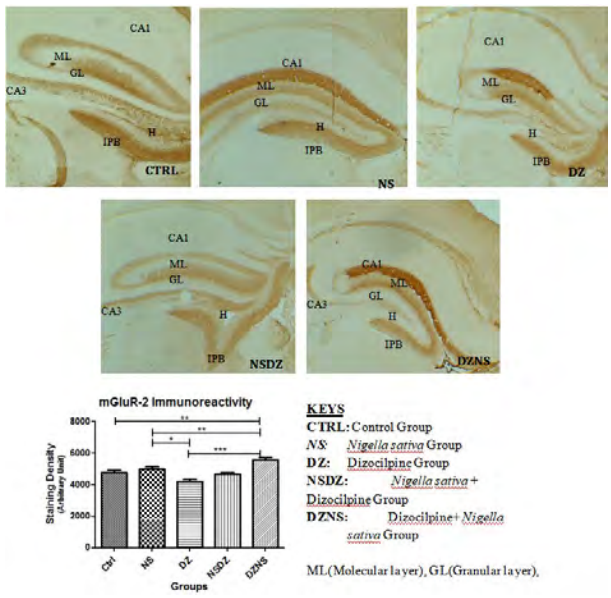

Figure 1. Immunostaining of mGluR-2 in the Coronal section through the Hippocampus across the Mice Groups. Antibody: mGluR-2

Corresponding author:
royhaan.folarin@oouagoiwoye.edu.ng

Nigella Sativa OIL MITIGATED LEARNING AND MEMORY IMPAIRMENT IN *Drosophila* MODEL OF ALCOHOL DEHYDROGENASE (ADH) DEFICIENCY

A.K. Akinbo[1,2,3,4], S.A. Kuye[1] and R.O. Folarin [1]

[1]Department of Anatomy , [2]Olabisi Onabanjo University , [3]Shagamu, [4]Nigeria.

Oil extracted from the seed of *Nigella sativa* has been widely used in the treatment of different diseases and ailments[1] in patients. *Drosophila* share approximately seventy-five percent homology with the human genome in disease-causing genes and representation of all major gene families found in humans. This makes them a cost-effective and ideal model for studying the role of genes and gene product in human neurological disorders and alcohol-related diseases. This research sought to investigate therapeutic potential of *Nigella sativa* oil on learning and memory functions in an adult of *Drosophila* model of alcohol dehydrogenase deficiency. The ADH flies used in this research were bioengineered to be alcohol dehydrogenase deficient. The present study also investigated if there were any general neuro-architectural difference (in terms of neuropiliary or structural layout distortion) in the cross section of the brain and omatidia (of the eyes) that related to the results obtained.

Aversive phototaxis suppression assay (APS) behavioral assay following the exposure to *Nigella sativa* oil was used in this research. Twenty virgin male and twenty virgin female of Oregon R and ADH fly strains were exposed to either normal media (feed) or media containing two percent *Nigella sativa* oil (experimental) for one week *ad libitum*. This assay exploits the positive phototactic behaviour in flies to train them to associate light with an aversive stimulus (in this case acetic acid). The apparatus used for this assay is the T-maze. It consists of the center column with the trap door and two independent chambers, a dark chamber (a vial wrapped with aluminum foil) and a light chamber. Adult flies were kept in the dark for 24 hours before the neurobehavioral assay was conducted. 160 flies were grouped into experimental (ADH male and female, Oregon R male and female) and control group (ADH male and female, Oregon R male and female) equally. The flies were first trained in order to evaluate their behavioural response to light and their visual system. They were transferred into the dark chamber in a red light room because *Drosophila* are insensitive to red light. After 30 seconds in the dark chamber, the lamp illuminating the light chamber was turned on. The trapdoor that separates the two chambers was slowly opened. The flies that walked into the light chamber within 10 seconds were used for the study, whereas those that didn't were excluded because this suggested problems in the visual system. After removing the visually-impaired, the experimental and control flies were grouped into 1 fly per vial for 10 vials across the 8 groups. Each fly was kept in the dark chamber with the trap door closed and light turned off allowing the fly to acclimatize in the dark for 30 seconds. A filter paper with acetic acid solution was placed in the light chamber. The trapdoor was opened and light was turned on. The fly was then allowed to walk into the light chamber. After one minute the fly was tapped back into the dark chamber. This process was repeated 10 times with 1 minute break in between. Flies that moved into the light chamber by the fourth trial were deemed as "fail" and removed from the experiment. For long term memory evaluation, the flies were transferred back into the feed and the assay was conducted again after 24 hours.

In short term memory test, memory was assessed immediately after the training and separation of visually impaired ones (pc(0)). The experimental group had a slightly better pass rate when compared to the control group as shown in Table 1. Long term memory was assessed after 24 hours (pc(24), where the experimental grouped showed a higher pass rate when compared to the control group (Table 1). The brain of the experimental and control *Drosophila* flies were dissected, processed for microscopy and sections stained in with h&e (Fig. 1). No significant anatomical developments were readily observed in the fly brains. Unfortunately, technical issues prevented detailed comparison of sizes and shapes.

Future studies will include immunohistochemical expression of dopaminergic (D1) and glutamatergic (mGluR2) receptors in order to further consolidate these these preliminary findings

References:

1. Ahmad *et al*. (2013). *Asian Pacific J.Trop. Biomed.* 3(5), 337.

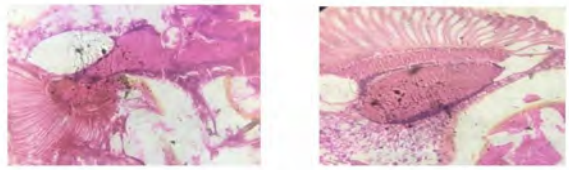

Figure 1. Histology of the *Drosophila* brain and eyes using H&E stain.

Table 1. Results of control and experimental at pc(0) and pc (24)

	CONTROL				EXPERIMENTAL			
	ADH		OREGON		ADH		OREGON	
	M	F	M	F	M	F	M	F
PC(0)✗	70	60	50	40	90	80	80	60
PC(24)✗	30	10	20	10	60	80	70	50

Corresponding author: hellabetty007@gmail.com

FRONTO-CORTICAL EFFECTS OF *Nigella sativa* OIL IN MPTP INDUCED PARKINSONISM IN BALB/C MICE

K.O. Adeniran [1], P.F. Folarin[1], B.S. Surajudeen[1], P.S. Ogunkunle[1], A.O. Olonade[1] and R.O. Folarin [1]

[1]Olabisi Onabanjo University, Ago-Iwoye, Nigeria

Parkinsonism is a degenerative neurological syndrome characterised by dopamine deficiency in the basal ganglia. However, cognitive impairment and dementia have also been implicated as pathophysiological features of the disease at both early and later stages respectively., there is still lack of holistic and non-detrimental therapy for the disease. *Nigella sativa* is a widely known therapeutic agent that is used in folklore medicine because of its anti-inflammatory abilities (Ahmad et al.,2013).1-methyl-4-phenyl-1,2,3,6-tetrahydropyridine (MPTP) is a known neurotoxicant inducer of parkinsonism in human. Consequent to the validity debates on the use of BALB/c mice strains in the modelling of Parkinsonism using MPTP, this study re-appraised the sensitivity and resistance of the BALB/c mice strain to MPTP and further investigated the roles of *Nigella sativa* oil (NSO) on the cognitive and other Parkinsonic endophenotypes elicited by MPTP in the BALB/c strain.

Fronto-cortical dopamine, fronto-cortical neuron density, recognition memory was measured (through the use of novel object recognition test), body weights and relative brain weights were studied in thirty-two (32) male albino mice, weighing between 18g -25g. They were divided equally into Control (administered with normal feed for 5 days), MPTP (administered with 18mg/kg MPTP i.p for 5 days), NS (administered with 1ml/kgbw NSO p.o. for 5 days), and NS+MPTP (administered with 1ml/kgbw NSO p.o. followed by 18mg/kg MPTP i.p for 5 days). The animals were weighed and euthanised 24 hours after last administration and following the behavioural assay. The brains were then removed. Neurochemical assay and the dopamine level was carried out on five of the mice and histological assay on others by staining with H and E stain.

Parkinsonic traits such as mild tremor, down-regulation of dopamine and fronto-cortical neurons (though insignificant at $p<0.05$) were recorded in the BALB/c mice administered with MPTP only,which affirms MPTP-sensitivity of the mice exhibiting these features. However, significant increase ($p<0.05$) in appetite, body weight, brain-body weight ratio, and recognition memory was also recorded in the MPTP-administered mice, though *Nigella sativa* was significantly prophylactic against the negative Parkinsonic features, as it helps to moderate the up-regulations(unusual features) that was induced by MPTP.

While this suggests selective MPTP sensitivity and resistance in BALB/c strains, this study recommends the investigation of possible beneficial potentials of MPTP as it could be used for recognition memory.

References:
1. Chiaravalloti, N. D. *et al*. (2014) J. Movement Disorder Society, 29(6), 765.
2.Al-Naqeep, G. *et al.* (2011) Evidence-Based Complementary and Alternative Medicine, 213628.
3. Langston, J. W. (2017). J. Parkinson's Disease, 7(1), S11.

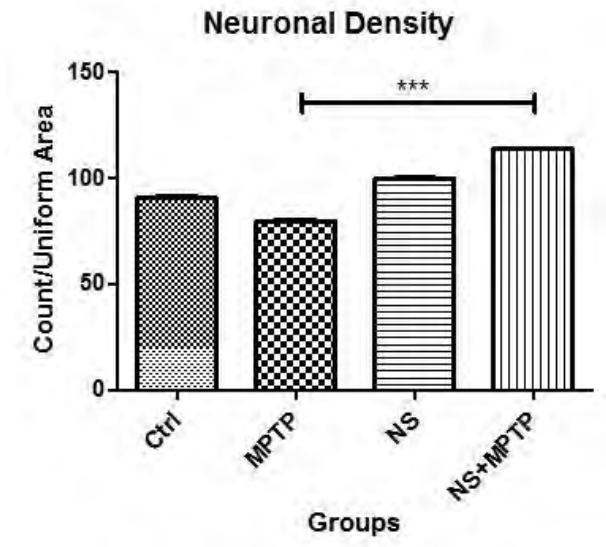

Figure 1. Neuronal density in mice across all four groups. There is no significant difference ($p<0.05$) across the four groups.

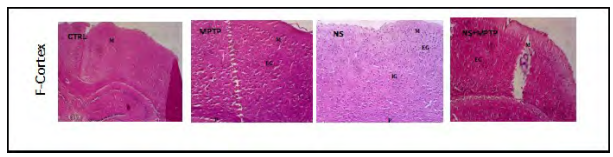

Figure 2. Photomicrographs of the frontal cortex stained with H&E stain across all mice groups as M (Molecular layer), EG (External Granular layer), IG (Internal Granular layer), P (Polymorphic). There is no significant difference ($p<0.05$) across the four groups of mice.

Corresponding author:
royhaan.folarin@oouagoiwoye.edu.ng

THE MORPHOANATOMY AND HISTOCHEMISTRY OF THE FOLIAR TRICHOMES OF *Combretum apiculatum* Sond. subsp. *apiculatum* (COMBRETACEAE)

M. Parusnath[1] and Y. Naidoo[1]

[1]School of Life Sciences, University of KwaZulu-Natal, Durban

Combretum apiculatum Sond. subsp. *apiculatum* is used in the traditional medicinal treatment of many diseases[1]. The plant's medicinal properties are putatively associated with phytocompounds present in foliar trichomes[2]. There are no reports on the microanatomy and histochemistry of the plant's trichomes, therefore, this study aimed to investigate the distribution, morphology and histochemistry of the glandular trichomes at different stages of leaf development by microscopical and histochemical analyses.

Emergent, young and mature *C. apiculatum* leaves were collected in a garden located in the University of KwaZulu-Natal (Westville). Trichome type, distribution and density were determined by photographing leaves of all stages using a stereomicroscope. To characterise trichome microanatomy, leaf sections from each stage were embedded in resin, stained with toluidine blue-O and viewed with a compound-light microscope. To further analyse trichome distribution and microanatomy, segments from leaves of each stage were chemically fixed, dried in a critical point dryer, secured onto aluminium stubs and sputter-coated with gold for viewing in a scanning electron microscope. The presence of phytocompounds within the trichomes were determined by the following histochemical stains: (a) Wagner reagent for alkaloids, (b) ferric chloride with sodium carbonate for phenols, (c) NADI reagent for terpenoids, resin acids and essential oils, (d) ruthenium red for pectins and mucilage, (e) toluidine blue-O for polysaccharides and polyphenols, (f) Sudan III and IV for total lipids, (g) Coomassie blue for total proteins and (h) acridine orange (under UV) for nucleic acids indicating cell viability. The sections were viewed in a compound-light microscope. Trichome density was quantified using the stereomicrographs by counting trichome occurrences in 1 mm^2 selections distributed evenly across the surfaces. A one-way ANOVA was conducted to determine statistical significance in density, with a significant level of 0.05.

The microscopical analyses revealed subsessile/sessile multicellular, peltate, glandular trichomes and singly arranged, uniseriate, non-glandular trichomes on all leaf stages. Trichome densities decreased from the emergent to mature leaves ($p < 0.05$), attributable to the leaf expansion theory[3]. Emergent leaves consisted of dense distributions of trichomes located in epidermal depressions along interveinal areas (fig. 1), suggesting emergence early during leaf development. Glandular trichome densities were high on the abaxial surfaces, whereas non-glandular trichome densities were greater on the adaxial surfaces. Developing, secretory and post-secretory trichomes were observed on all stages. Secretion occurred via cuticle rupture. Histochemistry revealed the trichome head cells to contain alkaloids, phenols, lignin, terpenoids, resin acids, pectins, mucilage, carboxylated and hydroxylated polysaccharides, polyphenols, total lipids, total proteins (fig. 2), and nucleic acids, indicating cell viability. These compounds possess medicinal properties, providing supporting evidence for the plant's traditional medical use[1]. Lignin prevents the backflow of compounds that could lead to trichome cell deterioration[2]. The use of *C. apiculatum* may benefit low-income communities due to affordability and accessibility. Further research is required to investigate modern therapeutic applications and drug development using the plant's leaves and exudates to determine suitable therapeutic concentrations.

References:
1. Aderogba, M., *et al*. (2012) South African Journal of Botany 79(2012), 125-131.
2. Bantho, S., Naidoo, and Y., Dewir, Y. (2020) South African Journal of Botany 131(2020), 104-117.
3. Scott-Brown, A.S., *et al*. (2016) Functional Plant Biology 43(12), 1170-1182.

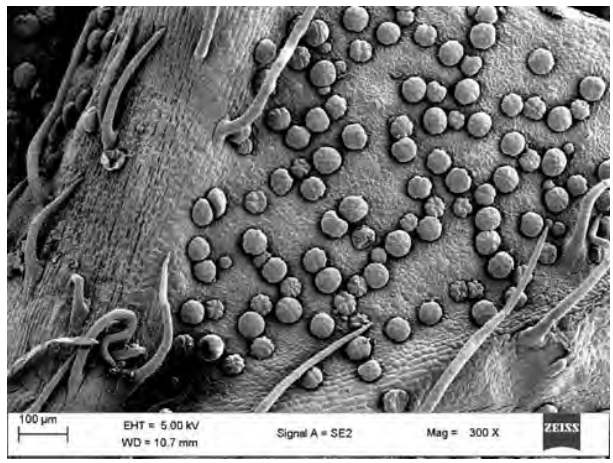

Figure 1. Distribution of glandular and non-glandular trichomes on an emergent leaf of *Combretum apiculatum.*

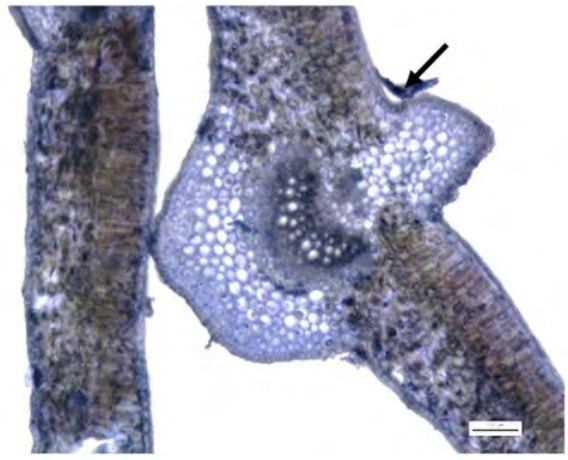

Figure 2. Histochemical localisation of total proteins (blue) in glandular trichome (arrow) within a young *Combretum apiculatum* leaf. (*scale bar = 100 µm)

Corresponding author: myuriparusnath@gmail.com

TRICKY TRICHODINIDS WITH DAUNTING DENTICLES

J. Hastings[1], L. Basson[1] and G.P. de Jager[1]

[1]Department of Zoology and Entomology, University of the Free State, Bloemfontein

Trichodinids are one of the most encountered aquatic ciliate groups that are easily identified by complex structures present in their aboral adhesive disc, referred to as denticles[1]. These ciliates are encountered on an extensive array of hosts, including vertebrates and invertebrates. A rather complex trichodinid was observed on the beaded topshell, *Oxystele impervia* (Menke, 1843), by Fantham in 1930[2]. This species was again identified more than three decades later by Sandon in 1965 as *Trichodina oxystelis* Basson and van As, 1992[3]. Due to the lack of sufficient taxonomic information, this trichodinid was later redescribed in 1992 from all five *Oxystele* species occurring along the southern African coastline[3]. This species exhibits extremely high morphological variation within populations. This variation might suggest the presence of more than one species on these trochids, or indeed a single species with high variation as previously described.

Pink-lipped topshells, *Oxystele sinensis* (Gmelin, 1971), were collected from the rocky shores of De Hoop Nature Reserve in Western Cape, South Africa. Host gills were then screened for ciliates with a Zeiss Primo Star HAL/LED compound light microscope. Wet smears were made for hæmatoxylin staining, to observe the nuclear apparatus, and dry smears for silver impregnation, to study the complex denticle ring. Material was also fixed in absolute ethanol for molecular analysis and glutaraldehyde for scanning electron microscopy (SEM). SEM material was prepared according to standard procedures and observed with a JEOL JSM_7800 Field Emission Scanning Electron Microscope at 5kV.

Trichodina oxystelis specimens encountered in this study have a distinctly disc-shaped body (Fig. 1A). The adoral side bears a ciliary spiral consisting of haplokinety and polikinety which runs along the periphery of the adoral surface, completing more than one full circle before plunging into the infundibulum (Figs 1A, B). A complex ciliary girdle used for locomotion is present on the aboral side (Fig. 1A). The latter structure consists of a short row of cilia separated from more complex rows of cilia with increasing lengths towards the adoral side. The structures of the adoral spiral and ciliary girdle are more easily observed in individuals where the cilia have been removed (Figs 1B, C). *Trichodina oxystelis* collected in the present study exhibited the same high variation in morphometric measurements and denticle morphology as recorded by Basson and van As in 1992. In a preliminary attempt to make sense of this variation, individuals were separated into large and small morphotypes. Certain morphological characteristics allowed for the placing of individuals into these groups, however, upon further investigation many intermediate forms and oddities were also encountered within the same population. Differences were also noted in the nuclear apparatus with the position of the micronucleus being encountered in two distinct positions, the +y (Fig. 2C) and -y[1] position (Fig. 2D), coinciding roughly with the two morphotype groups.

Data currently available regarding morphometrics and denticle morphology of *T. oxystelis* have not yet made it possible to determine what this variation implies. Molecular techniques will, however, be used to make sense of this perplexing species.

References:
1. Basson, L. and van As, J.G. (2006) Fish Diseases and Disorders, Vol 1, Protozoan and Metazoan Infections. Wallingford, CAB International.
2. Fantham, H.B. (1930) S. Afr. J. Sci. 27, 376.
3. Basson, L., van As, J.G. (1992) Syst. Parasitol. 22, 231.

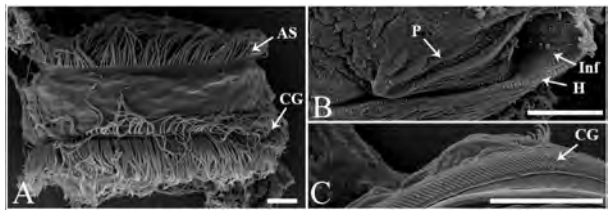

Figure 1. Scanning electron micrographs of *Trichodina oxystelis* Basson and van As, 1992. A: Body shape, adoral spiral (AS) and ciliary girdle (CG). B: Close-up of the infundibulum (Inf), Haplokinety (H) and Polikinety (P). C: Close-up of the bare kinetosomes of the complex ciliary girdle (CG) (Scale =5µm)

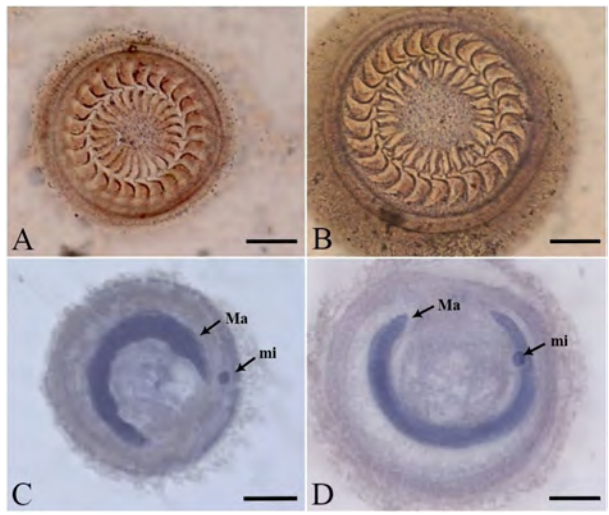

Figure 2. Light micrographs of *Trichodina oxystelis* Basson & van As, 1992. A & B: Silver nitrate impregnations depicting the variation encountered. C & D: Hæmatoxylin stained individuals, macronucleus (Ma) and the two positions of the micronucleus (mi), the +y (C) and the -y[1] (D), respectively. (Scale =10µm).

Corresponding author: BassonL@ufs.ac.za

A PRELIMINARY INVESTIGATION ON THE MORPHO-HISTOCHEMICAL ATTRIBUTES OF THE MEDICINAL PLANT, *Kedrostis nana* (LAM.) COGN

K. Doolabh[1] and Y. Naidoo[1]

[1]School of Life Sciences, University of KwaZulu Natal, Durban

The basis of most ancient traditional medicinal systems stemmed from chemically diverse compounds found in plants [1,2]. These active compounds may be localized in the leaves, stem, and root or microstructures such as trichomes or secretory glands [3].

South Africa is well endowed with rich plant biodiversity, of which only 13.8% of the floral species supply the majority of its people with an invaluable source of medicine [4,5]. Many of these medicinal plant species have been well documented and researched; however, some require further investigative elucidation.

Kedrostis nana (Lam.) Cogn. is a perennial herb of the Cucurbitaceae family[6], traditionally used to treat diabetes, cancer and haemorrhoids [7]. Research on this species have mainly highlighted the plant's traditional medicinal use by healers. There is little to no current research investigating the plant's micromorphology and chemical composition. Therefore, this preliminary study intends to examine the morpho-histochemical characteristics of the leaves and stems of *K. nana*.

A Nikon AZ100 stereomicroscope was used to observe the leaf and stem topography. For histochemical analyses, leaf and stem sections (200µm) were stained using the following tests: Ruthenium red (mucilage and pectin), Toluidine blue (general stain), Ferric chloride (phenolic compounds), Wagner's and Dittmar (alkaloids) and Calcofluor white (carbohydrates). Stained sections were viewed using a Nikon Eclipse 80i compound light coupled with a Nikon DS-Fil camera.

Further micromorphological assessments were accomplished using a scanning electron microscope (SEM). Leaf and stem segments (5mm^2) were quenched in a liquid nitrogen slush, freeze-dried to room temperature over 48 hours and analyzed using a LEO 1450 SEM.

Stereoscopic observations revealed a glossy, smooth leaf surface, lobed margins and a cordate base. Trichome density and distribution on the leaf epidermis were sparse; however, the stem had a dense indumentum. Non-glandular trichomes (NGTs) were distributed irregularly throughout the leaf and margin, whereas most glandular trichomes (GTs) appeared centrally on the leaf base. The presence of trichomes along the leaf margin is proposed to aid in plant defence against herbivory[3].

Results from the histochemical analyses showed that the leaf and stem contained bioactive compounds of medicinal significance such as carboxylate polysaccharides, phenols and macromolecules (Fig 1). Most of the bioactive compounds were confined mainly in the basal cells of trichomes and epidermis of the leaves and stems.

SEM examinations revealed uniseriate NGTs. Two types of these trichomes appear on the leaf and stem, *viz.* multicellular with a tapering end, and hook-like. Pilate GTs were also noted dispersed over the areas examined.

To our knowledge, this investigation is the first detailed study describing the plant's morpho-histochemical attributes. The results also add a basis to the plant's use as a traditional medicinal product. Phytochemical and pharmacological evaluations are required further to validate *K. nana* as a new candidate for drug development.

References:
1. Gurib-Fakim, A. (2006) Mol. Aspects Med. 27(1), 1.
2. Masaondo, N.A. and Makunga, N.P. (2019) S. Afr. J. Bot. 126, 40.
3. Fahn, A. (2000) New Phytol. 108(1), 229
4. Adebayo, S.A. and Amoo, S.O. (2019) S. Afr. J. Bot. 123, 214.
5. Van Wyk, B.E. and Gericke, N. (2007) People's Plants. A Guide to Useful Plants of Southern Africa. Pretoria, Briza.
6. Germishuizen, G. and Meyer, N.L. (2003) Plants of southern Africa: an annotated checklist. Pretoria, Strelitzia.
7. Deutschländer, M.S., Lall, N. and van de Venter, M. (2009) Pharm. Biol. 47(4), 348.

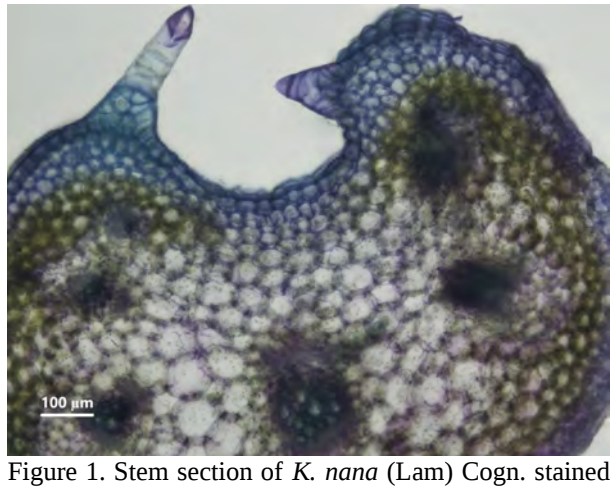

Figure 1. Stem section of *K. nana* (Lam) Cogn. stained with Toluidine blue showing carboxylated polysaccharides (blue), phenols (blue-green) and macromolucules (pinkish- purple)

Corresponding author: kareshma.doolabh@yahoo.com

MAKING EVERY ELECTRON COUNT: APPLICATIONS OF LOW DOSE ELECTRON PTYCHOGRAPHY

A.I. Kirkland[1,2]

[1]Department of Materials, Parks Road, Oxford, OX13PH UK, [2]The Rosalind Franklin Institute, Harwell Campus, Didcot, OX11 0QX UK

This lecture will describe recent developments in the use of Electron Ptychography for studies of materials, including biological structures at low electron dose.

The acquisition of a ptychographic dataset requires the collection of a series of far field diffraction patterns as a function of probe position at the specimen plane. The probes used can have a range of convergence angles and the required overlap that encodes the phase information can be in either real or reciprocal space. This dataset can then be used to recover the complex specimen object function using either iterative or non-iterative algorithms. The former includes the iterative Ptychographic engine (ePIE) and the latter a single side band approach or a full Wigner deconvolution. Importantly, ptychography is an inherently dose efficient technique, enabling effective phase reconstruction of radiation sensitive samples and if information outside the bright field disk is used can reconstruct super resolved data out to the diffraction limit.

One limitation in the use of the pixelated detectors required is that their readout speed is lower than that of the monolithic solid state detectors used for conventional bright and dark field STEM imaging. However, at low dose the sampling of the diffraction pattern in the far field is sparse and a pixelated counting direct electron detector can be operated in a binary mode to provide an effective speed increase that is approximately proportional to the bit depth used for counting. Hence for sparse data a binary counting mode can be used, and I will illustrate this approach using examples of radiation sensitive mesoporous materials at frame times of <1ms. I will also highlight recent developments in event driven detection which can provide effective frame rates of 1μs or less, matching or exceeding conventional monolithic solid-state detectors. The prospects for future higher frame rates using event driven detection with timings <100ps will also be described.

In the life sciences Cryo-electron ptychography (Cryo-EPt)[1] holds much promise particularly when used with a defocused probe to scan across a specimen with highly overlapped probe positions in the specimen plane. This can be applied in a variant of single particle analysis to provide 3D structures (Fig.1), taking advantage of the known resolution variation of the effective ptychographic transfer function with convergence angle (Fig. 1). The latter can be used to selectively transfer low, medium, and high spatial frequencies and multiple datasets can be Fourier synthesized to provide wide spatial frequency bandwidth transfer.

More recent work using ptychography to provide quantitative phase information from hybridinorganic / organic nanostructures will also be discussed using templated DNA scaffolds as an example.

Finally, the recent development of Fourier ptychography based on the acquisition of a series of TEM images recorded at different tilt angles to provide super resolution information over wide fields of view will be described. This technique is related to conventional ptychography and can utilize the same reconstruction algorithms. The parallel recording of multiple effective probe positions in an image for a single tilt is particularly applicable to studies of large-scale biological structures and / or molecules in a cellular context.

References:
1. Zhou, L. *et al.* (2020) Nature Communications **11**, 2773.

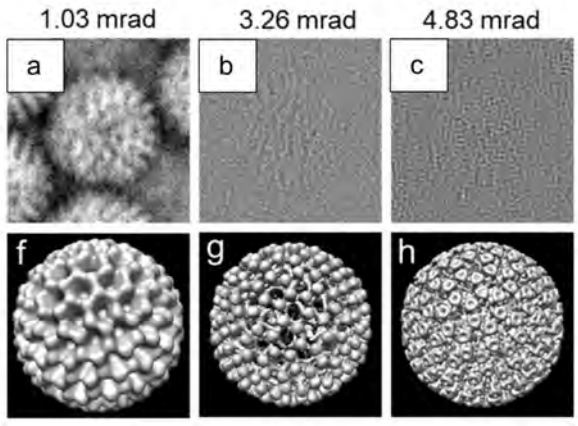

Figure 1. (a-c) Recovered ptychographic phase of a rotavirus as a function of convergence angle with corresponding 3 D density maps (f-h)

Corresponding author:
angus.kirkland@materials.ox.ac.uk

SHI INDUCED BULK ROTATION IN NON-AMORPHIZABLE TARGETS: A NiO CASE STUDY

J.H. O'Connell[1] and D.A. Douglas-Henry[2]

[1]CHRTEM, Nelson Mandela University, Port Elizabeth, [2]Trinity College, Dublin, Ireland

A swift heavy ion (SHI, E >1 MeV/amu) loses the largest part of its energy (>95%, 5–50 keV/nm along the ion trajectory) through excitation of the electronic subsystem of the target material. SHI penetration trough various insulators have shown quite different manifestations of structure transformations[1]: amorphous tracks (e.g. $Y_3Fe_5O_{12}$, α-quartz), defected crystalline tracks (e.g. Mg_2AlO_4, Al_2O_3, ZrO_2, NiO) or production of isolated point defects and color centers (e.g. MgO, alkali halides). This motivates research aimed at the understanding of mechanisms responsible for material modification. An interesting and relatively under studied effect of SHI irradiation at off normal incidence is that of induced rotation in materials. The effect was first observed in amorphous glasses and was explained via a continuum mechanics approach in[2]. Since then, rotation has been observed in several polycrystalline and single crystalline systems using mainly surface shifts and X-ray diffraction to measure rotation angle[3,4]. Recent electron microscope-based analysis proved this assumption to be incorrect and instead it is believed that rotation is a consequence of complex dislocation motion due to off normal ion hammering stresses.

Single crystal NiO specimens from MaTEK were irradiated up to $1.3x10^{14}$ cm^{-2} with 593 MeV Au ions at the M2 branch at GSI, Darmstadt, Germany. The irradiation chamber houses an online X-ray diffractometer and a 3-axis eulerian cradle as specimen mount (see Fig.1). Irradiated specimens were A case study of Au irradiated single crystal (001) oriented NiO will be presented as the simple NaCl structure limits the number of required slip systems when the irradiation geometry is suitably symmetric.In order to gain insight on the rotation mechanism, depth dependent rotation curves were extracted from electron backscatter diffraction maps (Oxford Nordlys detector in a JEOL JSM 7001F) of cross sectionally polished specimens and TEM (JEOL ARM 200F operating at 200 kV) was used to study the microstructure of irradiated specimens. Fluence dependent XRD spectra were obtained online during irradiation. TEM analysis revealed a high density of dislocations in the irradiated layer with visible ion tracks composed of void trains as shown in Figure 2.

Previous results suggested the creation of low energy dislocation systems where individual cells were freely rotating under the ion induced stress field. More recent analysis however showed that dislocation motion through the bulk is a more plausible explanation, and this model can better describe the experimental observations. Dislocation motion is driven by a macroscopic stress field induced by the off normal ion trajectories producing inclined latent tracks in the crystal. Boundary conditions enforced by the free surface at the top and the supporting unaffected bulk below leads to a stress state that is responsible for generation and separation of dislocations.

A new improved model was proposed to explain the mechanism responsible for observed crystal rotation due to SHI irradiation.

Acknowledgements
Siegfried Klaumuenzer for XRD measurements and a lot of discussion regarding stress states and dislocation generation and motion.

References:
1. Komarov, F.F. (2017) Physics-Uspekhi 60, 435.
2. Klaumuenzer, S. (2004) Nucl. Inst. Meth. B 215, 345.
3. Zizak, I. et al. (2009) Nucl. Inst. Meth. B, 267, 944.
4. Zizak, I. et al. (2008) Phys. Rev. Lett. 101, 1.

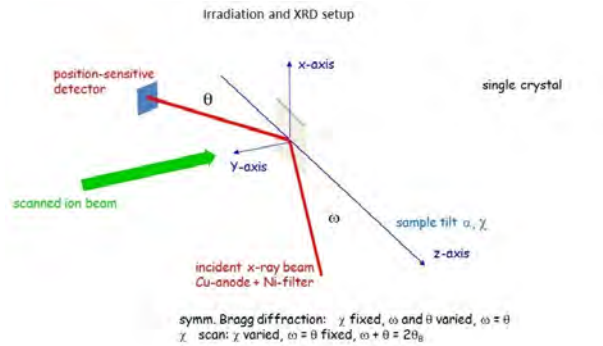

Figure 1. Irradiation and x-ray diffraction geometry

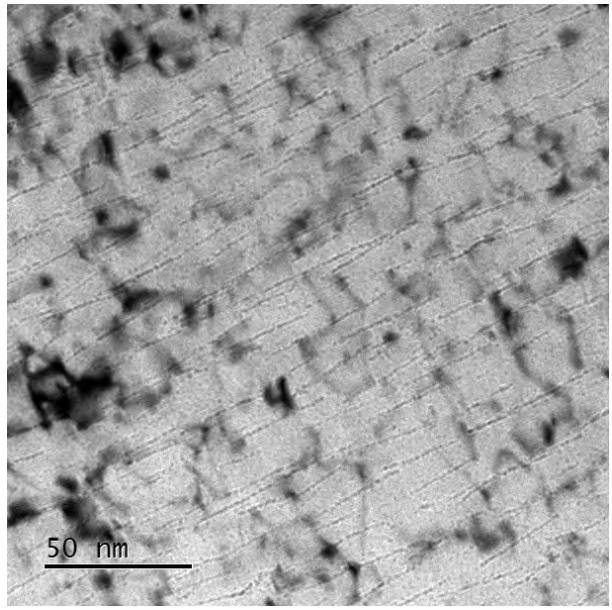

Figure 2. BF TEM micrograph of ion tracks and dislocations in 593 MeV Au irradiated NiO.

Corresponding author: jacques.oconnell@gmail.com

MOLECULAR DYNAMICS AND TEM INVESTIGATION OF SWIFT HEAVY ION TRACKS IN INSULATORS

R.A. Rymzhanov[1,2], J.H. O'Connell[3], N. Medvedev[4,5], A. Janse van Vuuren[3], V.A. Skuratov[1,6,7] and A.E. Volkov[1,8]

[1]Joint Institute for Nuclear Research, Dubna, Russia, [2]The Institute of Nuclear Physics, Almaty, Kazakhstan, [3]Nelson Mandela University, Port Elizabeth, South Africa, [4]Institute of Physics, Czech Academy of Sciences, Prague, Czech Republic, [5]Institute of Plasma Physics, Czech Academy of Sciences, Prague, Czech Republic, [6]National Research Nuclear University MEPhI, Moscow, Russia, [7]Dubna State University, Dubna, Russia, [8]P.N. Lebedev Physical Institute of the Russian Academy of Sciences, Moscow, Russia

Electronic stopping of a swift heavy ion (SHI) in a solid and further relaxation of the material causes the formation of nanometric modified regions around the ion trajectory. This feature is used in a wide range of applications such as creation of nanodots, production of track-etched membranes, nanostructuring of solids, etc. We discuss here the kinetics of track formation, track overlap and surface modifications in amorphizable and non-amorphizable solids irradiated with SHI studied through a combination of TEM based experiments and numerical simulations.

Single crystalline specimens were irradiated with high-energy heavy ions at the cyclotron complex of FLNR JINR (Dubna, Russia). High-resolution transmission electron microscopy (HRTEM) studies were carried out at the Centre for HRTEM at Nelson Mandela University (Port Elizabeth, South Africa).

An original multiscale model was applied to study the excitation and relaxation kinetics of targets exposed to swift heavy ions[1]. The approach couples the Monte Carlo code TREKIS[2] simulating excitation of electron subsystem with the classical molecular dynamics modeling of structure transformations. In order to compare results of simulations with the experimental data, the TEM images were simulated from MD super cells.

It was shown that SHI irradiation induces notably different damaged structures in amorphizable and non-amorphizable targets, despite similar deposited energy and almost identical sizes of the initially disordered regions after ion impacts[3]. MgO shows no clear SHI track formation. Ion passage in Al_2O_3 forms discontinuous, strained crystalline tracks, which coincide well with the HRTEM studies of irradiated samples[4]. A track in YAG is a cylindrical amorphous region that agrees well with the TEM data. This difference can be attributed to the strong recrystallization ability of MgO and Al_2O_3 in contrast to YAG.

The recrystallization of a damaged region after an SHI impact can be very fast (~20-70 ps), which does not allow detection of this effect directly through existing experimental techniques. One of the possible ways of an indirect study of such processes is a comparison of the morphology of interacting ion tracks at different fluences.

Simulations revealed that impacts of ions in Al_2O_3 at a short separation distance cause almost perfect annealing of the existing defective structure. Existing tracks recover only partially at a distance of ~6.5 nm between track centers forming a damaged region between the two tracks, which was also observed experimentally in TEM micrographs (Figure 1). It was demonstrated numerically and experimentally that the inter-track connection in YAG occurs at much shorter distances between the tracks confirming the absence of recrystallization in this material.

The simulations and experiments demonstrate noticeable differences in the surface damage between amorphizable and non-amorphizable materials. Recrystallization in MgO and CaF_2 almost completely recovers transient damage in the near surface region, forming crystalline hillocks, which is confirmed by TEM. YAG demonstrated almost no recovery of the transient disorder, forming a completely amorphous hillock and a track of a cylindrical shape. Protrusion of molten material and a final structure of surface defects are governed by the mobility of target atoms, surface tensions and recrystallization of a material during the ultra-short cooling period[5].

References:
1. Rymzhanov, R.A. *et al.* (2020) Nucl. Instrum. Meth. B. 473, 27.
2. Medvedev, N., Rymzhanov, R.A., Volkov, A.E.(2015) J. Phys. D 48(35), 355303.
3. Rymzhanov, R.A. *et al.* (2019) Sci. Rep. 9(1), 3837
4. Rymzhanov, R., Medvedev, N.A., Volkov, A.E.(2017) J. Phys. D 50, 475301.
5. Rymzhanov, R.A. *et al.* (2020) J. Appl. Phys. 127, 015901.

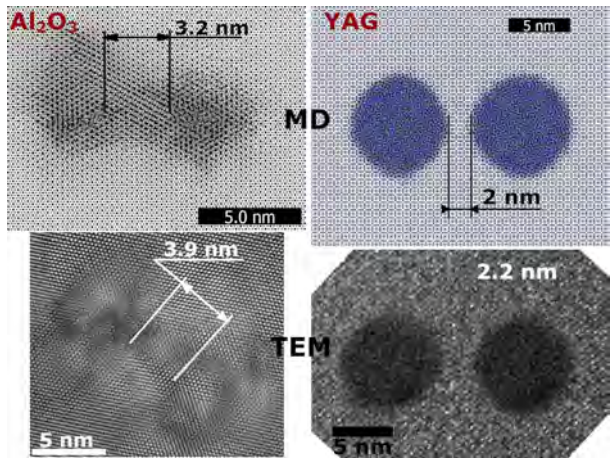

Figure 1. MD and TEM images of 700 MeV Bi ion tracks in Al2O3 and YAG in overlapping regime.O3 and YAG in overlapping regime.3 and YAG in overlapping regime. and YAG in overlapping regime.

Corresponding author: rymzhanov@jinr.ru

THERMODYNAMIC PARAMETERS FOR THE STABILIZATION AND TRANSFORMATION OF TETRAGONAL SHI TRACKS IN MONOCLINIC ZIRCONIA

M.E. Lee[1], J.H. O'Connell[1] and V.A. Skuratov[2]

[1]Centre for HRTEM, NMU, Gqeberha, South Africa, [2]FLNR, JINR, Dubna, Russia

Pure bulk zirconia (ZrO2) is a polymorphic oxide that exists in three different low pressure crystal structures below its melting point namely, the high temperature phases cubic and tetragonal as well as the low temperature monoclinic phase1. Irradiation of bulk polycrystalline monoclinic zirconia at irradiation fluences in the range 2 x 1012 – 1 x 1017 cm-2 have been shown to produce tetragonal grains which are stable at room temperature (RT)2. However, it was recently reported3 that individual ion tracks were produced in bulk monoclinic zirconia at fluences as low as 2 x 1010 cm-2. These ion tracks were shown by transmission electron microscopy (TEM) to produce non-continuous tetragonal latent tracks consisting of segments approximately 20-30 nm in length and rectangular cross section of the order 2.5 nm.The segments were aligned along the [001]t crystal axis and approximately 9° to the [100]m axis3. In this report we compare the room temperature stability of the tetragonal ion tracks as well as the mechanism for their transformation to the predictions by various thermodynamic models4.

Single crystalline monoclinic ZrO2 was irradiated along the [100]m with 167 MeV Xe ions to a fluence of 2x1010 ions.cm-2 at the FLNR, JINR, Dubna. Plan view and cross sectional TEM lamellae were prepared by a standard FIB lift out procedure using an FEI Helios NanoLab 650 and imaged in TEM and STEM mode using a JEOL ARM 200F TEM operating at 200 kV.

Although stressed, the tetragonal segments (Fig 1) were found to be stable at room temperature for several years. The TEM BF plan view image shown in figure 2 indicates that tracks within a critical spacing (less than 4nm) did not interact with each other. However, in situ thermal excitation (100-200°C) well below the bulk transformation temperature as well as in situ excitation by high energy electrons was able to transform the tetragonal phase back into the monoclinic phase leaving behind a train of defect clusters as is typical of ion tracks in non-amorphizable crystals.

It was therefore concluded that the stabilization of the high temperature phase was possibly due to two parameters namely the interfacial surface energy, which determined the critical crystallite size for RT stabilization of the tetragonal phase as proposed by the Garvie equation5 combined with the presence of excess oxygen vacancies within the tetragonal segments6. The proposed mechanism for the transformation of the tetragonal tracks to the monoclinic phase was therefore due to the release of the interfacial energy under heating with the diffusion of the oxygen interstitials to the stressed regions at the junctions between the tetragonal segments.

References:
1. Bailey J.E. (1964) Proc. R. Soc. A. Math. Phys. Sci., 279, 395.
2. Simeone D. et al (2004) Phys. Rev. 70, 134116.
3. O'Connell J.H. et al (2020) Nucl. Inst. Meth. Phys. Res. B, 473, 1.
4. Pitcher M.W. et al (2005) J. Am. Ceram. Soc., 88, 160.
5. Garvie R.C. (1965) J. Phys. Chem. 69, 1238.
6. Lu X et al (1997), J. Mater. Sci., 32, 6653.

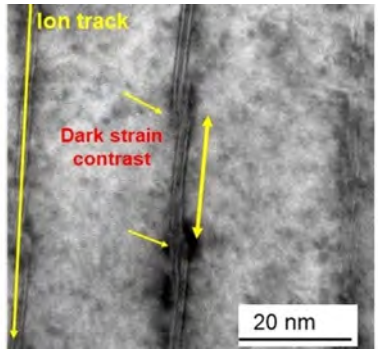

Figure 1. TEM BF cross sectional image of tetragonal ion tracks in monoclinic zirconia showing strain contrast at the junctions

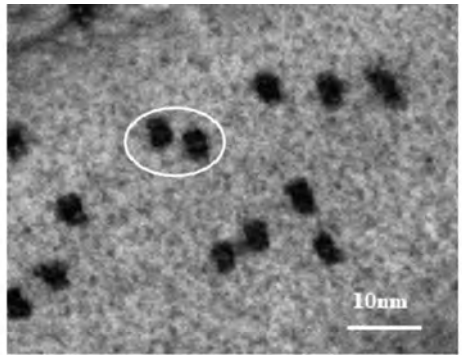

Figure 2. TEM BF plan view image of tetragonal ion tracks in monoclinic zirconia showing proximity of the tracks

Corresponding author: michael.lee@mandela.ac.za

ANNEALING - INDUCED MICROSTRUCTURAL CHANGES FOR SHI TRACKS IN POLYCRYSTALLINE SILICON NITRIDE

A Ibrayeva[1,2], J O'Connell[1], A Janse van Vuuren[1] and V Skuratov[3]

[1]Centre for HRTEM, Nelson Mandela University, Port Elizabeth, South Africa, [2]Institute of Nuclear Physics, Nur-Sultan, Kazakhstan, [3]Flerov Laboratory for Nuclear Research, Joint Institute for Nuclear Research, Dubna, Russia

Latent tracks are specific defects induced in solids due to the irradiation with swift heavy ions (SHIs) along an incident ion path. These tracks are typically a few nanometers in diameter and up to tens of micrometers in length[1,2]. Thermal annealing may result in a diminished track size as well as the possibility of material recovery and recrystallization[3-6]. The influence of annealing on the amorphization kinetics of ion tracks was mainly restricted to reports on crystalline oxides[3,4] and carbides[5,6]. However, to date there have been no reports on the recovery process induced by thermal annealing in nitride solids. Si_3N_4 is of interest as it is a potential candidate for an inert matrix fuel host material[7,8]. It is also the only nitride ceramic where latent ion tracks have been observed[8].

The aim of this work is to report on the thermal heating-induced changes of structural and morphological features for latent tracks in irradiated polycrystalline silicon nitride (p-Si_3N_4). Samples were irradiated with high energy xenon and bismuth ions at a fluence of 5×10^{11} cm^{-2} corresponding to a single-track mode. The recovery process was observed by imaging suitable specimens in a JEOL ARM 200F TEM operated at 200 kV. Specimen annealing was carried out in-situ using a Dens heating holder in the TEM and ex-situ using a tube furnace under an argon flow at temperatures in the range 100 - 1000°C.

The full recrystallization of amorphous areas in samples irradiated with Xe ions is observed at 800°C. Figure 1 demonstrates the typical dynamics of track density reduction during in-situ annealing. For the Bi ion-induced tracks complete recrystallization was not observed at 1000°C during in-situ heating as shown in figure 2(a). In comparison the ex-situ track recovery as shown in figure 2(b) revealed a strained region containing partially crystallized track material. The possible difference in behaviour may be related to the total annealing time, namely 10 seconds for in-situ and 20 minutes for ex-situ annealing. It was also observed that the recrystallization process was initiated in the temperature range 300 - 400°C for all specimens during both annealing modes.

The approximate temperature range of the recrystallization in polycrystalline silicon nitride is thus reported as 300 - 800°C in the case of tracks formed during irradiation with 220 MeV Xe, and 400 -1000°C in the case of 710 MeV Bi. The data obtained from this work was unable to provide a full explanation for the track recovery process. It was nevertheless concluded that the characterization of SHI defects in polycrystalline silicon nitride may provide an accurate evaluation of the lifetime of silicon nitride as a candidate material for application as an inert matrix fuel host.

Acknowledgement. This research was funded by the Ministry of Education and Science of the Republic of Kazakhstan (Grant No AP08856368).

References:
1. Ewing, R.C. et al. (2003) Rev. Miner. Geochem., 53(1), 387.
2. Zinkle, S.J. et al. (2002) Nucl. Instrum. Meth. Phys. Res. B, 191, 758.
3. Schauries, D. (2018). Ion Tracks in Apatite and Quartz. Springer Theses. Springer, Cham., 115.
4. Park, S., et al. (2015), Act. Mater., 93, 1.
5. Jiang, W., et al. (2011), J. Am. Ceram. Soc., 94(12), 4127.
6. Nasdala, L., et.al. (2001), Contr. Mineral. Petr., 141(2), 125.
7. Lee, Y.-W., et al. (2001), Met. and Mater. Int., 7(2), 159.
8. Janse van Vuuren, A. et al. (2020). Mater. Res. Exp., 7(2), 025512.

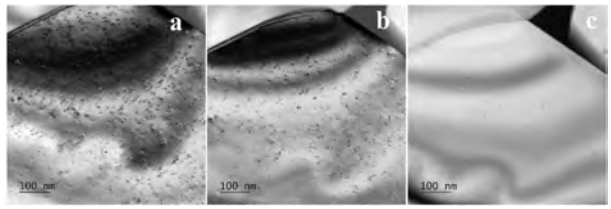

Figure 1. BF TEM images of p-Si_3N_4 irradiated with 220 MeV Xe at different temperatures due to in-situ annealing at (a) a room temperature; (b) 300°C; (c) 800°C.

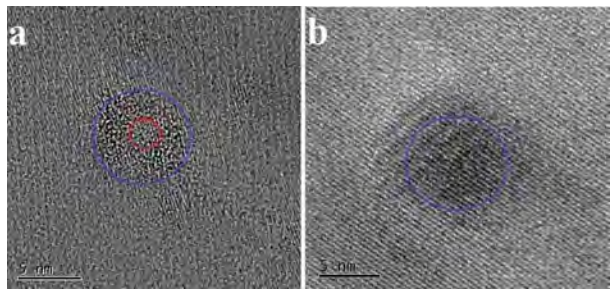

Figure 2. HR TEM images of p-Si_3N_4 irradiated with 710 MeV Bi at annealed at 1000°C (a) in-situ and (b) ex-situ. A red circle is used to mark an amorphous region in a track, blue circles – crystallized zones.

Corresponding author: a.d.ibrayeva@gmail.com

A HIGH-RESOLUTION TEM STUDY OF THE INTERACTION OF SWIFT HEAVY IONS WITH INSULATORS

A. Janse van Vuuren[1], A. Ibrayeva[1], J.H. O'Connell[1], R. Rymzhanov[2], V.A. Skuratov[2] and M. Zdorovets[3]

[1]CHRTEM, Nelson Mandela University, Gqeberha, South Africa , [2]FLNR, Joint Institute for Nuclear Research, Dubna, Russia, [3]Astana Branch of Institute of Nuclear Physics, Astana, Kazakhstan

Unlike low energy ions (E < 10 keV/amu), swift heavy ions (SHIs - E > 100 keV/amu) lose energy almost exclusively through electronic energy loss mechanisms as they traverse a target material, consequently they produce unique defect structures[1]. These ions induce a highly excited state within a cylindrical zone of small diameter along their trajectory. The excited volume can be tens of micrometres long but has a diameter of only a few nanometres. This high energy state is rapidly dissipated through the interaction of the electronic and atomic subsystems of the target material and depending on the thermophysical properties of the material may induce latent disorder. This disorder may range from point defects to phase-changes and even complete amorphisation but is highly dependent on both the material properties and the ion mass and energy. Since the disorder is induced along a narrow cylinder the resultant disorder is often referred to as a latent ion track[2]. Several models have been reported which describe the energy loss mechanism for these highly energetic ions. To date there is no agreement regarding the correct approach for the modelling of this interaction[3,4].

The aim of this study is the analysis of defect structures induced by SHIs by means of direct observation. HRTEM is the only technique available for the direct observation of the latent damage in insulators induced by swift heavy ions and hence the characterization of associated defects and the parameters that influence their evolution.

The stopping power (S_e) of the ion (i.e. its rate of energy deposition over distance) usually influences tracks size but has also been shown to have an effect in final track morphology as is observed in both $Y_3Fe_5O_{12}$ (YIG) and Si_3N_4 where tracks are discontinuous at lower S_e and continuous at higher S_e (Fig. 1). Evidence that impurities influence the threshold stopping power for track formation was observed in Al-doped Si_3N_4 in a sample irradiated with 167 MeV Xe to a fluence which induced amorphisation except for a small grain where EDS showed no detectable Al. (Fig. 2). The phase (or crystal structure) of the material has also been shown to play a role in latent track morphology as is observed in $YAlO_3$ (YAP) and $Y_3Al_5O_{12}$ (YAG) which have the same constituent atoms but differ in crystal structure however ions of similar stopping power induced tracks with a clear difference in diameters in these materials (Fig. 3). Irradiation temperature has also been observed to influence track morphology in YAP and YAG, but only at elevated temperatures (1000 K). A correlation between re-crystallization efficiency within ion tracks and lattice structure has also been observed in MgO, Al_2O_3 and YAG where the initial deposited energy is near identical but final track morphology is noticeably different[5]. Other parameters such as particle size and matrix effects for embedded nanoparticles have been shown to play a role in some these materials[6].

A review of the parameters which have been observed to play a role in the formation and morphology of latent ion tracks through HRTEM techniques will be presented.

References:
1. Avasthi, D.K., Mehta, G.K. (2011) Ion Matter Interaction, Dordrecht, Springer
2. Lang, M. et al., (2020) Comprehensive Nuclear Materials, Oxford, Elsevier
3. Fleischer, R.L., et al., (1965) J. Appl. Phys. 36, 3645.
4. Toulemonde, M., et al., (2002) NIMB, 166 903
5. Rymzhanov, R.A., et al. (2019) Sci. Rep. 9, 3837
6. Rogozhkin, S.V, et al., (2021) NIMB, 486, 1-10

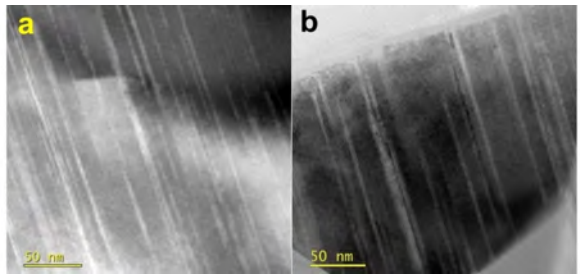

Figure 1. BF-TEM micrographs of Si_3N_4 irradiated with ions with S_e of (a) 22 keV/nm and (b) 31 keV/nm respectively

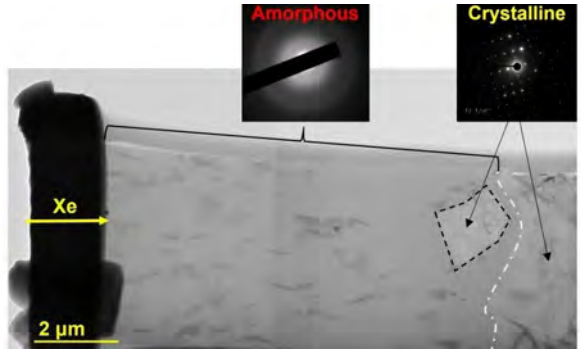

Figure 2. Cross-sectional BF-TEM micrograph of Al doped Si_3N_4 showing amorphous and crystalline regions.

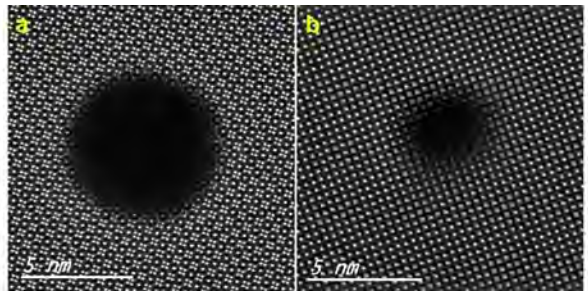

Figure 3. Planar HAADF STEM micrographs of (a) YAG and (b) YAP irradiated with ions of similar sopping power.

Corresponding author: arnojvv@gmail.com

THE INFLUENCE OF ZrB_2 ADDITIVES ON THE THERMAL STABILITY OF POLYCRYSTALLINE DIAMOND

M. Jivanji[1,2], D. Aldmington[1] and J.E. Westraadt[2]

[1]Element Six (Pty) Ltd, Springs, South Africa, [2]Centre for HRTEM, Physics Department, Nelson Mandela University, Gqeberha, South Africa

Polycrystalline diamond compacts (PDCs) are used extensively in the super abrasive industry. The material is typically manufactured by placing diamond powder onto a WC/Co substrate and sintering at high pressures (>5.5GPa) and high temperature (≈ 1450°C). The residual cobalt present in the microstructure after sintering is known to accelerate diamond degradation at temperatures above 700°C[1], leading to catastrophic failure of the PDC tool during application. The aim of this study is to modify the residual cobalt phase into a non-catalytic phase using ZrB_2 additives.

To this end, diamond powder was mixed with ZrB_2 powder in a 90:10 mass ratio, placed onto a WC-Co substrate, and sintered at 7 GPa and 1700°C. X-Ray diffraction (λ_{Co}=1.789 Å) was used for phase analysis. In-situ PXRD data were collected on a PANalytical X'Pert Pro diffractometer equipped with an Anton Paar HTK1200 reaction chamber. The in-situ heating was performed under vacuum (10^{-4}-10^{-6} mbar) using a stepped profile from 800°C up to 1100°C. Thin lamellae were removed from the binder phases using focused ion-beam (FIB)-SEM and mounted on a DENSsolutions heating chip. In-situ TEM was performed using a JEOL200F ARM Transmission Electron Microscope with HAADF-STEM/EDS capability. The samples were heated from 450°C – 900°C in intervals of ~100°C and imaged with HAADF-STEM. The presence of graphitic phases were confirmed using STEM-EELS analysis.

PXRD analysis (Fig. 1) shows that the ZrB_2-PCD sample consists of diamond, WC, ZrC, Co_2B and a B_6Co_{23}. The (200) cobalt peak observed in conventional PCD was not detected in the sample with ZrB_2 addition. The topographical view of the in-situ PXRD dataset of the standard PCD (Fig. 2), highlights that the onset of graphite formation occurred at 850°C, whereas graphite formation was only observed at 1050°C in the ZrB_2-PCD. HAADF STEM images (Fig. 3) show that the onset of graphitization in conventional PCD occurred after heating for 10 minutes at 800°C. Multiple graphitic nucleation sites were observed at this temperature. Graphitisation continued rapidly as the temperature was increased to 900°C. HAADF-STEM imaging of ZrB_2-PCD sample showed minor signs of graphite formation at 800°C. At 900°C, no additional nucleation sites were detected, and no appreciable growth in the existing graphite phases were observed. No signs of bulk graphitization was observed in this sample.

The results confirm that boron from the ZrB_2 additives combined with cobalt to form cobalt boride phases (Co_2B and B_6Co_{23}). No pure cobalt was present in the ZrB_2-PCD sample following HPHT sintering. Consequently, significantly improved thermal stability was demonstrated for the ZrB_2-PCD sample compared to standard PCD.

References:
1. Liu, C. *et. al* (2012) Int. J. of Refractory Metals and Hard Materials 31, 187.

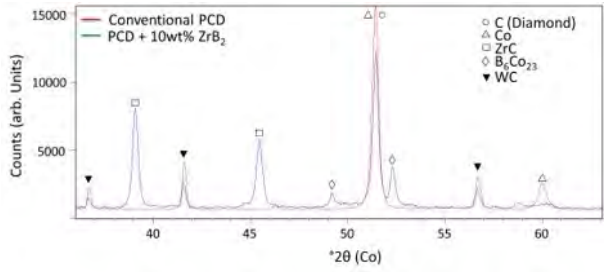

Figure 1. Comparative PXRD analysis of standard PCD and ZrB2-PCD.

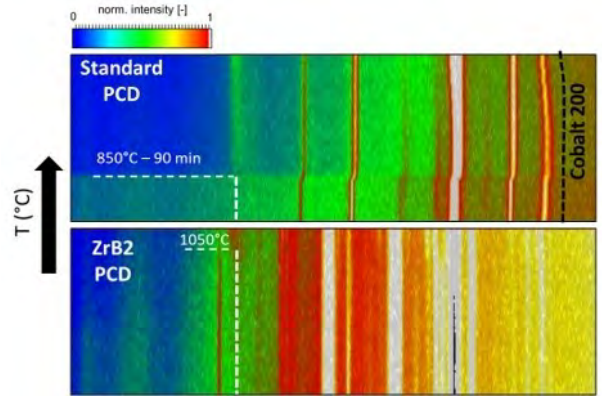

Figure 2. A topographical view of the in-situ PXRD data showing the onset of graphite formation (dashed line) in the conventional PCD sample compared to ZrB_2-PCD.

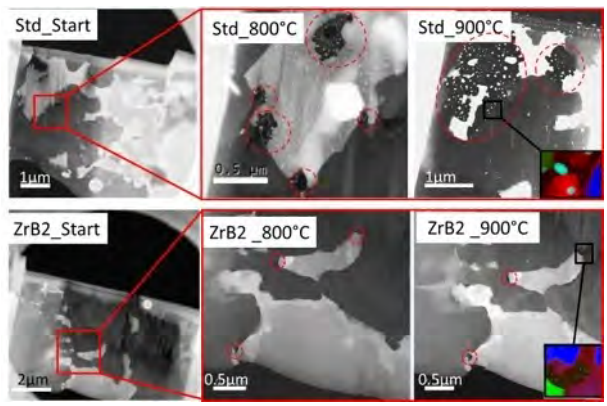

Figure 3. HAADF-STEM images of standard PCD (top) and the ZrB_2-PCD (bottom) samples after 10 minutes of heating at the various temperatures. The presence of graphitic carbon is indicated with red circles. The insert shows a STEM-EELS phase map of the binder/diamond interface, showing the distribution of diamond (blue), graphite (red) and cobalt (green).

Corresponding author: melisha.jivanji@e6.com

DYNAMIC RESTORATION MECHANISM OF Ti-0.162, Nb-0.394, Al-0.068, Fe 441 FERRITIC STAINLESS STEEL DURING HOT ROLLING

J.T Asante[1] and C.W Siyasiya[1]

[1]Deprtment of Materials Science and Metallurgical Engineering, University of Pretoria, Pretoria

High stacking fault energy materials such as ferritic stainless steels (FSSs) exhibit dynamic recovery as the main softening mechanism[1]. During hot rolling, substructures are formed in the material due to dislocation rearrangents[2] which are encouraged by the dynamic softening methods such as dynamic recovery, dynamic recrystallization, static recrystallization. This grade of FSSs exhibit low dislocation densities due to recovery. Hence when deformed, the grains are largely elongated and this limits the possibility of grain refinement by the hot rolling process[3]. Primarily, FSSs undergo dynamic recovery (DRV) due to easy cross-slip and climb which reduces the stored energy required for recrystallization. However, there are exceptions for some alloys that contains particles. The highly deformed regions around these particles serve as sites for nucleation of continuous dynamic recrystallization (CDRX)[4]. CDRX is caused by the continuous build-up of dislocations. This progressively increases the sub-grain misorientation and in the process refines the grains. This study identified the optimal finishing temperature to achieve grain refinement.

Isothermal compression tests using the Gleeble 1500 ® thermo-mechanical machine were used to study the dynamic restoration behavior after high temperature deformation of Ti+Nb dual stabilized 441 ferritic stainless steel received in as cast condition from Columbus Stainless Pty Ltd, South Africa with the composition of Fe-17.60Cr-0.013C-0.162Ti-0.394Nb-0.020N-0.17Ni-0.54Si-0.29Mn and 0.068Al, all in wt%. The strain rate was kept constant at 5/s following the hot rolling schedule in Table 1. Finite element analysis (FEA) was used to model the effective strain distribution during the rolling process to depict the region where deformation was high in the sample and was found to be at the center of the specimen. The SEM, equipped with EDS, was used to examine the species of the precipitates. The electron backscatter diffraction (EBSD) was used to examine the dynamic restoration mechanism by studying the evolution of low angle grain boundaries (LAGB) to high angle grain boundaries (HAGB) and their distribution.

The industrial benchmark rolling schedule with the lowest finishing temperature showed the highest recrystallization fraction followed by schedule T2. At lower finishing temperatures, where the Zener-Hollomon (Z) parameter is high (6.90×10^18 /s), dynamic recovery (DRV) was the dominant restoration mechanism. However, CDRX was seen to occur rapidly with the formation of more sub-structure that transformed to sub-grains. At higher finishing temperatures, these sub-structures were also noticed but in fewer fractions and the sub-grains were less fine. These recovery mechanisms were concentrated in the deformed zones around particles where nucleation of new grains occurred[5]. These particles were non-deformable carbonitrides ((Ti, Nb) C, N).

The secondary electron (SE) images shown in Figure 1 (a) and (b) shows that finishing hot rolling at lower temperatures introduces many sub-structures and sub-grains that aid in grain refinement. The new grains in Figure 1a are finer than those in figure 1b. This is confirmed by the amount of recrystallization shown in Figures 2(a) and (b). The particles serve as nuclei for the recrystallization of new fine grains through what is known as particle stimulated nucleation (PSN).

References:
1. Xu, X. et al. (2019) Mat. & Des. 180(107924), 1.
2. Dias, F.L. and Santos D.B. (2020) Metallogr. Microstruct. Anal. 9(1).
3. Mehtonen, S.V. et al. (2014) Mat. Sci. & Eng. A. 601.
4. Alaneme, K.K. and Okotete, E.A. (2019) J. of Science: Mat. & Dev. 4(1).
5. De Sequira, R.P., Sandium, H.R.Z. and Raabe D. (2012) Met. & Mat Trans. 44(A).

Table 1. Hot deformation schedule

Schedule	Parameter	Pass number				
		1	2	3	4	5
Control	Strain	0.3	0.2	0.2	0.15	0.15
	Temperature (°C)	1000	975	950	900	850
T1	Strain	0.3	0.2	0.2	0.15	0.15
	Temperature (°C)	1100	1070	1050	1030	**1000**
T2	Strain	0.3	0.2	0.2	0.15	0.15
	Temperature (°C)	1100	1070	1050	1030	**870**

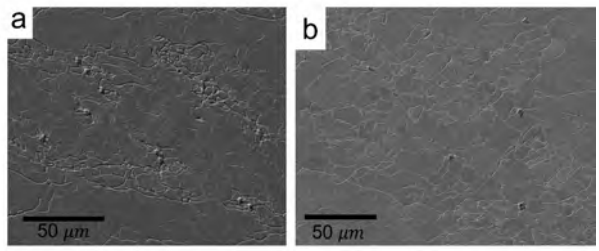

Figure 1. Microstructures of hot rolled steels showing recrystallisation and substructures (a) low finishing temperatures and (b) high finishing temperature

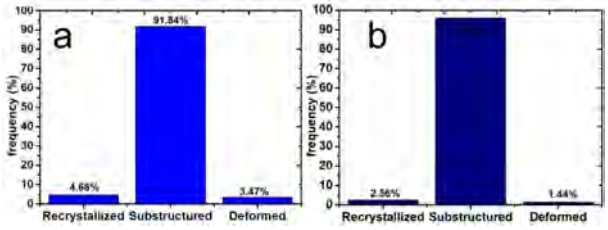

Figure 2. Recrystallization fraction and amount of substructure after deformation at (a) low finishing temperature and (b) high fnishing temperature

Corresponding author: u20747226@tuks.co.za

PRECIPITATE EVOLUTION DURING HOT ROLLING & IT'S IMPLICATION ON RECRYSTALLISATION IN 436 STAINLESS STEELS

M.Y. Salojee[1], C.W. Siyasiya[1], K.A. Annan[2] and J.S. Moema[3]

[1]Dept. of Material Science & Metallurgical Engineering, University of Pretoria, Pretoria, [2]Sasol Synfuels, Metallurgical Engineering Services, Regional Operations and Asset Services, [3]Advanced Materials Division (AMD), Mintek

Ferritic stainless steels (FSS) have come to the forefront in the last few decades due to instability in nickel price markets, making austenitic steels unattractive. Ferritic stainless steels do, however, succumb to the phenomenon of ridging[1]. Ridging arises from the textural properties of cast structures that subjects the material to clustering of grains with specific orientations. These clusters result in plastic anisotropy upon deformation, which emerges as ridges. Recrystallisation can be used to break down clusters of grain orientations[1].

Recrystallisation is driven by lowering of the crystal stored energy by the formation of strain-free grains. Larger precipitates encourage precipitation, whilst smaller precipitates hinder nucleation of dynamic recrystallisation by pinning grain boundaries. When recrystallisation is favoured around a precipitate, we refer to it as particle-stimulated nucleation (PSN). It is known that straining a sample can encourage the precipitation of particles, specifically niobium precipitates[2,3]. The following study sought to evaluate the evolution of Nb precipitates after deformation to determine the effect on recrystallisation.

The starting material was an as-cast columnar structure. Samples were mechanically ground, followed by mechanical polishing to 1µm using a diamond paste solution. Then, SEM samples were electropolished using A3® solution, and TEM samples were twin jet polished in A3® solution using a Tenupol-5. SEM imaging was done at 20kV accelerating voltage at a working distance of 20mm and 70º tilt. TEM imaging was taken on a Jeol 2100F FEGTEM at an accelerating voltage of 200kV, and contrasts were aligned until a clear image was produced. A Joel JSM 6300, Scanning electron microscopy (SEM), was used to evaluate the change in the size of precipitates before deformation, after deforming and from heat treatment alone. The first sample was homogenised at 1353 K for 300 s. It was then cooled over 15 s and deformed at a strain of 0.24 at 1273 K, cooled to 1223 K over 20 s, deformed at a strain of 0.3, cooled to 1203K over 25 s and deformed at a strain of 0.3. The sample was then quenched. Deformation was carried out at a strain rate of 5/s. The heat-treated sample was subjected to the same thermal cycle but without deformation. Both samples were processed in a Gleeble 1500™.

All samples were processed through ImageJ open-source software to characterise the change in precipitate size. It is shown in Figures 1 and 2 that larger precipitates (above 2.5µm) encourage recrystallisation more strongly than finer precipitates through PSN. The grain boundary map in Figure 2 shows recrystallisation around larger precipitates arrowed in green instead of finer precipitates dispersed in the matrix.

Precipitate sizes increased from the cast structure when heated and with the introduction of deformation. It is known that temperature provides energy to drive recrystallisation, and dislocations can assist in the diffusion of solute atoms for precipitate growth[4].

In conclusion, it can be said that deformation encourages the growth of precipitates. Large precipitates favour recrystallisation during hot rolling, which assists in the breaking down of the undesirable cast texture. The breakdown in texture improves the ridging resistance of FSS.

The authours would like to thank Mr Kurup for assistance with edits.

References:
1. Braga, F. V., Escobar D. P. (2016), J. Mater. Res., 31(5), 635-645.
2. Siqueira R. P., et. al., (2011) J. Mater. Science and Eng. A., 52(B), 3513-3519.
3. Siyasiya C. W., (2007) PhD Thesis, Pretoria, Department of Material Science and Metallurgical Engineering, University of Pretoria.
4. Shekhter, A., et. al. (2004), J. Metal. Mater. Trans. A, 35(A), 973-983

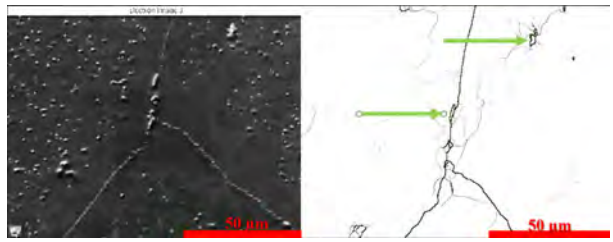

Figure 1. Figure 1. SEM image (left) and the corresponding grain boundary map from EBSD showing recrystallized grains around large precipitates, >2º grain boundaries in grey and >10º boundaries in black (right).

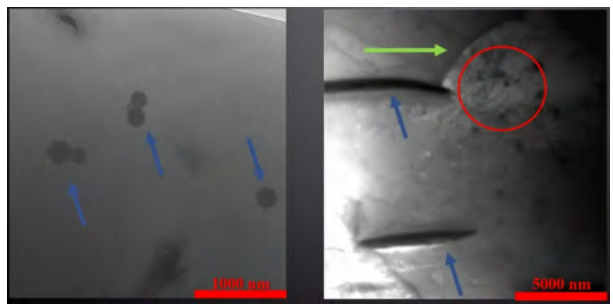

Figure 2. Figure 2. TEM bright field images show; on the left, no dislocation density with small precipitates (blue); on the right, a grain boundary (green arrow) next to an area with high dislocation density (red circle) around large precipitates (blue).

Corresponding author: u13271050@tuks.co.za

MICROSTRUCTURAL BASED LIFE ASSESSMENT OF 1CrMoV TURBINE ROTOR STEELS AFTER LONG-TERM SERVICE

H.S. Nyembe[1], J.H. Neethling[1] and J.E. Westraadt[1]

[1]Department of Physics, Centre for HRTEM, Nelson Mandela University, Gqeberha

The creep resistant low alloy 1CrMoV steels are used for high-pressure fossil steam turbine rotors. The creep resistance of 1CrMoV steels is primarily due to dispersion of alloy carbides and solid solution strengthening by substitutional atoms. Mitchell et al.[1] reported that the carbide phases, size, number, and composition change with service time for 1CrMoV rotors exposed at >510°C. The microstructural changes lead to the decrease of creep resistance and hardness. Dobrzanski et al.[2] found the relationship between the microstructural changes and extent of creep exhaustion for service exposed low alloy 1CrMo steels. This work compares conventional life assessment or creep damage estimation methods based on cavitation damage (CM) and hardness (HM) with the microstructural evolution in three 1CrMoV rotors after long-term service in creep conditions.

The samples for this study were obtained from the non-stressed *cold section* (C*)* and stressed hot section of three turbine rotors using a core sampling technique with repair by friction hydro pillar processing (weldcore™). The operation temperatures at these locations were 226°C and 515-550°C respectively. The hot section sample is divided into the *peak-stress* and *bulk* regions. The peak-stress region experienced a higher stress than the bulk region during service. BSE SEM imaging was used to examine cavities. The carbides were extracted from the Fe-matrix using carbon extraction replication and were further investigated using TEM-SAD, STEM-EDS, and TKD-EDS[3]. Hardness testing was also performed to investigate the degradation of the material over operating life.

Creep cavitation occurred in the peak-stress regions of all rotors and the estimated creep damage (t/t_R) is summarised in Tab. 1. In the rotors, both peak-stress and bulk regions showed the same thermally induced hardness decrease. The operating temperature and t/t_R estimated with hardness models are tabulated in Tab. 1. The two conventional life-assessment methods provided equivalent results considering their limitations. No significant differences were found in the microstructural changes occurring in the peak stress and bulk regions of the rotor. The TKD-EDS analysis revealed Fe-rich M_3C, CrFe-rich M_7C_3, FeCr-rich $M_{23}C_6$, Mo-rich M_2C, and V-rich MC carbide phases in the hot section as shown in Fig. 1. The carbide proportion and Fe/Mo ratio are presented in Tab. 1. The M_2C and M_7C_3 proportion increased and M_3C decreased with life fraction as shown in Fig. 2(a). The ratios of Fe/Mo and Fe/Cr in the composition of overall carbides decreased with life fraction as shown in Fig. 2(b). A direct correlation was found between the hardness reduction, life fraction, and quantitative assessment of the changes occurring in carbide phase proportion and composition.

The conventional methods are not useful towards the end of the component life. A direct correlation was found between the life fraction and evolution of carbide phase proportion and composition during service. The microstructural analysis indicates how far the carbide structure is from the equilibrium state which corresponds to the end of rotor life.

References:
1. D. R. G. Mitchell and C. J. Moss, Journal of materials engineering and performance 7 (5), 621.
2. J. Dobrzański, H. Krztoń and A. Zieliński, Journal of Achievements in Materials and Manufacturing Engineering 23 (2), 19.
3. H. Wang et al., Materials Characterization 181, 111.

Table 1. Estimated life fraction and operating temperature, carbide phase proportions and Fe/Mo ratio in overall carbide composition for rotors 1, 2, and 3.

	CM	HM		Phase Proportion (%)			Ratio
	t/t_R	T (°C)	t/t_R	M_3C	M_2C	M_7C_3	Fe/Mo
C				99	0.3	0.3	9.3
1	0.75	530	0.69	70	20	10	3.2
2	1	550	0.92	30	40	20	1.4
3	1	550	0.87				

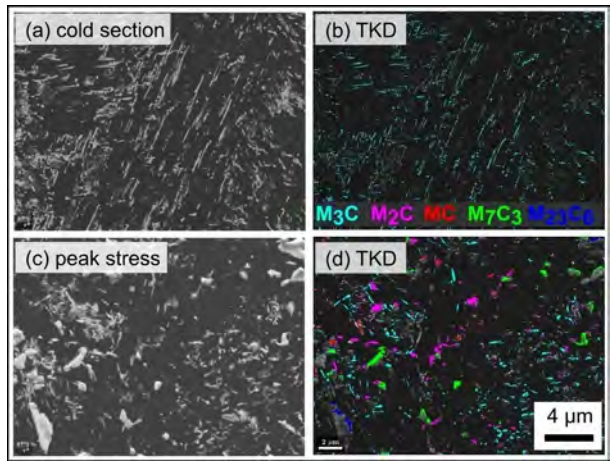

Figure 1. (a and c) SEM forward scattered images and the corresponding TKD phase map (b and d) obtained for the extraction replica sample.

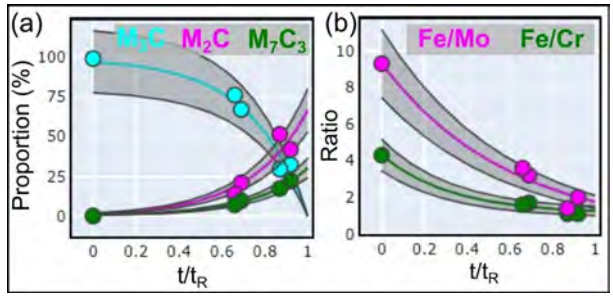

Figure 2. (a) M_3C, M_2C, and M_7C_3 proportions and (b) Fe/Mo and Fe/Cr as the function of life fraction.

Corresponding author: s216800609@mandela.ac.za

SIMULATION OF LONG-TERM HIGH TEMPERATURE EXPOSURE OF X20 STEEL THROUGH LABORATORY ACCELERATRED AGEING

S. Allies[1], R.D. Knutsen[1] and J.E. Westraadt[2]

[1]Centre for Materials Engineering, University of Cape Town, [2]CHRTEM, Nelson Mandela University, Gqeberha

The creep strength of X20 tempered martensitic-ferritic power plant steel is dependent on the condition of the metal when entering service and the stability of the microstructure/properties during service over very long periods, sometimes in excess of 200 kh. Unforeseen degradation of the steel microstructure during service can lead to premature failure by excessive creep damage. Although excursions in operating conditions can often account for accelerated microstructural changes leading to creep damage, variability in the initial state of the microstructure that arises from the steel processing stage can potentially cause the microstructure evolution path during service to deviate from expected behaviour. To test this hypothesis, variable initial microstructures must be exposed to conditions equivalent to long-term service exposure. However, completion of the study within a realistic timeframe requires simulation of the long-term high temperature exposure through accelerated ageing.

The aim of this study is the development of an accelerated ageing protocol through the selection of temperature-time combinations that produce equivalent microstructures after extended exposure at service temperature (nominally 550°C). The Larson Miller parameter (LMP)[1] is most commonly used to determine equivalent temperature-time combinations but suffers from the fact that the constant (C) in the expression is often assigned different values. For example, actual microstructural analysis of X20 steel yields a best fit for C=14[1], whereas C=20 or 30 is often used when fitting actual creep data. When considering accelerated ageing in the range 600-700°C for equivalent exposure time at service temperature (550°C), the exposure times can vary by up to an order of magnitude depending on the selection for the C constant in the range 14 – 30. Hence, there is uncertainty when relying on the use of an expression such as LMP, which points to the need to perform a systematic microstructural study. Our research focuses on investigating the development of microstructures within a range of temperature-time combinations and comparing them with microstructures which have evolved from normal exposure at service temperature and extended times up to 140 kh for the same X20 steel[2].

Advanced analytical microscopy is required to track the microstructural evolution during accelerated ageing. The microstructure of X20 steel is highly complex and the tempered martensite condition, which contains an abundance of precipitates less than 100nm in size, is indicated in an SEM-STEM image in Fig. 1. Tracking the microstructural changes requires characterisation of the decomposing martensite, as well as structure and compositional analysis of the precipitates as the total microstructure moves towards equilibrium. The microstructure after extended ageing is indicated in Fig. 2 which exhibits polygonization of the lath martensite microstructure evident in the tempered state (Fig. 1). In addition, the density of second phase particles and precipitates has reduced significantly. Although good morphological information can be obtained from thin foils in SEM-STEM mode (Figs. 1, 2), analytical TEM is required to analyse structure and composition of the precipitate population. To do this, our study will follow the characterisation approach defined by Wang et al[3], and by comparison with the findings of Aghajani[2], we will produce feasible simulations of the long-term service exposure for the X20 power plant steel.

References:
1. Salonen, J. and Auerkari, P. (1996) VTT Publication 208, 20.
2. Aghajani, B. (2009) PhD thesis, Univ. Bochum.
3. Wang, H. et al (2021) Mater. Charac. 181, 11396.

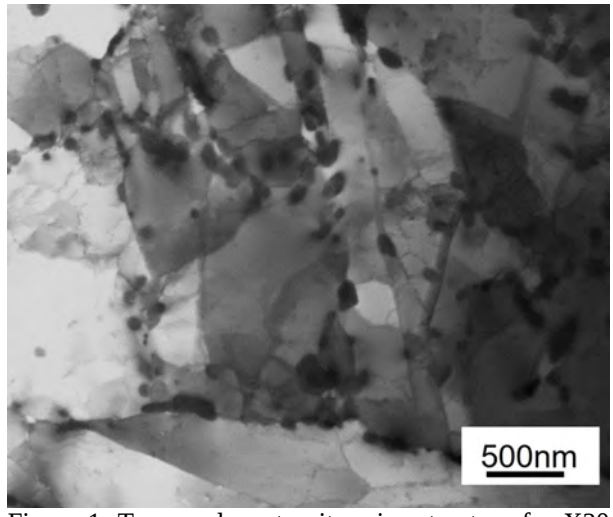

Figure 1. Tempered martensite microstructure for X20 steel (SEM-STEM, 30kV).

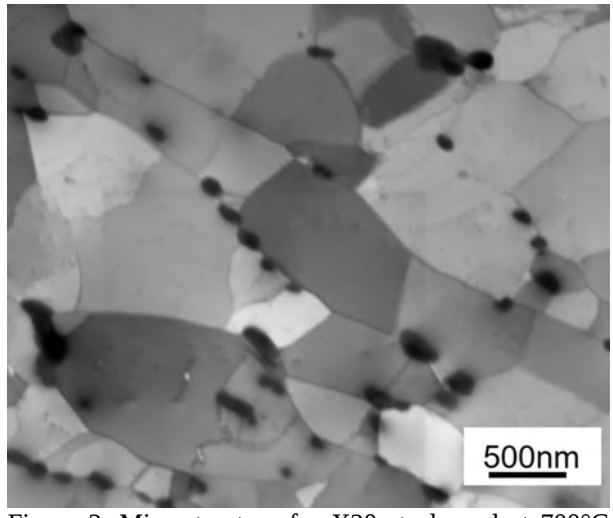

Figure 2. Microstructure for X20 steel aged at 700°C for 120 days (SEM-STEM, 30kV).

Corresponding author: allsor002@myuct.ac.za

MULTISCALE FEATURE ENGINEERING FOR MACHINE LEARNING STRUCTURE-PROPERTY MODELS FOR CARBON STEELS

L. Westraadt [1] and J.E. Westraadt[2]

[1]Physics Department, [2]Centre for HRTEM, Nelson Mandela University, Gqeberha, South Africa

Carbon manganese steels were historically used for high-temperature piping in petrochemical and electrical power generating plants[1]. The microstructure consists of ferrite and pearlite. During long-term service above 420 ºC the lamellar cementite structure of the pearlite either breaks up into spheriodite or converts into its thermodynamical stable phase graphite, leading to a decrease in the mechanical properties and possible catastrophic failure[1-2]. Small-punch creep (SPC) testing is a small sample (8 mm diameter; 0.5 mm thick) testing technique that can evaluate the material state of a steel by pressing the sample with a ceramic ball (2 mm) at high temperature (500 ºC) with a static load (296 N). The samples typically rupture after 10-1000 hours. The aim of this study is to train a machine learning model to predict this rupture-time using microstructural information collected on different length scales. This reduced order model can then be used to prioritise samples for testing.

The tested samples were cross-sectioned, mounted, polished, and etched using a 2% Nital solution for 10-20 seconds. The undeformed grip regions were imaged using optical microscopy (OM) (pixel size 0.8 µm; n = 93; 1250 µm x 450 µm) and secondary electron (SE) imaging (pixel size 0.1 µm; n = 56; 1000 µm x 250 µm) with a SEM. At the coarsest length scale, the pearlite volume fraction (VF) was determined by segmenting the OM greyscale images using image analysis software to distinguish between pearlite (dark) and ferrite (light) regions (Fig. 1a). At the intermediate length scale, the SE SEM images were segmented into three phases (ferrite, pearlite, spheriodite) (Fig. 1b) to quantify the degree of microstructural degradation by means of a ratio: pearlite%/(pearlite% + spheriodite%). At the finest length scale, the SE SEM images were segmented into two phases (ferrite, cementite carbides) to include finer pearlite features into the measurements (Fig. 1c). Spatial features including the degree of microstructure banding and pearlite lamellar spacing were implicitly quantified from Figs. 1a and c, respectively, using 2-point spatial correlations in combination with Principal Component Analysis (PCA)[3,4]. Various combinations of the quantified microstructural features were then used to train random forest regressors with rupture-time as the target variable (80:20 training-testing split). The root mean square error (RMSE) of model predictions made with the testing sets were used to evaluate model performance.

The testing errors of the models trained on the pearlite VF and the first 3 PCA scores obtained from the OM (Fig.1a) were 123±19 hours and 187±41 hours, respectively. These errors improved to 75±8 hours and 158±37 hours, respectively, when the degradation ratio determined from Fig. 1b was appended to the feature vectors. This shows that including the finer scaled features from the SE images improves model performance. The segmentation method shown in Fig. 1c, when combined with 2-point spatial correlations and PCA, has the potential to capture the pearlite lamellar spacing in addition to implicitly quantifiying the pearlite/spheriodite ratio without the reliance on manual segmentation which may be subject to operator bias. However, the performance of the model trained using these PCA scores showed no significant improvement over those trained using the OM images alone. This is likely due to the large variations in the quantitative measurements made over small areas (250 µm x 250 µm) with few pearlite colonies viewed in different orientations. Future work will focus on decreasing this measurement uncertainty through increasing image tile size and data augmentation techniques. The use of deep learning techniques to quantify microstructural features using convolutional neural networks and variational autoencoders will also be explored.

References:
1. Joo, M.S. (2012) PhD Thesis, Pohang University of Science and Technology.
2. Foulds, J.R. and Viswanathan, R. (2001) J. Mater. Eng. Perform. 10(4), 484.
3. Westraadt, J.E. (2022) Proc. 6th World Cong. Int. Comp. Mater. Eng. (ICME 2022)
4. Niezgoda S.R., Kanjarla A.K. and Kalidindi S.R. (2013) Int. Mater. Man. Inn. 2, 3.

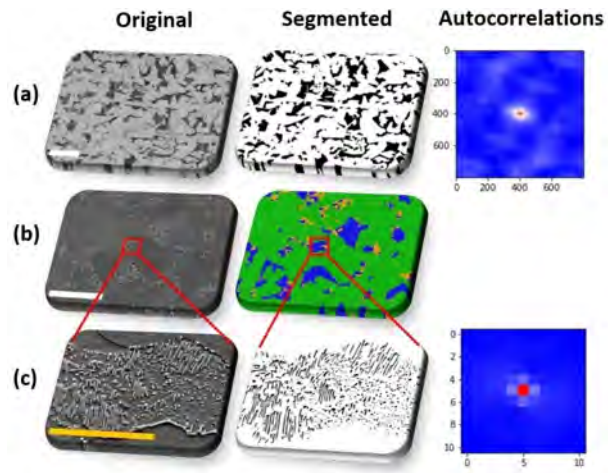

Figure 1. Original and segmented micrographs of increasing spatial resolution accompanied by 2-point spatial autocorrelations at the indicated scales. (a) Optical micrograph showing ferrite and pearlite (dark) regions. (b) Secondary electron (SE) micrograph revealing the degree of pearlite spheriodisation: ferrite (green), pearlite (blue), spheriodite (yellow). (c) SE image revealing pearlite substructure. Scale bars: white – 100 µm, yellow – 25 µm.

Corresponding author: lindsayw@mandela.ac.za

UNDERSTANDING THE PROCESS-STRUCTURE RELATIONSHIP OF VOx/MgO CATALYSTS PREPARED BY SOLUTION COMBUSTION SYNTHESIS USING TEM

P. Ntola[1], H.B. Friedrich[2], A.S. Mohamed[2], E.J. Olivier[3], A. Govender[4] and S. Singh[2]

[1]Department of Chemistry, Durban University of Technology, Durban, [2]School of Chemistry and Physics, University of KwaZulu-Natal, Durban, [3]Centre for HRTEM, Physics Department, Nelson Mandela University, Port Elizabeth, [4]Group Technology, Sasol South Africa (Pty) Ltd., Sasolburg

The conversion of the long-chain linear paraffins into value-added products such as olefins and aromatics is an important industrial process. The oxidative dehydrogenation (ODH) of n-octane may be seen as a viable route to produce the corresponding octenes and C8 aromatics[1]. In ODH of alkanes, the VO_x/MgO system has been reported to form minimum oxygenates and/or cracking products with reasonable selectivity towards ODH products[1]. To attain high activity and selectivity in ODH, it is important to find a catalyst that can activate the C-H bond[2]. This study reports findings of the structural characterization and application of VOx/MgO catalysts prepared by solution combustion synthesis (SCS) using different fuels on the oxidative dehydrogenation of n-octane.

The VO_x/MgO powders were prepared via SCS, using different fuels. The catalysts were then characterized using X-ray diffraction, Raman spectroscopy, SEM and aberration corrected TEM and related techniques. Testing of the catalysts was performed on a continuous flow, fixed-bed reactor operating in vertical flow mode. The resultant catalytic behaviour of the prepared catalysts varied in both conversion of octane and selectivity to ODH products. The differences in performance were found to depend on the microstructure and extent of vanadate phase formation, vanadate size and dispersion for each catalyst.

The microstructure of the different VO_x/MgO catalysts was characterized in the TEM using electron diffraction, hollow-cone diffractive imaging and elemental mapping using electron energy loss spectroscopy. The data demonstrated distinguishable differences in morphology, elemental distribution, phase composition and crystallite size and distribution for the catalyst powders investigated (Fig. 1). By correlating experimentally extracted microstructural parameters to calculated thermodynamic parameters we demonstrate the important role of the fuel in controlling the reaction kinetics and in turn the resultant microstructure of the catalyst. Specifically, we highlight the role of a fuel's reducing valency in regulating the maximum temperature and heating rate of a reaction.

The best performing catalyst with respect to conversion as well as octene (ODH) selectivity displayed synergistic effects caused by the co-existence of different magnesium vanadate phases (Fig 2). Based on the findings we propose a model of formation for the material system, demonstrating the potential of this novel one-step method for the controlled synthesis of VO_x/MgO powders for catalytic applications.

References:
1. E. A. Elkhalifa and H. B. Friedrich, (2011), Catalysis letters 141, 554.
2. H. Kung and M. Kung, (1997), Applied Catalysis A: General 157, 105.

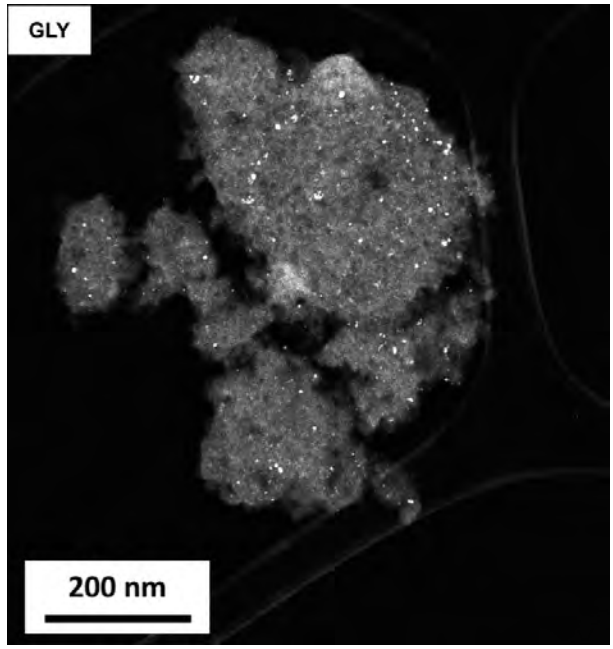

Figure 1. Hollow-cone diffractive TEM image of a VO_x/MgO catalyst powder prepared using glycine as fuel. The distribution of vanadate phases is seen as bright areas in the image.

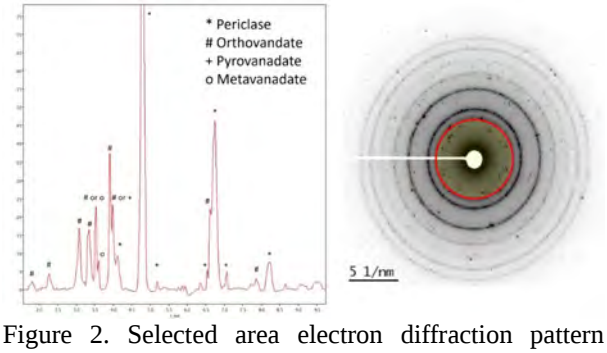

Figure 2. Selected area electron diffraction pattern (right) of a VO_x/MgO catalyst powder prepared using glycine as fuel with a rotationally averaged diffraction spectrum (left). The presence of different vanadate phases were identified.

Corresponding author: pinkies@dut.ac.za

STUDY OF THE EFFECTS OF PROMOTERS (MnO_X AND FeO_X) ON Co_3O_4/CeO_2 DURING CO-PROX

N. Ndila[1], M. nJensen[2] and P.J. Kooyma[1]

[1]Dep. of Chemical Engineeirng, University of Cape Town, [2]University of Oslo

Polymer electrolyte fuel cells are one of the alternative methods for delivering clean energy and are expected to be the future energy solution[1]. The anode of proton exchange membrane fuel cells has a Pt electrocatalyst which is susceptible to CO poisoning. CO adsorbs strongly onto the active sites of Pt, inhibiting dissociation of H_2. This results in a decrease in the efficiency of the fuel cells, hence, pure H_2 is required for these fuel cells[1]. Preferential oxidation of carbon monoxide (CO-PROX) is one of the most effective methods for H_2 purification for fuel cells[1-4]. Co_3O_4 based catalysts are highly active for CO-PROX. For these catalysts, the Co^{3+}/Co^{2+} redox pair has been identified as the active species. However, several studies have shown that Co_3O_4 catalysts deactivate at temperatures above 225ºC via the reduction of Co_3O_4 to metallic Co[2-4]. The effects of FeOx and MnOx promoters on the activity and phase stability of Co_3O_4/CeO_2 at temperatures of up to 450ºC during CO-PROX were investigated.

Co_3O_4 nanoparticles were synthesized via a solvothermal method[5]. The prepared nanoparticles were supported and promoted via ultrasonication-assisted wet impregnation. The prepared samples were characterized using transmission electron microscopes, energy dispersive x-ray spectroscopy, x-ray powder diffraction, hydrogen temperature-programmed reduction, and CO-probing.

XRD patterns showed no diffraction lines corresponding to Co_3O_4 and promoters. This might be because of their high dispersion of CeO_2. The elemental maps for Co showed that the Co_3O_4 nanoparticles are distributed on the support. Fig. 1 shows TEM images of both Mn and Fe promoted catalysts. The hydrogen reduction profile of the unpromoted catalyst shows that the reduction of Co_3O_4 commences at 170ºC and a degree of reduction of 96% is obtained. The addition of the promoters shifts the reduction onset temperature to higher temperatures. The reduction commences at 230ºC and 220ºC for 0.5 wt.% MnOx and FeOx promoted catalysts, respectively. Additionally, the degree of reduction was 85% and 82% for MnOx and FeOx promoted samples respectively.

The unpromoted sample achieved a maximum CO conversion of 75%, with CO methanation starting at 275ºC (See Fig. 2). The 0.5 wt.% MnOx promoted catalyst achieved 98% CO conversion, with CO methanation commenced delayed until 300ºC. Lastly, the 0.5 wt.% FeOx promoted catalyst achieved 100% CO conversion, with methanation also occurring only above 300ºC. During CO-PROX, H_2 oxidation is a competing reaction. The CO2 selectivity of all catalysts decreased with increasing temperature. The promoted samples had a CO2 selectivity of 100% below 180ºC, while for the unpromoted catalysts selectivity was 40%. Therefore, the addition of the promoters improved the catalytic performance and the stability of Co_3O_4/CeO_2.

References:
1. Rodrigues, A., et al. (1997) IECEC-97. 2,768-773.
2. Nyathi, N.T. (2016) MSc Thesis, University of Cape Town, South Africa.
3. Lukashuk, L., et al. (2016) Journal of Catalysis. 34, 1-15.
4. Khasu, M. (2017) MSc Thesis, University of Cape Town, South Africa.
5. Wolf, M., et al. (2017) ACS Journal. 8(5), 3985-3989

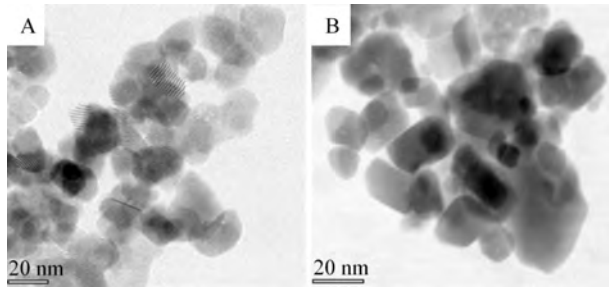

Figure 1. TEM images of Mn (A) and Fe (B) promoted Co_3O_4/CeO_2 catalysts.

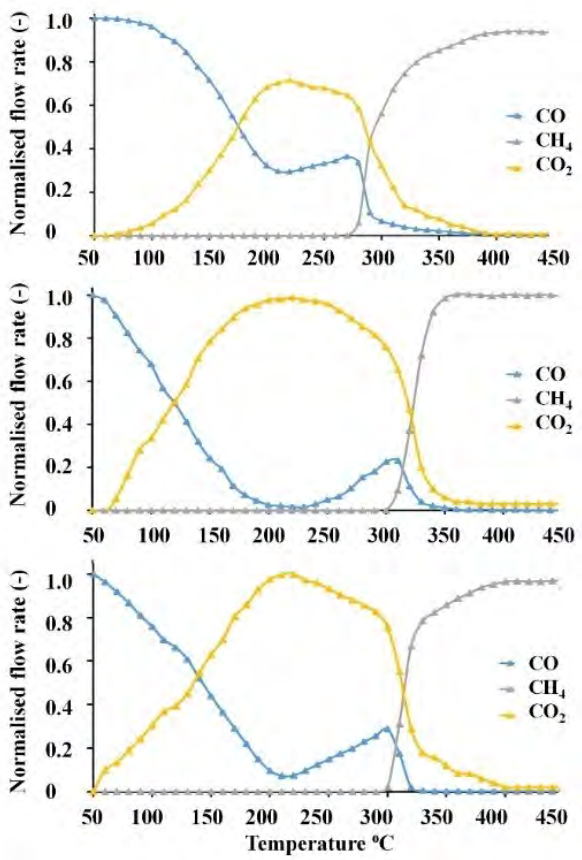

Figure 2. Outlet flow rates for unpromoted Co_3O_4/CeO_2 (top), 0.5 wt.% MnOx promoted (middle), and 0.5 wt.% FeOx promoted (bottom) catalyts.

Corresponding author: ndlnol010@myuct.ac.za

HR-EBSD ANALYSIS OF IN SITU STABLE CRACK GROWTH AT THE MICRON SCALE

A. Koko[1], T.H. Becker[2], E. Elmukashfi[3], N.M. Pugno[4,5] and T.J. Marrow[1]

[1]Department of Materials, University of Oxford, Oxford, [2]Centre for Materials Engineering, University of Cape Town, Cape Town, [3]Department of Engineering Science, University of Oxford, Oxford, [4]School of Engineering and Materials Science, Queen Mary University of London, London, [5]Department of Environmental and Mechanical Engineering, University of Trento, Trento

The J-integral (J) is widely used as a fracture criterion[1] coupled with analytical or finite element analyses that use knowledge of remote applied boundary conditions and geometry to perform structural integrity assessments. Recently, methods have been developed that use experimental data for the displacement fields around the cracks to solve the elastic strain field and calculate J. These analyses demonstrated that such local measurements could quantify J without knowing the external boundary conditions (i.e., load, crack length)[2,3]. Studying crack growth at the micron scale requires high-resolution data, and it is necessary to characterise the stress and strain fields in situ approaching the critical state for crack propagation. Furthermore, the analysis needs to be appropriate to inclined crack planes that are not necessarily well oriented for surface observations. In such cases, high-resolution electron backscatter diffraction (HR-EBSD) can be used to study the deformation in crystalline materials. HR-EBSD is a non-destructive surface analysis method that can quantify elastic strains and lattice rotations with a sensitivity of ~10^{-4} with high-resolution mapping of cross-correlated electron backscatter diffraction patterns. This study presents a novel approach to calculate the mixed mode J from the elastic deformation gradient tensors obtained from the near-surface membrane by HR-EBSD.

A crack was propagated under quasi-static conditions by in-plane compression of a (001) single-crystal silicon wafer. Figure 1a shows the fracture surface and the locations of the HR-EBSD measurements in-situ and subsequent FIB trench cuts that revealed its subsurface inclination. J and equivalent stress intensity factors (SIFs)were calculated from each HR-EBSD map (Figure 1b). The values with the smallest domain are erroneous due to noise and large strains close to the crack. Contours greater than 2 µm correspond to the encapsulation of the highly deformed field at the tip. The crack plane and the propagation direction are effectively constant between locations 5 and 12, as the crack propagated on the (131) plane in the [-310] direction with J = 2.23 ± 0.17 Jm^{-2}, with the equivalent SIFs as K_I = 0.31 ± 0.11, K_{II} = 0.48 ± 0.06, and K_{III} = 0.15 ± 0.06 MPa√m.

This method provides a direct and high-resolution solution for quantifying the elastic fields acting on a crack tip, using local measurements without knowing the external boundary conditions. The analysis can be applied to mixed-mode loading and in situ studies of quasi-static cleavage crack propagation. The present analysis is suitable for elastic deformation or small-scale yielding conditions, but more advanced decomposition algorithms must be employed for significant elastoplastic deformation[4].

References:
1. Singh R.K. and Parihar K.S. (1986) J. of Mater. Sci.21, 3921.
2. Becker T.H., Mostafavi M, Tait RB, and Marrow TJ. (2012) Fatigue Fract. Eng. Mater. Struct. 35, 971.
3. Molteno M.R. and Becker T.H. (2015) Strain, 51, 492.
4. Yu H. and Kuna M. (2021) Eng. Fract. Mech. 249, 107722.

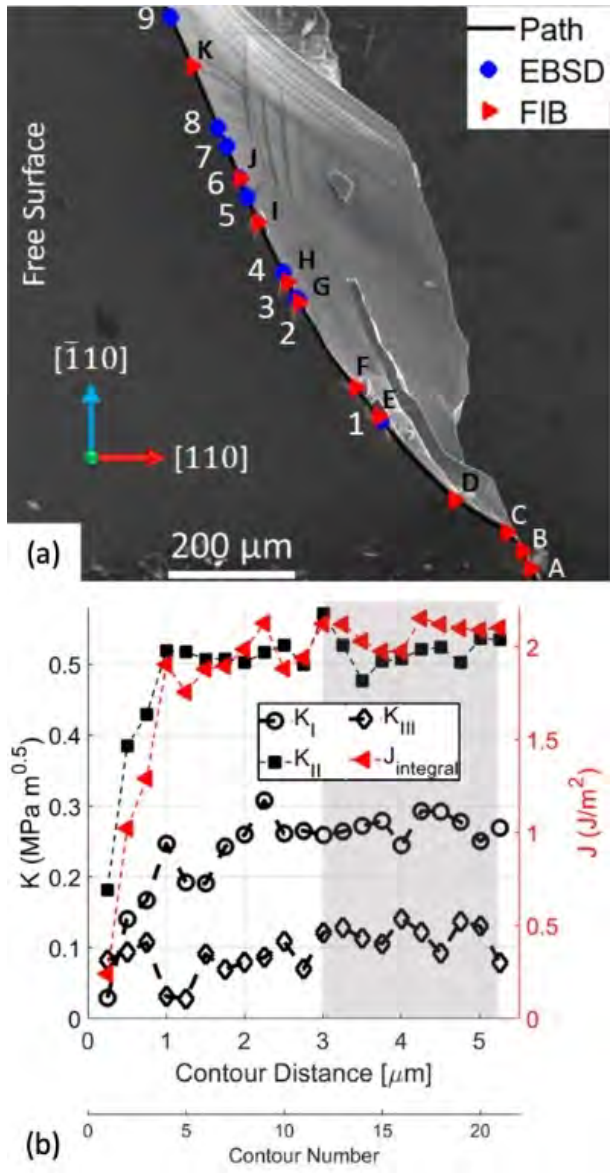

Figure 1. (a) SEM images of the fracture surface of the exemplar crack. (b) J and three-dimensional stress intensity factors as the contour of the integration domain expanded from the crack tip for position labelled 1 in (a).

Corresponding author: thorsten.becker@uct.ac.za

CHARACTERISATION OF TRANSPARENT CONDUCTIVE OXIDES USING TRANSMISSION KIKUCHI DIFFRACTION

J.E. Westraadt[1] and U. Heitmann[2]

[1]Centre for HRTEM, Nelson Mandela University, Gqeberha, South Africa, [2]Fraunhofer Institute for Solar Energy Systems ISE, Freiburg, Germany

Transparent conductive oxides (TCOs), such as IZO (ZnO:In), are widely used as transparent electrodes in solar cells. In recent years, spray pyrolysis has gained interest, as an alternative to sputtering, for the deposition of TCOs[1,2] as it is a simple and scalable deposition technique that does not require a vacuum. The nano-crystalline structure, orientation texturing, and interfacial oxide layers are of importance for the conductive properties of the TCO. In this study a nano-crystalline IZO layer deposited on a n-type poly-Si substrate is studied using transmission Kikuchi diffraction (TKD) and conventional TEM to understand the increase in resistivity when the IZO is deposited using spray pyrolysis.

The substrates used in this work are glass (0.7 mm thick Borofloat), silicon substrates (1 Ω.cm² n-type FZ silicon, 250 µm thick) with a TOPCon surface (thin tunnel oxide capped with a thin layer of highly doped (1 x 10^{20} cm^{-3}), n-type poly-Si. All depositions in this work were carried out at a substrate temperature of 375°C in atmosphere. The precursor solution was prepared by dissolving zinc acetylacetonate in acetic acid : methanol (1:25) to create a 0.2 M solution and adding 3 at% $InCl_3$ (In/Zn = 3 at %). After coating the semiconductor substrates with sprayed IZO, a metal contact (50 nm Ti / 50 nm Pd / 1000 nm Ag) was deposited. The coated substrates were then annealed in air at 300°C for 30 min. For the analysis of the crystal orientation and the interface between the deposited TCO and the substrate, ≈ 50 nm thick lamellas were prepared by focused ion beam (FIB). The samples were investigated using transmission Kikuchi diffraction (TKD) using a step size of 20 nm, an electron energy of 15 keV, and a sample tilt of −20° to the horizontal. The hexagonal crystal structure of ZnO (ICSD-26170) was used as a candidate phase for indexing the TKD patterns using traditional Hough-transform indexing in the Oxford Instruments Aztec v3.4 software.

Fig. 1a shows the band contrast (BC) and elemental maps of the Ag/Pd/Ti capping layers, IZO layer and the poly-Si/Si substrate. Fig. 1b is a bright-field TEM image showing the morphology of the deposited layers. Fig. 1c shows a bright-field image of the poly-Si/IZO interface. The poly-Si layer consists of a double layer and there is a >1 nm amorphous layer (possible oxide) at the poly-Si/IZO interface, which could explain the increase in resistivity of the device. Fig. 2a-c shows the results of the TKD orientation analysis. The indexing success rate of the ZnO layer was <50%, but it could still be used to map out the orientation of the ZnO crystallites. Further results on the use of dictionary indexing[3] for improved indexing of TKD patterns will be presented. In conclusion, the formation of interfacial oxide layers on the poly-Si layer could explain the increased resistivity of the sprayed IZO.

References:
1. Saha, J.K., Billah, M.M. and Jang, J. (2021). ACS Applied Materials & Interfaces 13(31), 37350.
2. Faber, H. *et al.* (2015). ACS Applied Materials & Interfaces 7(1), 782.
3. Chen, Y.H. *et al.* (2015) Microscopy and Microanalysis 21(3), 739.

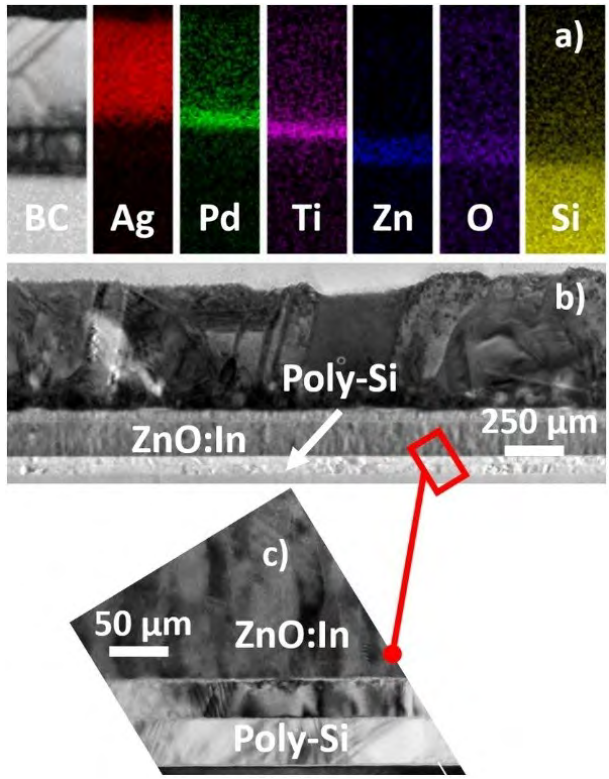

Figure 1. a) TKD-EDS analysis of the IZO layer with Ti-Pd-Ag capping layers, and b-c) bright-field TEM images showing the morphology of the poly-Si substrate and IZO layer interface.

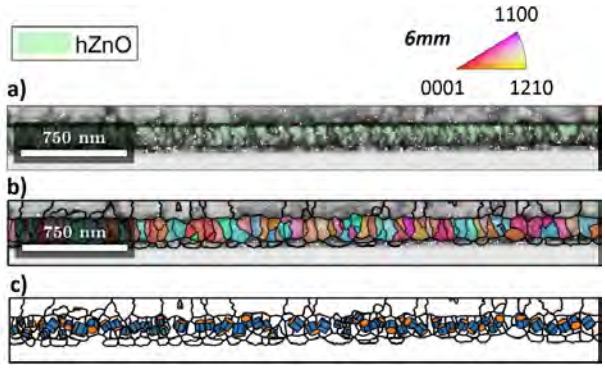

Figure 2. a) Phase map and BC overlay, b) IPF mean grain orientation of the IZO grains, and c) grain shapes indicating the preferential orientations of the IZO grains.

Corresponding author: johan.westraadt@mandela.ac.za

TEM STUDY OF THE NANOSTRUCTURE AND PHASE OF THE Ag-Pt SYSTEM

J.H. Neethling[1], J.H. O'Connell[1], E.J. Olivier[1] and S. Allies[2]

[1]Nelson Mandela University, Port Elizabeth, [2]Centre for Materials Engineering, Department of Mechanical Engineering, University of Cape Town

The silver-platinum (Ag-Pt) system is used as catalyst in the automotive, chemical and petroleum industries[1]. Although this alloy has a wide range of applications, knowledge of its thermodynamic properties is limited[1] and the Ag-Pt phase diagram is still being studied and revised[2]. In 2017 Hart and co-workers, together with the authors of this paper, revisited the revised Ag-Pt phase diagram by calculating the formation enthalpies of candidate Ag-Pt compounds and supporting the results with atomic resolution electron microscopy[2]. The calculations indicated that the $L1_1$ structure (space group #166) is the only stable Ag-Pt phase (50:50 composition) at ambient temperature. This finding was supported by high angle annular dark-field (HAADF) scanning transmission electron microscopy (STEM) investigations which revealed that the Ag-Pt alloy consists of nanodomains with $L1_1$ ordering together with non-ordered FCC domains[2]. Electron diffraction patterns of the Ag-Pt alloy partially supported the abovementioned findings of $L1_1$ and FCC phases, however, they also contain extra spots indicative of the presence of a second orientation with a fixed orientation relationship with respect to the $L1_1$ ordered domains. The best fit of the Ag-Pt electron diffraction patterns is provided by a combination the $L1_1$ phase withtwins on non-ordered {111} planes plus double diffraction. Although no twins were detected by TEM/STEM, dark field (DF) TEM imaging, using the extra diffraction spots, supports the proposed double diffraction mechanism. In order to exclude contributions of possible nanocrystal third phases (such as platinum or silver rich) to the diffraction patterns, more sections were cut from areas in the Ag-Pt sample with 50:50 composition and investigated in a JEOL JEM-ARM200F HRTEM operated at 200 kV. The experimental details of the Ag-Pt alloy may be found in references 2 and 4.

Fig. 1 is a HAADF STEM image of a focused ion beam (FIB) section of the Ag-Pt (50:50) phase showing a microcrystal of a Pt-rich phase (bright area) in the Ag-Pt matrix (grey) as well as porosity in the form of cavities (dark features). DF TEM of the Ag-Pt using the extra spots in the diffraction pattern (e.g. spot indicated by arrow in Fig. 2(a)), lights up the set of nanocrystals (bright areas in Fig. 2(b)) that contributes towards the diffraction spot. However, for spots generated by double diffraction due to nanotwins, the nanotwin boundaries will be visible as bright features in the DF image as can be seen in Fig. 2(b). Silver and platinum are immiscible across most of the compositional range[1]. However, Park *et al.*[3] has successfully synthesised the immiscible metals Ir and Au at the nanoscale which indicates that the immiscibility problem of certain metals may be overcome at the nanoscale[3]. This is most likely the reason for the current finding that the Ag-Pt alloy consists of nanodomains with $L1_1$ ordering together with non-ordered FCC domains[2] and nanotwins.

References:
1. Santoso, I. and Taskinen, P. (2018) Arch. Metall. Mater. 63, 191.
2. Hart, G.L.W. *et al.* (2017) Acta Materialia, 124, 325.
3. Park, S.H. *et al.* (2016) RSC Adv. 6, 3210
4. Neethling, J.H. *et al.* (2013) Proc. Microsc. Soc. South. Afr. 43, 86.

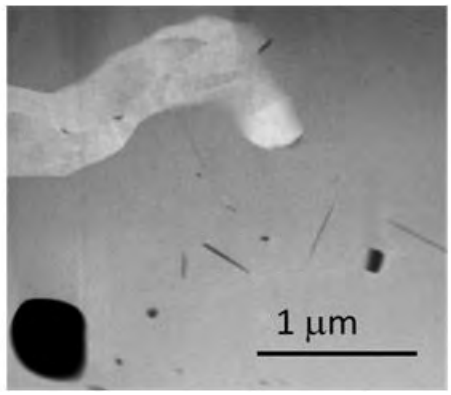

Figure 1. HAADF STEM image of the Ag-Pt phase (grey) showing a microcrystal of a Pt-rich phase (bright area) as well as some porosity (dark features).

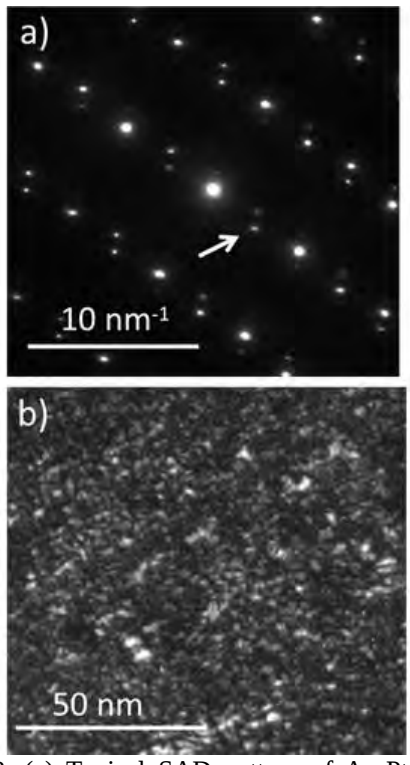

Figure 2. (a) Typical SAD pattern of Ag-Pt showing extra spots with corresponding DF image (b) generated by using the spot indicated by arrow in (a). The bright features in (b) are most likely nanotwin boundaries.

Corresponding author: jan.neethling@mandela.ac.za

EFFECTS OF FEMTO-LASER CHIP BREAKER AND Ni-Mo BINDERS ON AISI1213 TURNING USING NbC-BASED INSERTS

R.M. Genga[1,2,3], P. Zeman[4], J. Brajer[4], J. Malý[4], T. Primus[4], M. Pešice[4], S. Huang[5], J. Vleugels[5], S. Ngongo[6] and A Janse van Vuuren[6]

[1]Academic Development Unit, [2]DST-NRF Centre of Excellence in Strong Materials, [3]School of Mechanical, Industrial and Aeronautical Engineering, University of the Witwatersrand, Johannesburg, [4]Research Centre of Manufacturing Technology, Czech Technical University in Prague, Czech Republic, [5]Department of Materials Engineering (MTM), KU Leuven, Belgium, [6]Centre for HRTEM, Nelson Mandela University, Port Elizabeth

Laser processing (LP) has proven to be an important surface engineering enhancement technique via introduction of micro-features[1]. It has developed from nanosecond to picosecond and now femtosecond based technology[1], with the latter enabling high quality (minimal defects) large area patterning. Here, niobium carbide (NbC) – nickel (Ni) based cemented carbides were investigated as potential inserts for turning of AISI1213 steel due to the good sliding wear resistance of NbC-Ni, high temperature properties and chemical stability[2]. The machining performance can be improved through additions of TiC for secondary hardening, Mo for binder strengthening and femtosecond laser-based chip breaker on the inserts cutting edges.

Cutting inserts were produced from liquid phase sintered (LPS) NbC-10TiC-12Ni (R2-L), as well as spark plasma sintered (SPS) NbC-10TiC-12Ni (R2-S) and NbC-10TiC-12[0.7Ni-0.3Mo] (R2-M-S). During dry turning of AISI1213 steel, the cutting speed (v_c) was varied between 200-300 m/min, depth of cut (a_p) between 0.25-0.50 mm and feedrate between 0.1-0.15 mm/rev. Insert wear was characterised by optical microscopy, scanning electron microscopy (SEM) and annular dark field (ADF) scanning transmission electron microscopy (STEM).

Titanium carbide did not fully dissolve in the SPS compositions (R2-S and R2-M-S), and this was confirmed by EDS mapping (Fig. 1). Undissolved TiC has been reported to improve abrasion wear resistance at the cutting interface between NbC cutting edge and workpiece, improving tool life, particularly at high cutting speeds[2]. The presence of Mo in the R2-M-S was detected by SEM EDS, however, it was located in the binder and NbC phases by ADF-STEM mapping. Conversely, TiC dissolved fully in the LPS NbC compositions forming a (Nb,Ti) C solid solution[2].

Figure 2 shows optical images of the flank and rake faces of the of R2-S (original) and R2-S (with the femto-chip breaker) inserts after turning at v_c = 300 m/min and a_p= 0.25 mm for 10 minutes. High flank wear, chipping and build up edge (BUE) was observed on the cutting edge of original R2-S insert. Conversely, significantly lower flank wear and an absence of both chipping and BUE was observed in the R2-S with a femto-chip breaker, resulting in ~ 40% increase in tool life (Table 1). The improved tool life is attributed to the absence of the BUE, preventing attrition wear which leads to pull out of carbide grains and chipping on the cutting edge. Similar trends of significant increase in tool life with introduction of the femto-chip breaker was observed in the R2-L and R2-M-S inserts as well (Table 1). The R2-L insert had the best tool life due to a better combination of properties. Hence, R2-L insert performed better than the R2-S and R2-M-S, and the femtosecond chip breaker improved the tool life of all inserts.

References:
1. Casalino G *et.al* (2017) CIRP 62, 275.
2. Genga R.M. *et al.* (2020) Int. J. Refract. Met. Hard. Mater., 86, 105128.

Table 1. Mechanical properties and flank wear.

Insert	Flank wear rate (µ/min)		
	Original	Femto-Chip breaker	% Increase in tool life
R2-L	34.44	14.40	58.18
R2-S	37.63	22.57	40.02
R2-M-S	38.12	25.17	33.97

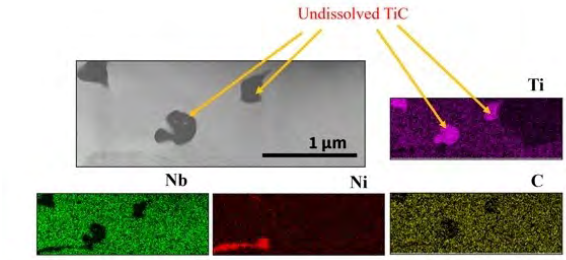

Figure 1. ADF-STEM image and EDS maps of SPS NbC-10TiC-12Ni (R2-S) sample, showing: Nb (green), Ni (red), C (yellow) and Ti (purple).

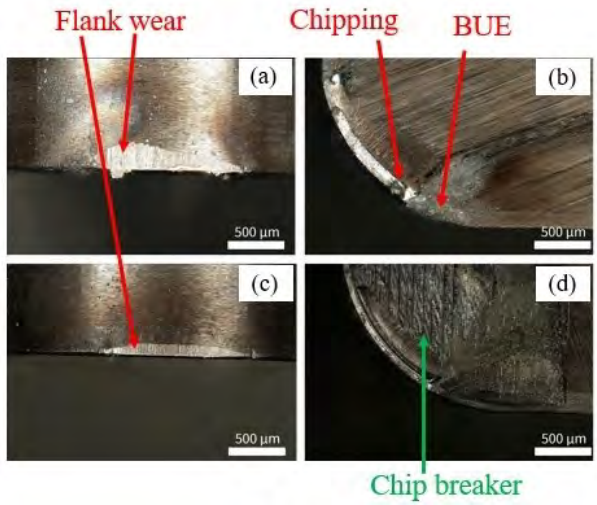

Figure 2. Optical images of the original R2-S insert showing (a) flank and (b) rake, and femto-chip breaker R2-S insert showing, (c) flank and (d) rake.

Corresponding author: Rodney.Genga@wits.ac.za

In-situ TEM heating investigation of fission product transport in post irradiated PBMR TRISO particle SiC layers

E.J. Olivier[1], J.H. Neethling[1] and J.H. O'Connell[1]

[1]Centre for HRTEM, Physics Department, Nelson Mandela University, Gqeberha

There have been significant research efforts in the field of advanced high temperature nuclear reactor technology aimed at determining a plausible transport mechanism for the release of Ag^{110m} from intact tristructural isotropic (TRISO) nuclear fuel during operation[1]. The inherent safety risks associated with this necessitates a detailed understanding of the mechanism(s) involved and is needed for future designs of advanced coated fuels. Initially it was thought that the release of Ag from intact irradiated TRISO fuels was due to classic solid-state diffusion of Ag independently through the SiC layer, the main barrier against the release of metallic fission products. Measurements of the solid-state diffusion coefficients of Ag in SiC obtained from out-of-reactor experiments were however found to be significantly smaller than that estimated from fractional Ag release measurements[2] obtained from post irradiation examinations of in-reactor fuels. Due to this discrepancy several different Ag transport models have been proposed[3]. Intra and inter granular migration routes such as dislocations and grain boundaries in SiC have been proposed as so called "short circuit" diffusion paths. More recently, a model based on the grain boundary migration of Ag, mediated by other metallic fission products, have been proposed[3]. Credence to this possibility was given by the discovery of Ag co-existing within palladium silicide nodules along grain boundaries in SiC layers of post irradiated TRISO fuels from the US AGR-1 program[3].

This paper presents findings from an in-situ heating transmission electron microscopy (TEM) characterization of TRISO particle SiC layers originating from the South African PBMR program and irradiated in the Advanced Test Reactor (ATR) as part of the Advanced Gas Reactor (AGR)-2 experiment. Previous findings from this material showed the presence of Ag in the SiC layer together with other metallic fission products. The aim of the study was to gain further insights about the nature of metallic fission products migration in SiC when subjected to dynamic heating in the TEM.

For this purpose, FIB lamellae were prepared from SiC layers of TRISO particles tested and carefully mounted on a DENSsolutions MEMS heating chip for use in a double tilt DENSsolutions four contact in-situ heating holder. The imaging and analysis were done using a double aberration corrected JEOL ARM200F operated at 200 kV. Fig. 1 shows a LAADF image of the SiC layer at the inner pyrolytic carbon and SiC interface. Examples of fission product agglomerations at grain boundary triple points are indicated by the red arrows. Fig. 2 shows a HRTEM image of such a fission product agglomeration taken at 1100 ºC showing crystallinity of the agglomerate at elevated temperatures. Overall, the findings of the study were consistent with a solid-state grain boundary migration mechanism as the dominant migration process for metallic fission products in the SiC layer.

References:
1. Nabielek, H., Brown, P. and Offermann, P. (1977) Nuclear Technology. 35, 483.
2. MacLean, H., Ballinger R., Kolaya L., Simonson S., Lewis N. and Hanson M. (2006) J. of Nucl. Mat. 357,3.
3. Van Rooyen, I.J., Olivier, E.J. and Neethling, J.H. (2016) Journal of Nuclear Materials. 476, 93

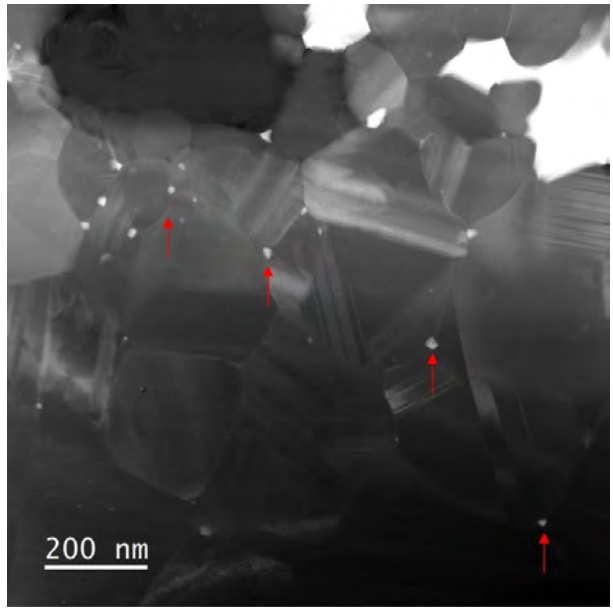

Figure 1. LAADF image of the inner pyrolytic carbon and SiC interface with fission product agglomerations shown by the red arrows.

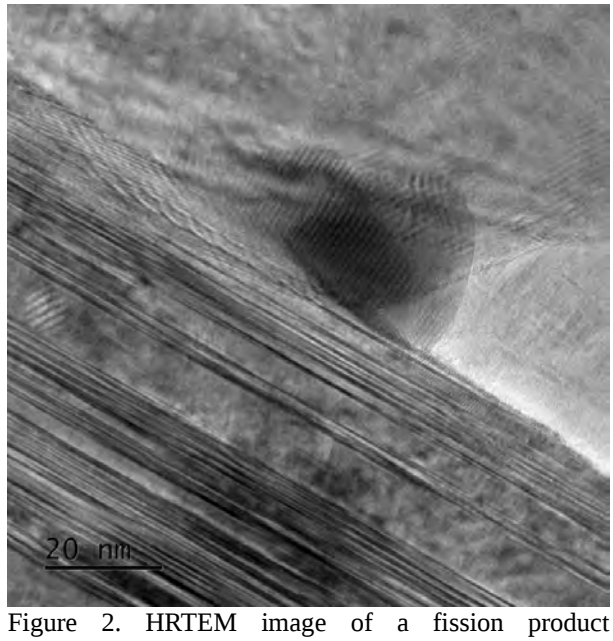

Figure 2. HRTEM image of a fission product agglomeration at 1100 °C showing crystallinity.

Corresponding author: jolivier@mandela.ac.za

TOOL LIFE OF NbC-BASED CERMETS DURING FACE MILLING OF AUTOMOTIVE GCI

M.S. Rabothata[1,2], N.P. Mphasha[1,2], K. Phaka[2], P. Zeman[3], R.M Genga[1,2,4], C. Polese[2,4], S. Huang[5] and J. Vleugels[5]

[1]Academic Development Unit, Wits University, [2]School of Mechanical, Industrial and Aeronautical Engineering, Wits University, [3]Research Centre of Manufacturing Technology, Czech Technical Universiy in Prague, [4]DSI-NRF Centre of Excellence in Strong Materials, Wits University, [5]Department of Materials Engineering, KU Leuven

Cermets, also known as cemented carbides, consist of a predominant hard but relatively brittle carbide phase (WC, TiC) and a metallic reinforcement binder (Co, Ni or Fe)[1]. Albeit the extensive use of WC-Co cemented carbides in tribological applications, niobium carbide (NbC) has been explored as replacement for tungsten carbide (WC). This is mainly due to the growing supply risks and unstable market prices associated with both WC and Co[2]. Furthermore, WC-Co cutting tools exhibit poor chemical stability during machining of steels and cast irons[3].

NbC has better high temperature properties than WC[4]. Nickel can retain its ductile FCC structure at below solidus temperatures[5]. Additionally, Ni has better resistance to corrosion and oxidation compared to Co and can improve hot hardness and resistance to thermal cracking in NbC-based cemented carbides[4]. Despite the promising properties exhibited by both NbC and Ni, NbC-based cutting tools produced by conventional liquid phase sintering (LPS) methods yield low hardness and fracture toughness compared to the WC-Co based cutting tools[6]. Hence, rapid pulsed electric current sintering (PECS) techniques are now used to improve the properties of NbC-based cermets. In this study, the effects of titanium carbide (TiC) and titanium carbonitride (TiC_7N_3) additions as grain growth inhibitors and secondary hardening phases[1,6], and laser surface modification (LSM) on tool life performance during dry face-milling of automotive grey cast iron (GCI) were investigated.

For this purpose, cutting inserts produced by PECS with powder compositions (i) NbC-12Ni (wt%) (N2S), (ii) NbC-10TiC-12Ni (wt%) (R2S), and (iii) NbC-10TiC_7N_3-12Ni (wt%) (TCN1S), were used. A LD50C femtosecond laser was used to create shark skin (S) and pyramid (P) patterns on the cutting edges of the inserts. Machining tests were carried out on a MAHO MH70 milling machine using the milling conditions given in Table 1. The feed (f) of 0.1 mm/tooth and the radial depth of cut (a_r) of 80 mm defined by the diameter of the insert holder (F75SN12080) were kept at constant for all cutting conditions. The machining forces were measured using a Kistler force dynamometer and, the flank wear and crater wear were evaluated using a Nikon optical microscope.

The additions of both TiC and TiC_7N_3 reduced the tool life of the blank (N2S) cutting inserts, from 20 min to 8 min (R2S) and 6 min (TCN1S), respectively. This was attributed to the increased hardness (HV_{30}) and reduced fracture toughness (K_{IC}) in R2S and TCN1S due to those additions[1,6]. The resultant cutting forces in all inserts increased by ≥1% thanks to LSM. Further, LSM improved tool life irrespective of the composition, enabling the inserts to complete the machining duration of 20 min. The flank wear rates (FWR's) of all inserts was < 6.5µm/min and LSM reduced the flank wear rate (FWR) of all the inserts except for N2S (S). The improved tool life and reductions in FWR can be attributed to self-carbide coating layers produced during LSM and resulting in enhanced abrasion and attrition wear resistance in the cutting inserts[6]. Fig. 1 shows the optical microscopic images of the maximum flank wear (VBmax) of (a) N2S, (b) TCN1S (S) and (c) R2S (P) cutting edges, including the respective crater wear (d).

References:
1. Upadhyaya, G.S. (1998) Cemented Tungsten Carbide Production, Properties and Testing. Kanpur, Indian Institute of Technology
2. Rizzo, A. *et al*. (2020) Materials, 13
3. Woydt, M. and Mohrbacher, H. (2015) Int. J. Refract. Met & Hard Mat, 49
4. Sarin, V. *et al*. (2014) Comprehensive Hard Materials. UK, Elsevier
5. Penrice, T.W. (1987) J. Mater. Shaping Technol. 5,35
6. Genga, R.M. *et al*. (2020) Int. J. Refract. Met & Hard Mat, 86 (105128)

Table 1. Face-milling test parameters.

Cutting speed (m/min)	Depth of cut, a_p (mm)	Spindle speed (rpm)	Feed rate (mm/min)
200	1	800	80

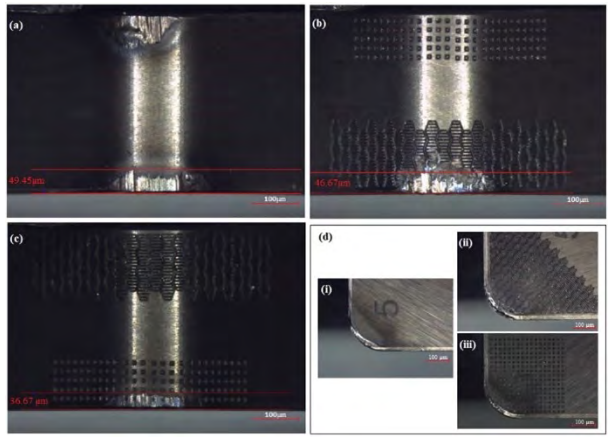

Figure 1. Optical microscopy images showing VBmax of (a) N2S, (b) TCN1S (S) and (c) R2S (P), and (d) the crater wear of the respective cutting edges.

Corresponding author: mahlatse.rabothata@wits.ac.za

EFFECTS OF TiC_7N_3 ADDITIONS AND SINTERING TECHNIQUE ON THE MICROSTRUCTURAL PROPERTIES OF NbC-BASED CERMETS

M.S. Rabothata[1,2], N.P. Mphasha[1,2], R.M. Genga[1,2,3], C. Polese[2,3], P. Zeman[4], S. Huang[5], J. Vleugels[5], A. Janse van Vuuren[6] and N.B. Nelwalani[7]

[1]Academic Development Unit, University of the Witwatersrand, Johannesburg, [2]School of Mechanical, Industrial and Aeronautical Engineering, University of the Witwatersrand, Johannesburg, [3]DSI-NRF Centre of Excellence in Strong Materials, University of the Witwatersrand, Johannesburg, [4]Research Centre of Manufacturing Technology, Czech Technical University in Prague, Czech Republic, [5]Department of Materials Engineering, KU Leuven, Belgium, [6]CHRTEM, Nelson Mandela University, Port Elizabeth, [7]School of Mining, Metallurgy and Chemical Engineering, University of Johannesburg, Johannesburg

Traditionally, cemented carbides consisting of tungsten carbide (WC) bonded with a ductile cobalt (Co) matrix are used in rock drilling, metal machining, and mining[1]. Extensive use of WC-Co parts in engineering applications is due to their superior mechanical properties and excellent wear resistance. However, due to supply constraints and fluctuating market prices for WC and Co, niobium carbide (NbC) and nickel (Ni) have been studied as alternative materials[2,3]. NbC has comparable Vickers (HV_{30}) hardness (~19.6 GPa) to WC (~22.4 GPa) and offers good high-temperature chemical stability[3]. At all temperatures below the solidus (1454.85 °C), nickel retains its ductile face-centered cubic (fcc) structure, providing good high-temperature properties[3]. Spark plasma sintering (SPS) and the inclusion of TiC_7N_3 as a secondary hardening phase can improve the hardness and abrasion resistance of NbC cemented carbides[1].

To study the effect of TiC_7N_3additions on the microstructural and mechanical properties of NbC-based cemented carbides, powders with compositions NbC-12Ni (wt%) (N2-S), NbC-10TiC_7N_3-12Ni (wt%.) (TCN1-S) and NbC-10TiC_7N_3-12Ni (wt%.) (TCN1-L), were investigated. N2-S and TCN1-S were prepared by SPS, while TCN1-L was prepared by liquid phase sintering (LPS). The sintered samples were characterised by optical microscopy, scanning electron microscopy (SEM), and annular dark field (ADF) scanning transmission electron microscopy (STEM).

The backscattered SEM image of N2-S shows smaller carbide grains with poor binder distribution, see Fig. 1. This can be attributed to the lower sintering temperature and shorter dwell time during SPS, which prevented continuous Ostwald ripening. Better densification was achieved for TCN1-L (98.51%) than TCN1-S (97.63%), due to sufficient inter-diffusion between TiC_7N_3, NbC, and Ni during LPS resulting in smaller and more evenly distributed Ni binder pools, see Fig. 2. The addition of TiC_7N_3 resulted in higher Vickers hardness values irrespective of the sintering technique (Table 1). However, TCN1-S had higher hardness than TCN1-L due to restricted inter-diffusion of TiC_7N_3 owing to shorter dwell times during SPS, resulting in undissolved hard phases. The increase in fracture toughness (K_{IC}) during LPS of TCN1-L is ascribed to better binder distribution and the inter-diffusion of NbC and TiC_7N_3 grains into each other. Microstructure evolution revealed that the additions of TiC_7N_3 may be beneficial in improving the material properties of NbC-based cemented carbides, especially in LPS.

References:
1. Upadhyaya, G.S. (1998) Cemented Tungsten Carbide Production, Properties and Testing. USA, Noyes Publications.
2. Penrice, T.W. (1987) J. Mater. Shaping Technol. 5, 35.
3. Genga, R.M. *et al.* (2018) Int. J. Refract. Met. Hard Mater. 73, 111.

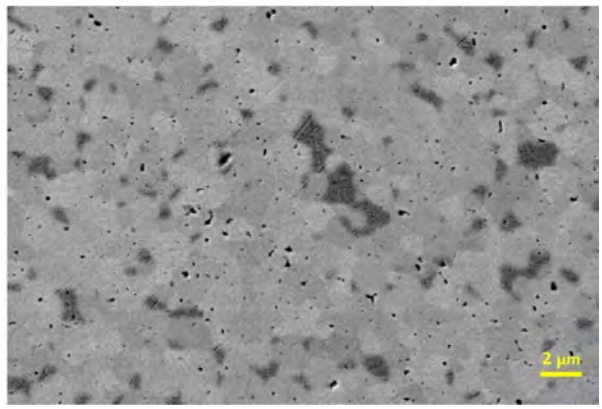

Figure 1. SEM-BSE image of N2-S, showing NbC (light) and Ni (dark contrast) with smaller NbC particles

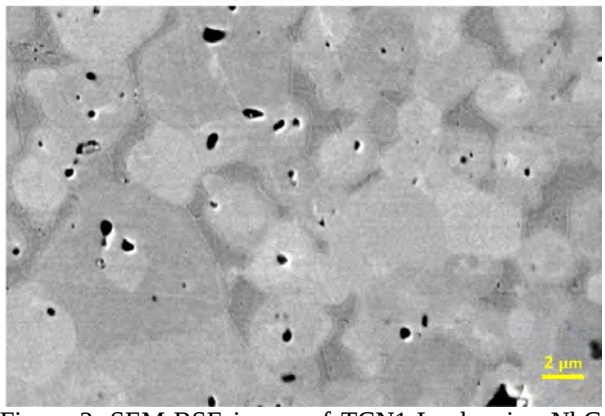

Figure 2. SEM-BSE image of TCN1-L, showing NbC (light) and Ni (dark contrast) with more rounded NbC particles

Grade	HV_{30} (GPa)	K_{IC} (MPa·m$^{0.5}$)
N2-S	11.73±0.33	5.72±0.10
TCN1-S	13.70±0.32	5.50±0.06
TCN1-L	12.77±0.13	9.31±0.53

Figure 3. Mechanical properties of NbC-based materials

Corresponding author: 673306@students.wits.ac.za

PRODUCTION OF $SrVO_3$ THROUGH CO-PRECIPITATION SYNTHESIS AND ANNEALING IN REDUCING ATMOSPHERE.

E. Lee[1], R.A. Harris[1], J.J. Terblans[1] and H.C. Swart[1]

[1]Deparment of Physics, Unversity of the Free State, Bloemfontein, South Africa

Transparent conductive oxides (TCO's) thin films have received a significant amount of interest over recent years due to their properties of being transparent in the visible light region while still being electrically conductive. Currently, indium tin oxide (ITO) films are the most widely used TCO, making up close to 90 % of the commercial applications such as: displays, electronic and energy devices. However, indium resources are of great concern due to its increasing scarcity, resulting in limited supply and higher cost[1]. Strontium vanadate ($SrVO_3$) a cubic perovskite was first synthesised in the 1950's and later shown to exhibit metal-like electronic properties[2]. Here we report on the effect of annealing time on the crystal structure and morphology of $SrVO_3$.

A 0.34 M $Sr(NO_3)_2$ (Sigma-Aldrich, ≥ 98.0 %) as well as a 0.34 M NH_4VO_3 (Sigma-Aldrich, ≥ 99.0 %) solution, were prepared. Both solutions were combined to form a cream-coloured precipitate and stirred for 2 h. Using a centrifuge, the precipitate was separated and washed firstly with distilled water three times and finally with ethanol also three times, each time separating the precipitate from the liquid using the centrifuge. An oven heated to 100 °C was used to dry the precipitate for 12 h. The dried precipitate was crushed using a mortar and pestle to ensure that the particle sizes were homogenous before being annealed at 650 °C for 24 h. After annealing the product was separated into three separate portions. The first portion was annealed at 1000 °C for 8 h in a reducing atmosphere (5% H_2/Ar). The second and third portions were annealed in a 5% H_2/Ar atmosphere at 1000 °C for 24 h and 48 h. respectively Phase analysis was performed using an X-ray diffractometer (XRD) (Bruker D8 Advance) using CuKα radiation (λ = 0.15406 nm). The size and morphology of the samples were examined using a field emission scanning electron microscope (JEOL JSM7800F FESEM).

The effect of annealing time on the morphology of $Sr_2V_2O_7$ as prepared sample is shown by the FE-SEM micrographs in Fig 1. With increasing annealing time, the initially distinct and separated $Sr_2V_2O_7$ grains started to increase in size and became more agglomerated. Fig 2 shows the XRD pattern of the as prepared powder product and the effect of annealing time of the final phase of the product. All reflections of the XRD pattern of the as prepared product showed the formation of $Sr_2V_2O_7$ with a triclinic crystal structure in space group *P*1. With an annealing time of 8 h, a phase transformation from a triclinic to a trigonal crystal structure was observed and found to be $Sr_3(VO_4)_2$ in space group *R*3*m*, with some triclinic structure still present. Increasing the annealing time to 24 h yielded only $Sr_3(VO_4)_2$ trigonal structures. Finally, at 48 h annealing, a transformation from trigonal to cubic was seen. The cubic crystal structure was that of $SrVO_3$ in space group *Pm*3*m* with some $Sr_3(VO_4)_2$ still present.

$SrVO_3$ was successfully synthesised using the co-precipitation method. The FE-SEM micrographs showed the effect of annealing time on the morphology of the $Sr_2V_2O_7$ sample. And the XRD patterns showed the transformation of the sample from a $Sr_2V_2O_7$ triclinic to a $SrVO_3$ cubic crystal structure during annealing in the presence of a reducing atmosphere.

References:
1. Lokanc, M., Eggert, R. and Redlinger, M. (2015) The Availability of Indium: The Present, Medium Term, and Long Term, Colorado, NREL.
2. Kestigian, M.J., Dickinson, J.G. and Ward, J. (1957) J. Am. Chem. Soc. 79, 5589.

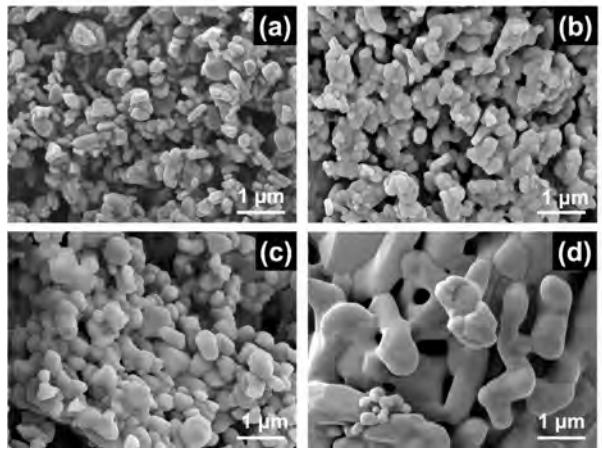

Figure 1. FE-SEM micrographs of (a) as prepared $Sr_2V_2O_7$ and with annealing time of (b) 8 h, (c) 24 h and (d) 48 h.

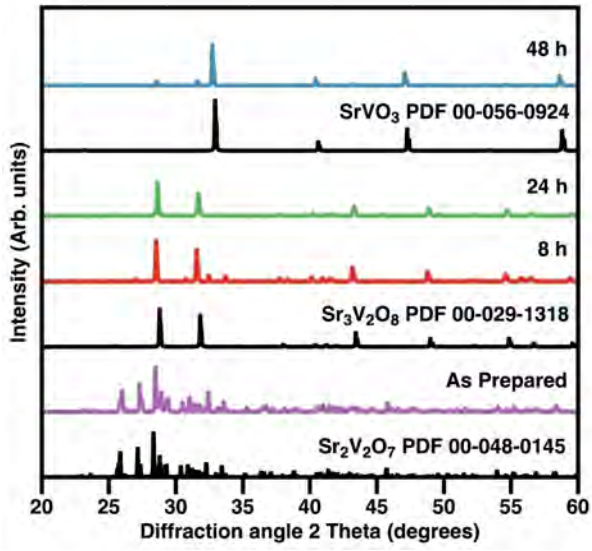

Figure 2. X-ray powder diffraction patterns of the as prepared $Sr_2V_2O_7$ and after various annealing times.

Corresponding author: LeeE@ufs.ac.za

SINGLE ELECTRON TRANSPORT IN SEMICONDUCTOR NANOSTRUCTURED DEVICES

N. Hanief[1], H. Howe[2] and M.D. Blumenthal[1]

[1]Dept. of Physics, University of Cape Town, South Africa, [2]London Centre for Nanotechnology, University College London, United Kingdom

Electron pumping devices have been optimized over several decades following the advancement in micro- and nano-fabrication techniques. This has motivated for the ongoing quest to acquire a new current standard for quantum metrology applications. The International System of Units (SI) has recently (2018) been revised to factor in a method that solely utilizes the fundamental constants of nature, i.e. the elementary charge, *e* and Planck's constant, *h*[1]. This enables single electron transport (SET) pumping devices to be utilized for determining the electrical base unit of current. The quantum metrological triangle (QMT), related through Ohm's law by the Josephson voltage and the quantum hall resistance standards will be completed by the high accuracy and precise definition of current in terms of *e* and *h*.

SET is facilitated by the use of quantum electron pumping (QEP) devices. These devices are fabricated using molecular beam epitaxy such that a heterostructure is created in the form of a two-dimensional electron gas (2DEG). The low dimensionality of semiconductor devices coupled with the ultra-low temperatures achieved by a cryogen-free dilution refrigeration unit allows for quantum effects to occur[2,3]. The 2DEG can be further confined to a 1D quantum wire and a 0D quantum dot (QD) which allows for the measurement of SET. The QD is created with tunable gate barriers that are fabricated using electron beam lithographic (EBL) techniques (Fig.1). This highlights the role of microscopy within this study as the QD can only be achieved through intricate EBL pattern design on the 2DEG heterostructure. The patterning software is used to design gated features on the heterostructure surface which are lithographically processed as part of the SEM. The exposed regions are thermally evaporated with 15nm Ti and 60nm Au to create the tunable gate barriers. Electrons from the 2DEG source reservoir (S) can tunnel through the QD towards the drain, (D). As the barrier oscillates with an applied voltage, the single electron is confined to the QD and furthermore transported across the QD (left schematic in Fig.1). This SET is measured for low level quantized current output (within the nA range) and high-level frequency output (within the GHz range) such that high accuracy measurements are achieved for the current standard. AlGaAs 2DEG heterostructures were used for the QEP devices with nanostructures fabricated using a finger-gated design (Fig.1). The measurements were carried out at various temperatures within the milli-Kelvin (mK) range.

The generated pumped current during the electron transfer yields characteristic pump maps which can be affected by varying parameters. The pump map refers to the pumped current plot generated from the voltage force applied to the tunable gate barriers. The exit gate is kept fixed, and the entrance gate is oscillated above and below the exit gate voltage. The modulation of the gate barriers at a frequency *f*, generates a current that can be plotted such that a pump map is generated for the transport of a single electron. The temperature dependence is considered for SET across a QD and the pump maps are measured with high sensitivity for the accuracy of quantised current pumping. This is characterized using the flatness of the measured pump map plateaus. A model for electron capture within the tail and shoulder regimes of the plateau regions for pumped current is formulated giving insight to the dominating quantum mechanisms that form which drive the transfer of single electrons across a QD.

The authors hereby thank the National Research Foundation, for their support and the Electron Microscope, UCT and the London Centre for Nanotechnology, UCL for the use of their facilities.

References:
1. Scherer, H., Schumacher, H. (2019) Annalen der Physik. 531(5), 1.
2. Rahimi-Iman, A. (2021) Semiconductor Photonics Nanomaterials and Quantum Structures. Switzerland, Springer Nature.
3. Davies, J.H. (1998) The Physics of Low Dimensional Semiconductors. NY, Cambridge University Press.

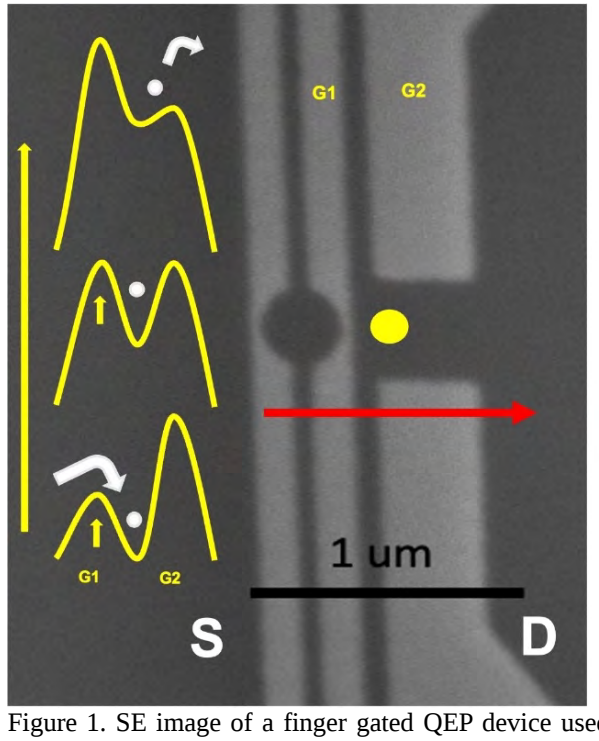

Figure 1. SE image of a finger gated QEP device used to pump electrons in the direction of the red arrow. The QD is shown in yellow and the left side schematic indicates the gates (G1 and G2) which are oscillating to facilitate SET.

Corresponding author: nasheeta.hanief@uct.ac.za

TEM TOMOGRAPHY AT ROOM TEMPERATURE

A. Ziegler[1]

[1]Microscopy and Microanalysis Unit, The University of the Witwatersrand, Johannesburg

Electron tomography (ET) using a Transmission Electron Microscope (TEM) is excellently suited to capture and map the three-dimensional (3D) structure of electron transparent matter. In other words, the focus is on the determination of shape and structural information employing only a set of 2D projections from a 3D sample. This generally applies to all soft as well as biological matter, i.e., polymers, cells or organelles, but also to nano-sized solid-state matter that does not consist of too high atomic-number elements. The key parameter is the electron transparency of the sample. Other important characteristics of the sample material include radiation hardness (or dose or beam sensitivity).

Advancements in technology, i.e., hard and software, over the last 20 years allow automation of almost the entire tomographic process. Exceptions to this are the sample preparation and insertion into the TEM sample holder. Pioneers in this TEM technique, who developed most of the tomographic best-practice routines were the Life Scientists that have non-crystalline, non-periodic, non-symmetric, beam sensitive, biological objects that primarily tend to reside in a liquid growth environment[1,2]. The challenges they faced were multiple and they managed to succeed in solving many of them. The list includes: the low-dose TEM, ultra-sensitive direct-electron imaging detectors suitable for extremely low-signal-to-noise ratios[3], large area detectors to view large ROIs, TEM sample autoloaders, Cryo-TEM setups (high-angle tilting), cryo-preservation of biological samples in their near-native environment (frozen-hydrated or vitrified samples), tomography acquisition routines (initially manual, but later software controlled), 3D reconstruction algorithms in real as well as in Fourier space, analysis of Cryo-TEM images of very low-contrast, and last but not least visualization, detection and segmentation, as well as feature extraction algorithms for TEM-tomography results.

A less known and applied 3D-TEM reconstruction techniques (among the solid-state TEM scientists at least), that was also developed by the life-sciences Cryo-TEM community is the single-particle analysis approach to 3D structure reconstruction[4].

Today, almost all of their solutions and developments are applied in the solid-state TEM tomography domain. TEM-tomography development in the solid-state sciences is primarily discrete-tomography, which uses a much smaller number of projections of the sample orientation.

In the following, some of these Cryo-TEM-tomography techniques and developments will be presented and its applicability to room-temperature samples discussed. The focus will be on the actual TEM instrument, the tilt-series acquisition (challenges and solutions), and the 3D reconstruction and visualization options available. 3D reconstruction examples of soft-matter samples (polymers films, tetrapods), Fig. 1, and biological matter will be given.

References:
1. DeRosier, D., Klug, A. (1968) Nature 217(5124), 130.
2. Frank, J. (2006) Electron Tomography. Springer-Verlag New York.
3. Ziegler, A. Graafsma, H. (2014) Detectors for Electron and X-ray Scattering and Imaging Experiments, In-situ Materials Characterization Across Spatial and Temporal Scales, Springer Series in Materials Science 193.
4. Förster, F., Hegel, R. (2007) Cellular Electron Microscopy, Methods in Cell Biology, Elsevier Science 79, 741.

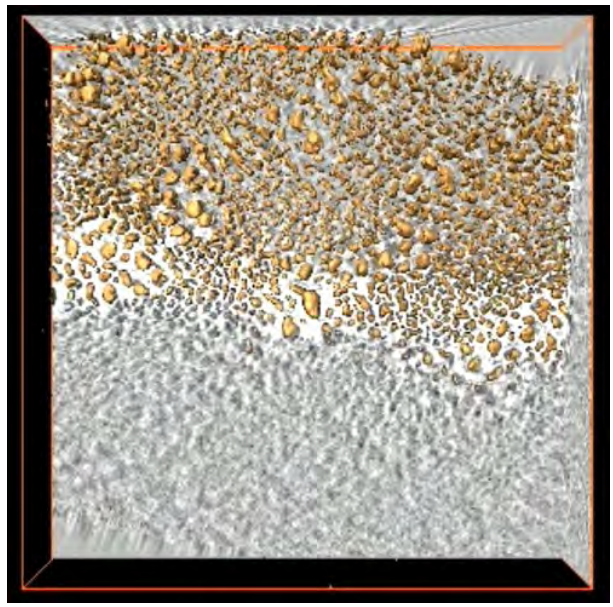

Figure 1. Top-view of a thin, Au-particle containing polymer film that was prepared with a laser interference pattern.

Corresponding author: alexander.ziegler@wits.ac.za

AN IN-SITU HEATING TEM INVESTIGATION OF CELL FORMATION IN THE AA5182 ALUMINIUM ALLOY

G. K. Morrison[1,2], J. E. Olivier[3], C. Lang[2], N. Nasiri[2], A. Janse van Vuuren[3] and S. George[1]

[1]Centre for Materials Engineering, University of Cape Town, , [2]School of Engineering, Macquarie University, [3]Centre for HRTEM, Nelson Mandela University

Aluminium alloys are used for applications in which their good corrosion resistance and high strength-to-weight ratio are important[1]. AA5182 can end stock (CES), used in the manufacture of beverage cans, requires mechanical properties that are consistent and isotropic. CES produced by Hulamin, however, intermittently exhibits an anisotropic reduction in mechanical properties which can lead to beverage can failure. The aim of this work is to investigate the microstructural evolution which affects the tensile strength of CES; and hence to make recommendations, regarding CES production, to Hulamin.

The major steps in CES production are ingot casting, hot rolling, cold rolling, and coil coating. Initial investigation determined that coil coating is the only step in which temperature/time may vary from batch to batch. Furthermore, thermal excursions during coil coating may reach 210°C, which is sufficient to cause recovery of the cold-rolled alloy[2]. Investigation of microstructural evolution during heating of any aluminium alloy is however difficult and seldom successful, as atomistic processes can occur rapidly[2]. Our investigation used in-situ heating in a Transmission Electron Microscope (TEM) to overcome this difficulty, since it enabled observation of temperature-dependent microstructural change in real time. AA5182 sheet, 0.208mm thick, was received from Hulamin in the H48 condition, after cold rolling. Tensile testing of samples, both cold rolled and heat treated in a salt bath at 210°C, showed a reduction in tensile strength after heat treatment, from 398MPa to 362MPa. Following this confirmation of the change in mechanical properties during the brief thermal excursion, microstructural change was investigated. Electron transparent specimens were prepared from the as-cold rolled CES, using Focused Ion Beam (FIB) milling; then placed on a MEMS heating chip, and observed during in-situ heating in a JEOL JEM-ARM200F TEM.

TEM investigation showed that in the cold-rolled condition, the specimen exhibited dislocation loops and entangled dislocations, as seen in Figure 1. During in-situ heating of the as-cold rolled sample at 210°C, the dislocation loops were rapidly replaced by cell structures indicative of recovery. Figure 2 is a micrograph of the area in Figure 1, viewed at the same tilt, after this thermal excursion. The dislocations are seen to have formed a cellular structure. This microstructural change, observed during the in-situ TEM investigations, is consistent with the observed tensile strength reduction. The use of in-situ TEM has enabled us to identify the CES production step which results in rapid microstructural changes and consequent mechanical property changes. This allows us to recommend closer control of coil coating to Hulamin, in order to achieve the required AA5182 standards.

The assistance of the Centre for High Resolution TEM at NMU is gratefully acknowledged.

References:
1. Yu, X., Zhao, Y., Wen, X., et al. (2005). Mater. Sci. Eng. A, 394(1), 376–384.
2. F. Humphreys and M. Hatherly, (2004) Recrystallization and Related Annealing Phenomena (Second Edition), pp. 169–213, Oxford: Elsevier.

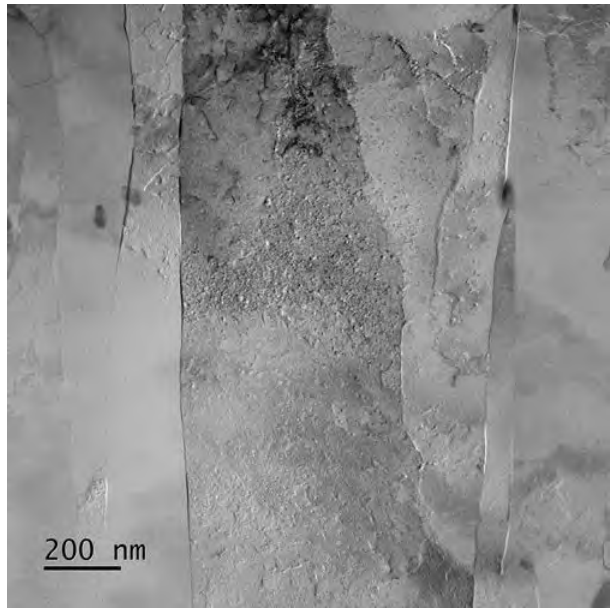

Figure 1. TEM micrograph showing as-cold rolled CES material with dislocation loops in the grain.

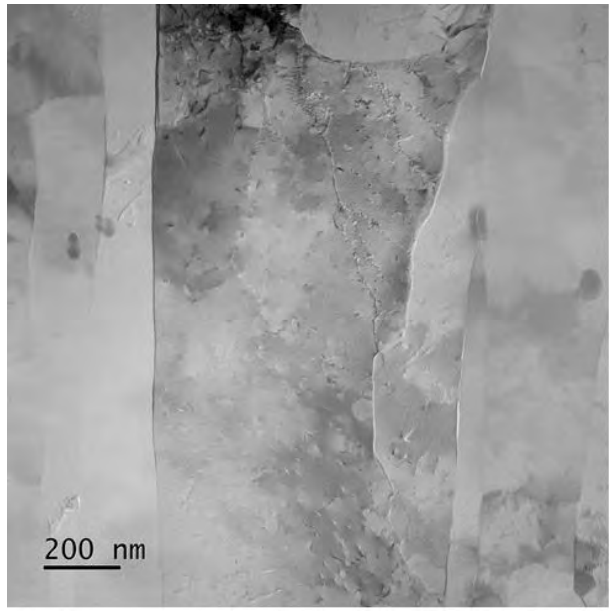

Figure 2. TEM micrograph of CES material with cell structures after 5 seconds of in-situ heating at 210°C.

Corresponding author: mrrgra008@myuct.ac.za

OPTIMIZATION OF THE ADDITION OF NIOBIUM AS A BETA STABILIZER IN A TITANIUM ALLOY FOR MEDICAL APPLICATIONS

K.E. Mrwata[1], C.W. Siyasiya[1] and N.K. Arthur[2]

[1]Department of Materials Science and Metallurgical Engineering, University of Pretoria, South Africa, [2]CSIR Photonics Centre, Laser Enabled Manufacturing, Pretoria Campus, South Africa

The additive manufacturing (AM) industry is growing[1, 2]. AM offers many advantages compared to traditional manufacturing methods, i.e., investment casting, in the aerospace, automotive, medical, dentistry, and consumer products/electronics industries that prioritize customization of components[3]. AM is predominantly concentrated in the products/electronics, automotive and medical industries[4]. The medical industry has emphasized research into titanium (Ti) and its alloys, particularly Ti-6Al-4V[5]. Ti-6Al-4V, an alpha and beta alloy (α+β) with 6 wt.% Al and 4 wt.% V, is the most understood and applied Ti alloy in AM research and has become the preferred alloy because its combination of strength-to-weight ratio, corrosion resistance, and biocompatibility have made it an appealing choice in the medical industry[6, 7]. Despite Ti-6Al-4V being the preferred choice, there are issues of cytotoxicity associated with vanadium (V) and neurological disorders with aluminium (Al) that have led to research into alternative β stabilizing alloying elements that may safely replace vanadium[8, 9]. The addition of niobium (Nb) increased the β phase and hardness for investment casting; according to the study by Fikeni, et al., using two binary alloys Ti+13Nb where x was either 13 or 28 wt.%, fabricated by investment casting, where the authors observed an increase in β phase with increased in Nb wt.% was accompanied by an increase in hardness and concluded that the increase in β phase correlated with the increase in hardness[10].

This study aims to determine whether AM and the addition of Nb into the alloy Ti-6Al-4V will optimize the β phase and, subsequently, the mechanical properties, in particular the hardness. An investigation into the effect of beta stabilizer, Nb, on the β phase, microstructure, and hardness of alloy Ti-6Al-4V to find the optimum Nb concentration was conducted. Samples of Ti-6Al-4V, containing varying amounts of Nb, were created using AM laser engineering net shaping (LENS™). The phase and microstructure of the cross-section surface of samples Ti-6Al-4V+13Nb and Ti-6Al-4V+28Nb were analysed using microscopic analysis techniques followed by Vickers hardness testing.

Grade 23, Ti-6Al-4V, alloy powder and elemental Nb metal powder were used as the feedstock material used in this study to create test samples. The test samples were created in a controlled environment of argon with oxygen levels below 10 ppm using an in-situ direct energy deposition (DED) process. The flowrate of the Nb powder was changed in accordance to achieving the designated 13 and 28 wt.%. The printed samples were cut laterally to reveal the cross-section surface then metallographic preparation was done. A significant increase in the β phase was observed with an increase in Nb wt.%, 60% and 91% for Ti-6Al-4V+13Nb and Ti-6Al-4V+28Nb respectively, from electron backscattering diffraction (EBSD) phase analysis. Figure 1 summarizes the results from EBSD, scanning electron microscopy (SEM) including energy dispersive spectroscopy (EDS). In addition, the hardness measurements increased from 209 $HV_{0.3}$ to 377 $HV_{0.3}$ for Ti-6Al-4V+13Nb and Ti-6Al-4V+28Nb, respectively. This increase may be attributed to solid solution strengthening combined with the discrepancy in the distribution and concentration of defects between the alloys. Alloy Ti-6Al-4V+28Nb, Figure 1 (d) has a larger amount of un-melted Nb and lower porosity, unlike Ti-6Al-4V+13Nb, Figure 1 (c) that has a higher density of pores and fewer un-melted Nb. The β phase in the alloy Ti-6Al-4V increased with the increase in Nb wt.% which also increased the hardness, thus, Ti-6Al-4V was optimized using AM and with the addition of 28 wt.% Nb.

References:
1. Javaid, M. and A. Haleem (2019). Alexandria J. of Medicine 54(4): 411-422.
2. Saboori, A., et al. (2017). Appl. Scis 7(9).
3. M. Peters, et al. (2003). Titanium and Titanium Alloys: Fundamentals and Applications. Cologne, WILEY-VCH Verlag GmbH & Co. KGaA, Weinheim.
4. Verhoef, L. A., et al. (2018). Energy Plyc 112: 349-360.
5. Maina, M. R. (2016). Advanced Manufacturing Techniques Using Laser Material Processing. Pennsylvania, IGI Global.
6. Damisih, et al. (2018). AIP Conf. Proc. 164.
7. M. Peters, et al. (2003). Cologne, WILEY-VCH Verlag GmbH & Co. KGaA, Weinheim.
8. Litak, J., et al. (2022). Materials (Basel) 15(10).
9. Severino Martins, J. R. and C. R. Grandini (2012). J. of Appl. Physics 111(8).
10. Fikeni, L., et al. (2021). Mtrls. Today: Proc. 38, 913-917.

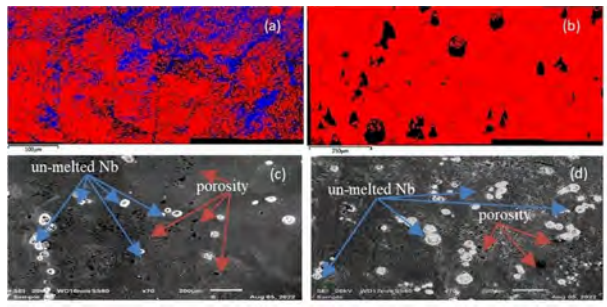

Figure 1. Figure 1: EBDS phases maps of α phase (blue) and β phase (red) for TiAl6V4+13Nb (a) and TiAl6V4+28Nb (b) at 100 µm and 200 µm, respectively. Defects and their distribution were identified within both alloys, TiAl6V4+13Nb (c) and TiAl6V4+28Nb (d), as un-melted Nb and porosity using SEM.

Corresponding author: u11031906@tuks.co.za

INFLUENCE OF SINTERING TEMPERATURE ON THE MECHANICAL PROPERTIES OF SINTERED ZrO_2/Si_3N_4 DOPED Ti6Al4V

O.A Ogunmefun[1], B.L Bayode[1] and P.A Olubambi[1]

[1]Centre for Nanoengineering and Tribocorrosion, School of Mining, Metallurgical and Chemical Engineering, University of Johannesburg, South Africa

Ti6Al4V matrix has improved in its specific strength, wear resistance, and elastic modulus over the decades and would continue to be the most used material in both biomedical and aerospace industries because of its superior mechanical properties achieved through appropriate microstructures for the targeted application[1,2]. Si_3N_4 ceramic is one of the few monolithic ceramic materials that can tolerate high thermal shock and temperature changes[3]; also Zirconia (ZrO_2), as reinforcement, enhances the fracture toughness of ceramics[1]. The matrices of Ti-alloy/ceramics are useful in aerospace engines because of their potential high temp strength[2].

In this study, the effect of sintering temperature on the refractory powders, Si_3N_4 and ZrO_2 (14 and 15) wt. % was investigated on Ti6Al4V alloy (Ti64) at different temperatures, viz 950 ºC (A), 1100 ºC (B), and 1200 ºC (C). The weighted and admixed powders were placed in the hybrid pulsed electric current sintering (PECS) furnace and were sintered in a vacuum environment through the 3-different temperature regimes. The externally applied pressure employed was 50 MPa, dwell time at 600 seconds, and sintering rate of 100 ºC/min. A field emission scanning electron microscope (JEOL JSM-7900F), equipped with energy dispersive X-ray spectroscopy (Aztec), was used for the microstructural analysis. The relative density, compact hardness, and fracture toughness of the composites were conducted.

Figure 1 (A1-C1) shows the backscattered electron (BSE) images and EDS micrographs showing various degrees of morphologies and intensity peaks of the samples of sintered composites of Ti6Al4V/$14ZrO_2/15Si_3N_4$ at stepped temperatures, (A_T); (B_T); and (C_T). A clear display of two distinct phases comprising both the αTi and βTi phases are pertinent for all the specimens. The stability of these dual phases is believed to be due to the presence of Al and V respectively, as substantiated by the EDS peaks above. The BSE images shows phase contrast info of the composites, with the brightly colored region (white patches) of the microstructure depicting phases dominated by elements with higher atomic number, ZrO_2, while a relatively dark colored region depicting phases with lower atomic numbers, Si_3N_4, both dispersed in the matrix of Ti6Al4V, the greyish region in the microstructure.

Figure 1(C1) is a uniform matrix dispersion of the reinforcement particles at an elevated temperature of 1200 ºC with homogeneous composite, free of porosity or cracks, as also reported by Babapoor, et al.[4], in similar experimentation. However, the reinforcement particles appear coarse in specimens (A1) and (B1) with porous microstucture[4] as revealed by BSE images. As the temperature increased through (B_T) and (C_T), a better consolidation of powders were achieved; the porosity variance also improved same. The relative density, fracture toughness and the vicker's microhardness tests values of the sintered composites were seen to increase with an increasing sintering temperature (A_T); (B_T) and (C_T) at 92.12, 97.51, and 99.61%, relative density ; 0.2294, 0.2187, and 0.4237 $MPam^{0.5}$, fracture toughness; and 491.3, 768.59, and 1161.4 HV, microhardness confirming specimen (C1) at 1200 ºC to have the highest mechanical test values. This remarkable enhancement in mechanical property can be attributed to a decreased porosity, homogenization of the microstructure, and increase in relative density[3,4] experienced more in specimen (C1). The results also confirmed the effectiveness of PECS technique for the densification of Ti6Al4V/$14ZrO_2/15Si_3N_4$ at 1200 ºC.

References:
1. Semetse, L., *et al.* (2020). Proc. Materials Today. 28, 468
2. Bowen, P. and Carry, C. (2002) Powder Technology. 128. 248.
3. Jeje SO. *et al.* (2019) InIOP Conference Series: 1, 012018.
4. Babapoor, A. *et al.* (2018) Ceramics Intl., 44(12), 14541.

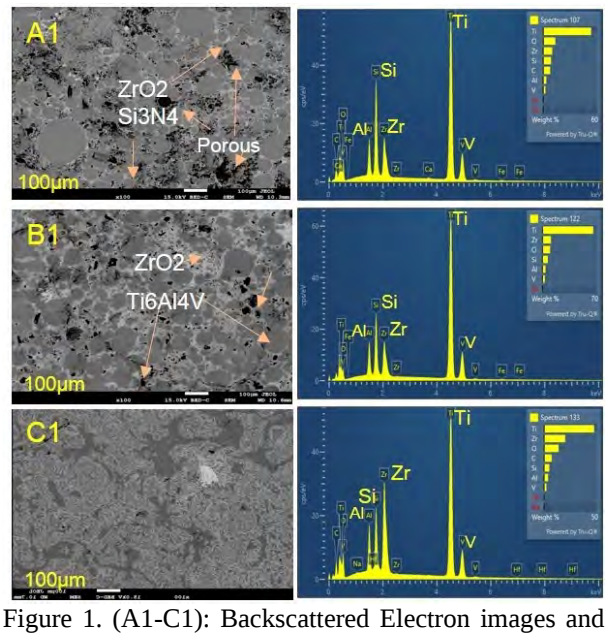

Figure 1. (A1-C1): Backscattered Electron images and EDS spectra of sintered composites at temperatures (A_T) 950 ºC; (B_T) 1100 ºC; and (C_T) 1200 ºC

Corresponding author:
ogunmefunolakunleanthony@yahoo.com

WEAR BEHAVIOUR OF SPARK PLASMA SINTERED TiAl ALLOY

M.R. Mphahlele[1,2], P.A. Olubambi[2] and E. Olevsky[3]

[1]Department of Mechanical Engineering, Durban University of Technology, South Africa, [2]Department of Engineering Metallurgy, University of Johannesburg, South Africa, [3]College of Engineering, San Diego State University, CA, United States

$Ti_{48}Al_{48}Cr_2Nb_2$ alloy possesses superior properties such as lightweight, high strength, and considerable corrosion resistance. However, the widespread use of this TiAl alloy has been restricted by its insufficient surface hardness and wear resistance. Consequently, the alloy is seldom used in wear-intensive applications[1]. Several studies have since been focused on improving their wear resistance through various methods, including surface modification, lubrication, reinforcements, manipulation of process conditions, and utilization of advanced manufacturing techniques[2]. Processing technique such as spark plasma sintering (SPS) has been shown to improve materials' mechanical and wear properties by restricting grain growth due to being a relatively fast process compared to hot pressing[3]. In this work, the SPSed $Ti_{48}Al_{48}Cr_2Nb_2$ alloy was characterized for wear properties.

The dry sliding wear tests were carried out on spark plasma sintered $Ti_{48}Al_{48}Cr_2Nb_2$ alloy, using an Anton Paar ball-on-disk tribometer (TRB[3]). All tests were conducted to cover a distance of 600m using a load of 10N. Before and after test weights were taken using a weighing balance to determine the wear volumes and wear rate of the materials according to the following equations[4]: $V=\Delta w/\rho$, where V is the volume of material loss, Δw is the weight before test-weight after test and ρ is the density of the material.

The scanning electron (SE) backscatter micrograph (Figure 1) shows the microstructure features of the TiAl alloy sintered at 1175 ℃ at a heating rate of 100 ℃/min for 7.5 minutes. The sintered sample displayed a duplex- structure with lamellar colonies and equiaxed grain sizes typically in the range of 5 µm – 30 µm. The duplex structure is associated with good ductility and strength, but creep properties are compromised[5]. Figure 2 presents an SE image of a wear track for the SPSed TiAl alloy. A lower magnification scale was selected to reveal the wear width profiles of the sintered samples. The wear tracks in the TiAl alloy showed a width of 893µm and indicate the presence of a third body that steadily overtakes the counter ball and the sample surface. TiAl alloy exhibited shallow grooves and a circumscribed wear track, proving that the alloy is sufficiently resistant to deformation. The resistance is plausibly due to the good hardness demonstrated by the TiAl and the favourable duplex microstructure thus, resulting in low material volume loss as presented in Table 1. The good wear resistance validates the potential of TiAl alloys for wear applications.

The authors appreciate nGAP for financial support.

References:

1. Wang, L. et al. (2020) Compos. Part B: Eng. 198, 108223.198, 108223.
2. Li, X. et al(2018) Mat. Research Express. 5(8), 086502.5(8), 086502.
3. Miriyev, A. et al. (2016) J. of Alloys and Compounds 678, 329-336.678, 329-336.
4. Wen, S. and P. Huang (2012) Principles of Tribology. United States, Wiley Online Library.
5. Lamirand, M. et al. (2006). Metall. Mater. Trans. A 37(8), 2369-2378.37(8), 2369-2378.

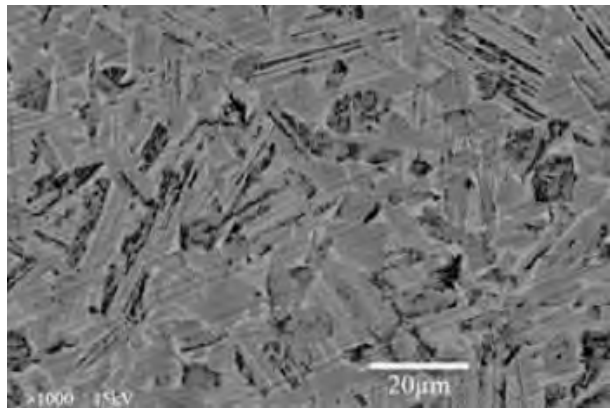

Figure 1. SEM-Back Scattered image of TiAl alloy.

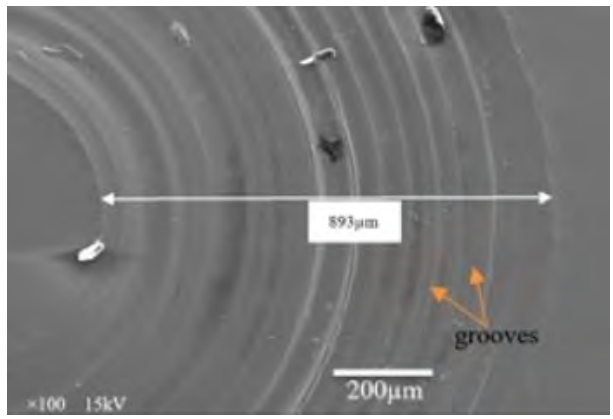

Figure 2. SEM image of wear track on TiAl alloy

Table 1. Hardness and volumetric wear loss of TiAl alloy.

Hardness (GPa)	Material Volume Loss (g/cm3)
3.446±0.0924	0.00336±3.1E-4

Corresponding author: ramimphahlele@gmail.com

DEVELOPMENT OF BETA TYPE TITANIUNM BASED ALLOYS FOR DENTAL APPLICATIONS

K Dyal Ukabhai[1,2], I.A Mwamba[3,2] and L.A Cornish[1,2]

[1]School of Chemical and Metallurgical Engineering, University of the Witwatersrand, Johannesburg, , [2]DSI-NRF Centre of Excellence in Strong Materials, hosted by the University of the Witwatersrand, Johannesburg, [3]Advanced Materials Division, Mintek, Randburg

Biomedical materials are often used in various parts of the human body to improve the lives of many people. Ageing populations increase demands for biomedical materials with long life-spans that do not require revision surgery. The main reason for dental implant failure is peri-implantitis[1], which is caused by bacteria, and leads to failure. Typical materials used are 316L stainless steel, Co-Cr alloys and Ti-alloys[2]. Biomedical materials need to have high corrosion and wear resistance, be highly biocompatible and have a comparable elastic modulus to bone. For these reasons, Ti-alloys have gained more usage recently, due to their high specific strength, excellent corrosion resistance, low elastic modulus, inertness to the body environment, and superior biocompatibility. The β-type alloys are currently being developed the most, due to their low elastic moduli, and high strength for load-bearing uses[3]. Thus, it would be advantageous to develop a β-type Ti-based alloy, without toxic elements (e.g. Al and V)[3] and additions of copper for antimicrobial properties[4] and ruthenium to improve the corrosion resistance[5].

Three compositions: Ti-15Mo-0.1Ru-5Cu, Ti-15Ta-0.1Ru-5Cu and Ti-15Mo-10Ta-0.1Ru-5Cu (wt%) were identified as being mainly β at room temperature using the TTTI3 database and Thermo-Calc. The alloys were made by cold compacting 99.9% pure elemental powders and melting them in a button arc furnace. The samples were then cut, mounted, ground and polished. They were etched using Kroll's reagent and investigated using back scattered electron in a ZEISS Sigma 300 VP scanning electron microscope (SEM). Compositional analysis was done with energy dispersive X-ray spectroscopy (EDS) using an Oxford instruments x-act Penta FET precision detector. X-ray diffraction (XRD) on a Bruker D2 phaser was used to confirm phases. Hardness tests were done on a FM-700 micro hardness tester using 300g force and a dwell time of 10s.

XRD gave Ti_2Cu peaks that were very small, which is consistent with the 5 wt% Cu compositions. Figs. 1 and 3 show mainly (βTi) and Ti_2Cu, and Fig. 2 shows (αTi) and Ti_2Cu. The Ti_2Cu phase (needed for the antimicrobial properties) was found between the needles (Fig. 2) and was the dark phase in Figs. 1 and 3. The hardnesses of the three alloys were 336 ± 9.5, 375 ± 7.8 and 388 ± 12 HV respectively, the hardest was Alloy 3. Alloys 1 and 3 (Figs. 1 and 3) can be considered metastable β-type Ti-alloys, which is close to the targeted β type alloy. Therefore, it is suitable for further testing for potential use as a dental alloy. Alloy 2 (Fig. 2) was not suitable as it had no (βTi).

References:
1. Persson, G.R. and Renvert, S. (2014) Clin. Imp. Dent. Relat. Res. 16(6), 783.
2. Zhang, Y.S. et al. (2017) Mater. Sci. Eng. 696, 360.
3. Zhang, L.C. and Chen, L.Y. (2019) Adv. Eng. Mat. 21, 1801215.
4. Liu, R. et al. (2016) Sci. Rep 6, 29985.
5. Biesiekierski, A. et al. (2014) Mater. Design 59, 303.

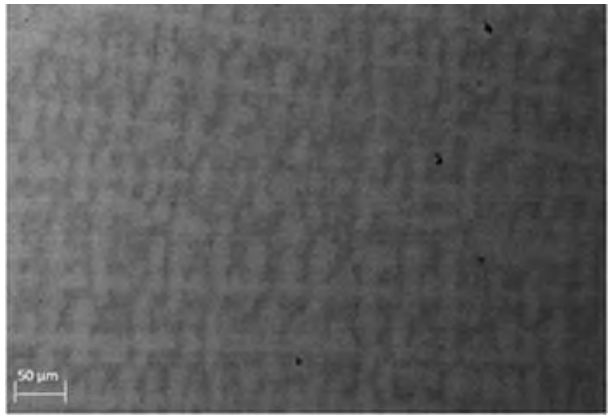

Figure 1. SEM-BSE image of Ti-15Mo-0.1Ru-5Cu (wt %) (Alloy 1) showing Ti_2Cu (dark) and (βTi) (light).

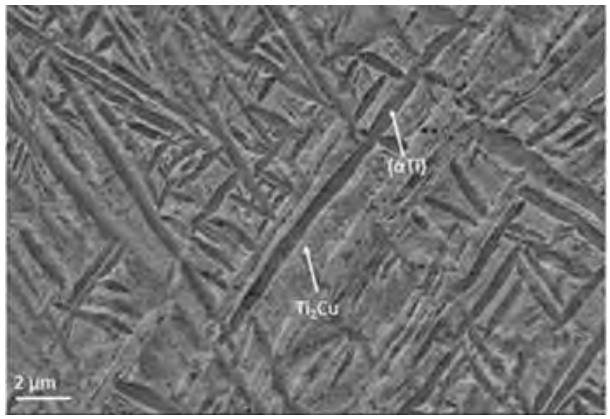

Figure 2. SEM-BSE image of Ti-15Ta-0.1Ru-5Cu (wt %) (Alloy 2) showing Ti_2Cu (light contrast) and (αTi) (dark and medium).

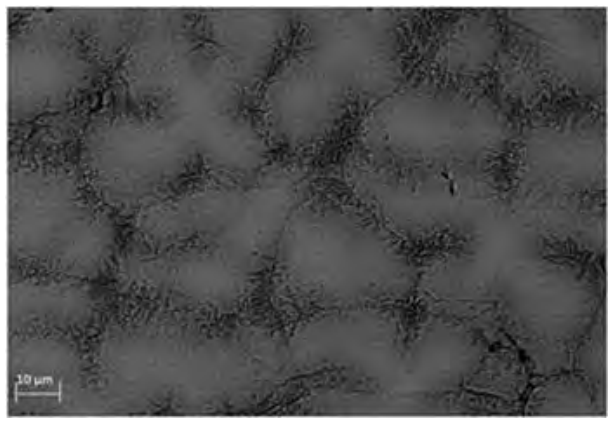

Figure 3. SEM-BSE image of Ti-15Mo-10Ta-0.1Ru-5Cu (wt%) (Alloy 3) showing (βTi) (light) and Ti_2Cu (dark).

Corresponding author: 669011@students.wits.ac.za

Ti_3Al EMBRITTLEMENT IN TEMPORARY HYDROGEN ALLOYED Ti-6Al-4V

V.N. Vilane[1,2], R.D. Knutsen[1] and J.E. Westraadt[2]

[1]Centre for Materials Engineering, Department of Mechanical Engineering, University of Cape Town, [2]Centre for High Resolution Transmission Electron Microscopy, Nelson Mandela University, Gqeberha

Temporary hydrogen alloying (THA) can refine cast Ti-6Al-4V microstructures and improve mechanical performance. However, THA does not automatically improve performance, it can also reduce the ductility to severe embrittlement[1] because of hydrogen promoted titanium aluminide (Ti_3Al) precipitation. The effect of oxygen on the promotion of Ti_3Al precipitation, and the effect of residual hydrogen on Ti-6Al-4V embrittlement is known. Less known is the effect of hydrogen on the promotion of Ti_3Al precipitation, particularly the effect of precipitated Ti_3Al on tensile ductility. This study discusses hydrogen promoted Ti_3Al formation and highlights its consequent effect on the tensile ductility of hydrogenated-dehydrogenated (HDH) Ti-6Al-4V.

Wrought Ti-6Al-4V was converted to simulated cast (Sim. Cast) Ti-6Al-4V by annealing at 1100 ºC for 2 hours. Sim. Cast tensile rods were hydrogenated to 20at. %H at 650 ºC, and subsequently dehydrogenated at 675 ºC (HDH 675) or 750 ºC (HDH 750). Similarly, control samples (HDH 675 control) were annealed at 650 ºC and vacuum annealed at 675 ºC. Inert gas fusion was used to evaluate oxygen and hydrogen concentrations. Tensile properties were evaluated at room temperature. EBSD and *EDS* were performed in the SEM (JEOL 7100) and TEM (JEOL 2100 LaB_6) respectively to determine phase content and composition. X-ray diffraction (XRD) using *Cu K*-alpha radiation confirmed constituent phases at a bulk scale.

In Fig.1, hydrogen treatment improved the yield strength in HDH 675 and HDH 750 samples by 100 MPa from 770 MPa (Sim. Cast) to 870 MPa (HDH treated). Fig.1. shows that a 75 ºC decrease in dehydrogenation temperature from 750 ºC to 675 ºC caused a 46±15 % loss in ductility. The strength increase and ductility loss is only observed in hydrogen treated samples. Inert gas fusion confirmed that the observed ductility loss is not caused by hydrogen or oxygen. The EDS maps in Figs.2b-c uncover detail on a V rich hydride lath and its surrounding region; where the uneven partitioning of aluminium (Al), to Al rich and Al lean regions can be observed. Selected area diffraction (SAD) from the Al-rich region, supports Ti_3Al precipitation in hydrogenated Ti-6Al-4V. Fig.3a shows that only HCP and BCC (beta) phases are present in HDH 675. In Figs.3a-b, dehydrogenating at 675 ºC removed hydrogen and consequently decomposed hydrides, but it retained the Al partitioning (in EDS-Al). The supporting SAD analysis (insert Fig.3b), confirms Ti_3Al precipitates in the Al rich regions of the HDH 675 sample. Complementary XRD analysis also confirmed Ti_3Al in HDH 675 and the absence thereof in HDH 750. The Ti_3Al in Al rich regions and the preferred crack propagation along these regions explains the 46±15% ductility loss in HDH 675. During hydrogenation, alpha (α) transforms to hydrogen saturated beta (β_H),[2] Al is rejected from the β_H and concentrates in adjacent regions, ultimately stabilizing Ti_3Al.[2] Cooling past the hydride region promotes a β_H to V rich hydride transformation. Fig.3b shows that dehydrogenating at 675 ºC retained Al enrichment, therefore 675 ºC does not promote sufficient Al diffusion to dissolve Ti_3Al when compared to 750 ºC.

References:
1. Vilane, V.N., Knutsen, R.D. and Westraadt, J.E. (2022) Mater. Char. 184, 111698.
2. Sun, P., *et al*. (2015) Acta. Mater. 84, 29.

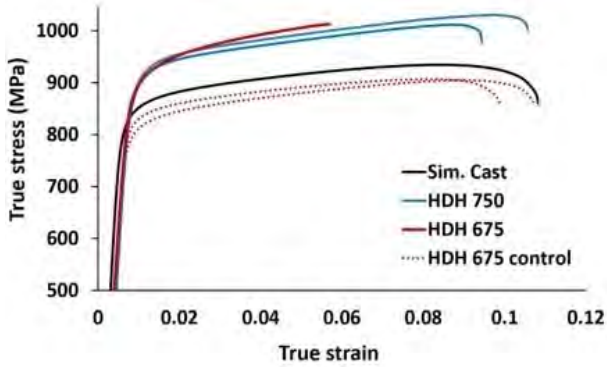

Figure 1. Tensile ductility of Sim. Cast, HDH treated (675, 750) and HDH 675 control samples.

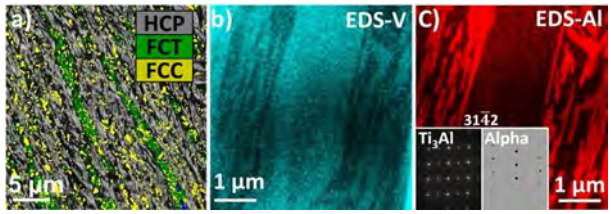

Figure 2. Hydrogenated Ti-6Al-4V a) EBSD showing alpha (grey) FCC (yellow) and FCT (green) hydrides. In b-c), EDS shows V, Al partitioning across a hydride lath. The absence of superlattice reflections on the simulated [31-42] alpha SAED (grey) confirms Ti_3Al in the Al-rich region.

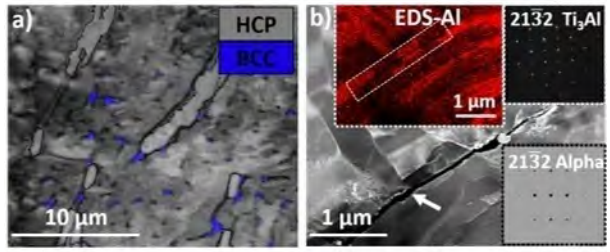

Figure 3. HDH 675 Ti-6Al-4V a) EBSD showing alpha (grey) beta (blue) phases. In b), HAADF STEM/ EDS-Al maps show crack propagation (arrow) along Al-rich (red) regions. Insert b), the absence superlattice reflections on the simulated [21-32] alpha SAED (grey) confirms Ti_3Al precipitates in HDH 675.

Corresponding author: velile.vilane@mandela.ac.za

SPINODAL DECOMPOSITION OF Ti-6Al-4V-xH MARTENSITE

V.N. Vilane[1], R.D. Knutsen[2] and J.E. Westraadt[1]

[1]CHRTEM, Nelson Mandela University, Gqeberha, [2]Centre for Materials Engineering, University of Cape Town

Thermo-hydrogen processing (THP), which is principally performed to refine and strengthen the microstructure of Ti-6Al-4V, can be executed via a number of different process pathways[1]. These include the single step hydrogenation-dehydrogenation treatment, decomposition of hydrogen saturated beta phase during slow cooling (eutectoid transformation), and isothermal ageing of hydrogenated martensite. Critical to all these processes is the complete removal of hydrogen after grain refinement has been achieved to avoid embrittlement. Unfortunately, embrittlement can also be caused by the precipitation of Ti_3Al (α_2) that can evolve due to localized Al enrichment associated with the presence of hydrogen during THP[2]. Although α_2 is reported to occur in Ti-6Al-4V after very long-term ageing between 500-600ºC, the mechanisms for accelerated formation during THP are not well understood. Our study examines the events leading to α_2 formation during hydrogenation and subsequent martensite ageing using a combination of XRD and analytical TEM.

Ti-6Al-4V rods were hydrogenated in Ar/15%H_2 atmosphere at 650ºC for 12 hours to dissolve 20-25at% hydrogen. The partial martensite-retained beta microstructure was formed after quenching from the solution treatment above the modified beta-transus, and subsequently reheated to 580ºC for 3 hours to decompose (age) the martensite. The final step involved dehydrogenation at 675ºC for 3 hours. XRD was performed in a Bruker D8 diffractometer (Co-Kα radiation) to obtain bulk microstructure information which was correlated with phase identification using SEM-based EBSD, TKD and EDS analysis (JEOL7100F). Electron transparent foils were extracted from selected martensite locations using an FEI Helios FIB-SEM and high angle annular dark field (HAADF) imaging was performed in STEM mode in the Cs corrected JEOL-ARM200F. The crystal structure was identified by comparing the d-spacings in selected area diffraction (SAD) patterns or fast Fourier transforms (FFT) to a referenced standard which was modelled in the Java Electron Microscopy Software (JEMS).

Localised Al enrichment was identified after ageing at 580ºC in the form of compositional nano-banding in martensite (Fig. 1). The local Al enrichment is indicated at over 16at% whereas the Al level in homogeneous martensite should be 7-8at%. There is a corresponding decrease in V level associated with Al enrichment and vice versa suggesting partitioning of Al and V in opposite directions. In addition, advanced ordering has been identified within the Al-rich bands that is consistent with the formation of α_2. In the case when hydrogen is absent, martensite decomposition in Ti-6Al-4V occurs by classical nucleation and growth to form α+β with expected Al/V partitioning[3]. Furthermore, α_2 is only expected to occur after several days ageing at 500-600ºC. Consequently, the composition fluctuations in Fig.1 prompt the consideration of spinodal decomposition. Previously, spinodal decomposition has been proposed during ageing of martensite in Ti-Mo alloys where Mo causes formation of orthorhombic martensite (α″)[4]. The α″ martensite is intermediate between α-phase and hcp martensite and this instability gives rise to uphill diffusion during ageing. Since the fraction of α″ is known to increase with hydrogen level in Ti-6Al-4V-xH and is confirmed in our XRD results, it is reasonable to account for the occurrence of composition fluctuations (nano-banding) during ageing at 580ºC by a similar spinodal decomposition mechanism. The resulting enhanced Al partitioning promotes accelerated α_2 formation which is retained after dehydrogenation at 675ºC

References:
1. Froes, F.H., Senkov, O.N. and Qazi, J.I. (2003) Int. Symp. Proc. & Fabrication Adv. Materials XI, 295.
2. Vilane, V.N., Knutsen, R.D. and Westraadt, J.E. (2022) Mater. Charac., 184, 111698.
3. Gil Mur, F.X., Rodriguez, D. and Planell, J.A. (1996) J. Alloys Compds. 234, 287.
4. Davis, R., Flower, H.M. and West, D.R.F. (1979) Acta Metall. 27, 1041.

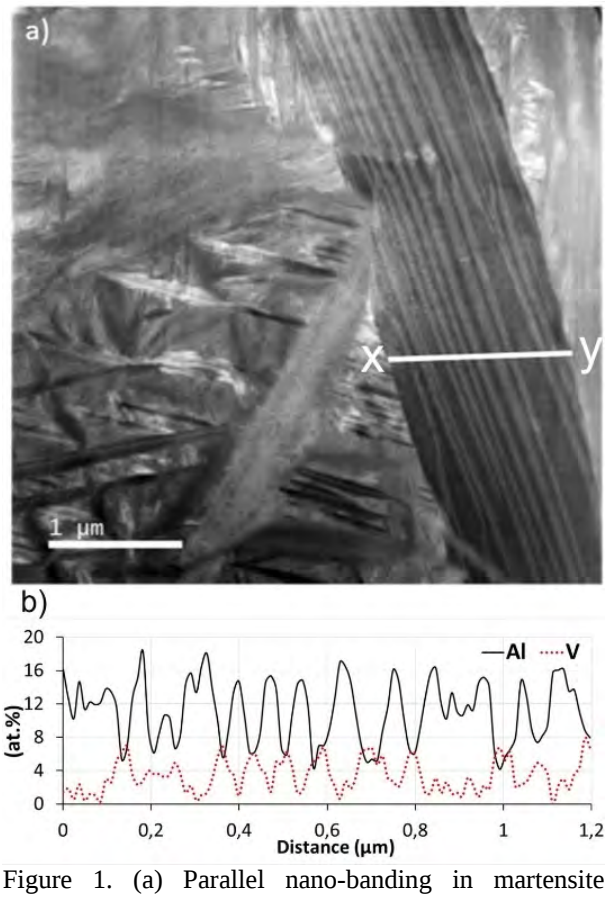

Figure 1. (a) Parallel nano-banding in martensite (HAADF-STEM image at 200kV), (b) shows Al and V levels across X-Y in (a) measured by EDS.

Corresponding author: Robert.Knutsen@uct.ac.za

DISLOCATION DENSITY MEASUREMENT IN FATIGUE TESTED AISI316 USING X-RAY DIFFRACTION

D Ramasimong[1], J Westraadt[2] and R Knutsen[1]

[1]EPPEI Specialisation Centre in Materials and Mechanics, University of Cape Town, , [2]Dept. Centre for High Resolution TEM, Nelson Mandela University

The evaluation of material deformation post cycling loading is often performed using microscopic techniques such as transmission electron microscopy (TEM) and electron backscattered diffraction (EBSD). However, each of these techniques have their own limitations.1,2 TEM is subject to large scatter due to the small areas (25 μm^2) that are typically investigated and preparation is often time consuming. X-ray diffraction (XRD) 3 is a bulk on-destructive technique that can characterise the crystallographic structure of materials over larger areas (~ 1 cm^2), requires less data processing and the data acquisition can be automated for a batch of samples. During cyclic loading, dislocations are formed. The evolution of dislocation density in steels is an important aspect of the mechanical response. It could potentially be used as a fingerprint to relate the material state to the life-consumption fraction in materials subject to fatigue conditions. In this study, a quantitative analysis of varying deformation states in austenitic stainless-steel specimens is evaluated using XRD against conventional and known qualitative destructive techniques, i.e. EBSD and TEM. Annealed AISI 316 samples subjected to various room-temperature tensile fatigue cycling (annealed, 500k, 1M, 3M and 11M cycles respectively) with a peak stress of approximately 320 MPa. An as-received material state was also added in the analysis and jointly characterised using EBSD and TEM for a qualitative comparison to the more representative XRD method. The broadening of XRD peaks can be attributed to the contributions of the a) diffractometer and b) material state of the sample. The contributions of the instrument are typically determined by characterising a standard sample with a known material state. LaB6 is a NIST standard, with a large crystallite size and zero micro-strain, that is typically used to determine the instrumental peak profile contribution, by scanning the standard on the diffractometer and then performing peak-profile analysis. The various contributions to the XRD peak profile can only be separated by whole pattern analysis (Rietveld refinement) or by analysing several peaks of a pattern using the Williamson-Hall (W-H) method. The results indicated that laboratory based XRD peak-profile analysis was successful in the quantification of micro-strain (dislocation density) and the crystallite size for specimens in the study. The accuracy and precision of extracted parameters such as the micro-strain as shown in Fig 1 vary in relation to material states and are sensitive to the data fitting methods, sample surface preparation, and the material state and must thus be interpreted with care. EBSD analysis of material samples showing the misorientation to mean modelled for of all material states is shown in Fig 2. The EBSD results mostly show good qualitative agreement with the XRD analysis. TEM analysis was used to qualitatively visualise the individual dislocations but is very time-consuming to perform quantitatively and the results are subject to large scatter. The study indicated that the technique used is viable to determine dislocation density. However, care must be taken to standardise the sample preparation, instrument calibration, and data processing pipeline for reliable measurements.

References:
1. Morito, S., Nishikawa, J., Maki, T. (2003) ISIJ International 43(A), 1475.
2. Gussev, M. N., Leonard, K. J. (2019) Journal of Nuclear Materials 517, 45.
3. Ungar, T. (2001) Materials Science and Engineering A(309), 14.

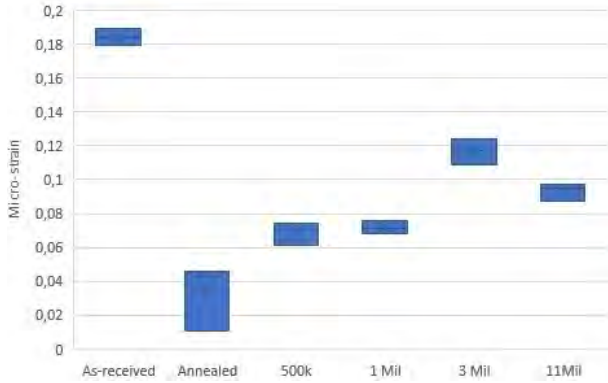

Figure 1. Microstrain measurements for material states.

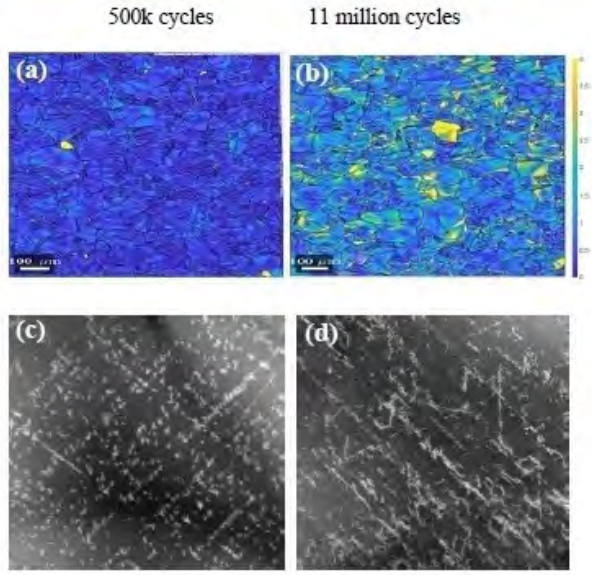

Figure 2. EBSD images of (a) 500k and (b) 11M and ADF-STEM images of (c) 500k and (d) 11M samples.

Corresponding author: ramasid@eskom.co.za

EFFECT OF SINTERING TEMPERATURE ON THE MICROSTRUCTURE AND HARDNESS OF LOW-DENSITY STEELS

J.K. Thobejane[1], T. langa[2], J.W. Van der Merwe[1,3], D.E.P Klenam[1] and M.O. Bodunrin[1,3]

[1]School of Chemical and Metallurgical Engineering, University of the Witwatersrand, [2]Department of Metallurgy, University of Johannesburg, [3]DSI-NRF CoE in Strong Materials, University of the Witwatersrand

Modern engineering materials being used for structural and automotive applications must meet the requirements of lightweight, high strength and low-cost. These requirements are due to stringent policies aimed at reducing carbon footprint in the environment[1, 2]. Low-density steels (LDS) meet these requirements. These alloys have been investigated as potential replacements for conventional steel and cast iron in the automotive industry[1]. In developing LDS, Al is an important alloying element. Thus, every 1 wt% Al results in ~1.3 wt% weight reduction in steel[2]. Up to 12 wt% Al have been added to Fe and other alloying elements, mainly Mn and C, to make different grades of low-density steels[1]. However, excessive addition of Al formed brittle phases like *k*-carbide precipitates or FeAl-type B2 at the grain boundaries of the matrix. These carbides cause abrupt loss of ductility[1, 2]. To suppress the formation of intergranular *k*-carbides, high Mn content and up to 5wt % Cr are added[2].

LDS are commonly produced using commercial vacuum induction melting technique[1-3], but effort to produce these alloys locally using laboratory vacuum arc furnace or vacuum induction furnace have resulted in loss of Al due to evaporation. To avoid significant loss of Al due to casting, spark plasma sintering technique (HHPD 5 FCT system) was explored in developing four austenitic LDS: Fe-20Mn-12Al-1.5C, Fe-30Mn-12Al-1.5C, Fe-20Mn-12Al-1.5C-5Cr and Fe-30Mn-12Al-1.5C-5Cr. This approach has been rarely employed in producing LDS. The effect of different sintering temperatures (1000 and 1100°C) on the microstructure and hardness of the sintered LDS were evaluated. Sintering pressure was kept constant at 50 MPa and the soaking time was 5 minutes. Microstructural examination was performed using an Olympus GX14 optical microscope (OM) and ZEISS E-Sigma field emission scanning electron microscope operated in back scattered electron mode (SEM-BSE). Hardness measurements were taken using FM700 Future Tech Vickers microhardness tester.

Sintering of Fe-20Mn-12Al-1.5C at 1100°C resulted in large austenite (γ-Fe) grains, while a fine microstructure was obtained when sintering was performed at 1000°C for the same alloy (Fig. 1). This trend is consistent in the remaining alloys. The SEM-BSE presented in Fig. 2 show that the alloys consisted of the following phases: the light region which is the γ-Fe phase, the black region which is the Al_2O_3 phase, and the dark grey region which represent the *k*-carbide carbides[3]. Phase compositions were determined using energy dispersive x-ray spectroscopy. Hardness measurements were taken in the γ-Fe region and in the vicinity of the carbide region. As indicated in Fig. 3, the hardness values of the carbide region were generally higher than that of the γ-Fe region. The error bars indicate that there is no significant influence of sintering temperature on the hardness of the phase constituents of the sintered low-density steels. The average hardness values (350 - 500 Hv) of these sintered low-density steels are similar to the hardness values reported by previous authors[3] on cast or sintered low-density steels.

References:
1. Chen, S., Rana, R., Haldar, A., and Ray, R. (2017) Prog. in Mater. Sci. 89(2), 151.
2. Moon, J., Ha, H.Y., Kim, K.W. et al., (2020) Sci. Rep. 10, 12140.
3. Liu, J., Chen, W., Jiang, Z., Liu L., and Fu, W. (2017). Vacuum 137(4), 136.

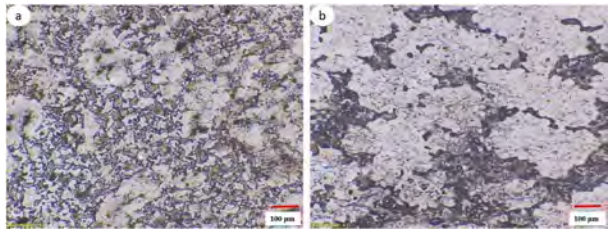

Figure 1. OM image showing the microstructure of Fe-20Mn-12Al-1.5C sintered at (a) 1000°C and (b) 1100°C

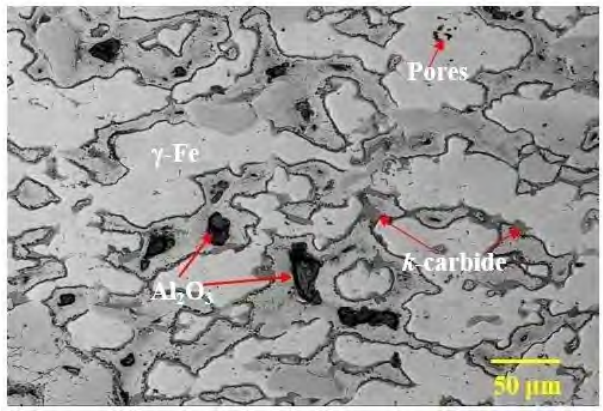

Figure 2. SEM-BSE image of Fe-30Mn-12Al-1.5C LDS sintered at 1000°C.

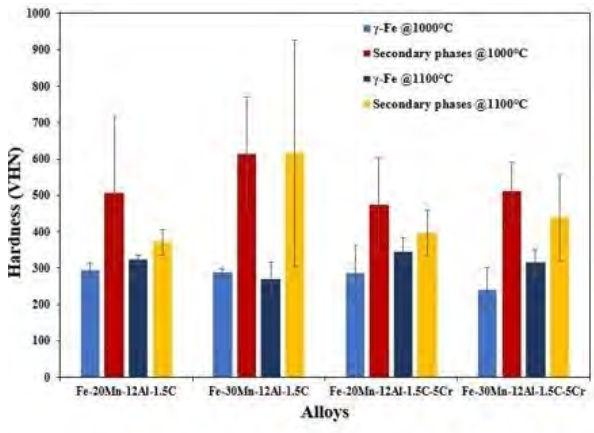

Figure 3. Hardness of sintered LDS.

Corresponding author: michael.bodunrin@wits.ac.za

FORMATION OF MODIFIED Z-PHASE IN A 12Cr1MoV TMF STEEL DURING LONG-TERM CREEP

W.E. Goosen[1] and J.E. Westraadt[1]

[1]Centre for High-Resolution TEM, Nelson Mandela University, Gqeberha, South Africa.

Tempered martensite ferritic (TMF) steels with 9-12% Cr are creep-resistant steels that are used for steam pipes, turbines and boilers in fossil fired steam power plants. Several older power stations at Eskom use grade X20 (12Cr1MoV) steels for high-pressure steam piping. Metal carbides ($M_{23}C_6$) and metal carbonitrides (MX) act as pinning agents, impeding free-dislocation movement and suppressing the movement of grain boundaries during creep[1]. Coarsening of $M_{23}C_6$ and formation of Laves phase as well as the dissolution of MX decreases the pinning forces exerted by the particles and ultimately resulting in a creep-strength breakdown. Microstructural investigations performed on TMF steels have shown that this creep-strength breakdown in 11-12% Cr TMF steels is associated with the transformation of fine MX into larger modified Z-phase (CrVN) particles [2, 3].

The microstructural evolution of 12Cr1MoV TMF steel samples has been the subject of several investigations[4], but modified Z-phase was not observed in any of the samples and the MX precipitate population was found to be stable up to 139 kh. The present study reports on the evolution of modified Z-phase in a 12Cr1MoV TMF steel exposed to long-term interrupted creep-testing and the development of quantitative characterisation techniques for investigating this important transformation.

Four identical samples were tested at 550°C with an applied stress of 120 MPa. Three interrupted experiments were tested to various creep-strain values, and one sample was taken to rupture after 139 kh. Extraction replicas and thin-foils were prepared from the gauge[5] and thread sections and quantitatively investigated using scanning transmission electron microscopy (STEM) combined with energy dispersive X-ray spectroscopy (EDX) and electron energy loss spectroscopy (EELS) on a JEOL2100 (LaB_6) TEM fitted with an Oxford X-Max (80 mm^2) X-ray spectrometer and a Gatan Quantum GIF electron energy loss spectrometer. EFTEM elemental map colour overlays (10 per material state) were segmented using standard image analysis and quantitative measurements of the phase fraction (f_v), precipitate size (d_m), number density (N_v) and average spacing (λ) were performed.

Fig. 1 shows the EFTEM elemental map for the starting material and the gauge section of the sample creep-tested to failure (139 kh). Clear evidence for the formation of modified Z-phase (orange particles) was visible which was confirmed using selected area electron diffraction. Fig. 2 shows that the formation of modified Z-phase was accompanied by a decrease in the phase fraction of MX precipitates.

In this study, the phase fraction of modified Z-phase in the highly deformed fracture region was significantly higher (f_v: 0.40 ± 0.02%) compared to the uniformly elongated zone (f_v: 0.23 ± 0.20%) for the sample tested to rupture. This suggests that localized creep-strain and increased stress due to necking promoted the formation of modified Z-phase.

The quantitative results of this study can be used as a benchmark for 12Cr1MoV grade steels when service exposed components are evaluated. Furthermore, the quantitative microstructural characterisation techniques demonstrated in this study can be applied to quantitatively characterise the finest microstructural features (MX) which are considered critical to the creep-strength of 9-12% TMF steel grades.

References:
1. Kostka, A. *et al.* (2007) Acta Mat. 55(2), 539.
2. Danielsen, H.K. and Hald, J. (2006) Energy Mater. 1(1), 49.
3. Sawada, K., Kushima, H. and Kimura, K. (2006) ISIJ Intern. 46(5), 769.
4. Aghajani, A., Somsen, C. and Eggeler, G. (2009) Acta Mater. 57(17), 5093.
5. Wang, H. *et al.* (2021) Mat. Char. 181, 111396.

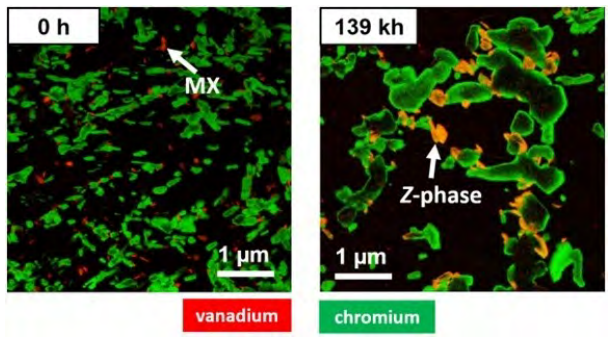

Figure 1. EFTEM elemental maps shown as a colour overlay for the starting material (0 h) and the uniformly elongated gauge section of the sample creep-tested to failure (139kh) collected from extraction replicas.

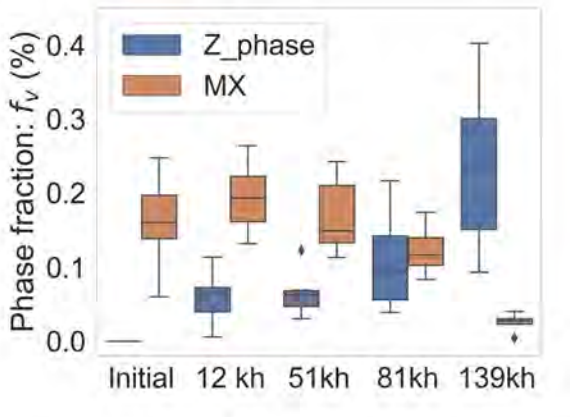

Figure 2. Phase fraction of MX and modified Z-phase precipitates in the gauge sections as a function of creep-testing time for data collected from the thin-foils.

Corresponding author: William.Goosen@mandela.ac.za

DISLOCATION DENSITY MEASUREMENT IN AISI316L STAINLESS STEEL USING ELECTRON CHANNELING CONTRAST IMAGING (ECCI)

L.C. Pullen[1], J.E. Westraadt[1], D. Ramasimong[2] and R.D. Knutsen[2]

[1]Centre for HRTEM, Department of Physics, Nelson Mandela University, [2]Centre for Materials Engineering, University of Cape Town

Dislocations influence the mechanical properties of materials, such as its strength and ductility, and they play a vital role in the plastic deformation of crystalline materials[1]. The dislocation density of a material can be determined using either direct imaging or via indirect techniques. Imaging techniques include conventional transmission electron microscopy (CTEM), annular dark field (ADF) scanning transmission electron microscopy (STEM), and electron channeling contrast imaging (ECCI)[1]. X-Ray diffraction line profile analysis[2], electron backscatter diffraction (EBSD) misorientation analysis, and hardness measurements can be used to indirectly determine the dislocation density of a material[3].

ECCI makes use of the fact that the backscattered electron (BSE) yield is strongly dependent on the orientation of the crystal lattice planes with respect to the incident electron beam, due to channeling. Slight local distortions in the crystal lattice due to dislocations cause a modulation in the BSE intensity, allowing the dislocation to be imaged. The aim of this study is to quantitatively compare ECCI and ADF-STEM imaging characterisation techniques for determining dislocation density in AISI 316L steel samples.

AISI316L rod samples were subjected to cold drawing, followed by annealing and then to a room-temperature cyclic tensile fatigue test (11M cycles) with a peak stress of approximately 350 MPa. The ECCI was performed on the electropolished surface, using a BSE detector at a working distance of 4 mm with a 20 keV electron beam. The ADF-STEM imaging used a 20 mRad incident STEM-probe convergence semi-angle with an annular dark field (ADF) detector. The camera length was chosen such that the signal over a collection angle range of 18 mRad (inner) and 47 mRad (outer) was captured. The samples were imaged at 10 locations and then segmented using image analysis to locate the dislocations in the image. The average dislocation densities (ρ) were estimated using the line-intercept method in conjunction with the relationship: $\rho = 2N/Lt$, where N is the number of intersections, L is the total line length, and t is the probe depth in the ECCI analysis and the foil thickness in the STEM analysis, which was estimated to be 100 nm for both imaging techniques[1].

Fig. 1 shows the ECCI (a ; c) and ADF-STEM (b ; d) images of the fatigued-tested and cold drawn samples. The two imaging techniques gave similar image contrast, and the cold drawn sample had a significantly higher dislocation density as compared to the annealed (not shown) and fatigued-tested sample. This was supported by the quantitative dislocation density analysis (Fig. 2).

ECCI is a relatively straight-forward imaging technique that can be performed over large areas in the SEM on conventionally prepared samples. However, the dislocation contrast is dependent on the crystal orientation and uncertainties regarding the segmentation and probe-depth estimations can strongly influence the dislocation density measurements. Future studies will measure the thickness of the foil samples using convergent beam diffraction and use machine learning based segmentation image analysis techniques to better identify the dislocations in the images.

References:
1. Gutierrez-Urrutia, I., Raabe, D. (2011) Scripta Materialia 66, 343.
2. Pešička, J. *et al.* (2003) Acta Materialia 51, 4847.
3. Andrea, B. (2019) Automatic Characterization of dislocation Structures via Scanning Electron Microscopy. Masters' Thesis. Politecnico Di Torino.

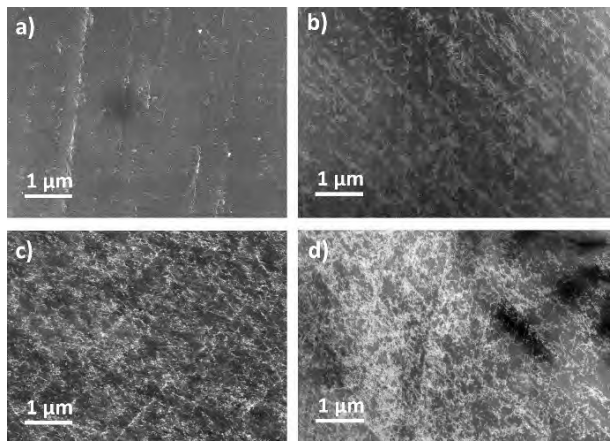

Figure 1. ECC images of a) 11M and c) cold drawn and ADF-STEM images of b) 11M and d) cold drawn 316L steel samples.

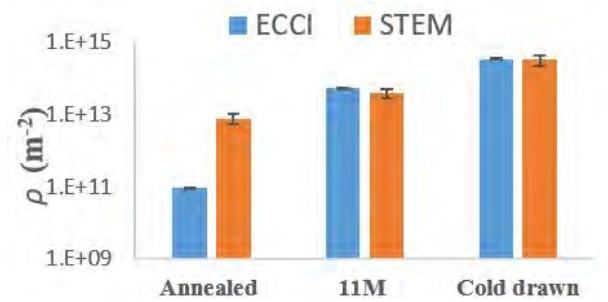

Figure 2. A comparison of the results of the average dislocation densities, as determined using both ECCI and ADF-STEM. Error bars indicate the standard error of the mean (n=10).

Corresponding author: s215323548@mandela.ac.za

STRUCTURAL CHARACTERIZATION OF AMORPHOUS AND CRYSTALLINE MOLYBDENUM PHOSPHIDE CATALYSTS FOR HYDROGEN EVOLUTION REACTION

S.S. Nkabinde[1,2] and N. Moloto[1]

[1]Molecular Science Institute, School of Chemistry, University of the Witwatersrand, Johannesburg, , [2]Centre for Catalysis, Department of Chemical Engineering, University of Cape Town, Cape Town

The current demand for energy across the globe has resulted in accelerated depletion of fossil fuels. This decline has sparked interest towards the discovery of renewable sources of energy. Hydrogen has been proposed as an alternative renewable energy carrier capable of meeting today's energy demand.[1] The challenge with using hydrogen as a fuel is that it does not occur freely in nature, it must be harvested from other compounds such as H_2O. Lately, the hydrogen evolution reaction (HER) has proven to be a promising method to produce hydrogen. HER ($2H^+ + 2e^- \rightarrow H_2$) involves the conversion of hydronium ions (H^+) in an acidic solution to molecular hydrogen (H_2) in the presence of an electrocatalyst.[2] An electrocatalyst plays an important role in HER as it allows for hydrogen to be produced using the least amount of energy. Hydrogen production technologies use expensive Pt catalysts that hinders large scale application. Herein, we report on cheap and abundant amorphous and crystalline molybdenum phosphide (MoP) for use as alternative electrocatalysts to Pt in the HER.[3]

Amorphous MoP (A-MoP) nanoparticles were synthesized using colloidal synthesis by heating a mixture of $MoCl_5$, 1-octadecene (solvent and reducing agent) and trioctylphosphine (phosphorus source) in a 3-necked flask at 340 ºC for 6 h. Subsequently, A-MoP nanoparticles were converted into crystalline MoP (C-MoP) by annealing at 800 ºC in N_2 for 2 h. The structural characteristics of the MoP nanoparticles were studied using HRTEM (JEOL JEM 2100, 200 kV). The HER performance of the nanoparticles was assessed using a conventional 3-electrode configuration in 0.5 M H_2SO_4.

Figure 1 (a) shows that A-MoP had a quasi-spherical morphology with an average size of 2.2 ± 0.32 nm. The HRTEM image (Figure 2(b)) of A-MoP showed no lattice fringes, confirming the amorphous nature of the nanoparticles. After annealing to form C-MoP (Figure 1(c)), the nanoparticles grew to an average size of 11.7± 1.76 nm. The increase in size was due to the fusion and growth of the already formed amorphous nanoparticles in response to a temperature increase. The HRTEM image (Figure 1(d)) of C-MoP showed lattice fringes of the (100) plane with interplanar spacing of 0.278 nm. XRD pattern of A-MoP displayed a broad reflection characteristic of amorphous material, whereas that of C-MoP was identified as the hexagonal phase of MoP (PDF 00-024-0771). Figure 2 shows the catalytic activity results for Pt/C, A-MoP, and C-MoP nanoparticles. As a benchmark, the HER activity of Pt/C displayed excellent activity, achieving current densities of 10 mA.cm^2 at low overpotential of 36 mV. To achieve 10 mA.cm^2, A-MoP and C-MoP required an overpotential of 235 and 317 mV, respectively. The low overpotential of A-MoP indicated that it was more active than its crystalline counterpart. The high activity was attributed to the small size of the nanoparticles and high density of unsaturated sites present in A-MoP. This study provided insight into a possible strategy for developing highly efficient HER catalysts

References:
1. Zou, X. and Zhang, Y. (2015) Chem. Soc. Rev. 44, 5148-5180.
2. Shiva, X. and Himabindu V. (2019) Mater. Sci. Technol. 2, 442-454.
3. Nkabinde, S., *et. al.* (2020) New J. Chem. 44, 14041-14049.

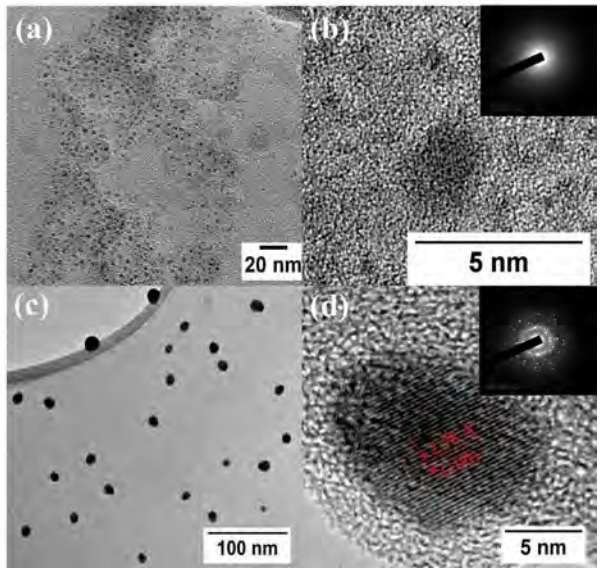

Figure 1. (a) TEM image of amorphous MoP, (b) HRTEM image of amorphous MoP, (c) TEM image of crystalline MoP and (d) HRTEM image of crystalline MoP.

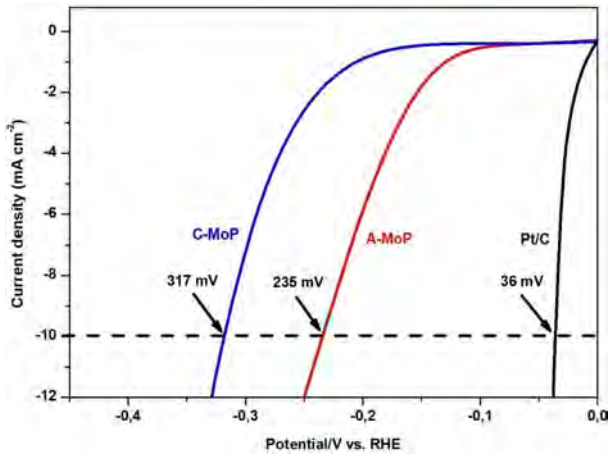

Figure 2. Linear sweep voltammograms of Pt/C, A-MoP and C-MoP electrocatalysts.

Corresponding author: siya.nkabinde@uct.ac.za

STRUCTURAL MODIFICATION OF ZSM-5 NANOSHEETS BY PHOSPHORUS-TREATMENT FOR C16 HYDROCRACKING REACTIONS

T Tahier[1] and P J Kooyman [1]

[1]University of Cape Town

Hydrocracking remains a significant technology used to produce middle distillates from Fischer-Tropsch waxes. The hydrocracking process involves breaking down of heavy hydrocarbons into lighter hydrocarbons in the presence of hydrogen. ZSM-5 has been extensively utilized for cracking of hydrocarbons, due to its uniform pore structure, strong acidity, and hydrothermal stability. On the other hand, the application of ZSM-5 is sometimes limited by diffusion limitations caused by micropores and acid sites that easily generate carbon deposition resulting in catalyst deactivation. In recent years, several studies have been performed to overcome these restrictions, including the synthesis of zeolite nanosheets and chemical modification of zeolites.[1,2]

Long diffusion pathways can be overcome by decreasing the thickness of the zeolite crystals, thereby reducing the diffusion path length and facilitating molecular diffusion.[2] This has been realized by the synthesis of zeolite nanosheets, through the introduction of mesopores in the microporous structure *via* templating strategies.[2] Post synthesis modification of ZSM-5 with phosphoric acid has been used to tune the physicochemical properties of the zeolite, by altering acid sites, improve hydrothermal stability and prevent dealumination, thus leading to enhanced catalytic activity in processes such as fluid catalytic cracking.[3,4] The ideal phosphorous-loading method used to increase the cracking activity and selectivity toward light olefins depend on the Si/Al ratio, phosphorous precursor, phosphatation conditions and calcination treatment.[3]

There is plenty of evidence in the literature concerning the promoting effect of phosphorus on the catalytic activity of ZSM-5. Although, the type of interactions between phosphorus and the zeolite framework and the effects of these interactions on the long-range order of the zeolite framework remain unclear. The present study investigates the structural modifications of the zeolite framework upon phosphorus-treatment using various analytical techniques. ZSM-5 nanosheets were modified with a P/Al ratio of 6 using H_3PO_4. XRD patterns (Figure 1) of the unmodified sample contained reflections characteristic of ZSM-5 nanosheets. There was a drastic decrease in crystallinity of the phosphorus modified sample, which is attributed to framework defects caused by dealumination. There was no change in the crystal structure of P-ZSM-5-NS since no other reflections were present.

TEM analysis of ZSM-5-NS and P-ZSM5-NS is shown in Figure 2 and Figure 3, respectively. The random arrangement of the nanosheet layers is clearly visible in the unmodified catalyst compared to P-ZSM-5_NS. The lattice striations and pore channel openings seen in ZSM-5-NS (Fig. 2) disappear in the treated zeolite, indicating decreased stability and validates the XRD results.

References:
1. Ji, Y., et al. (2017) J. Sol St. Chem. 251, 7.
2. Choi, M., et al. (2009) Nat. Lett. 461, 246.
3. Danisi, R. M., et al. (2018) Phys. Chem. Chem. Phys. 20, 27766.
4. Sang, Y. and Li, H. (2019) J. Sol. St. Chem. 271, 326.

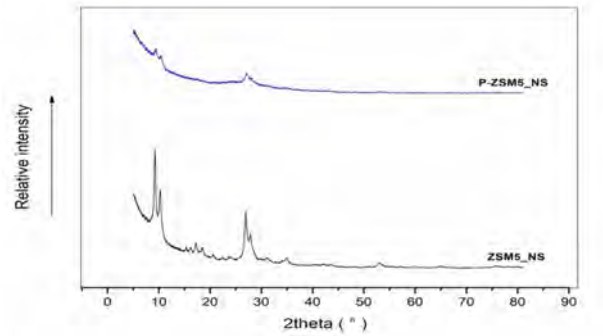

Figure 1. XRD patterns of parent and P-modified ZSM-5-NS catalysts.

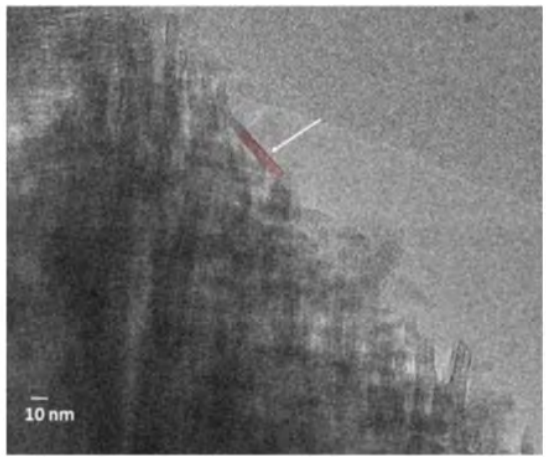

Figure 2. TEM image of parent ZSM-5-NS catalyst.

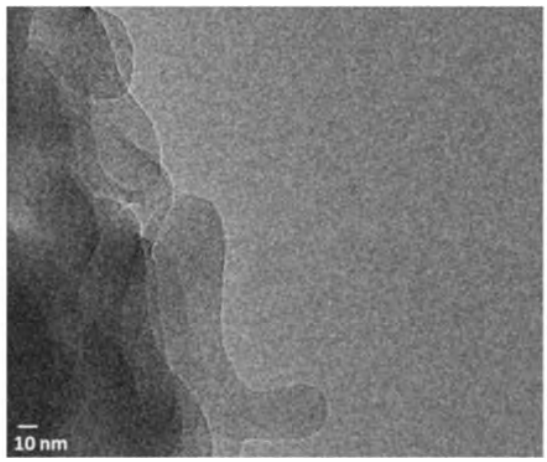

Figure 3. TEM image of phosphorus-modified ZSM-5-NS catalyst.

Corresponding author: tayyibah.tahier@uct.ac.za

SYNTHESIS OF NOVEL MICRO AND NANOSTRUCTURED MIXED-METALS OF WO_3 PHOTOCATALYSTS FOR THE REDUCTION OF CO_2

M Mgolombane[1], E.J. Olivier[2] and A.S. Ogunlaja[1]

[1]Department of Chemistry, Nelson Mandela University, Summerstrand, Gqeberha, South Africa, [2]Centre for HRTEM, Department of Physics, Nelson Mandela University, Summerstrand, Gqeberha, South Africa

The occurrence of global warming, a phenomenon of increasing average air temperature near the surface of the Earth over the past centuries, has been associated with increasing levels of greenhouse gas emissions (e.g., CO_2, CH_4, N_2O) into the atmosphere. CO_2 is a significant greenhouse gas accounting for three-fourths of global atmospheric emissions due to the rapid burning of fossil fuels such as oil, coal, natural gases, and deforestation.[1] Photo-driven reduction of CO_2 using solar energy is a promising solution to simultaneously address the environmental and energy impacts predicted from global warming. Semiconductors such as ZnO, Fe_3O_4 SnO_2, and TiO_2 have been widely used for the decomposition of different organic pollutants.[2] However, these materials are known to lose efficiency upon solar irradiation due to microstructural modifications occurring over time.[3] They also suffer from inherent limitations in the generated recombination rates of electron-hole pairs.

This study aims to address these drawbacks by engineering a heterostructure photocatalyst incorporating commonly used metals/metal-oxides with other supplementary supportive components. For this purpose, tungsten trioxide (WO_3), another promising photocatalyst was used as the main structural component. It is visible-light active with a bandgap of 2.7 e*V* with several advantages, including excellent light sensitivity oxidative stability, low cost, and environmentally friendly. This work incorporates Ag/Cu/MoS2 and Ag/Fe/MoS2 $_2$ and Ag/Fe/MoS_2 are incorporated into WO_3 supports, exhibiting a tube-like morphology. The WO_3 supports were synthesized using polystyrene as a structural template. Polystyrene pellets were dissolved in dimethylformamide and electro-spun into fibers. The produced fibers were then soaked in an ammonium meta-tungstate solution for up to three hours. The precursor solution was obtained by dissolving ammonium meta-tungstate into a mixture of deionized water and ethanol. After soaking, the fibers were rinsed with ethanol, dried, and calcined up to 500 ^oC. Subsequently, Ag/Cu/MoS_2 and Ag/Fe/MoS_2 were loaded onto the WO_3 supports using conventional impregnation techniques and calcined. The obtained yellow powders were characterized using FTIR, XRD, SEM, TEM, and UV-Vis.

Figure 1 shows an SEM image of a typically prepared pure WO_3 support, calcined at 500 ^oC exhibiting a hollowed centre. This is due to the disintegration of the fibers used during calcination as confirmed by FTIR analysis. Figure 2 shows a higher magnification image of the surface exhibiting a nanostructured morphology. An alignment of WO_3 particles along the tube length was observed. Overall, the inner and outer diameter of the WO_3 tubes were confirmed to depend on the diameter of the template fiber and the duration of adsorption of the W precursor solution onto the template. The extent of nano-structuring on the tube surfaces was found to depend on the calcination temperature used and the total duration of calcination, including that done as part of the impregnation process. Further findings will be presented related to the metal/metal oxide phases loaded onto the WO_3 support and the effect on measured bandgap modification.

References:
1. Leggett, J., Pepper, W., and Swart, R. (1992). IPCC Supplement
2. Ulman, M.; Aurian-Blajeni, B.; Halmann, M. (1982) Isr. J. Chem. 22, 177–179
3. Channei, D *et al.* (2014) Sci Rep 4, 5757

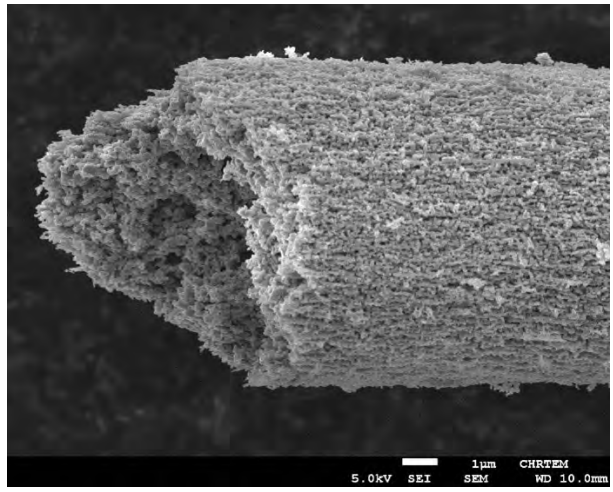

Figure 1. Secondary electron SEM image of a WO_3 tube.$_3$ tube.

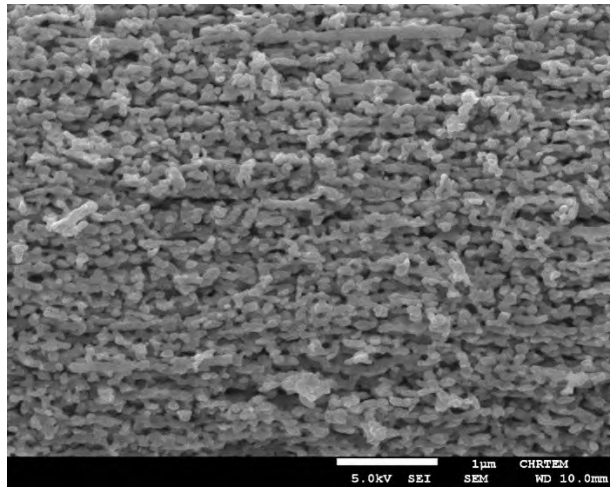

Figure 2. Secondary electron SEM image of a WO_3 tube surface morphology.$_3$ tube surface morphology.

Corresponding author: s214232514@mandela.ac.za

DEVELOPMENT OF HYDRODESULFURIZATION CATALYSTS FOR THE REFRACTORY SULFUR COMPOUNDS: EFFECT OF CHELATIG LIGANDS AND SUPPORT

S. Majodina[1], Z.R. Tshentu[1], E. J. Olivier[2] and A.S. Ogunlaja[1]

[1]Department of Chemistry, Nelson Mandela University, Summerstrand, Gqeberha, South Africa, [2]Centre for HRTEM, Department of Physics, Nelson Mandela University, Summerstrand, Gqeberha, South Africa

Crude oil is a complex blend of hydrocarbons, non-hydrocarbon compounds, and heavy metals containing variable quantities of sulfur-, nitrogen-, and oxygen-containing compounds.[1] The combustion of fuel, produced from crude oil, leads to the emission of sulfur oxides (SO_x) into the atmosphere.[2] This may result in negative environmental and health impacts. Furthermore, sulfur compounds in the fuel deactivate the catalysts used for fuel refinement and in automotive catalytic converters. Accordingly, there is a drive to reduce sulfur levels in fuel to <10 ppmS.

Several studies have been conducted to remove sulfur from fuels,[2] mostly focused on removing refractory sulfur compounds due to the difficulty in removing sulfur. Currently employed hydrodesulfurization (HDS) catalysts cannot produce fuels complying with the future standards of fuel quality.[3] HDS catalysts are made up of metallic components; Co (Ni) and Mo (W), on porous supports. The catalytic activity depends on the amounts of active phases (NiWS or CoMoS) present as well as the total active surface area.[2,3] Currently employed HDS catalysts (e.g. $CoMo/Al_2O_3$) exhibit low activity in removing sulfur in refractory sulfur compounds. This is because of strong metal-support interaction (SMSI). Different strategies have been employed to develop improved HDS catalysts, such as the addition of chelating ligands, and the application of different supports. The addition of chelating agents such as ethylenediaminetetraacetic acid (EDTA), and citric acid (CA) improves the catalytic activity by producing more active phases on the catalyst.[2,3] While TiO_2 in bimetallic metal oxides support (TiO_2-Al_2O_3) improves SMSI and acts as a promoter, hence, more active sites.

The aim of this study is to develop HDS catalysts with enhanced catalytic performance for the removal of sulfur in refractory organosulfur compounds. Herein, the study of CoMo supported on alumina was conducted by studying the effects of chelating ligands; EDTA, CA, and Acetic Acid (AA) on dibenzothiophene (DBT) HDS catalytic activity and catalyst microstructure. The study of TiO_2-Al_2O_3 support was also conducted to investigate the effect of TiO_2 on γ-Al_2O_3 by the sol-gel method. CoMo catalysts were synthesized using hydrothermal (HT) and co-impregnation methods for chelate catalysts. Cobalt(II) nitrate hexahydrate and ammonium molybdate tetrahydrate with a Co/Co+Mo molar ratio of 0.33 was prepared in deionized water. The mixture was impregnated on alumina support and left to mature for chelated catalysts, while for $CoMo/Al_2O_3$ the mixture was transferred into a reactor for HT. The catalysts were activated through sulfidation using a Parr reactor at 4 MPa, 300 ˚C for 4 hrs. For TiO_2-Al_2O_3 support, Pluronic (P123) triblock copolymer, aluminum sec-butoxide, and titanium butoxide at a molar ratio of Ti/Al 0.2 and 0.4 were dissolved in ethanol with an appropriate amount of nitric acid to adjust the pH. The products were dried and calcined.

Table 1 shows each prepared catalyst and measured catalytic activity. Microstructural characterization of each catalyst was done using XRD, XPS, SEM, TEM, and UV-Vis diffuse reflectance spectroscopy. **Figure 1** shows a SEM micrograph of a typically prepared catalyst exhibiting an irregular morphology with small needle-like features. Overall the improved catalytic activity of ligand modified catalysts could be ascribed to a reduction in SMSI, with $CoMo\text{-}CA/Al_2O_3$ yielding the highest activity, due to higher MoS_2 dispersion.

References:
1. Saleh, T. A. (Ed.). (2015). Applying nanotechnology to the desulfurization process in petroleum engineering. IGI global.
2. Shafiq, I., (2020). Catalysis. Reviews. 64(1), 1-86.
3. Budukva, S.V., et al. (2019). Catalysis Today.
Corresponding author: *s217553532@mandela.ac.za*

Catalysts	HDS (%)	BP	PhCH	TOF(h^{-1})
$CoMo/Al_2O_3$	43	21	4	31
$CoMo\text{-}EDTA/Al_2O_3$	90	63	23	56
$CoMo\text{-}AA/Al_2O_3$	94	71	27	84
$CoMo\text{-}CA/Al_2O_3$	98	76	18	150

Figure 1. Catalytic performance of CoMo catalysts.

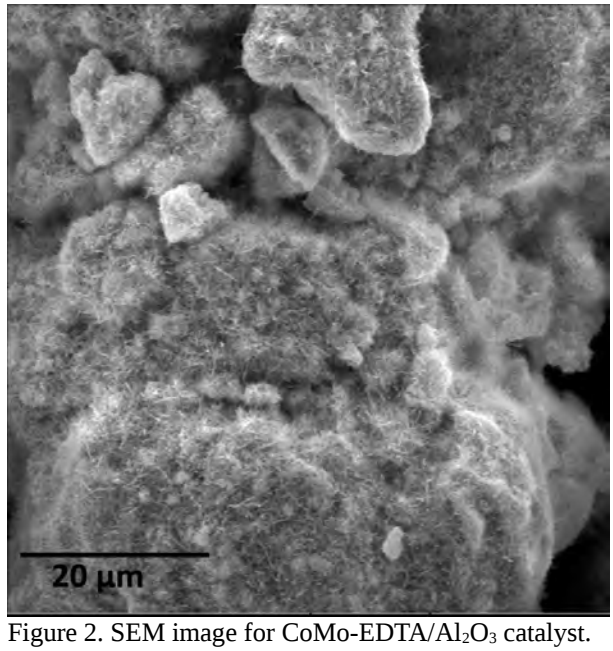

Figure 2. SEM image for $CoMo\text{-}EDTA/Al_2O_3$ catalyst.

Corresponding author: jaco.olivier@mandela.ac.za

STRUCTURAL EFFECTS OF HIGH-ENERGY HEAVY ION IMPACT IN NANOCRYSTALLINE Y-Ti-O AND Y-Al-O

A Ibrayeva[1,2], A Mutali[2,3], J O'Connell[1], A Sohatsky[4], V Skuratov[4] and I Ivanov[2]

[1]Centre for HRTEM, Nelson Mandela University, Port Elizabeth, South Africa, [2]Institute of Nuclear Physics, Nur-Sultan, Kazakhstan, [3]L.N. Gumilyov Eurasian National University, Nur-Sultan, Kazakhstan, [4]Flerov Laboratory for Nuclear Research, Joint Institute for Nuclear Research, Dubna, Russia

High-energy (swift) heavy ion irradiation (E ≥ 1 MeV/nucleon - SHIs) induces the formation of specific defects in solids, particularly in dielectric crystals. These are sometimes observed as so-called latent ion tracks. Disordered regions around the ion trajectory are only formed when the electronic energy loss exceeds a certain threshold level which is material dependent[1-3]. The size and morphology of tracks are usually deduced from TEM imaging as it is the only method for direct observation of such defects[4].

Y-Ti and Y-Al nano-oxides are of interest for nuclear applications and it is therefore important to study their properties under irradiation[1,5-7]. To date, only findings on nanoparticles embedded in oxide dispersion strengthened (ODS) steels have been reported. Structural analysis of $Y_2Ti_2O_7$ in EP450 ODS steel irradiated with high energy Kr and Xe ions yielded an estimated threshold ionization energy loss for track formation of S_{th} ~7.4-9.7 keV/nm[7]. Neither individual latent tracks nor any amorphization have been observed in $Y_4Al_2O_9$ particles in KP4 ODS alloys even after irradiation with 710 MeV Bi ions up to a fluence of 1.5×10^{13} cm^{-2} [8]. On the contrary, ion irradiation with similar energies have produced tracks which are visible to TEM with an average radius of 4.8 nm in un-imbedded nanoparticles[9], and the threshold stopping power was estimated to be ~8 keV/nm. These results suggest that the surrounding metallic matrix plays a significant role in the formation of microstructural damage via SHI impact. Unfortunately, there is almost no data regarding the irradiation-induced microstructural features of Y-Ti and Y-Al oxide nanoparticles in the absence of a surrounding matrix. This work continues the work started in[9] and extends on the TEM based analysis of structural changes in nanocrystalline $Y_4Al_2O_9$ and $Y_2Ti_2O_7$ irradiated with SHIs.

The aim of this investigation is the microstructural analysis of radiation-induced damage in nanocrystalline $Y_4Al_2O_9$ and $Y_2Ti_2O_7$ using high resolution (S)TEM techniques.

Visible tracks were observed by TEM in $Y_2Ti_2O_7$ and $Y_4Al_2O_9$ samples irradiated with xenon and bismuth ions with the electronic stopping powers S_e ≥ 7-8 keV/nm. Typical TEM images are shown in Figure 1. The latent tracks in these materials are continuous amorphous regions along the incident ion trajectory. No tracks were observed in $Y_2Ti_2O_7$ where S_e < 2 keV/nm, and in $Y_4Al_2O_9$ where S_e < 3 keV/nm. Tracks were observed only in the smallest particles or near the edges of larger particles at 2-3 keV/nm < S_e < 7-8 keV/nm.

In general, our results suggest that thermal transport across the oxide-metal interface layer plays a crucial role in track formation in embedded nanoparticles. In addition, irradiation-induced tracks in isolated nanoparticles of yttrium titanate were found to be almost twice as large as in similar sized nanoparticles embedded in a steel matrix.

Acknowledgements. This research was funded by the Ministry of Education and Science of the Republic of Kazakhstan (grant No AP09058081) and the National Research Foundation of South Africa (Grant No 70724).

References:

1. Moll, S. et al. (2010) Nucl. Instrum. Meth. Phys. Res. B, 268, 2933.
2. Ewing, R.C. et al. (2003) Rev. Miner. Geochem., 53(1), 387.
3. Zinkle, S.J. et al. (2002) Nucl. Instrum. Meth. Phys. Res. B, 191, 758.
4. Awazu, K., et al. (2006) J. Appl. Phys, 100(4), 044308.
5. Lang, M. et al. (2010), Nucl. Instrum. Methods Phys. Res. B, 268, 2951.
6. Monnet, I. et al. (2012), J. Nucl. Mater., 424, 12.
7. Skuratov, V.A. et al. (2015), J. Nucl. Mater., 456, 111.
8. Skuratov, V.A. et al. (2016), Nucl. Instrum. Meth. Phys. Res. B, 374, 102.
9. Ibrayeva, A., et al. (2022), Nucl. Mater. Ener., 30, 101106.

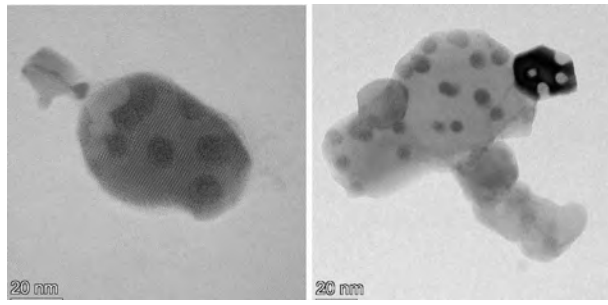

Figure 1. BF TEM images of nanocrystalline $Y_4Al_2O_9$ irradiated with S_e ≈ 27 keV/nm (left) and nanocrystalline $Y_2Ti_2O_7$ irradiated with S_e ≈ 15 keV/nm (right)

Corresponding author: a.d.ibrayeva@gmail.com

EFFECT OF SHI IRRADIATION ON MICROSTRUCTURAL CHANGES OF SELENIUM IMPLANTED POLYCRYSTALLINE SILICON CARBIDE

T.S. Mabelane[1], Z.A.Y. Abdalla[1] and T.T. Hlatshwayo[1]

[1]Dept. of Physics, University of Pretoria, Pretoria, South Africa

Safety of modern high-temperature nuclear reactors is enhanced by encapsulating the fuel elements by CVD-layers of pyrolytic carbon and silicon carbide (SiC) to prevent the fission products release. SiC is the main barrier of fission products (FPs), hence the migration behaviour of radioactive FPs in SiC is vital.

The purpose of this study is to investigate the effect of swift heavy ions (SHI) irradiation on microstructural changes of selenium (Se) ions implanted polycrystalline SiC.

Se ions of 200 keV were implanted into polycrystalline SiC wafers to a fluence of 1×10^{16} cm^{-2} at room temperature (RT). Some of the as-implanted samples were irradiated with bismuth (Bi) of 710 MeV to different fluences of 1×10^{12} and 1×10^{13} cm^{-2} at RT. The unirradiated and irradiated samples were then annealed at a temperature of 1000 °C for 10 h. The morphological and structural changes were monitored by scanning electron microscopy (SEM) and Raman spectroscopy, respectively.

Fig. 1 shows the Raman spectra of the pristine, as-implanted, irradiated, and annealed samples. The spectrum obtained from the pristine sample indicates the characteristics Raman modes of SiC[1,2]. Implantation resulted in partial disappearance of the characteristics SiC Raman peaks and appearance of broad bands at around 500, 800 and 1420 cm^{-1}. After irradiation, the Raman characteristics features became more visible as compared to as-implanted sample. In all implanted then irradiated/ unirradiated samples, after annealing, the broad bands disappeared while the Raman characteristics peaks became more pronounced.

SEM micrograph of pristine showed that the surface contains some polishing marks. Implantation resulted in a flat and featureless surface. Irradiation resulted in non-significant change on the surface morphology. SEM micrographs after annealing showed that crystallites became clearly visible for unirradiated sample and less pronounced for irradiated samples.

The observed broad bands at 500, 800 and 1420 cm^{-1} after implantation are caused by Si-Si, Si-C and C-C vibrations, respectively. The observation indicates total amorphization of SiC[1]. The clear visibility of the Raman characteristic peaks after irradiation indicates some recovery of the SiC crystalline structure[2]. The disappearance of the broad bands and reappearance of pronounced characteristic SiC Raman peaks after annealing indicate a considerable recrystallization of the samples[1].

The flat and featureless surface after implantation is due to sputtering of the surface atoms induced by energetic particles bombardment, and the swelling in the amorphous layer, which is in good agreement with the Raman results[1,2]. The lack of change in surface morphology observed in irradiated samples implies that the resulted changes are below the SEM detection limit[2]. The observed appearance of crystals in the unirradiated and irradiated samples after annealing indicate recrystallization and healing of some defects which agrees well with Raman results[1,2]. It may be concluded that irradiation with SHIs has limited recrystallization.

References:
1. Abdalla, Z.A.Y., et al. (2021) Nuclear Inst. and Methods in Physics Research B. 487, 30.
2. Abdelbagi, H.A.A., et al. (2019) Nuclear Inst. and Methods in Physics Research B. 461, 201.

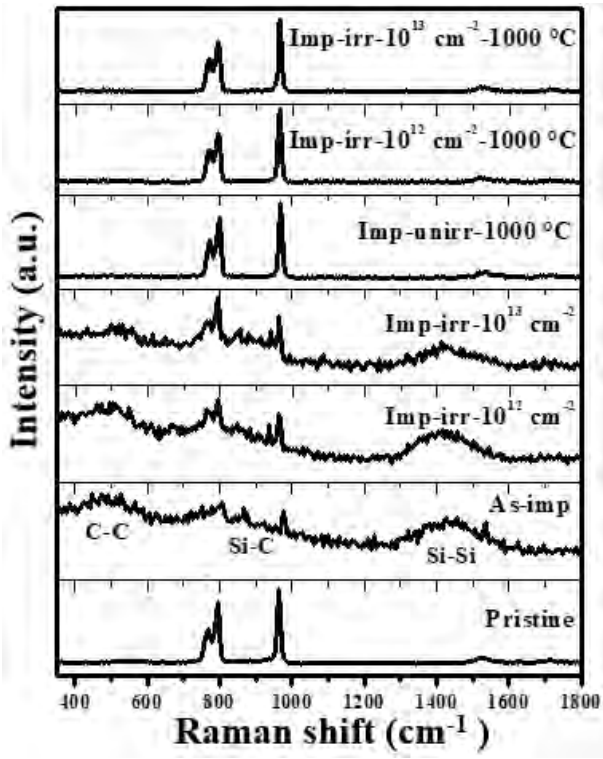

Figure 1. Raman spectra of the pristine SiC after implantation, irradiation and annealing at 1000 °C.

Corresponding author:
mabelanetshepo1997@gmail.com

MICROSTRUCTURAL EVOLUTION OF POLYCRYSTALLINE SILICON CARBIDE CO-IMPLANTED WITH SILVER AND HELIUM AT 350 °C

S.Z. Mtsi[1], Z.A.Y. Abdalla[1] and T.T. Hlatshwayo[1]

[1]Dept. of Physics, University of Pretoria, Pretoria 0002, South Africa

In modern nuclear reactors, safety is accomplished by coating the fuel particle with chemical vapour-deposited layers of carbon (C) and silicon carbide (SiC), in which SiC is the main barrier to fission products[1]. Under normal operation or accidental conditions, the SiC layer is exposed to various fission products, including silver (Ag), in the presence of helium (He). Ag is one of the fission products that is released by the coated fuel during operation, while He is known to form bubbles in SiC. It is imperative to consider that the findings of this study are closely related to what is happening in the reactor.

This study reviews the effect of He bubbles on silver-implanted SiC, which acts as the primary barrier to the containment of fission products in modern high-temperature gas cooled reactors (HTGRs). To this aim, polycrystalline SiC substrate were implanted with Ag ions at the energy of 360 keV to a fluence of 2×10^{16} cm^{-2} at 350 ºC, and some Ag pre-implanted samples were also injected with He ions of 17 keV energy to a fluence of 1×10^{17} cm^{-2} at a temperature of 350 °C.

Both Ag implanted and co-implanted samples were isochronally annealed at temperatures ranging from 1000 ºC to 1300 ºC in steps of 100 ºC for 5 hours. Several physicochemical techniques were used for the microstructural characterization of as-implanted and annealed samples. The stress, radiation damage and its annealing were characterized using Raman spectroscopy. The morphological changes were characterized using scanning electron microscopy (SEM). The surface topography of co-implanted samples before and after annealing was characterized using the dimension icon AFM system in contact mode. AFM micrographs were analyzed using the Nano Scope Analysis software over the scan area of 20 µm × 20 µm.

Fig. 1 shows the SEM micrograph of the co-implanted as-implanted sample has darker round structures and a few bright irregular shaped structures. To further investigate whether these features on the co-implanted samples are blisters or holes, the atomic force microscopy was used to analyze the surface topography of the co-implanted samples. Fig. 2 shows the AFM micrographs of the Ag & He-SiC co-implanted sample. The AFM micrograph have bright and darker areas on their surfaces. Bright areas indicate the topographical height, and the darker areas indicate the topographical depth. The bright areas are He blisters caused by helium bubbles inside SiC. Since helium is inert, it tends to get trapped and cluster in vacancies, thus creating extended defects[2]. The nucleation of helium in vacancies causes the formation of bubbles filled with helium gas resulting in surface blistering[3]. As internal pressure builds up in these blisters, they exfoliate the surface, causing holes to form[4]. Annealing at higher temperatures will cause more blisters to exfoliate, resulting in more holes on the surfaces.

As a result of the He implantation, blisters and some holes were formed on the surface of SiC indicating He bubbles and some cavities within the implanted region. Annealing will cause the appearance of more holes in the expense of blisters indicating more cavities and less bubbles in the implanted region.

References:
1. Malherbe, J. B. (2013) J. Phys. D, 46, 473001.
2. Daghbouj, N., et al. (2021) Appl. Surf. Sci. 552, 149426.
3. Li, B.S., Wang, Z.G. and Zhang, H.P. (2015) Thin Solid Films, 590, 64–70.
4. Daghbouj, N., et al. (2019) Appl. Surf. Sci. 466, 141–150.

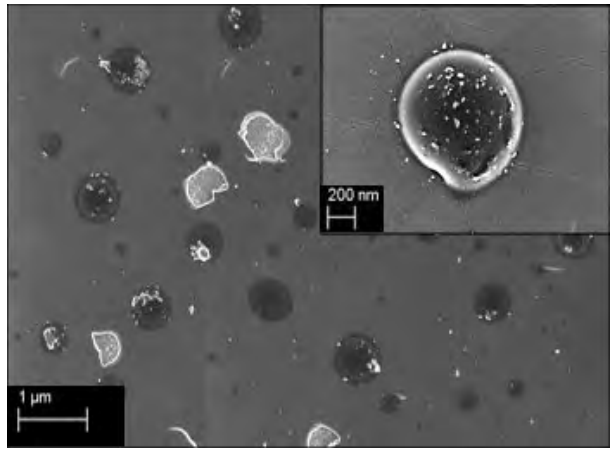

Figure 1. SEM micrograph of co-implanted SiC sample before annealing.

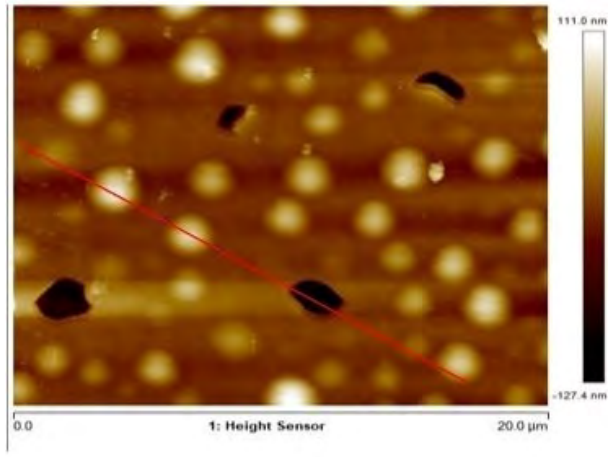

Figure 2. AFM two-dimensional micrographs of co-implanted SiC sample before annealing.

Corresponding author: u14254744@tuks.co.za

INFLUENCE OF Ag^+ ION IMPLANTATION ON THE MORPHOLOGY OF ZnO NANORODS

K Lefatshe[1], D Sebuso[1], M Madhuku[2] and C Muiva[1]

[1]Department of Physics and Astronomy, BIUST, [2] iThemba LABS, Tandem and Accelerator Mass Spectrometry Laboratory

The wide band gap of ZnO permits a strong absorption of the UV spectral region. Results on photocatalytic applications of ZnO NRs for degradation of pharmaceuticals, pesticides, textile dyes as well as energy conversion are reported[1,2]. Doping, coupling with other semiconductors, dye sensitization, use of sacrificial agents, composites, polymer immobilization etc,[5] have been employed to tune the properties of ZnO from a diversity of perspectives in order to obtain improved photoactivities[3-5]. Ion implantation provides a possibility to inject controllable amounts of impurities at accurate depth of a semiconductor. This technique is not dependent on the solubility and diffusivity of the dopants[6]. Ion species, ion fluence, accelerating energy and post implantation treatment influence the degree of surface modification. Besides introducing impurities, bombardment of ions can also alter the morphology of the nanostructures thus modifying its surface dependent properties. In this study, two common techniques the SEM and AFM were employed to study the variation of the morphology of ZnO NRs as induced by implanted Ag^+ ions. The effect of ion fluence is investigated.

Ag^+ ions were accelerated at a voltage of 50 keV at varying fluence of 1.0×10^{15}, 2.0×10^{15}, 3.0×10^{15}, 1.0×10^{16} and 3.0×10^{16} ions/cm^2. No post implantation treatment was done. A Zeiss MERLIN field emission scanning microscope (FESEM) was used for the examination of the surface morphology and elemental composition of the implanted films. A Bruker dimension edge atomic force microscope (AFM) was employed to study the topological parameters of the films, using the tapping mode.

Fig. 1 shows top surface view FESEM images of Ag^+ ion implanted ZnO NRs films. The images indicate a high density of elongated nanostructures. Similar morphologies were observed before Ag^+ ion implantation, indicating that Ag^+ ions did not destroy the much-required 1D morphology. Increasing the ion implantation fluence results in the distension of the nanorods as observed. No cracks or voids were observed. Elemental analysis indicated the presence and spatial distribution of Ag^+ ions in ZnO NRs.

Fig. 2 is a display of the 3D AFM images of ZnO films following Ag^+ ion implantation. The images were analysed to study the influence of the ion fluence on various parameters including the surface roughness and grain height. The surface roughness (R_{rms}) tends to considerably intensify with escalation in the fluence of the Ag^+ ions up to fluence 3 x 10^{15} ions/cm^2. Above which, a decline in the R_{rms} is recorded. The increase in R_{rms} could indicate a possibility of the formation of the micro-void structure and sputtering events on the growing films from the ion implantation process. Conversely, the decrease in the surface roughness at high fluences during ion bombardment could be justified as due to the increase in the surface diffusion processes.

In conclusion, the implantation of Ag^+ ions on ZnO NRs do not destroy the 1D nanostructure, but however, modifies the roughness of the film. Increased roughness results in an increased mass transfer and hence, an improved rate of photocatalysis.

References:
1.Chan, Y., et al, (2013) J. Sol-Gel Sci Techno,66, 399.
2.Ghoniem, M., et al (2021) Orient. J. chem., 37, 609.
3.Munawar, T., et al (2020) Cera. Int.46,2421.
4.Lin, D., et al (2009) Chem. of Mat.,21, 3479.
5.Ikram, M., et al, (2021) Carbohydr Polym, 269,1.
6.Song,X., et al (2018). Adv. Ene. Mat. 8,1

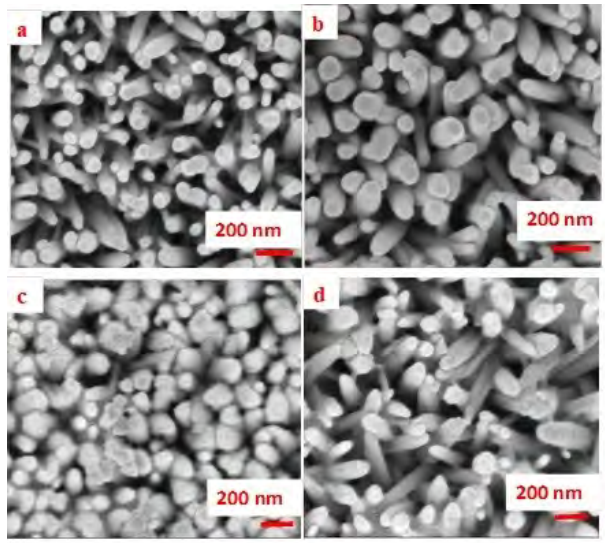

Figure 1. FESEM images of Ag^+ ion implanted ZnO at fluences of (a) 2.0×10^{15}, (b) 3.0×10^{15} and (c) 3.0×10^{16} ions/cm^2.

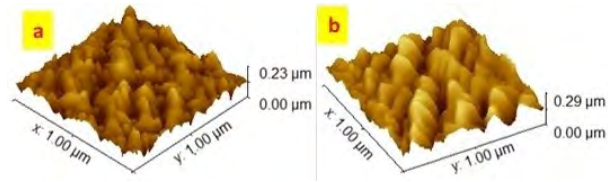

Figure 2. 3D AFM images of low energy Ag^+ ion implanted ZnO samples at fluences of (a) 1×10^{15} and (b) 1×10^{16} ions/cm^2.

Corresponding author:
kebadiretse.lefatshe@studentmail.biust.ac.bw

EFFECT OF MICROSTRUCTURE ON CORROSION BEHAVIOR OF AISI 316 L STAINLESS STEEL IN SIMULATED BODY FLUID.

N.K. Ngeleshi[1], B.A. Obadele [2], B.C. Mashabela[1], X.F. Nukeri[1] and P.A Olubambi[1]

[1]Metallurgical Engineering, University of Johannesburg, Johannesburg, [2] Materials Science, Botswana International University of Science and Technology, Palapye

Metallic biomaterials are used in medical devices in humans more than any other family of materials. The corrosion resistance of an implant material affects its functionality and durability and is a prime factor governing biocompatibility. Over 90% of implant failures made by the 316L austenitic stainless steel are caused by the crevice and pitting corrosion according to the retrieved implants studies[1]. Some toxic cations such as Ni^{2+}, Mo^{6+} and Cr^{3+} once released from 316L stainless steel in the body are claimed to be toxic and destroy the cells[2]. However, when structures are exposed to a corrosive environment, it is not surprising that the different phases exhibit different corrosion behaviors. This leads to preferential corrosion of specific constituents of the alloy[3]. This work investigated the effect of delta (δ) ferrite on corrosion behavior of hot rolled 316L stainless steel in a saline environment.

The body environment is harsh and raises several challenges with respect to corrosion control. To minimize thede limitations, many techniques have been used including heat-treatment of biomaterials. AISI 316L specimens were solution treated for 1 h in temperature range of 1050–1200 °C and subsequently quenched in water to evaluate the effect of delta ferrite on corrosion behavior. The hot rolled and heat-treated steel samples were investigated using a field emission scanning electron microscope (JEOL JSM-7900F), equipped with energy dispersive X-ray spectroscopy (Oxford Instruments), operated at 10 kV accelerating voltage, and a working distance of 10 mm was used for the microstructural analysis. The electrochemical measurements of the samples were performed using open circuit potential (OCP), potentiodynamic polarization and electrochemical impendence spectrometry (EIS) techniques with the aid of Visio stat 4 software available on Princeton Applied Research VersaSTAT 4.

Significant grain growth of specimens was observed as the annealing temperature increased. Specimens exhibited a fully austenitic matrix phase as per thermodynamic phases prediction, XRD and SEM analysis. Furthermore, the samples show better corrosion resistance as opposed to specimens that display both phases (γ and δ). The morphology of delta ferrite phase was identified in the heat-treated specimen in the austenite matrix before corrosion as shown in Fig. 1a. Stable and consistent pits were found on the δ-phase surface displaying vermicular or global morphology[4] which is a likely cause of the deterioration in corrosion resistance as shown in Fig. 1(c,e). While Fig. 1 (b, d, f) confirm via EDS point analysis the presence δ-phase within pits and γ as the matrix. These results indicate the effectiveness of heat-treatment whish leads to a fully austenitic phase formation with improved corrosion resistance of AISI 316L which is advantageous in biomedical applications.

References:
1. Al-Mamun, N. and Mairaj, D.K. (2020) Journal of Biomaterials 45(1), 1.
2. Doran, A. and Rushton, N. (1998) Journal of Biomaterials 19(7), 9.
3. Sedriks, A.J. (1996) Corrosion of Stainless Steel. 2nd Edition, Wiley-Interscience, New-York.
4. David, S.A. (1981) Journal of Welding 60(4), 1.

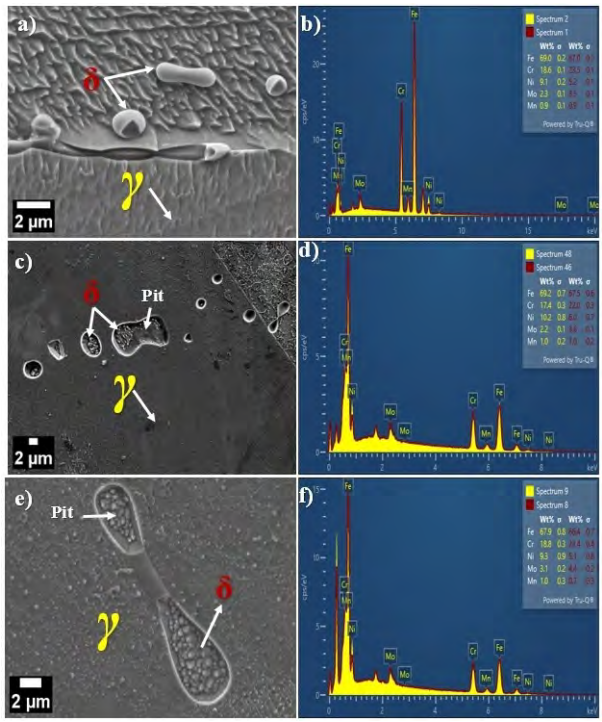

Figure 1. Figure 1. (a) Vermicular and globular morphology of delta ferrite (δ), (c) and (e) preferential delta ferrite phase dissolution in the austenite matrix phase (γ).

Corresponding author: ngeleshik@gmail.com

ASSESSMENT OF THE SIZE OF NANOPARTICLES BY USING X-RAY DIFFRACTION AND SCANNING ELECTRON MICROSCOPY

T. M. Abdalkreem[1], R. E. Kroon[1] and H. C. Swart[1]

[1]Department of Physics, University of the Free State, Bloemfontein, South Afria

Upconversion phosphors absorb two low energy photons and emit one photon of higher energy[1]. Upconversion nanophosphors exhibit size dependent optical properties that are not observed in their bulk counterparts, hence they may find wide range of applications in biology, medicine and forensics[2]. The upconversion efficiency of lanthanide ions may be enhanced when they are close to metallic nanoparticles by plasmonic effects which can amplify the intensity of incident illumination[3]. As part of a prototyping process that is being developed for assessing different types of plasmonically enhanced upconverting nanophosphors, accurate size determination of nanoparticle sizes is required.

In this study Y_2O_3 has used as a host of the upconverting nanophosphor owing to its excellent chemical and physical properties. Y_2O_3 was synthesized by the homogenous precipitation method using $Y(NO_3)_3.6H_2O$ and urea as starting materials, using different annealing temperatures[4]. The crystallite sizes of the Y_2O_3 samples were evaluated using X-ray diffraction (XRD) measured with a Bruker Advance D8 diffractometer by means of Williamson-Hall plots. This is a convenient method that gives the average crystallite size. To check the results and assess the uniformity of the size, images were obtained of the samples using a JEOL JSM-7800F scanning electron microscope.

Fig. 1 shows the XRD pattern of Y_2O_3 annealed at 700 °C for 2 h together with reference data for Y_2O_3 (PDF no. 861326). The five most intense peaks were used with a Williamson-Hall plot to determine the average crystallite size of 17 nm. The same material was dispersed in ethanol and a drop placed on a SEM sample holder. Fig. 2 shows a SEM image of the particles. ImageJ software was used to measure the size of 25 particles, with a result of 146 ± 21 nm.

According to the results, the crystallite size measured by XRD was much smaller than the particle size obtained by SEM. This indicates that each particle observed in the SEM image actually consists of many smaller crystallites, rather than being a single crystal. Additionally, direct observation of the particles using SEM also gives information of the size distribution of the particles. This illustrates the importance of checking particle size assessments from XRD using direct observation with electron microscopy.

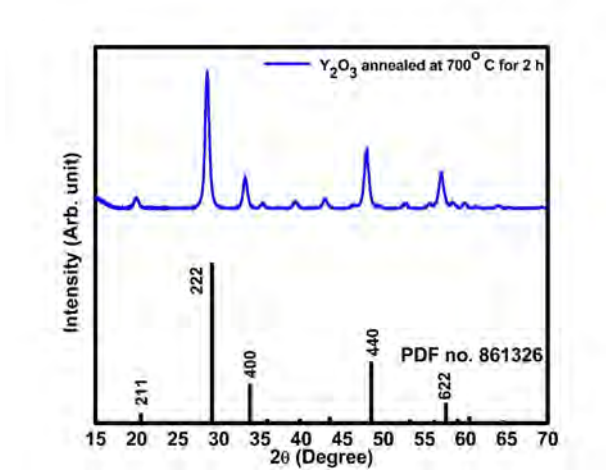

Figure 1. XRD pattern for Y_2O_3 samples annealed at 700 °C for 2 h with reference data of Y_2O_3 PDF no. 861326

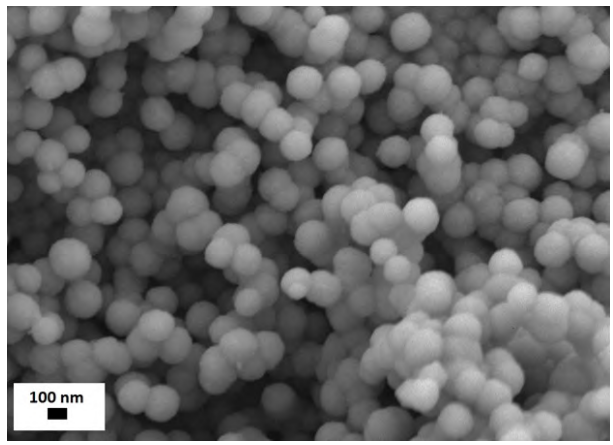

Figure 2. SEM image of Y_2O_3 sample

Corresponding author: talalph24@gmail.com

References:

1. Nadort, A., Zhao, J., and Goldys, E.M. (2016) Nanoscale 8, 13099.
2. Chen, G., et. al. (2014) Chem. Rev. 114, 5161.
3. Ntwaeaborwa, O.M. (2022) Luminescent Nanomaterials. USA, Jenny Standford.
4. Zaitsev, S. V. et al. (2019) J. Appl. Phys.125, 123102.

BACK-ANNEALING OF HOT DIP GALVANISED STRIP STEEL MICROALLOYED WITH VANADIUM

J.S. Steyn[1], J.E. Westraadt[2], K.M. Banks[1], C.W. Siyasiya[1] and R.J. Mostert[1]

[1]Dept. of Materials Science and Metallurgical Engineering, University of Pretoria, South Africa, [2]Centre for HRTEM, Nelson Mandela University, Gqeberha, South Africa

Back-annealing, also known as recovery or partial annealing can produce a high-strength strip steel with acceptable formability.[1] However, it is difficult to utilise in practice due to rapid recrystallisation once a critical temperature is reached. This could lead to inconsistent mechanical properties in the final product. A possible solution is to retard the kinetics of restoration through precipitation of carbonitride particles, by alloying the steel with V, Ti or Nb.[1] The aim of this study is to compare the progress of recrystallisation of an experimental C-Mn-V-N hot dip galvanized (HDG) strip steel grade with commercial C-Mn and Nb-Ti HDG grade after 85% cold reduction.

The annealing cycles experienced during galvanising were simulated using a Bähr-dilatometer. The temperature-time cycles were expressed as the Larson-Miller parameter: $M = (T + 273)(\log(t) + 20) \times 10^{-3}$, where T is the temperature in Celsius and t the time in seconds. Vickers hardness measurements (HV_5) were performed on the samples after simulated annealing to track the state of recovery. The samples were cut into 3 mm disks and polished to a colloidal finish for quantitative XRD, BSE-SEM and EBSD analysis to determine the degree of recovery. Extraction replicas were prepared from fully recrystallised samples. The precipitate species that formed in the micro-alloyed steels were identified using energy-filtered (EF)TEM elemental mapping.

Fig. 1 shows how the addition of alloying elements (Ti-Nb; V-N) increases the hardness and increases the annealing parameter range for the recovery process compared to the C-Mn steel. Fig. 2a shows a HAADF-STEM image with an EFTEM elemental map (Fig. 2b) of precipitates in the experimental grade C-Mn-V-N sample. The addition of vanadium and nitrogen resulted in the formation of intermediate sized (~50 nm) V(C,N) particles which appear to agglomerate around larger AlN particles, but this observation could be due to the sample preparation method. Fig. 3 shows the EBSD inverse pole figure (IPF) orientation maps taken normal to the rolling direction. The cold-rolled sample shows elongated grains aligned with the rolling direction and a high degree of relative misorientations within the grains, compared to the equiaxed structure and relatively low grain misorientations of the fully recrystallised sample.

This shows that alloying the steel with V-N increases hardness and also increases the annealing range required for recovery. Results on the use of XRD peak-profile analysis for dislocation density measurement and quantitative grain-orientation analysis will be presented to show the microstructural evolution of the C-Mn-V-N sample during back-annealing.

References:
1. Ray, R.K., Hutchinson, B. and Ghosh, C. (2011) International Materials Reviews 56(2), 73.

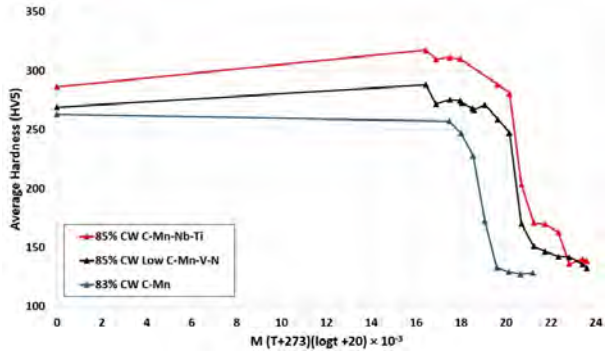

Figure 1. Hardness measurements for the steel grades after various high-temperature exposures.

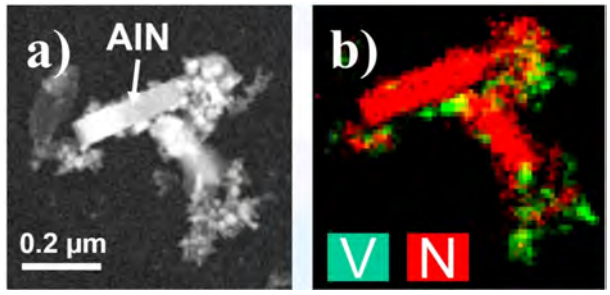

Figure 2. HAADF-STEM image and b) EFTEM elemental map of precipitates in the fully recrystallised C-Mn-V-N grade.

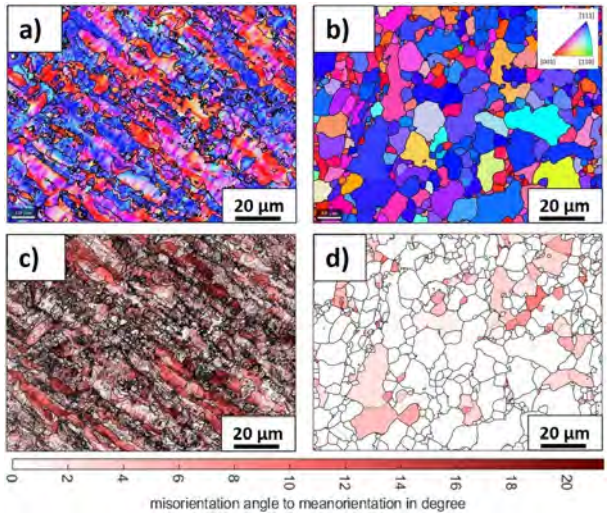

Figure 3. IPF orientation maps of the a) cold-rolled and b) fully recrystallised C-Mn-V-N samples respectively, with the corresponding relative misorientations (c and d) within the grains.

Corresponding author:
johannes.steyn@arcelormittal.com

ANALYSIS OF NANOCRYSTALLINE DIAMOND LAYERS DEPOSITED ON ZIRLO

S. Ngongo[1], A. Janse van Vuuren[1], J. H. Neethling[1] and I. Kratochvílová[2]

[1]Centre for HRTEM, Department of Physics, Nelson Mandela Metropolitan University, Gqeberha, [2]Institute of Physics, Academy of Sciences Czech Republic, Prague

Nanocrystalline diamond (NCD) layers have been considered as accident tolerant coatings on zirconium alloy (ZIRLO) fuel tubes in nuclear reactors[1]. This is due to their outstanding properties, which include high thermal conductivity, low chemical reactivity and high temperature stability. Since ZIRLO fuel tubes act as a barrier between the water coolant and nuclear fuel, waterside corrosion and the penetration of hydrogen and oxygen into the ZIRLO limits the lifetime of the fuel[2].

In this study the viability of NCD as a protective coating on ZIRLO is investigated with a specific focus on the microstructure.

A ZIRLO sample was coated with a homogeneous NCD layer in a microwave plasma-enhanced linear antenna chemical vapor deposition system using a gas mixture of H2 + CH4 + CO2, a process pressure of < 1 mbar and a temperature of approximately 600 °C[1]. The NCD coated ZIRLO samples were sectioned using a diamond wire saw and transmission electron microscopy (TEM) lamellae were cut using a ThermoFisher Helios NanoLab focused ion beam (FIB). The TEM lamellae were investigated in a JEOL 2100 LaB6 TEM operated at 200 kV.

Figure 1 (a) is a bright field (BF) TEM micrograph of a section cut from the NCD coated sample showing the NCD layer on ZIRLO with (b) a spotted ring SAD pattern from the diamond layer with 111, 220 and 311 reflections highlighted. Figure 2 (a) is an annular dark field (ADF) STEM micrograph showing the NCD layer, zirconium oxide and amorphous carbon (deposited during the FIB process), with (b) the corresponding EELS map of the diamond layer and surrounding material.

Earlier reports indicated that the NCD layer contained a combination of both sp^3-hybridized (> 96%, diamond) and sp^2-hybridized (< 5%, graphite) phases of carbon[1]. However, the SAD results in figure 1 show no visible contribution from a graphite phase. This result is confirmed by EELS analysis (Figure 2). The EELS spectra exhibit a diamond peak at ~294 eV and a broader amorphous carbon peak, which emanates from the protective carbon coating used in the FIB section preparation process. There is no indication of the presence of graphite in these spectra, at least within the detection limits of EELS. This finding is consistent with the results of other workers who have investigated NCD grown by Hot-Filament Chemical Vapor Deposition[3]. The results confirm the presence of the sp^3–hybridised diamond phase for the NCD layer as well as a very thin intermediate amorphous carbon layer between the NCD and ZrO2 layers.

The amorphous carbon layer might lead to delamination of the diamond protective layer during the oxidation process, which would expose the ZIRLO to further oxidation.

References:
1. Škarolíd, J. et al. (2017) Sci. Rep. 7, 14.
2. Kratochvílová, I. et al. (2019) Corrosion Science, 163, 108270
3. Wiora, M. et al. (2008) Diamond & Related Materials, 927-930.

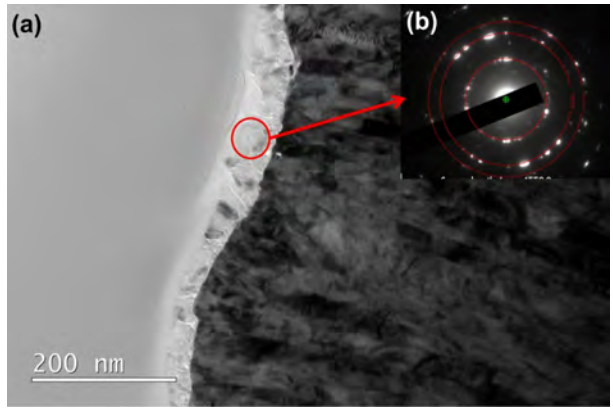

Figure 1. BF TEM (a) micrograph of section cut from the NCD coated sample and (b) SAD pattern of the diamond layer.

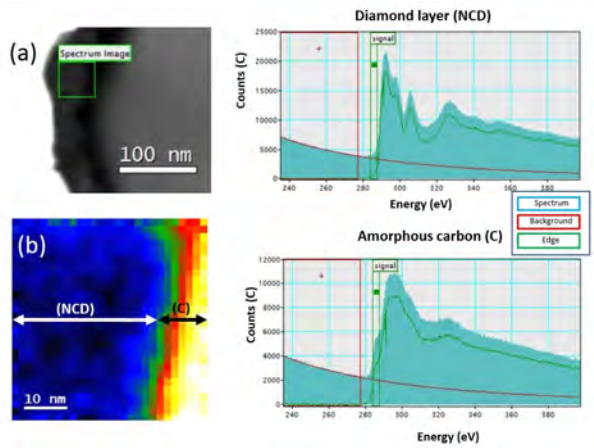

Figure 2. (a) ADF STEM micrograph showing the NCD layer, oxide and amorphous carbon. (b) EELS map showing the location of diamond and amorphous carbon within the lamella.

Corresponding author: ngongosamkelo@gmail.com

SYNTHESIS AND CHARACTERIZATION OF $TiO_2@Co_xO_y$ CORE-SHELL NANOPARTICLES FOR USE IN FISCHER TROPSCH SYNTHESIS

R. Rikhotso[1], E.J. Olivier[2], G. Mhlongo[1] and A. Govender[3]

[1]Council for Scientific and Industrial Research, Pretoria, South Africa, [2]Centre for HRTEM, Physics Department, Nelson Mandela University, [3]Group Technology, Sasol South Africa (Pty) Ltd., Sasolburg

Cobalt-based catalysts are widely used for the low-temperature Fischer-Tropsch reaction (LTFT) to produce middle distillates and long-chain linear hydrocarbons. Despite their high cost, these catalysts are preferred because of their high activity, high selectivity to linear paraffin's, low water-gas shift activity and stability to deactivation by water. To justify the higher costs associated with cobalt catalysts, various efforts are made to ensure that it operates for a longer period and retain good activity[1].

Regeneration of deactivated cobalt catalysts has been examined as a method to improve the economics of the overall cobalt-based Fischer-Tropsch process[2]. Another method to lower the cost of the cobalt-based catalyst is to replace the non-catalytically active cobalt in the catalyst with a cheaper alternative which would result in the formation of a core-shell structure[3]. The applicability in the use of such core-shell structures within the proposed industrial processes, however, depend on the uniformity of Co distribution around the chosen core material and the structural stability of the catalyst after activation and during reaction.

In this work core-shell catalyst precursors with titania, TiO_2, as core and cobalt oxide, Co_xO_y as shell was synthesised. Titania was chosen due to its well-known use as support material for Co based catalysts and measured photocatalytic activity. The core-shell catalyst precursors were prepared using a simple precipitation route using cobalt carbonate, ammonium carbonate and ammonia solution as reactants to produce a Co_xO_y shell around a TiO_2 core[3]. The aim was to coat the TiO_2 core with different targeted shell thicknesses (0.3 nm, 0.6 nm and 0.9 nm) to investigate the dependency of shell thickness on the uniformity and coverage of the Co coating on the titania nanoparticles. Furthermore, different approaches, such as multi-step coating strategies, varying Co precursor concentration in solution and different calcination temperatures and times were investigated to enhance Co coverage on the titania nanoparticles.

Characterization of the synthesised materials was done using a double Cs corrected JEOL ARM 200F operated at 200 kV in STEM mode. Elemental mapping to determine the extent of Co coverage was done using EELS spectrum imaging.

Preliminary results show that the 0.3 nm and 0.6 nm thick samples have an estimated coverage of around 90% of the core while the 0.9 nm shell did not successfully cover the core. Significant Co_3O_4 clustering and agglomeration were observed for the 0.9 nm shells. The 0.6 nm shell showed the best coverage and uniformity of the 3 targeted shell thicknesses (Figure 1).

These initial findings suggest that there may exist a maximum achievable Co shell thickness, after synthesis of the $TiO_2@Co_xO_y$ core-shell system, which would enable uniform coverage of Co on the nanoparticle surfaces. Further studies will include investigations of the stability of the Co_xO_y shell upon reduction to a metallic state during activation of the catalyst.

References:
1. Khodakov, A.Y., Chu, W. and Fongarland, P. (2006) Chem. Rev., 107, 1692
2. Saib, A.M. et al. (2010) Catal. Today, 154, 271
3. Govender, A. et al. (2016) Mater. Charac., 121, 93

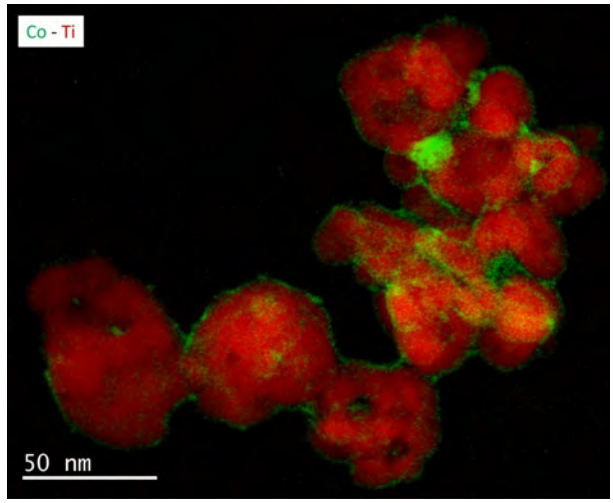

Figure 1. EELS elemental mapping of a core-shell $TiO_2@Co_3O_4$ covered by 0.6 nm of Co_xO_y demonstrating roughly 90% shelling/surface coverage of the TiO_2 core.

Corresponding author: rrikhotso@csir.co.za

CARBON FIBERS GROWN FROM A COPPER NANOPARTICLE ENCAPSULATED WITHIN HOLLOW CARBON SPHERES

M.S Maubane-Nkadimeng[1,2], P.M Gangatharan[1] and N.J Coville[1]

[1]DSI-NRF Centre of Excellence in Strong Materials and the Molecular Sciences Institute, School of Chemistry, University of the Witwatersrand, Johannesburg, [2]Microscopy and Microanalysis Unit, University of the Witwatersrand, Johannesburg

Research in the synthesis and applications of nanomaterials has grown exponentially in recent years. Control of nanostructures using catalysts, capping agents, templates etc. has led to an understanding of the methods used to grow these nanostructured materials. Studies on the synthesis of nanostructures in small nano-confined environments has been well documented. However, these nanostructures (eg. metals/oxides) are formed in open-ended structures (for example in a carbon nanotube), and the confinement is not in all dimensions[1,2].

In order to synthesize nanomaterials that are fully confined and to develop simple procedures to make nanostructures with controlled dimensionality, we have used hollow carbon spheres (HCSs) as our model container. In particular, we have chosen to grow helical carbon fibres inside a HCS using a Cu catalyst[3]. HCSs were synthesized using a template method and were infiltrated with Cu ions (1%) to produce CuO particles[4].

Transmission electron microscopy (TEM) images of HCSs revealed a spherical morphology (od = ca. 310 nm; wall thickness = ca. 90 nm) with encapsulated Cu particles after reduction with H2 (d = ca.20 nm). (Fig. 1) Acetylene was then used as a carbon source to grow helical CNFs within the HCS using a chemical vapor deposition technique. In the reaction the CuO is reduced to Cu and TEM EDX confirmed the presence of Cu. Temperature programmed reduction profile showed that the CuO was converted to Cu at 195 ºC. A helical carbon fibre grown from the two sides of the Cu particle is shown in Fig. 2. The diameter and helicity of the many CNFs and the Cu particle size were analysed and the diameter and helicity of the synthesized CNFs was influenced by the Cu content within a hollow carbon sphere, the limited Cu sintering inside a sphere as well as the dimensions of the sphere.

To establish whether the carbon fibre did indeed grow inside the hollow sphere, TEM tilting experiments were carried out around both the alpha (max. 58 degrees) and beta axis (max. 28 degrees) and showed both Cu particles prior to reaction and the grown fibres were located inside the HCS.

The procedures employed suggest that the philosophy of building other structures (and molecules) with any elements within confined nanoreactors is possible.

References:
1. Restrepo, C.V., Villa, C.C. (2021) Environ. Nanotechnol. Monit. Manag. 15, 100428.
2. Din, I.U., Shaharun, M.S., Naeem, A., Alotaibi, M.A., Alharthi, A.I, Bakht, M.A., Nasir, Q. (2020) Ceramics International 46(11), 18446.
3. Li, H., Zhao, J., Shi, R., Hao, P., Liu, S., Li, Z., Ren, J. (2018) Appl. Surf. Scie. 436, 803.
4. Li, S., Pasc, A., Fierroa, V., Celzard, A. (2000) J. Mater. Chem. A, 4, 12686.

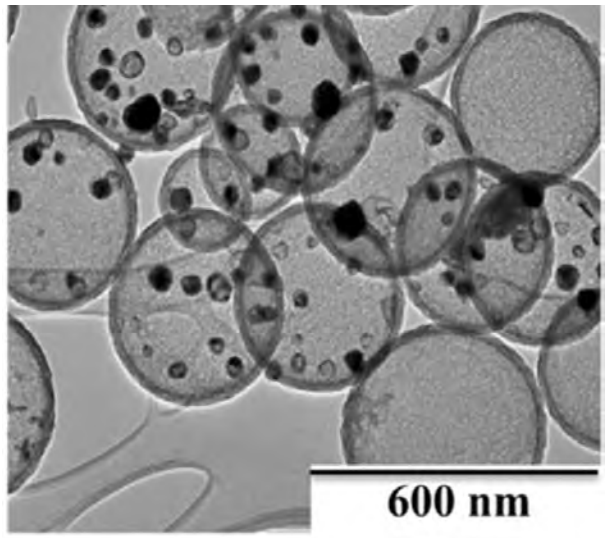

Figure 1. TEM micrograph of encapsulated Cu nanoparticles within the HCS.

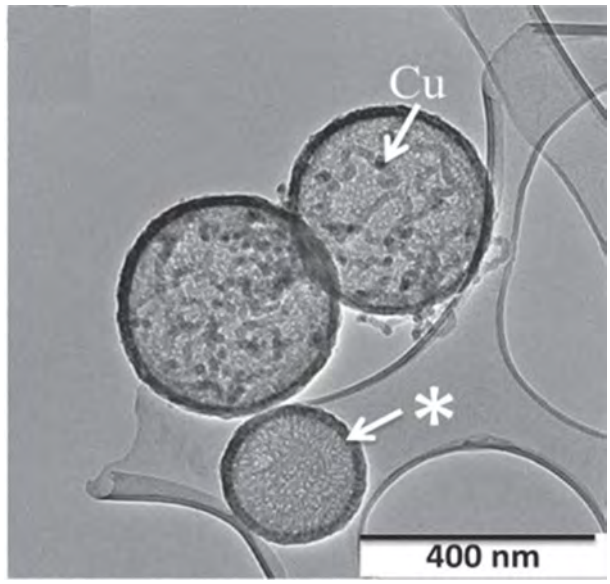

Figure 2. Carbon fibre grown from the encapsulated particle. A HCS that contains no Cu particles is shown by *. Some CNFs can be seen growing outside the HCSs due to Cu particles deposited outside of the carbon shell.

Corresponding author: manoko.maubane@wits.ac.za

STUDY OF THE IMMOBOLISATION OF PALLADIUM BY SILICON AND ZIRCONIUM IN GRAPHITE

G. Mtwazana[1], A. Janse Van Vuuren[1] and J.H. Neethling[1]

[1]Centre for HRTEM, Nelson Mandela University, Gqeberha

Certain high temperature gas reactor designs use TRISO-coated particles as fuel. The TRISO-coated particle consists of a fuel kernel and coating layers of porous pyrolitic carbon (PyC), inner high-density PyC, silicon carbide (SiC) and outer high-density PyC. The SiC layer serves as the main barrier to fission product release[1]. However it has been reported that the radioactive fission product Ag^{110m} can escape from intact TRISO particles[2]. It was also found that the fission product palladium (Pd) significantly enhanced the migration of silver along grain boundaries in SiC[3,4].

This paper investigates the feasibility of using Pd traps such as Si and ZrC in the inner PyC layer of TRISO particles to capture the Pd and prevent it from migrating to the SiC layer by forming immobile silicide compounds in the case of Si. It is proposed that without Pd in the SiC, the migration rate of Ag in SiC will be significantly reduced at normal operating temperatures.

Graphite discs (used to simulate PyC) were implanted with 137,5 keV Si^+ and 190 keV Zr^+ ions to doses of 8,27 $x10^{15}$ Si ions.cm^{-2} and $5x10^{15}$ Zr ions.cm^{-2}. Pieces of implanted graphite discs, with a layer of Pd powder on the implanted surface, were subsequently annealed at temperatures of 600 and 900 °C for 20 min. TEM samples were cut using a focused Ion Beam (FIB) and analysed using a JEOL 2100 TEM.

Fig. 1 (a) is a HAADF STEM micrograph of Si implanted graphite annealed in contact with Pd powder at 600 °C for 20 min. The bright particles are the Pd on the Si implanted graphite as indicated in the figure. Fig. 1 (b) is a HAADF STEM micrograph showing the location of the EDS line scan across a Pd particle and into the Si implanted graphite. The corresponding EDS line scans for Pd, C and Si are shown in (c) together with the location of the implanted graphite surface. The similarity of the Pd and Si line scans indicate that at 600 °C, the Si rapidly diffused out of the graphite and into the Pd particles. The same result was obtained after annealing at 900 °C for 20 min. which is indicative of the high chemical reactivity of Pd and Si to form a silicide[3]. The current study revealed that the palladium silicide formed will most likely be immobile in graphite (and PyC) at temperatures up to 900 °C.

The EDS results of the Zr implanted graphite annealed in contact with Pd at 600 and 900 °C indicated that Zr did migrate into Pd but the reaction was less pronounced than that of Si. Since the results suggest that the palladium silicide formed will be most likely immobile at 900 °C and since a Si source is already used to grow the SiC layer, the incorporation of Si into the inner PyC layer of a TRISO particle during manufacturing would be easier and more effective as a Pd trap than ZrC.

References:
1. Minato, K., *et al*. (1997) J. Nucl. Mater. 246, 215.
2. Nabielek, H., Brown, P.E., and Offerman, P. (1977) Nucl. Technol. 35, 483.
3. Neethling, J.H., O'Connell, J.H. and Olivier, E.J. (2012) Nucl. Eng. Des. 251, 230.
4. Olivier, E.J., Neethling, J.H. and Van Rooyen, I.J. (2020) J. Nucl. Mater. 532, 152043.

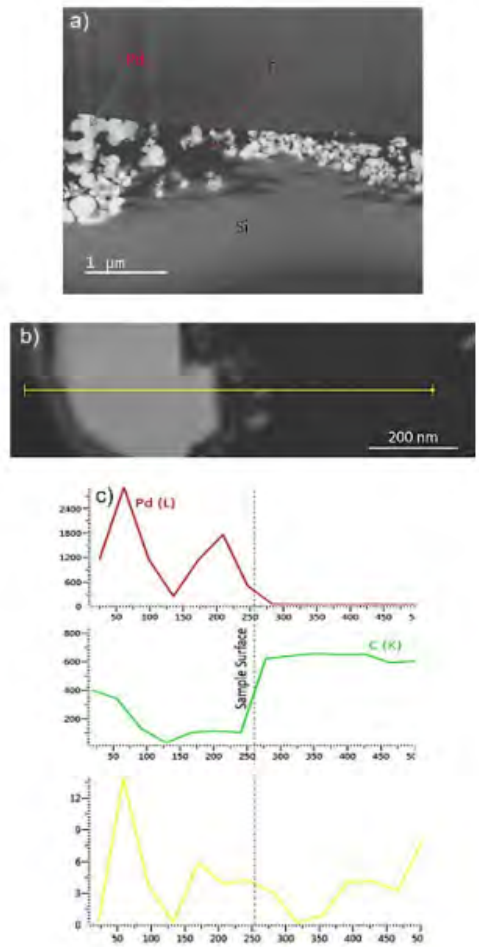

Figure 1. (a) Cross-section view HAADF STEM micrograph of graphite implanted with Si and annealed at 600 °C in contact with Pd powder. (b) HAADF STEM micrograph showing the location of the EDS line scan across a Pd particle and into the Si implanted graphite. The corresponding EDS line scans for Pd, C and Si are shown in (c) together with the location of the implanted graphite surface.

Corresponding author: s220020132@mandela.ac.za

CHEMICAL ANALYSIS OF NANO-SIZED STEEL PRECIPITATES USING SCANNING ELECTRON MICROSCOPY

N.W. Mfuma[1], W.E. Goosen[1] and J.E. Westraadt[1]

[1]Center for HRTEM, Physics Department, Nelson Mandela University, Gqeberha.

Tempered martensite ferritic (TMF) creep-resistant steels with 9-12% Cr are used for steam pipes, turbines and boilers in fossil fired steam power plants. Metal carbides ($M_{23}C_6$) rich in *chromium* and metal carbonitrides (MX) rich in *vanadium* act as pinning agents, impeding free-dislocation movement and suppressing the movement of grain boundaries during creep[1]. Coarsening of $M_{23}C_6$ and formation of *molybdenum* containing Laves phase as well as the dissolution of MX during long-term operation decreases the pinning forces exerted by the particles, ultimately resulting in a creep-strength breakdown. Quantitative analysis of the precipitates in the steel can potentially be used as an indicator of the material state for remnant life assessments.

Chemical analyses of the small precipitate phases are usually conducted using scanning (S)TEM-EDS or energy-filtered (EF)TEM methods on a thin-foil or carbide extraction replica sample[2], since the beam-specimen interaction volume dominates the resolution that can be achieved on conventional bulk samples analysed with SEM-EDS[3]. However, most industrial power utilities do not have on-site access to a TEM to perform this analysis, while access to SEMs with EDS capability is more common. This study reports on SEM-EDS chemical analyses performed on conventionally prepared TEM samples for quantitative analysis of precipitates down to 50 nm in size for 9-12% Cr TMF steels.

Three sample preparation techniques were used in this study. *Bulk* samples were hot mounted in phenolic resin (conductive resin) and then mechanically polished using successively finer polycrystalline diamond suspensions down to 0.25 µm and finally with 50 nm colloidal silica in an etchant. *Thin foil* samples of 3 mm diameter were prepared by mechanically grinding and fine polishing a sample to a final thickness of 100 µm and then jet electro-polished with a solution of 5% Perchloric acid in ethanol with a voltage of 21 V until a perforated hole is formed. Finally, carbon *extraction replica* samples extract precipitates from the surface of a pre-polished bulk sample onto ~30 nm thick carbon layer. SEM-EDS elemental mapping was performed using different incident beam energies (5 keV, 15 keV and 30 keV) for 5 minutes using a 4 nA beam current and a 20 nm pixel size, to obtain elemental maps (25 µm x 20 µm) of Cr-K, Mo-L and V-K displayed using a linear intensity scale for the three sample preparation methods. SEM-EDS quantitative analyses (results not shown) performed in point mode of the different precipitates were conducted using the same incident beam energies.

Fig. 1 shows a BSE image and a Cr-K SEM-EDS elemental map taken from a bulk sample. Light grey precipitates (yellow arrows) indicate the location of the Cr-rich $M_{23}C_6$ precipitates. Although the larger $M_{23}C_6$ precipitates can be distinguished from the background, several smaller precipitates visible in the BSE image are not resolved in the elemental map. Fig. 2 shows the BSE image and various SEM-EDS elemental maps taken from a thin-foil (~100 nm) service exposed TMF steel sample. The Cr-rich $M_{23}C_6$ precipitates down to 150 nm in size were resolved in the elemental map. In addition, the Mo-rich Laves phase and the fine (<< 100 nm) V-rich MX precipitates can also be resolved from the respective elemental maps.

This shows that SEM-EDS precipitate analyses preformed on conventional TEM samples resulted in improved spatial resolution compared to analyses performed on bulk samples. However, care must be taken when interpreting SEM-EDS quantitative elemental analyses on thin TEM samples since the bulk *ZAF*-correction factors will no longer be valid.

References:
1. Kostka, A. *et al.* (2007) Acta Mat. 55(2), 539.
2. Wang, H. *et al.* (2021) Mat. Char. 181, 111396.181, 111396.
3. Goldstein, J. I. *et. al* (2009). Scanning electron microscopy and X-ray microanalysis. New York: Springer.

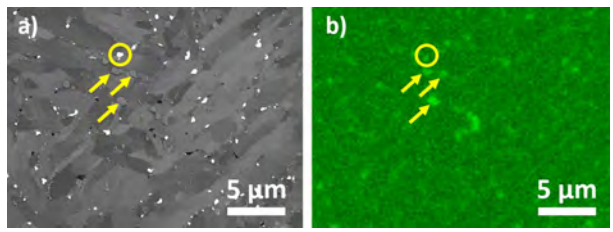

Figure 1. a) BSE image and b) Cr-K elemental map (15kV) showing the location of the larger $M_{23}C_6$ precipitates (arrows) and Laves phase (circle).

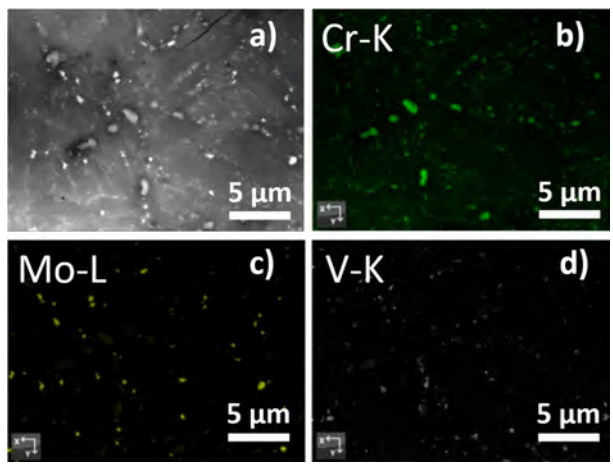

Figure 2. a) BSE image and elemental maps (15kV) of b) Cr-K ($M_{23}C_6$), c) Mo-L (Laves phase), and d) V-K (MX) showing the different precipitates species in an aged TMF steel.

Corresponding author: johan.westraadt@mandela.ac.za

SCANNING TUNNELING MICROSCOPY: INSIGHTS FROM FIRST PRINCIPLES CALCULATIONS

A. M. Ukpong[1,2]

[1]TCCMMP Group, School of Chemistry and Physics, University of KwaZulu-Natal, [2]NITheCS, Pietermaritzburg

Scanning tunneling microscopy (STM) imaging relies on the quantum tunneling of electrons through the potential barrier between a sharp probe tip and a conducting sample surface to attain atomic-scale spatial resolution.[1] The technique has been known for over four decades,[2] yet it still capable of providing useful information for materials characterization today. There are several examples of the design and deployment of single active sites on the surface of platinum group metals (PGMs)-based catalysts where atomic-level imaging has been beneficial in materials development. Such catalytic materials play pivotal roles in the development of technology for chemical processes, clean energy generation, and pollution control, among others.[3]

Herein, first principles calculations are performed on the surfaces of single-phase materials to obtain STM images of metallic surfaces. The calculations are performed using the grid-based projector augmented wave (GPAW) code.[4] To illustrate its broad use in materials analysis and development, computed STM maps of radical hydrogen species adsorbed on metallic surfaces are presented to illustrate the insights its yields in aiding the design and development of catalytic materials. Accurate atomic-level imaging of the cross section of a material can also play a crucial role in alloy development. These two examples show practical scenarios in which STM imaging is capable of providing complementary information on the surface characterization in a cost-effective way.

Figure 1(a,b) shows the spin density maps of an adsorbed hydrogen atom on the unalloyed Pt(100) and Pd(111) surfaces, respectively. The color contrasts in the computed STM maps denote the magnitude of the tunnelling spin conductance in amperes per volt (A/V). The bright halos in Fig. 1 denote the adsorbed hydrogen atom. From the total energy of hydrogen adsorption at high-symmetry sites of the Pt(100) surface, the hollow site is the most favorable. The high contrast at hydrogen sites suggests that STM could aid the identification of single-atom species adsorbed on a material surface during a reaction. Also, it can aid the selective functionalization of substrates, identification of active sites and defect fingerprinting.

Figure 2 shows the SEM micrograph of an experimental alloy of 3%Ir-42%Ni-Rh composition showing that nickel oxide has already formed at 1600 °C (a), and the STM map of nickel oxide computed at 0 K (b). When in-situ STM imaging of the alloy is combined with the SEM image, or with a computed high-temperature STM map, insights into the oxidative evolution of alloy surface and the high-temperature corrosion of the surface are obtainable. This is useful for obtaining the optimum alloy composition at which the oxide skin is minimal. This is because in-situ STM images will be sensitive to minor changes in alloy composition and elemental concentration. Sensitivity permits the design optimization of alloy composition for inhibiting the formation of the oxide skin.

The atomic resolution of the STM maps show that first principles calculations performed within density functional theory convolutes the geometric and electronic structures. The high constrast of the images suggest that in-situ STM imaging can capture the sensitivity of the local structure to changes in the ambient environment. This is useful for analyzing the real-time evolution of a surface during a reaction. Precision STM imaging are thus beneficial in linking structure to function. Overall, when STM imaging is combined with insights from other approaches of materials characterization better insights are obtained.

References:
1. Binning, G., et al. (1982) Phys. Rev. Lett. 49, 57.
2. Anirban, A. (2022) Nat. Rev. Phys. 4, 291.
3. Cooper, C. et al. (2015) Johnson Matthey Technology Review, 59, 257.
4. Mortensen, J. J. Hansen, L. B. and Jacobsen, K. W. (2005) Phys. Rev. B 71, 035109.

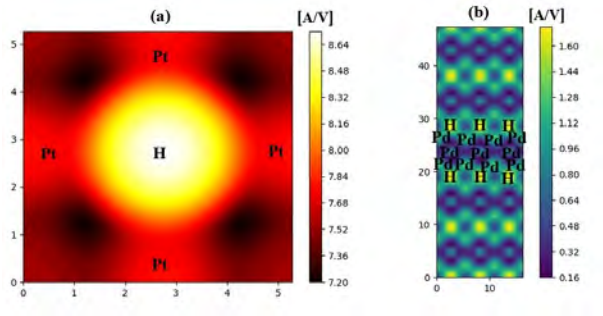

Figure 1. Spin density maps around a surface hydrogen radical adsorbed on (a) the 1×1 primitive cell of the Pt(100) surface (b) the 2×5 supercell of the Pd(111) surface, respectively.

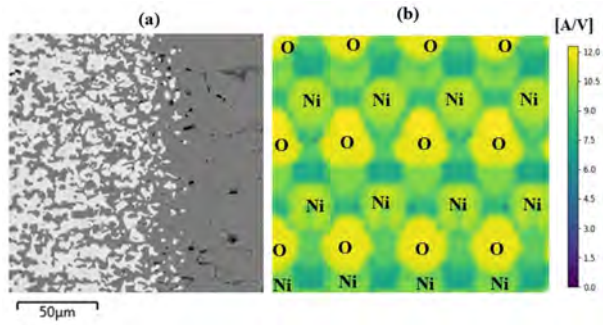

Figure 2. SEM micrograph of the microstructure in an experimental alloy composition (3%Ir-42%Ni-Rh) showing the formation of nickel oxide at 1600° C (a) and the computed 0-K STM map of the pristine (111) surface of the nickel oxide layer (b).

Corresponding author: ukponga@ukzn.ac.za

DEVELOPMENT AND CHARACTERISATION OF ANTIBACTERIAL TITANIUM-BASED ALLOYS WITH COPPER FOR BIOMEDICAL APPLICATIONS

L Spotose[1,2], N.S. Phala[1,2], C. Polese[1,3] and L.A. Cornish[1,2]

[1]School of Chemical and Metallurgical Engineering, University of the Witwatersrand, , [2]DSI-NRF CoE in Strong Materials, hosted by the University of the Witwatersrand, and DSI Collaborative Programme in Additive Manufacturing, [3]School of Mechanical, Aeronautical and Industrial Engineering, University of the Witwatersrand

Titanium and its alloys are used biomedically, including dental implants, due to their favourable combination of properties: low density, high strength, corrosion resistance, excellent biocompatibility and good osseointegration[1]. The widely used Ti-6Al-4V alloy has concerns as Al been associated with Alzheimer diseases and phosphorus deficiency in the blood and bone, while V appeared to be cytotoxic and show carcinogenic properties[1].Hence the development of new alloys with non–toxic elements is necessary.

The aim of this study is to develop a Ti-based alloy that is not toxic and has improved corrosion resistance as the human body has different electrolytes which contain corrosive species. The addition of 5 mass% copper promotes good antibacterial properties as well as balanced mechanical properties in Ti-Cu based alloys[2]. Small ruthenium additions enhance corrosion resistance without changing the microstructure of the alloy[3].

The titanium alloys were selected using Thermo-Calc and four alloys were chosen as their (α+β) phase proportions were similar to Ti-6Al-4V, which was used as a reference alloy[3]. The alloys were: Ti-6Ta-1.5Zr, Ti-6Ta-1.5Zr-5Cu, Ti-6Ta-1.5Zr-0.2Ru and Ti-6Ta-1.5Zr-5Cu-0.2Ru (mass%). High purity powders were mixed in the required ratios and cast in a button arc furnace. The samples were submerged in phosphate buffered solution to test their corrosion resistance. Open circuit potential was measured for up to 17 hours and potentiodynamic polarisation was carried out at 37°C.

The corrosion rates of all the alloys were: Ti-6Ta-1.5Zr (0.00021 mm/y), Ti-6Ta-1.5Zr-5Cu (0.00014 mm/y), Ti-6Ta-1.5Zr-0.2Ru (0.00030 mm/y) and Ti-6Ta-1.5Zr-0.2Ru-5Cu (0.00022 mm/y). Ti-6Ta-1.5Zr-0.2Ru had the highest corrosion rate as compared to other alloys and all were below the recommended rates[4] in biomedical applications which is 0.13 mm/y. Fig. 1 shows the microstructure of the Ti-6Ta-1.5Zr-0.2Ru before the corrosion test and Fig. 2 shows the microstructure of Ti-6Ta-1.5Zr-0.2Ru afterwards. There was corrosion damage, as well as some scratches from handling. Table 1 shows the EDX results of Ti-6Ta-1.5Zr-5Cu (mass%) before and after the corrosion tests, the EDX was done on an area of 20x20 μm^2 on five different places and the average was taken to represent the bulk composition. The EDX results shows that there were minor losses of Ta and Zr, but higher losses of Cu (almost 50%), which shows that some of the Cu was lost. However, this is beneficial since the antimicrobial action occurs when copper is in the surrounding solution[5].

References:
1. Jingjing, Z., et al. (2020), Calphad.
2. Liu, J., et al. (2014), Mat. Sci. Eng. C, 35, 392.
3. Spotose, L. and Cornish, L.A. (2021) African Inclusive Microscopy Network's Student Symposium.
4. Bhola, R., et al. (2011), Trends Biomater Artif. Organs, 25(1) 34
5. Li, M., et al. (2016), Adv. Healthc. Mater., 5(5), 557.

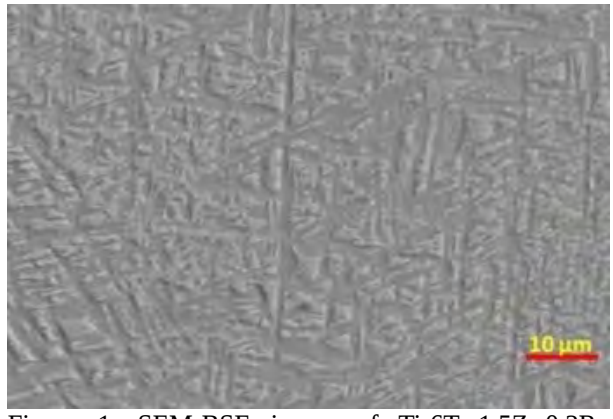

Figure 1. SEM-BSE image of Ti-6Ta-1.5Zr-0.2Ru (mass%) before corrosion, showing (βTi) (light contrast) and (αTi) (dark contrast).

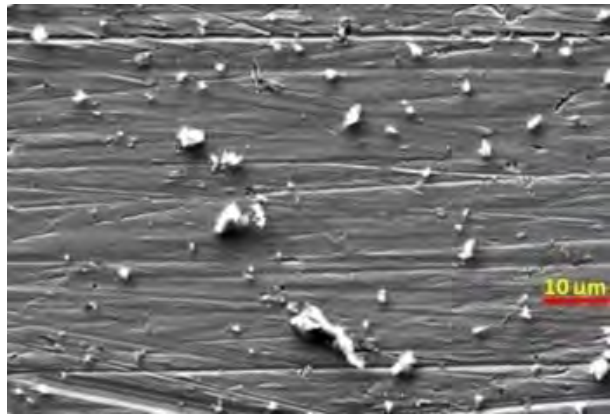

Figure 2. SEM-BSE image of Ti-6Ta-1.5Zr-0.2Ru (mass%) after corrosion, showing (βTi) (light contrast) and (αTi) (dark contrast).

Table 1. Overall EDX analyses of Ti-6Ta-1.5Zr-5Cu (mass%) before and after corrosion.

	EDX analysis (mass%)			
	Ti	Ta	Zr	Cu
Before corrosion	86.0±1.2	5.9±0.5	3.1±0.5	4.9±0.7
After corrosion	90.0±0.3	5.0±0.5	2.1±0.6	2.3 ±0.1

Corresponding author: 820850@students.wits.ac.za

ANALYSIS OF $In_xGa_{1-x}As$ EPILAYERS BY INFRARED SPECTROSCOPY AND ELECTRON MICROSCOPY

J.A.A. Engelbrecht[1], S. McKee[2], W.E. Goosen[1], E.G. Minnaar[1] and A. Janse van Vuuren[1]

[1]HTREM Facility, NMU, [2]Hermanus Magnetic Observatory

$In_xGa_{1-x}As$ ternary structures have attracted attention for use in optical devices such as laser diodes[1], photo detectors[2] and optical modulators[3]. Knowledge of the material properties is hence of great importance in device design to obtain the best device performance. For example the optical properties of fabricated devices depend inter alia on the band gap and refractive index of the grown material. Various electrical and optical techniques are available to determine the band gap[4,5]. The band gap is dependent on the indium concentration, and it is the purpose of this investigation to report on a comparison of the band gap energy as a function of the indium concentration as determined by Fourier Transform Infrared (FTIR) reflectance spectroscopy and energy dispersive X-ray spectroscopy (EDS).

Epilayers of $In_xGa_{1-x}As$ with different indium concentrations were grown using an Epitor 04 organometallic vapor phase epitaxial deposition reactor. Semi-insulating or silicon-doped GaAs substrates orientated 2θ off (100) towards <110> were used at growth temperatures 610 - 690ºC. Samples were subsequently analyzed by infrared reflectance spectroscopy using a Bruker 80V FTIR/Raman spectrophotometer, fitted with a Pike 10Spec specular reflection unit that enabled near-normal incidence. 32 Scans were taken at a resolution of 8 cm^{-1} over a wavelength region from 0.5 – 50 nm. EDX spectra were obtained from an Oxford EDS SDD detector fitted to a JEOL JSM-7001F scanning electron microscope and processed using Aztec EDX software to determine the indium concentration for each sample. Infrared reflectance spectra yielded a sharp peak where the photon energy of the incident radiation equals the band gap energy (Fig. 1). The indium atomic percent (at%) concentrations were determined from the SEM-EDX spectra (Fig. 2). These values were used to determine the band gap energy by substituting the indium molar concentration values x into the equation of Nahory et al[6]. The experimental values for the band gap as determined by EDS and IR are compared to the theoretical values calculated from the equation proposed by Nahory et al[6], as presented in Table 1.

It is therefore concluded that the results from the infrared reflectance data are in good agreement with values calculated from the theoretical expression and those obtained by the EDS technique. The advantage of the IR technique is that it is a rapid non-contact method without the requirement of any sample preparation.

References:
1. Temlin, H., et al (1983) Appl. Phys. Lett. 42, 845.
2. Mohammed, K., et al (1985) Appl. Phys. Lett. 47, 597.
3. Wakita, K., et al (1986) Electron. Lett. 22, 907.
4. Yu, L.S., et al (1999) Appl. Phys. Lett. 10, 1419
5. Holtz, M., et al (2001) J. Appl. Phys. 89, 7977.
6. Nahory R.E., et al (1978) Appl. Phys. Lett. 33, 659.

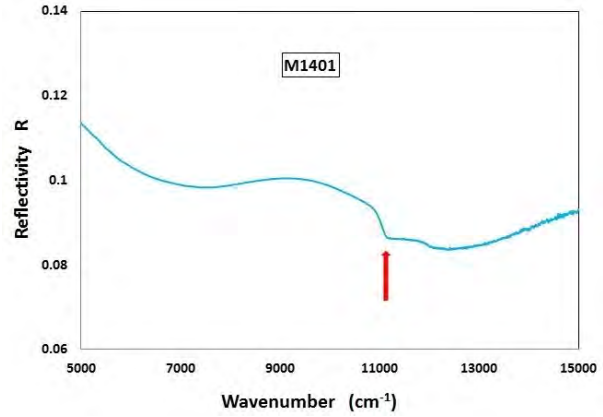

Figure 1. Infrared reflectance spectrum of sample M1511; red arrow indicating the peak for obtaining the band gap..

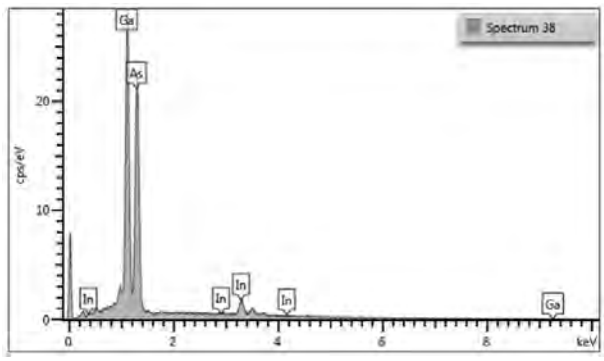

Figure 2. EDX spectrum of $In_xGa_{1-x}As$ epilayer of sample M 1511, from which the band gap of this epilayer was obtained.

SAMPLE	THEORY (eV)	EDS (eV)	IR (eV)
M1403	1.40	1.40	1.40
M1408	1.37	1.34	1.36
M1455	1.38	1.38	1.39
M1511	1.20	1.21	1.22
M1561	1.25	1.24	1.24

Figure 3. Band gap values comparing theory to results obtained by EDS analysis and IR reflectance.

Corresponding author:
Japie.Engelbrecht@mandela.ac.za

MICROSTRUCTURE AND MECHANICAL PROPERTIES OF CREEP-EXHAUSTED 14MoV6-3 STEEL AFTER REGENERATIVE HEAT TREATMENT

T. Masole[1,2], L.A. Cornish[1,2] and M.O. Bodunrin[1,2]

[1]School of Chemical and Metallurgical Engineering, University of the Witwatersrand , [2]DSI-NRF CoE in Strong Materials, hosted by the University of the Witwatersrand

The 14MoV6-3 steel has been used in the manufacture of seamless tubes and pipes since the early 1960s. These pipes are used extensively in the fossil power plant industry because they can operate at elevated temperatures, typically 540°C, and pressures reaching 3.75MPa for extended periods of time. The properties of this steel are due to microstructural stability given by a heat treatment that results in a microstructure of a mixture of ferrite, bainite, and sometimes pearlite[1]. During extended service at creep inducing conditions, the microstructure undergoes changes which lead to degradation in mechanical properties[2]. To recover the mechanical properties and increase safe operation of these creep-exhausted components, regenerative heat treatment can be used[3]. The aim of this research is to determine the effect of a specific regenerative heat treatment on the microstructure and mechanical properties of a creep-exhausted 14MoV6-3 steel.

Regenerative heat treatment was done on a creep-exhausted 14MoV6-3 steel pipe which had been in service for 277 452 hours at 540°C and 3.75MPa and compared to an unused 14MoV6-3 steel. The regenerative heat treatment comprised normalising at 930°C for 1 h followed by tempering at 720°C for 3h in a Phoenix CAHO H961 furnace. Room temperature tensile and impact tests were performed on the unused, creep-exhausted and regeneratively heat treated 14MoV6-3 steels with three samples from each steel condition to determine the ultimate tensile strength (UTS), 0.2% proof strength ($R_p0.2$), percent elongation (el%) and impact energy. The unused, creep-exhausted, and regeneratively heat treated samples were sectioned, mounted, ground, polished and etched using Vilella's reagent. Microstructural examination was performed in a ZEISS Sigma 300VP scanning electron microscope (SEM) using secondary electrons.

Fig. 1 shows the microstructure of the unused 14MoV6-3 steel, which comprised ferrite and pearlite with precipitates decorating some ferrite grain boundaries. Fig. 2 shows the regenerated microstructure with agglomerated ferrite and Fe_3C particles inside the pearlite colonies, fewer grain boundary precipitates and smaller ferrite grains. The grain sizes were 19.21±6.88, 16.25±8.07 and 13.59±9.05µm for the unused, creep-exhausted and regeneratively heat treated steels, respectively. Fig. 3 shows that of the steel conditions, the creep-exhausted steel had the highest UTS and $R_p0.2$ and the lowest impact energy and el% due to the ~15% grain size reduction when compared with the unused steel. This was contrary to the decreased UTS and $R_p0.2$ and increased grain size reported by Golański[2]. The regenerative heat treatment resulted in a UTS and el% almost equal to and impact energy higher than that of the unused steel which means it successfully restored the mechanical properties.

References:
1. Williams, K.R., Wilshire, B. (1981) Materials Science and Engineering 47(2), 151.
2. Golański, G. (2010) Journal of Pressure Vessel Technology 132(6), 0645031.
3. Kumanin, V.I., Kovaleva, L.A., Sokolova, M.L. (1995). Met Sci Heat Treat 37(4), 136.

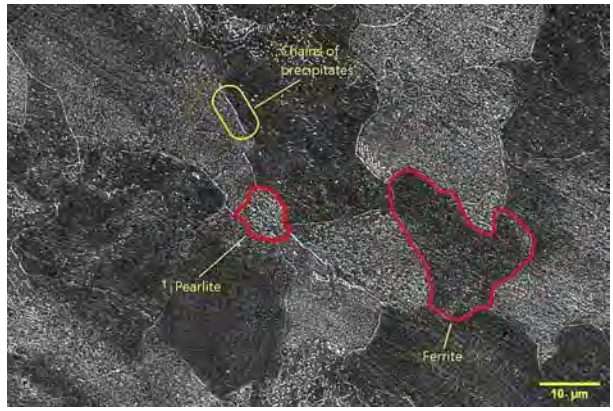

Figure 1. SEM-inLens SE image showing the ferrite + pearlite microstructure of unused 14MoV6-3 steel.

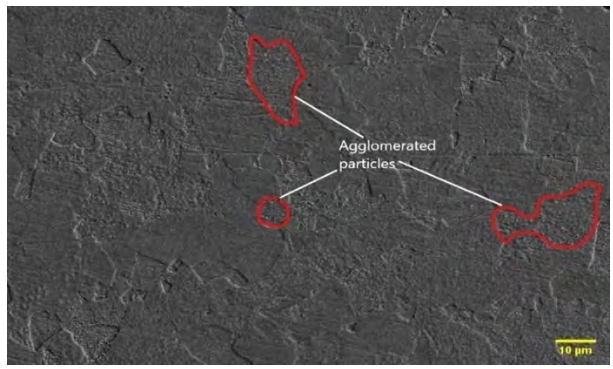

Figure 2. SEM-SE image showing agglomerated pearlite microstructure of regeneratively heat treated 14MoV6-3.

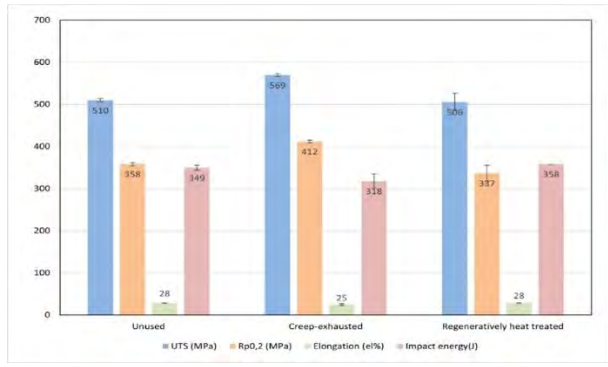

Figure 3. Mechanical properties of unused, creep-exhausted and regeneratively heat treated 14MoV6-3 steel.

Corresponding author: 1762618@students.wits.ac.za

THE SYNTHESIS AND CHARACTERIZATION OF GOLD@TIN(IV) OXIDE NANOCOMPOSITE MATERIALS

T. Makgale[1]

[1]University of Pretoria

In recent years, one of the most important topics of research has been devoted to the synthesis of metallic nanostructures with controlled sizes, shapes, architecture, composition, and properties. The purpose has been to acquire the nanostructures of gold, silver, gadolinium, and platinum, because these structures have proven to be the ideal building blocks in various applications including localized heat generation[1] , energy harvesting[2] , biosensing, optoelectronics, and catalysis[3] . However, many of these metallic nanostructures suffer significant drawbacks related to particle agglomeration and the formation of extended complex particle linkages. That is, many of their special properties are usually lost in the case of two or more particle interactions.

To improve the applicability of these materials, specifically of Gold (Au), which has profound properties allowing for a variety of potential applications related to its localized surface plasmonic resonance activity (LSPR), catalytic activity and bio-sensitivity and -compatibility. This study investigated the stabilizing effect of Tin(IV) oxide (SnO_2) on Au nanostructures, which naturally resulted in the fabrication of stable Au@SnO_2 (pronounced Tin(IV) oxide coated Au) nanoocomposite materials with improved applicability. Thus the improvement in their applicability is afforded from having SnO_2 coating acting as a distance holder phase, preventing core particle-particle interactions that would otherwise significant. Additionally, the core/shell composites may also allow for multiple properties to coexist in one material.

The synthesis of the Au@SnO_2 nanocomposite materials is a two-step process. The resulting nanocomposite materials were characterized using UV-VIS spectroscopy to measure the colloidal absorbances and evaluate their colloidal stabilities. Transmission electron microscopy (TEM) was used to study the various Au@SnO_2 systems to reveal the morphologies, structures, and particle distribution.

Three different Au@SnO_2 nanocomposite material systems of the core/shell architectural type were synthesised as depicted in the TEM micrographs in figures 1. These systems consisted of Au nanospheres (OD nannomaterials having sizes <100 nm in all directions) with average particle diameter of ~60 nm and ~208 nm , nanorods (1D nanomaterials having sizes <100 nm in two directions) have average legnths of 131 nm and 202 nm (diameter ~70 nm), and finally nanoprisms (2D nanomaterials with sizes <100 nm in only one direction, usually defined by thicknesses of a few atoms) have average areas of 15574 nm^2 and 18199 nm^{-2}, before and after coating with suitable amounts of the SnO_2 secondary distance-holder phase, respectivly. Figure 2 shows the absorption spectra of the colloids solutions of Au nanostructures uncoated and coated. The surface plasmon resonance (SPR) observed for the SnO_2 coated and uncoated Au nanosphere solutions had maxima at 550 and 522 nm, respectively. Those for Au nanorods indicated two maxima (corresponding to the transverse and longitudinal SPR) at 560 and 702 nm before coating, and at 562 and 710 nm after coating. For Au nanoprisms the maxima are observed at 562 nm before and after SnO_2 coating. The red shifts in the SPR bands of these SnO_2 coated Au nanostructures are due to the refractive index of the SnO_2 coating material. Furthermore, from the SPR spectra particularly for Au nanospheres, it can be observed that the SPR band for the coated nanospheres remains narrow from month to month compared to the uncoated nanosphere. Which is a clear indication of enhanced stabilization due to the coating material.

References:
1. Yuan, N., et al. (2015). J. Physics D: Applied Phys. 49(055302), 1-1.
2. Mohammadnia, A, et al. (2020). Energy Conservation management, 112352, 205.
3. Myeongju, K., and Younghun, K. (2020). Elsevier, 600(124957).

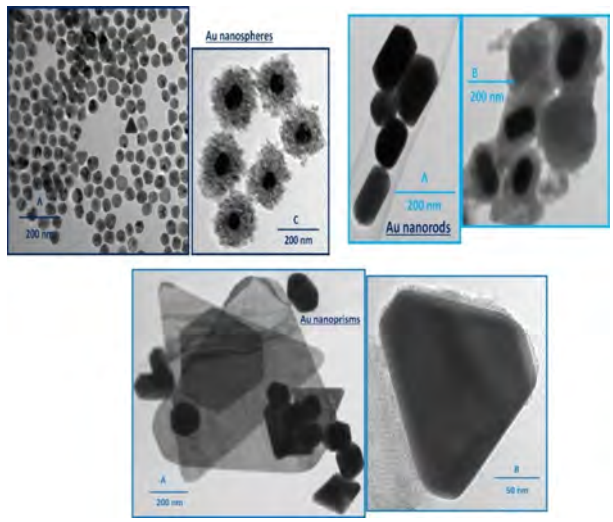

Figure 1. TEM micrographs showing the morphologies of gold nanospheres, nanorods, and nanoprisms before and after SnO_2-coating.

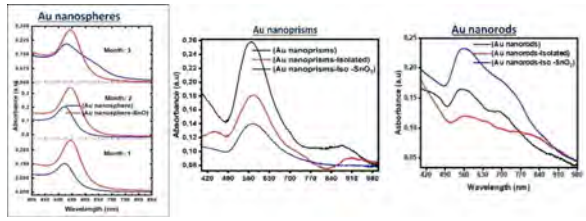

Figure 2. UV-VIs spectra showing the SPR bands of gold nanospheres, nanorods, and nanoprisms before and after SnO_2-coating.

Corresponding author: u14007739@tuks.co.za

INFLUENCE OF COATING TECHNIQUES ON THE STRUCTURAL AND OPTICAL PROPERTIES OF α-Fe_2O_3 NANOSTRUCTURES

A. Holtzhausen[1] and M.M. Diale[1]

[1]Department of Physics, University of Pretoria, Clean and Green Energy

Hematite (α-Fe_2O_3) is an abundant, cost-efficient n-type semiconductor with good thermal stability in aqueous mediums. Furthermore, it has a small indirect bandgap ranging from 1.9~2.2 eV which makes it favourable for photoelectrochemical water splitting[1]. Due to its stability, abundance and cost, hematite has been used for various applications in lithium batteries, pigments, photocatalysts and as photo anodes in photoelectrochemical water splitting[2].

In this study, the influence of coating techniques of hematite (α-Fe_2O_3) thin films was studied. Hematite thin films were synthesized on fluorine-doped tin oxide glass substrates, using two colloidal-based techniques namely dip coating and chemical spray pyrolysis. A solution of iron(III)nitrate nonahydrate ($Fe(NO_3)_3.9H_2O$, Sigma Aldrich, AR, 99%) was prepared as precursor solution. Four thin film layers were synthesized using dip coating and chemical spray pyrolysis. Thereafter, all films were annealed for one hour at 500 ºC to perform the calcination from magnetite (γ-Fe_2O_3) to hematite (α-Fe_2O_3). The morphological, optical, and structural properties of hematite were studied. X-ray diffraction was performed to study the structural properties of α-Fe_2O_3. Six peaks for α-Fe_2O_3 were identified from X-ray diffraction studies: (012), (104), (110), (024), (122) and (124). The corundum structure and high purity of hematite were confirmed by the (104) and (110) phases. Raman spectroscopy was used to confirm the structural and magnetic properties of α-Fe_2O_3. Seven vibrational modes of α-Fe_2O_3 in the first Brillouin zone were found using Raman spectroscopy: two A_{1g} and five E_g modes, confirmed from group theory. This furthermore confirmed the polycrystallinity of hematite. Using field emission scanning electron microscopy (FE-SEM), amorphous mesoporous hematite nanoparticles were found as seen in figure 1 and 2. Average grain intercept was used to determine the grain sizes averaged at 45.82 and 50.00 nm respectively. Optical studies were performed by ultraviolet-visible spectroscopy, which indicated good absorbance onset at 596.75 and 608.57 nm. From this work it was determined that coating techniques could contribute to the optical, structural, and morphological properties of hematite for applications in photoelectrochemical devices.

Furthermore, a modified annealing approach was used to determine the effects of annealing time from 30 mins to 1 hr on the structural, optical, and electronic properties of hematite thin films. Scanning electron microscopy indicated an increase in film thickness with annealing time. Ultraviolet-visible spectroscopy revealed a decrease in bandgap with prolonged annealing. Photocurrent measurements were performed by Mott-Schottky and linear scanning voltammetry analysis. A two-fold increase in photocurrent from 1.65 x 10^{-4} A.cm^{-2} to 4.77 x 10^{-4} A.cm^{-2} was found when annealing duration was increased. This study showed that an increase in annealing time influences the optical, structural, and electrical properties of nanostructured hematite thin films.

References:
1. Kong, H. et al. (2020) Journal of Physics and Chemistry of Solids. 144, 109504.
2. Souza, F.L. (2018) Anais da Academia Brasileira de Ciências. 90, 745.

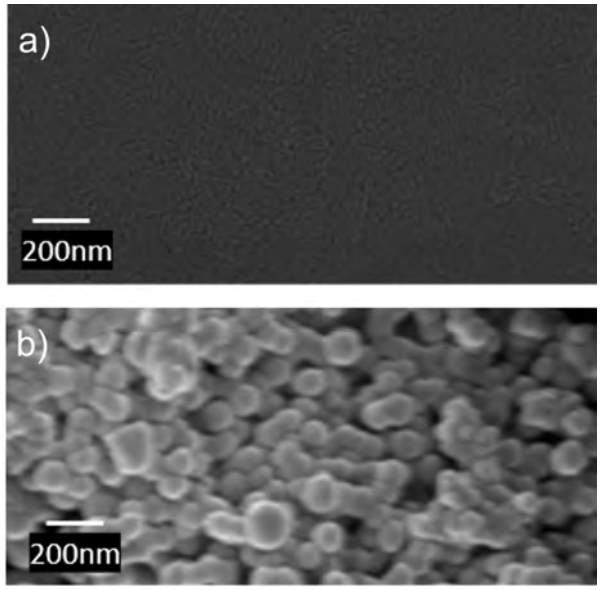

Figure 1. FE-SEM micrographs of α-Fe_2O_3 nanoparticles prepared by (a,b) chemical spray pyrolysis.

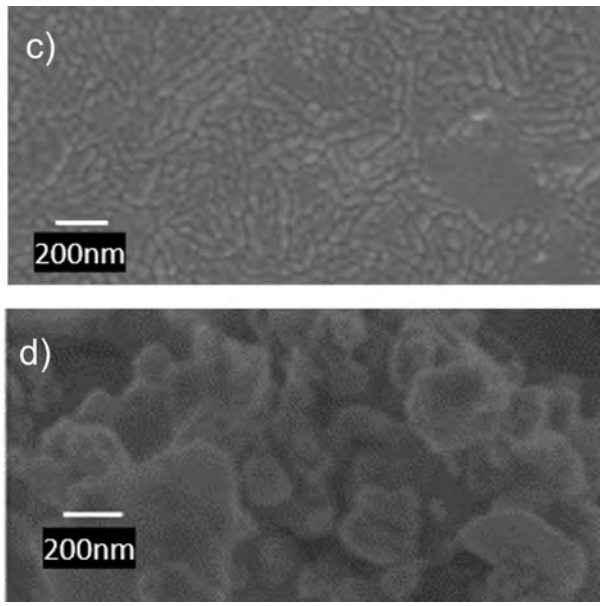

Figure 2. FE-SEM micrographs of α-Fe_2O_3 nanoparticles prepared by (c,d) chemical spray pyrolysis.

Corresponding author: mmantsae.diale@up.ac.za

EFFECTS OF MECHANICAL ALLOYING ON SPARK PLASMA SINTERING OF Fe-Ni-Si POWDERS

B.L. Bayode[1], A.O. Ogunmefun[1], T.S. Tshephe[1], M.M. Ramakokovhu[2] and Peter Olubambi[1]

[1]Center for Nanomechanics and Tribocorrosion, University of Johannesburg, Johannesburg, South Africa, [2]Institute of Nanoengineering Research, Tshwane Universiy of Technology, Pretoria, South Africa

Suitable Fe-Ni based alloys containing dissolved Si element are used as soft magnetic materials with good permeability in the design and fabrication of electrical and electronic component parts, for example in the fuel injection systems of internal combustion engines [1].

The control of grain size and size distribution, and compositional homogeneity remains a challenge in the fabrication of Fe-Ni-Si alloys by conventional fabrication techniques such as casting[2]. This limitation can be minimized by Spark plasma sintering (SPS), a novel powder metallurgy technique, which involves the use of predetermined powder formulations with desirable compositions and blends of particle sizes[1]. However, SPS is also plagued with the challenge of achieving full densification and effective metallurgical bonding of particles[2]. To obviate this challenge, mechanical alloying of precursor powders has been identified as an effective technique to ensure pre-alloying of powders have been achieved before being subjected for sintering in the SPS. This study, presents the effects of mechanical alloying of precursor powders (Fe70-Ni20-Si10, at%) and their subsequent spark plasma sintering performance. The powders were ball-milled using a gentle planetary ball mill (Retsch PM100 CM), at 12,18 and 24 hours respectively, at a speed of 350 rpm and ball-to-powder ratio of 10:1. Furthermore, spark plasma sintering was used to consolidate the alloyed Fe-Ni-Si powders to full densities by sintering at 900 ^{o}C at a dwell time of 5 minutes, and the mechanical properties measured.

As-milled powders coated with Iridium for EDS elemental mapping analyses and sintered solids were polished using standard grinding, polishing plates and cloths with diamond suspension pastes down to 1 µm sizes.A field emission scanning electron microscope (JEOL JSM-7900F), equipped with energy dispersive X-ray spectroscopy (Oxford Instrument AZtec software), operated at 20 kV accelerating voltage, a probe current of 818 pA and a working distance of 10 mm was used for the microstructural analysis. Phase identification of sintered specimens was done on a PANalytical Empyrian multi-platform X-ray diffractometer.

In Fig 1 A – D, the distribution of morphological and elemental characteristics of the powders are shown. Fig1A shows the elemental mixed powders with Ti and Ni appearing spherical in shapes, while the Si particles are platelike[3]. Ti particles are bigger in size than the Ni. Fig. 1B-C show an effective degree of alloying and decrease in average particle size of powders with increase in the milling time. Furthermore, at a lower milling time of 12 hrs (Fig 1B), the particles show good chemical homogeneity, whereas, as the milling time increased, precipitation of silicon particles (purple colour) was noticed. With increased milling time up to 24 hrs, greater amount of Si precipitation was noted from the powders, Fig. 1D. This precipitation of Si could be ascribed to the possible effects of increasing diffusion of impurities from the milling media into the powders during increased milling time[2]. These results indicate the effectiveness of the mechanical alloying parameters for pre-alloying of Fe-Ni-Si powders for subsequent SPS processing.

References:
1. Ismail, M.H. *et al.* (2012) Materials Letters 70, 142.
2. Hussein, M.A., Suryanarayana, C. and Al-Aqeeli, N. (2015) Materials & Design 87, 693.
3. Gordin, D. M. *et al.* (2008) Advanced Engineering Materials 10(8), 714.

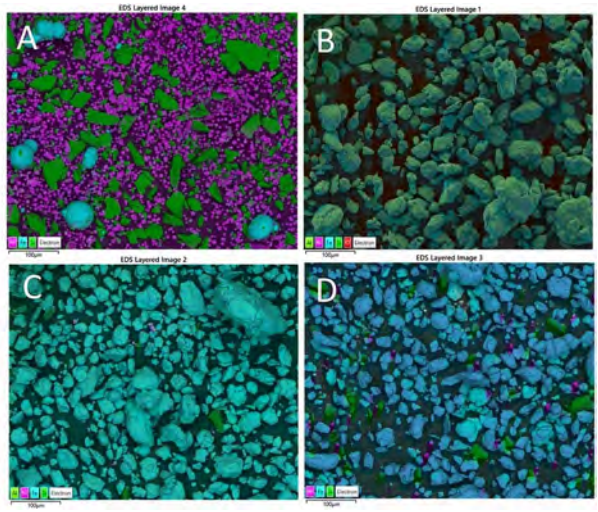

Figure 1. Figure 1. EDX Elemental Mapping: (A) Elemental powder mixtures (B) 12 hrs milled. (C) 18 hrs milled. (D) 24 hrs milled.

Corresponding author: bamlaw1st@gmail.com

IMMERSION STUDIES OF PLASMA SPRAYED HYDROXYAPATITE COATINGS DEPOSITED ON GEOMETRICALLY DIFFERENT Ti-6Al-4V ALLOY SUBSTRATES

U. Dockrat[1], T.T. Thabethe[1], J.B. Malherbe[1] and T. Nstoane[2]

[1]Dept. of Physics, University of Pretoria, Pretoria, [2]South African Nuclear Energy Corporation SOC Limited

A biomaterial is described as any material of synthetic or natural origin, which has the ability to repair or replace a function or a portion of the body in a secure, reliable, economic and physiologically acceptable manner to improve quality of life[1]. Biomaterials may be classified into bio-inert, bio-resorbable and bio-active. The bio-active materials, such as Hydroxyapatite (HAp), upon contact with the human body, interacts with the environment and grows to become part of the component. HAp is the second most thermodynamically stable and the least soluble of the calcium phosphates after fluorapatite (FAp)[2]. HAp contains many mineral and chemical similarities with that of natural bone and therefore it has been widely studied for the use of biomedical application as bone implants[3]. However, HAp exhibits weak mechanical properties such as brittleness. A metallic substrate with durable mechanical properties, coated with HAp, would therefore yield better stability. The HAp coating should have the ability to bond with the surrounding bone tissue and accelerate bone regeneration together with strong mechanical properties to withstand load-bearing applications[3].

This study focuses on investigating two sets of geometrically different titanium (Ti-6Al-4V) alloy substrates that were coated with HAp by air plasma spraying. Both sets of samples were immersed in Simulated Bodily Fluid (SBF) for varying time periods (0;7;28;56 days) to determine the biofunctional performance of the coatings. SEM, EDS and XRD were used to compare the surface morphology and microstructure of the coatings on both substrate geometries before and after immersion.

Samples were immersed in SBF with ionic concentrations as shown in Table 1. The surface morphology of the samples with cylindrical and plat-disk geometries, immersed in SBF for 7 days, are shown in Fig. 1 and 2 respectively. After immersion of the samples in SBF for 7 days an increase in porosity and a decrease in surface roughness is observed. Both surfaces appear similar with a lot of glassy regions. Cracks are now wider and also appear longer. There appears to be partially molten splats with spherulites grouped together. The weight percentage composition of the two samples before and after immersion was collected using EDS spot analysis. Analysis of the coating for both sample geometries after immersion for 28 days reveal the presence of Mg, Na, O and Ca with the latter two showing the highest concentrations. The presence of Mg and Na are related to the interacting of the sample with the SBF. For the flat disks the weight percentage of O was found to be much lower than that of the sample with cylindrical geometry with P having a slightly higher weight percentage. The wt% of P and Ca were found to decrease with immersion time due to nucleation taking place on the coating. XRD data showed visible structural changes after immersion in the SBF, supporting SEM data. There appeared to be an increase in the crystallinity of HAp.

References:
1. Park, J. and Lakes, R. (2010) Biomaterials. New York, Springer.
2. Dorozhkin, S. (2009) Biology and Medicine. 2(2), 399.
3. Kattimani, K., Kondaka, S. and K. Lingamaneni. (2016) BTRI. 7.

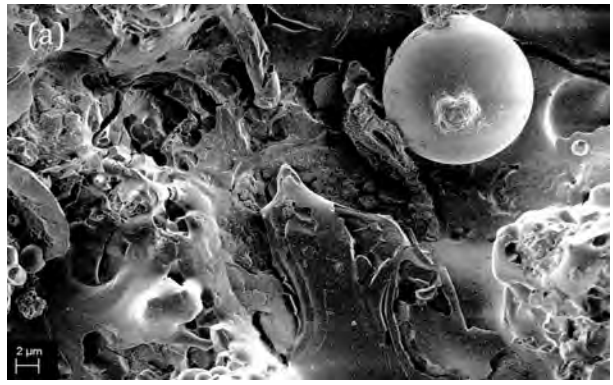

Figure 1. Scanning electron micrograph of HAp coating surface for the cylinder sample, after immersion for 7 days.

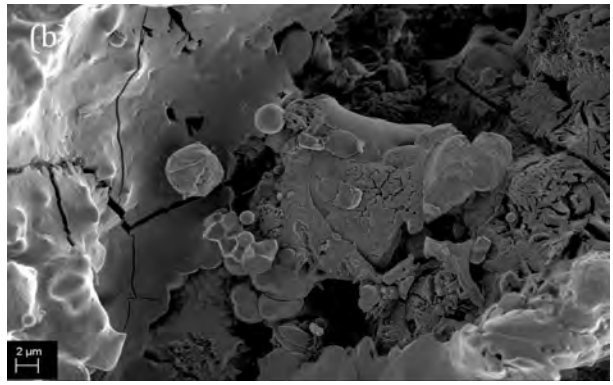

Figure 2. Scanning electron micrograph of HAp coating surface for the flat disk sample, after immersion for 7 days.

Table 1. Concentration of ions for blood plasma & SBF.

Ionic species	Ionic concentration of blood plasma in	Ionic concentration of *rSBF* in
Ca^{2+}	2.5	2.5
HPO_4^{2+}	1.0	1.0
Na^{+}	142.0	142.0
Cl^{-}	103.0	103.0
Mg^{2+}	1.5	1.5
K^{+}	5.0	5.0
SO_4^{2-}	0.5	0.5
HCO_3^{-}	27.0	27.0

Corresponding author: u17029245@tuks.co.za

COROSION BEHAVIOUR OF AUSTENITIC LOW-DENSITY STAINLESS STEELS IN SIMULATED BODY FLUIDS

MO Bodunrin[1,2], A Dladla[1], N Rundora[1] and D.E.P Klenam[1]

[1]School of Chemical and Metallurgical Engineering, University of the Witwatersrand, [2]DSI-NRF CoE in Strong Materials, University of the Witwatersrand

In the last few years, there has been a rapid increase in the demand for bioimplants. One of the major reasons for this is the increase in global population of older adults that are 60 years old or more[1]. Older adults are more prone to bone injuries that are aggravated by diabetes and other diseases that comes with ageing. Titanium, stainless steel and cobalt based alloys are metallic biomaterials that have continued to dominate the bioimplant market. Of these dominant biomaterials, titanium alloys are considered the gold standard owing to their low density, good corrosion resistance and excellent biocompatibility[2]. Titanium implants are not readily available to many patients because of the high cost of titanium alloys. Consequently, cheaper alternative like stainless steel implants, are mostly utilised. In developing countries where patients are mostly middle-or-low-income earners, 316L stainless steel implants are preferred. While the problem of cost is largely addressed when stainless steel implants are used, the high density and high elastic modulus of stainless steels pose other medical issues like osteopenia and revision surgery. By 2030, the percentage of older adults residing in the developing countries would exceed 70%[1]. This suggests that affordability of implant materials will be a major concern for middle-or-low-income patients who need implants. Hence, disability index may further increase at an alarming rate. To avoid this problem, either cheaper titanium alloys for making affordable implants are developed or low-density stainless steel (LDSS) implants are produced. There has been more research efforts on the cost reduction of titanium alloys[2].

In this study, the initial step of assessing the suitability of developing LDSS as bioimplant material was taken. Low-density stainless steels were considered because of their lower elastic modulus in comparison with conventional stainless steels[3]. Fe-(20 or 30)Mn-(12 or 15)Al-(0.5 or 1.5)C-5Cr austenitic LDSS were developed using electric arc melting. The density of the alloys was at least 14% less than the density of 316L stainless steel. The as-cast LDSS were subjected to microstructural examination using optical microscope and scanning electron microscope (SEM). The corrosion behaviour of the alloys were evaluated in two simulated body fluids, 0.9 wt% NaCl and Hanks balanced salt solution (HBSS). Open circuit potential and linear polarisation scans were performed on both commercial grade 316L stainless steel and austenitic LDSS in the as-cast condition. The corrosion rates were determined following ASTM standard G102-89. The microstructure of the corroded samples were analysed using SEM.

The results show that the microstructure of the as-cast LDSS consisted of austenitic matrix and M_7C_3 dendritic phase. From the polarisation curves in Fig. 1a, it can be seen that the corrosion potential of the as-cast LDSS are lower than that of 316L stainless steel. This indicates that thermodynamically, the as-cast austenitic LDSS are more susceptible to corrosion in 0.9 wt% NaCl. However, their corrosion rates were lower than that of 316L stainless steel especially in Fe-30Mn-15Al-1.5C-5Cr alloy i.e. ~0.12 mm/yr for 316L against ~0.015 mm/yr for the LDSS. The low corrosion rate suggest that kinetically, the as-cast LDSS has superior corrosion behaviour in comparison with 316L stainless steel. Similar trend was observed in HBSS (Fig. 1b) where corrosion rate was much lower in Fe-30Mn-15Al-1.5C-5Cr LDSS (~0.009 mm/yr) compared to 316L stainless steel (~0.086 mm/yr). The SEM image of the corroded sample is shown in Fig. 2, pitting corrosion which resulted from selective attack at the M7C3/matrix interface of the dendrites was observed. This is consistent in all the alloys investigated in both media. It is envisaged that the corrosion performance of LDSS can be further enhanced through microstructure control. This can be achieved through thermomechanical processing of these steels. This is currently being investigated.

References:
1. United Nations, World Population (2015) https://www.who.int/health-topics/ageing#tab=tab_1, Ageing.
2. Bodunrin M.O, Chown, L.H., Omotoyinbo J.A. (2020) materials Today Proceedings 38, 564-569.
3. Moon, J, Ha H.Y., Kim, K.W. et al., (2020) Sci Rep 10, 12140.

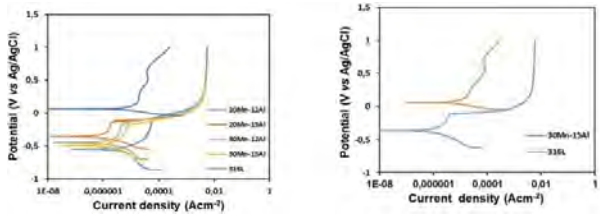

Figure 1. *Polarisation curves of 316L stainless steel and low-density steels in (a) 0.9 wt% NaCl and (b) HBSS.*

Corresponding author: michael.bodunrin@wits.ac.za

TUNING PREPARATION – INDUCED RELAXATION DYNAMICS IN HETEROGENEOUS POLYMER FILMS

A. A. Mulama[1,2], A. O. Oduor[1] and G. Reiter[2]

[1]Department of Physics and Materials Science, Maseno University, Kisumu, Kenya, [2]Department of Physics, University of Freiburg, Freiburg, Germany

The ever growing demand of miniaturization, increased functionality, high performance and low cost for microelectronic products and packaging require tuning of polymer properties. This can be done through polymer blending and annealing which enhances maximum performance of the polymer films. Forcing a polymer to spread on a substrate it does not like leaves the resulting film unstable[1]. Dewetting is the process through which the film tries to minimize the contact with the substrate, resulting in a retraction of the fluid from the surface (Figure 1a)[1,2]. Dewetting experiments on thin polymer layers allow for precise probing of viscoelastic properties. Despite the rapid progress in the dewetting of thin polymer films, there are still open questions regarding the symmetry breaking of thin films[1].

The dewetting of polymer blends consisting of different mixtures of polymers, e.g. semi-flexible and rod-like polymers embedded in a coil-like polymer has so far not been intensively investigated. The additional degrees of freedom of the stiff component and the possibility of a developing anisotropy are expected to cause strong deviations of the dewetting process compared to flexible polymer dewetting[1-4]. The study used dewetting as a characterization tool to demonstrate that viscoelastic properties of thin isotactic poly(*para*-methylstyrene) (iP*p*MS) films can be regulated and tuned by blending with isotactic polystyrene (iPS) under ageing conditions and substrate interactions[3,4]. Further characterization on the spin-coated films was done by optical microscopy (OM), atomic force microscopy (AFM), X-ray diffractometry (XRD) and differential scanning calorimetry (DSC)

The iP*p*MS - iPS films were aged at temperatures below glass transition temperature of iP*p*MS . Ageing temperature was found to have a direct influence on the dewetting dynamics in iP*p*MS - iPS films[3]. Further, the preparation - induced residual stresses in the deposited iP*p*MS - iPS films were found to be sources of damage for the films and decreased with ageing temperature. The dewetting of iP*p*MS - iPS revealed asymmetric rims and logarithmic laws were applied in explaining the observed non-linear viscoelastic properties (Figure 1b). Preparation-induced residual stresses, the corresponding relaxation times as well as the rupture probability of iP*p*MS - iPS films varied by orders of magnitude following scaling relations. Thinner films (≤ 100 nm) exhibited high residual stresses accompanied by shorter relaxation times compared to thicker films (> 100 nm). The experimental findings suggest that dewetting in heterogeneous polymer films can enhance properties and hence maximize the performance of thin polymer films for nano-fabrication applications if appropriate processing conditions are chosen.

References:
1. Chandran, S. et al. (2017) ACS Macro Lett., 6, 1296-1300.
2. Gabriele, S. et al. (2006) Journal of Polymer Science: Part B: Polymer Physics, 3022-3030.
3. Mulama, A. A. et al. (2020) Macromolecules, 53(20), 9122 – 9130.
4. Mulama, A. A. et al. (2019) Macromolecules, 52(20), 7894 – 7903.

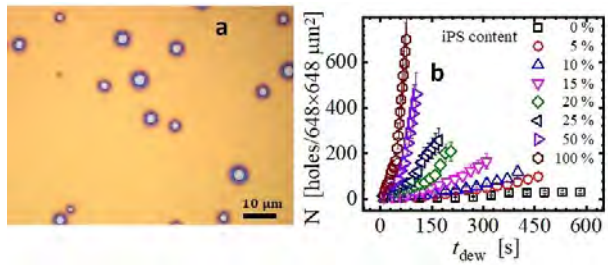

Figure 1. (a) Micrographs showing dewetting dynamics in the iP*p*MS – iPS blend system (5 % of iPS content) at a dewetting temperature of 200 ˚C and dewetting time ~ 60 seconds, (b) A graph of Number of holes observed per an area of 648 × 648 µm2 against dewetting time at different concentration of iPS due to differences in residual stresses in the spin-coated films.

Corresponding author: mulamaustine@gmail.com

MICROSTRUCTURE EVALUATION OF Ti-35Nb-10ZrO-5Ta-xCu PREPARED BY SPARK PLASM SINTERING FOR BOIMEDICAL APPLICATION

R.A. Busang[1], M.L. Teffo[1], B.J. Babalola[2] and B.L Bayode[2]

[1]Institute of Nanoengineering Research, Tshwane University of technology, Department of Chemical, Metallurgical and Materials engineering, Tshwane., [2]Centre for Nanoengineering and Tribocorrosion, University of Johannesburg, Johannesburg

Titanium based materials are widely used in different engineering applications because of their excellent combination of high strength, low density, and corrosion resistance. In biomedical applications, they are used to restore functionality of human body parts that have undergone trauma or diseases[1,2].

According to Lutjering4, Titanium and its alloys can be categorized as the following phases: α, near α, (α + β), β & near-β. To get from α phase to β phase, pure titanium must be subjected to temperatures above 882 °C. The first requirement of biomedical materials is that they must be bio-compatible and should not cause any detrimental side effects or pain and be long lasting[3]. Through the addition of certain alloying elements to Ti it may fulfil these requirements.

The fabrication of this alloy by conventional casting technique is associated with certain inherent flaws. Thus, in this study a beta Ti-35Nb-10ZrO-5Ta-xCu (0-5%) has been developed through spark plasma sintering of mechanically alloyed precursor powder mixtures. The aim is to investigate the effect of Cu additions on the microstructure and crystallographic characteristics of this alloy with specific focus on the mechanical and corrosion behavior of the sintered alloys. Sintering parameters used include temperature of 1200 ˚C, a pressure of 50 MPa, heating rate of 100 ºC/min, and a holding of 10 minutes.

The resulting sintered samples were first subjected to standard metallographic sample preparation, and thereafter analyzed in a field emission scanning electron microscope (JEOL JSM-7900F), equipped with energy dispersive X-ray spectroscopy (Oxford Instrument), operated at 10 kV accelerating voltage and at a working distance of 10.1 mm. Phase identification of sintered specimens was also done on a PANalytical Empyrian X-ray diffractometer.

The microstructural characteristic of the sintered samples is presented in Figure 1. Regions with distinctly different contrast is observed in the microstructure viz: dark regions, light grey and dark grey regions. Information obtained from the EDS and XRD analyses, suggested the darkest region to be the alpha phase, while grey regions are the beta phases. In Figure 1A, the microstructure is seen to be predominantly composed of the beta phase, with a small proportion of isolated alpha phase at the grain boundaries of the beta phase. However, with the addition of Cu to the base alloy in successive 1% increments (Figure 1B-F), the proportion of alpha phase is seen to increase. At 2% Cu addition (Figure 1C), the alpha phase becomes predominant, precipitating on the grain boundaries of the beta phase. Concurrently, relatively small alpha-beta lath precipitates formed within the beta grains. The proportion of these laths, as observed in Figures 1(C-F) increases with increasing Cu addition.

Furthermore, the light grey and dark grey microstructures were found to be Nb-rich and Ni-lean beta phases respectively. It is also noted that as Cu content increases, the Nb-rich beta phase depletes in proportion. The observed microstructural evolution that occurred in this study could be attributed to the effect of changes in the reactivity potential of participating elements due to the addition of Cu[4]. The beta phases are found to be rich in Cu as well as beta stabilizing elements such as Nb and Ta, while the alpha phases are devoid of Cu and thus, have minimal amounts of the beta stabilizing elements. The changes in microstructures are found to affect the wear and corrosion behavior of the alloys. The addition of Cu lowers the coefficient of friction and improves wear resistance; however, at 5% Cu addition a slight improvement in corrosion resistance is observed when immersed in NaCl solution.

References:
1. Bo-Qiong, L., et al. (2019) Rare metals. 38, 6.
2. Hussein, M.A., Suryanarayana, C. and Al-Aqeeli, N. (2015) Materials & Design. 87, 693.
3. Konopatsky, A.S., et al. (2017) Mater. Sci. and Eng. A, 702, 301
4. Lutjering, G. (1999). Mater. Sci. and Eng. A. 263, 117.

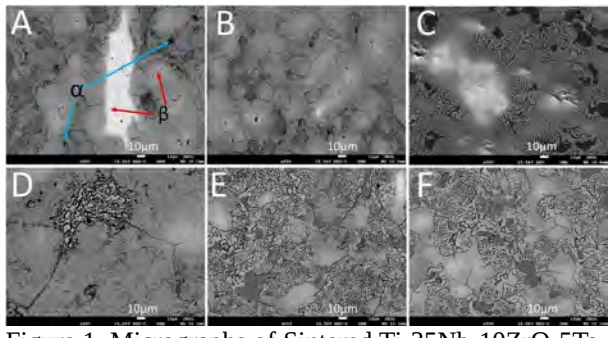

Figure 1. Micrographs of Sintered Ti-35Nb-10ZrO-5Ta-x%Cu: (A) 0% Cu, (B) 1% Cu, (C) 2% Cu, (D) 3% Cu, (E) 4% Cu and (F) 5% Cu.

Corresponding author: busangkgantso81@gmail.com

CHARACTERISATION OF VO_x/MgO CATALYSTS PRODUCED USING SOLUTION COMBUSTION SYNTHESIS: A MIXED FUEL APPROACH

S. Padayatchee[1], H.B. Friedrich[1], P. Ntola[2], A. Govender[3] and E.J. Olivier[4]

[1]School of Chemistry, University of KwaZulu Natal, Durban , [2]Department of Chemistry, Durban University of Technology, Durban, [3]Group Technology, Sasol South Africa (Pty) Ltd., Sasolburg, [4]Centre for HRTEM, Physics Department, Nelson Mandela University, Port Elizabeth

Converting olefins and aromatics by oxidative dehydrogenation (ODH) with O_2 is an alternative route to the conventional thermodynamically challenged alkane dehydrogenation[1]. Supported vanadium oxide catalysts are popular in oxidation reactions because they exhibit the best stability and the highest steady-state activity[2]. Solution combustion synthesis (SCS) has distinct advantages which are simplicity of method, short reaction times, and the capability to regulate microstructure and thereby the activity and selectivity of catalysts[3]. Previous findings have shown the applicability of synthesizing VO_X/MgO catalysts with SCS using a single fuel[4].

In this study, VO_x/MgO catalysts were synthesized via SCS using a mixed fuel approach with magnesium nitrate hexahydrate ($MgNO_3.6H_2O$) and ammonium metavanadate (NH_4VO_3) as precursors with a targeted 15wt% V_2O_5 loading. The purpose of the study was to investigate the use of mixed fuels to further regulate the temperature-time history of each reaction towards a desired microstructure. For this purpose, catalysts were prepared using the fuels Glycine (GLY), Hydrazine hydrate (HH) and Urea (UR) in mixed (1:1) binary formulations as shown in Table 1.

Table 1 also shows the relative phase abundance and type of vanadate phase formed for each catalyst produced, along with the measured surface area obtained from XRD (with Rietveld refinement), and BET respectively. The microstructure of each catalyst was characterised by SEM and aberration corrected TEM using a double aberration corrected JEOL ARM200F. Figure 1 shows a hollow-cone diffractive image of a catalyst prepared using mixed GLY and HH as fuel. The bright regions indicate the positions of vanadate phases distributed on the MgO catalyst support formed during reaction.

Preliminary findings indicate that the use of a GLY/HH as mixed fuel leads to a catalyst with microstructure indicative of a high temperature rapid combustion process. This is consistent with the combustion behaviour of both GLY and HH as single fuels. Overall the GLY/HH catalyts yielded the highest surface area in combination with the formation of the preferred pyro vanadate ($Mg_2V_2O_7$) phase, close to the targeted V_2O_5 loading. The catalysts prepared using UR as component in the mixed fuel yielded materials with an overall lower surface area as compared to the GLY/HH catalyst, indicative of a slower combustion process also consistent with the single fuel behaviour of UR. Further findings related to the microstructure of each catalyst as compared to the catalysts produced using single fuels will be discussed.

References:
1. Friedrich, H.B. *et al.* (2006) Applied Catalysis A: General 297, 81.
2. Dasireddy, V.D.B.C *et al.* (2012) Applied Catalysis A: General 421–422, 58.
3. Kingsley, J.J. and Patil, K.C. (1988) Materials Letters 6, 427
4. Ntola, P. *et al.* (2022) Materials Chemistry and Physics 278, 125602

Table 1. XRD and BET findings of the VO_x/MgO catalysts prepared using mixed fuels.

Catalysts	XRD Abundance wt%	Vanadate phases	BET (surface area)
VOx/MgO (UR/GLY)	5.3%	$Mg_3(VO_4)_2$	14.7 sq. m/g
VOx/MgO (GLY/HH)	15.6%	$Mg_2V_2O_7$	37.7 sq. m/g
VOx/MgO (HH/ UR)	17.0%	$Mg_3(VO_4)_2$	23.7 sq. m/g

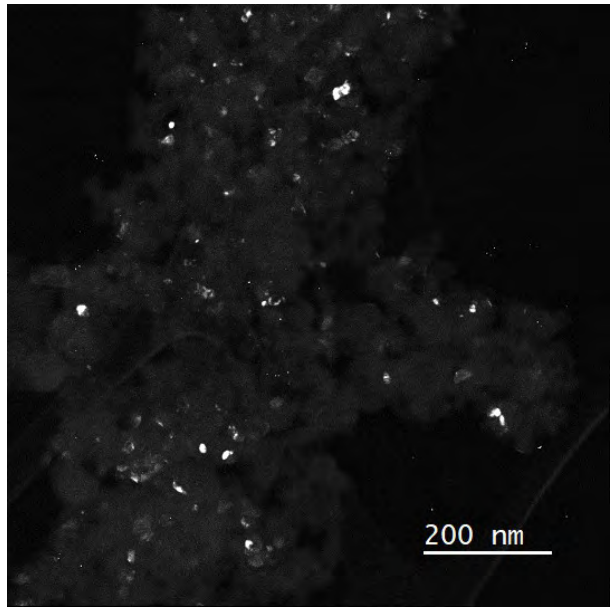

Figure 1. Hollow-cone diffractive image of a GLY/HH catalyst. The bright regions indicate the positions of vanadate phases.

Corresponding author: 21002028@dut4life.ac.za

Author Index

Linking materials performance to microstructure

In Situ Lab for ZEISS FE-SEM

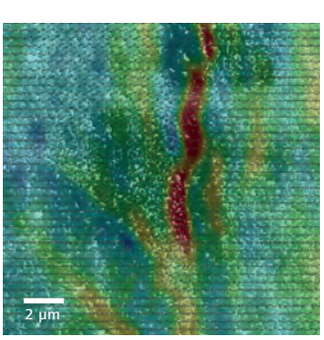

Implement unattended automated *in situ* workflows with the *in situ* lab for your ZEISS FE-SEM. Combine a tensile or compression stage, a heating unit, and high-temperature detectors with EDS or EBSD. Control all components from a single PC. Collect highly reproducible, precise, and reliable data with high throughput. Create statistically representative results. Process your data using digital image correlation.

zeiss.com/fesem-insitu
info.za@zeiss.com

ZEISS

Seeing beyond

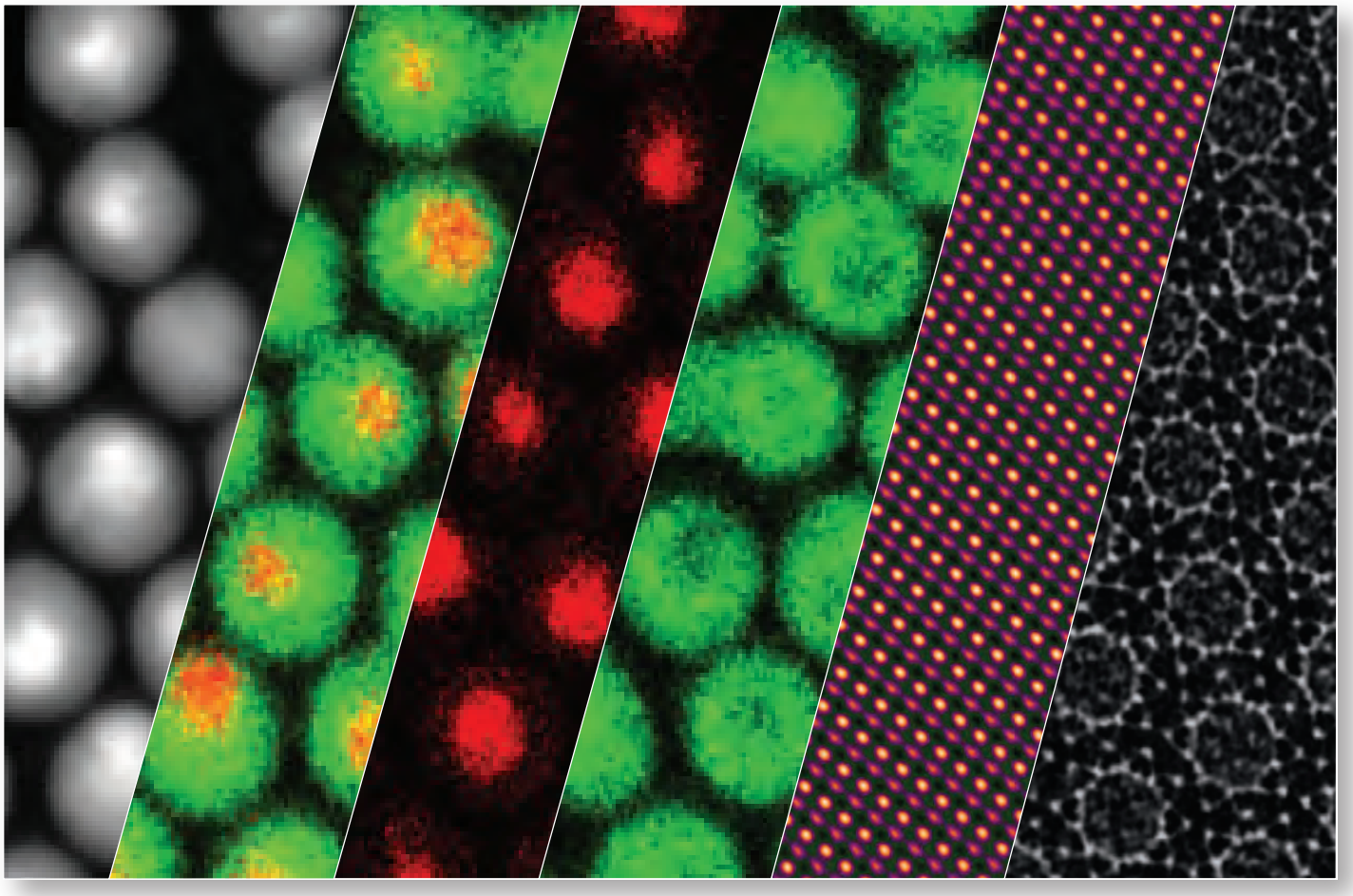

Breaking Barriers with Today's Most Powerful Workhorse S/TEM

The F200 does more to change the accepted views of uncorrected S/TEM than ever before. Its enhanced cold field-emission source, large-area silicon drift detectors, and electron optics stability are the foundation for capabilities that exceed the expected.

- Atomic-scale imaging – even for thick specimens
- High spatial resolution – even at low kV
- Spatially-resolved analytical information with EDS/EELS
- Optimum Bright Field (OBF) STEM – Maximum S/N at low dose
- Light element detection

With the F2, you'll never have to compromise. Get the performance you need in one powerful TEM that does more than you'd expect.

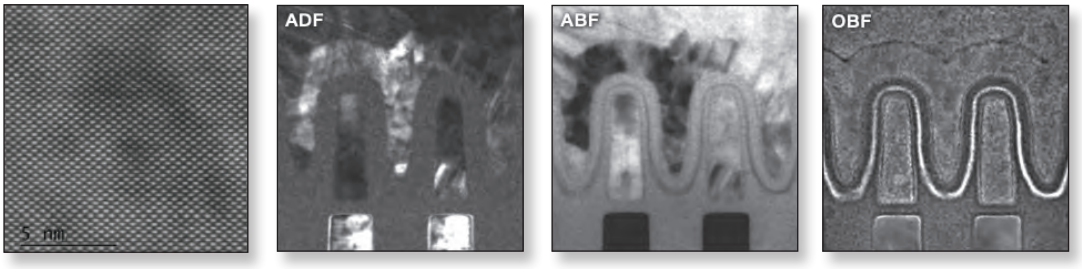

JEOL

www.jeol.com

For more information, contact Angstrom Scientific on
(011)462-1347 • sales@angstrom.co.za • www.angstrom.co.za